NEW ANTIBACTERIAL NANOMATERIALS BASED ON GALLIUM, GOLD AND HYDROXYAPATITE

Mario Kurtjak

Doctoral Dissertation
Jožef Stefan International Postgraduate School
Ljubljana, Slovenia

Supervisor: Prof. Dr. Danilo Suvorov, Jožef Stefan Institute, Ljubljana, Slovenia
Supervisor: DDr. Marija Vukomanović, Jožef Stefan International Postgraduate School, Ljubljana, Slovenia

Evaluation Board:
Prof. Dr. Boris Turk, Chair, Jožef Stefan International Postgraduate School, Jožef Stefan Institute, Ljubljana, Slovenia
Prof. Dr. Rok Kostanjšek, Member, University of Ljubljana, Biotechnical Faculty, Ljubljana, Slovenia
Prof. Dr. Dragan Uskoković, Member, Institute of Technical Science of the Serbian Academy of Sciences and Arts, Belgrade, Serbia

MEDNARODNA PODIPLOMSKA ŠOLA JOŽEFA STEFANA
JOŽEF STEFAN INTERNATIONAL POSTGRADUATE SCHOOL



Mario Kurtjak

NEW ANTIBACTERIAL NANOMATERIALS BASED ON GALLIUM, GOLD AND HYDROXYAPATITE

Doctoral Dissertation

NOVI ANTIBAKTERIJSKI NANOMATERIALI NA OSNOVI GALIJA, ZLATA IN HIDROKSIAPATITA

Doktorska disertacija

Supervisor: Prof. Dr. Danilo Suvorov

Supervisor: DDr. Marija Vukomanović

Ljubljana, Slovenia, May 2017

Acknowledgments

First of all, I would like to express my large gratitude to my supervisors Prof. Dr. Danilo Suvorov and DDr. Marija Vukomanović for choosing me such an interesting topic, for believing in me, being very supportive and patient with me, and giving many useful suggestions that improved my planning of experiments, organisation of results, presentations and publications. I am particularly thankful to DDr. Marija Vukomanović for guiding me through (especially in the beginning), helping me with the experiments, analyses and explanations of the results, but giving me also the necessary freedom. And foremost for her great effort by which the requirements were always carried out on time despite my lack of good time planning. I would like to thank Prof. Danilo Suvorov for giving me the opportunity to carry out my doctoral work at the K-9 department, which I found a perfect place for an inquisitive young researcher to fulfil his curiosity, realise his ideas and become an independent creative scientist. Here I would also like to thank the Slovene Research Agency (ARRS) for funding young researchers. Then I would also like to thank certain people who importantly contributed to the presented doctoral thesis:

- Univ. Dipl. Fiz. Andraž Krajnc for doing the nuclear magnetic resonance experiments;
- Univ. Dipl. Kem. Lovro Kramer for conducting the cytocompatibility tests;
- my dear colleagues Univ. Dipl. Inž. Kem. Tehn. Nemanja Aničić and Univ. Dipl. Inž. Kem. Inž. Tilen Sever for creating a brainstorming atmosphere in the office, in which many problems were solved through our fruitful scientific conversations and debates and our close friendship was established. Nemanja has also done the TGA/DSC analyses and Tilen has built a Schlenk line for the thermal decomposition experiments;
- Dipl. Inž. Fiz. Damjan Vengust for always being there, ready for many useful scientific discussions and for teaching me the first steps in electron microscopy;
- Dr. Boštjan Jančar for the subsequent course and training in transmission electron microscopy;
- Dr. Dejan Klement and Dr. Matjaž Spreitzer for the XRD experiments on the Empyrean X-ray diffractometer;
- technical associate Silvo Zupančič for the measurements of the specific surface area.

Finally, I would like to thank my family for their encouragement and support, understanding my commitment to the doctoral work and accommodating to my new lifestyle although it has affected their lives very much as well.

Abstract

Modified hydroxyapatite with antibacterial properties and high biocompatibility with mammalian cells is very desirable in many biomedical applications. The increasing problem of bacterial resistance against conventional antibiotics calls for investigation of alternative antimicrobials, such as metal ions and nanomaterials. In this thesis, different modifications of hydroxyapatite based on gallium and gold are explored to obtain new antibacterial materials with low toxicity: incorporation of Ga^{3+} ions, attachment of Ga nanoparticles to hydroxyapatite, attachment of functionalised gold nanoparticles on the Ga(III)-doped hydroxyapatite and attachment of functionalised Ga/Au core/shell nanoparticles onto hydroxyapatite. The physicochemical properties, ion-release characteristics in physiological conditions, antibacterial performance against *P. aeruginosa*, *E. coli* and *S. epidermidis*, and *in-vitro* cytotoxicity for mammalian cells (L929 mouse fibroblasts, IMR-90 human lung fibroblasts and U2OS osteosarcoma cells) are presented. Incorporation of Ga(III) into hydroxyapatite occurs in a thin amorphous surface layer of hydroxyapatite by substitution of Ca^{2+}. Different morphologies were obtained by adding Ga^{3+} ions at different stages of the hydroxyapatite synthesis and different Ga(III) contents by varying the Ga^{3+} concentration. The release of Ga^{3+} ions from the Ga(III)-containing hydroxyapatite depended on the overall amount of Ga in the material, while the biological response was mediated by the composition of the amorphous surface layer. The mainly Ca-phosphate amorphous surface layer resulted in a low antibacterial efficiency, while the mainly Ga-phosphate amorphous surface layer resulted in a high antibacterial efficiency, but also cytotoxicity. The widest concentration range (from 0.3 g/L to at least 1 g/L) of antimicrobial action against *P. aeruginosa* and low toxicity to mammalian cells was obtained at 4 wt% of Ga(III) and by adding Ga^{3+} ions during transformation of the precursor octacalcium phosphate/hydroxyapatite crystals to the final hydroxyapatite crystals. Nanocomposites of Ga nanospheres on hydroxyapatite laths/plates with different Ga content (6 to 32 wt %), different average Ga particle size (15 to 40 nm) and different width of Ga particle size distribution were also prepared and two different synthesis methods were compared. Nanocomposites with optimum properties were obtained by an ultrasonic emulsification method without using any surfactants and the antibacterial action was found to be primarily a result of the dissolution of the Ga nanoparticles and consequent local release of Ga^{3+} ions. The nanocomposite containing 16 wt % of Ga NPs with diameters of 22±11 nm exhibited better antibacterial properties against *P. aeruginosa* and lower *in-vitro* cytotoxicity for human lung fibroblasts IMR-90 and mouse fibroblasts L929 (efficient antibacterial action and low toxicity from 0.1 to 1 g/L) than a comparable nanocomposite of hydroxyapatite and silver nanoparticles (efficient antibacterial action and low toxicity from 0.2 to 0.25 g/L). Addition of a gallium component (incorporation of Ga(III) into the disordered surface layer or attachment of Ga NPs) provided the hydroxyapatite with antibacterial action against *P. aeruginosa*, but not against *E. coli* and *S. epidermidis*, whereas the functionalised nanogold component provided the antibacterial properties against *E. coli* and *S. epidermidis* but not against *P. aeruginosa*. Both antibacterial components were

successfully combined in a nanocomposite composed of the optimum hydroxyapatite with incorporated Ga^{3+} ions and Au nanoparticles functionalized with arginine attached to its surface. This material is efficient against *E. coli*, *S. epidermidis* and *P. aeruginosa* and has a wide concentration range of antibacterial efficiency with low cytotoxicity (from 0.2 to 0.75 g/L). Such nanocomposites with combined antimicrobial effect present an innovative way for prevention and cure of bacterial infections and seem a promising human-friendly alternative for antibiotics and Ag-based antibacterial materials in treatments of infections by bacteria resistant to antibiotics.

Povzetek

Modificirani hidroksiapatit z antibakterijskimi lastnostmi in dobro biokompatibilnostjo s sesalskimi celicami je zelo zaželen v mnogih biomedicinskih aplikacijah. Pri tem predstavlja resno težavo pomanjkanje novih antibiotikov in čedalje manjša učinkovitost obstoječih zaradi hitrega razvoja in širjenja bakterijske odpornosti na antibiotike. Zato je smiselno iskati alternativna antimikrobna sredstva, kot so kovinski ioni in nanomateriali. V priloženi doktorski disertaciji sem raziskoval različne modifikacije hidroksiapatita na osnovi galija in zlata z namenom razviti nove antibakterijske materiale z nizko toksičnostjo. Te modifikacije so: vgrajevanje Ga^{3+} ionov, pritrditev Ga nanodelcev na hidroksiapatit, pritrditev funkcionaliziranih zlatih nanodelcev na z Ga(III) dopirani hidroksiapatit in pritrditev funkcionaliziranih Au nanolupin z Ga jedrom na hidroksiapatit. V disertaciji so predstavljene fizikalno-kemijske lastnosti dobljenih materialov, sproščanje ionov pri fizioloških pogojih, antibakterijsko delovanje proti *P. aeruginosa, E. coli* in *S. epidermidis* ter *in-vitro* citotoksičnost za sesalske celice (L929 mišje fibroblaste, IMR-90 človeške pljučne fibroblaste in U2OS osteosarkoma celice). Vgrajevanje Ga(III) v hidroksiapatit poteče v tanki površinski amorfni plasti hidroksiapatita z zamenjavo Ca^{2+}. Različne morfologije sem dobil z dodajanjem Ga^{3+} ionov v različnih fazah sinteze hidroksiapatita, različne vsebnosti Ga(III) pa s spreminjanjem koncentracije Ga^{3+}. Sproščanje Ga^{3+} ionov iz Ga(III)-vsebujočega hidroksiapatita je bilo odvisno od celotne vsebnosti Ga v materialu, medtem ko je na biološki odziv bistveno vplivala sestava površinske amorfne plasti. Pretežno Ca-fosfatna plast je vodila do nizke antibakterijske učinkovitosti, pretežno Ga-fosfatna plast pa do visoke antibakterijske učinkovitosti, a hkrati tudi citotoksičnosti. Najširše koncentracijsko območje (od 0,3 g/L do vsaj 1 g/L) antibakterijskega delovanja proti *P. aeruginosa* in nizke toksičnosti za sesalske celice je bilo doseženo pri 4 masnih % Ga(III) in dodajanju Ga^{3+} ionov med transformacijo prekurzorskih kristalov iz oktakalcijevega fosfata/hidroksiapatita v končne kristale hidroksiapatita. Pripravil sem tudi nanokompozite Ga nanokroglic na hidroksiapatitnih deščicah/ploščicah z različno vsebnostjo Ga (6 do 32 masnih %), z različno povprečno velikostjo Ga delcev (15 do 40 nm) in z različno širino porazdelitve velikosti ter primerjal dve različni metodi sinteze. Nanokompozite z najboljšmi lastnostmi sem dobil z metodo ultrazvočne emulzifikacije brez uporabe surfaktantov. Antibakterijsko delovanje teh materialov je izviralo pretežno iz raztapljanja Ga nanodelcev in posledičnega lokalnega sproščanja Ga^{3+} ionov. Nanokompozit, ki je vseboval 16 masnih % Ga nanodelcev s premeri 22±11 nm, je imel boljše antibakterijske lastnosti in manjšo *in-vitro* citotoksičnost kot primerljivi nanokompozit hidroksiapatita in srebrovih nanodelcev. Nanokompozit z Ga nanodelci je namreč kazal učinkovito antibakterijsko delovanje proti *P. aeruginosa* ter nizko toksičnost za pljučne fibroblaste IMR-90 in mišje fibroblaste L929 v koncentracijskem območju od 0,1 do 1 g/L, medtem ko je bilo takšno območje koncentracij v primeru nanokompozita z Ag nanodelci le od 0,2 do 0,25 g/L. Dodatek galijeve komponente (vgrajevanje Ga(III) v neurejeno površinsko plast ali pritrditev Ga nanodelcev) je hidroksiapatitu priskrbel antibakterijsko aktivnost proti *P. aeruginosa*, toda ne tudi proti *E. coli* ali *S. epidermidis*, medtem ko je funkcionalizirano nanozlato omogočilo antibakterijsko delovanje

proti *E. coli* in *S. epidermidis*, ne pa proti *P. aeruginosa*. Obe antibakterijski komponenti sta bili uspešno združeni v nanokompozitu iz optimalnega hidroksiapatita z vgrajenimi Ga^{3+} ioni in Au nanodelcev, funkcionaliziranih z argininom in pritrjenih na površino hidroksiapatita. Ta material je učinkovit proti *E. coli, S. epidermidis* in *P. aeruginosa* in ima široko koncentracijsko območje antibakterijske učinkovitosti z nizko citotoksičnostjo (od 0,2 do 0,75 g/L). Takšni nanokompoziti s kombiniranim antimikrobnim učinkom predstavljajo inovativen in učinkovit način preprečitve in zdravljenja bakterijskih infekcij, ki je obetavna alternativa za antibiotike in antibakterijske materiale na osnovi Ag pri zdravljenju okužb z bakterijami, odpornimi na antibiotike.

Contents

List of Figures **xvii**

List of Tables **xxiii**

Abbreviations **xxv**

Symbols **xxvii**

1 Introduction **1**
1.1 The Antibiotic Resistance Problem . . . 1
1.1.1 Antibacterial action of antibiotics . . . 4
1.2 Antibacterial Inorganic Ions . . . 5
1.2.1 Categorization and the main representatives . . . 5
1.2.2 Antibacterial mechanisms . . . 8
1.2.2.1 Reactive oxygen species . . . 8
1.2.2.2 Antioxidant inactivation . . . 10
1.2.2.3 Protein dysfunction and loss of enzyme activity . . . 10
1.2.2.4 Impaired membrane function . . . 11
1.2.2.5 Interference with nutrient assimilation . . . 11
1.2.2.6 Effect on nucleic acids . . . 11
1.2.3 Bacterial resistance to metal ions . . . 12
1.2.4 Cytotoxicity of metal ions . . . 13
1.3 Antibacterial Action of Nanomaterials . . . 13
1.3.1 Categorization and the main representatives . . . 13
1.3.2 Antibacterial mechanisms . . . 15
1.3.2.1 Reactive oxygen species . . . 15
1.3.2.2 Dissolution of nanoparticles and local release of antibacterial ions . . . 17
1.3.2.3 Nanosize-specific mechanisms . . . 18
1.3.3 Gold nanoparticles . . . 19
1.3.4 Multiple targets and cytotoxicity . . . 20
1.4 Gallium . . . 21
1.4.1 Ionic gallium . . . 21
1.4.2 Elemental gallium . . . 23
1.4.3 Ga nanoparticles . . . 25
1.4.3.1 Properties . . . 25
1.4.3.2 Synthesis . . . 28
1.4.4 Biomedical properties of Gallium(III) . . . 31
1.4.4.1 From diagnostic and anticancer to antimicrobial agent . . . 31
1.4.4.2 Mechanisms of antibacterial action . . . 33
1.4.4.3 Bacterial resistance to Ga(III) . . . 36

1.4.4.4 Cytotoxicity and medical applicability of Ga(III) 38
1.4.5 Gallium-containing nanoparticles for biomedical applications 40
1.5 Antibacterial Materials for Bone/Tooth Replacement and Repair 41
1.5.1 Hydroxyapatite and other calcium orthophosphates 42
1.5.2 Incorporation of antibacterial ions into hydroxyapatite 46
1.5.2.1 Effect of ionic gallium on bone growth 48
1.5.2.2 Incorporation of gallium ions into calcium phosphates . . . 48
1.5.3 Nanocomposites from antibacterial nanoparticles and hydroxyapatite 49

2 Aims, Scope and Hypotheses 53
2.1 Aims 53
2.2 Scope 53
2.3 Hypotheses 54

3 Experimental Work 57
3.1 Materials 57
3.1.1 Specifications of the reagents used for the syntheses 57
3.1.2 Specifications of the reagents and chemicals used for the analyses . . 58
3.1.3 Growth media and cells 59
3.2 Synthesis Methods 59
3.2.1 Synthesis of hydroxyapatite 59
3.2.1.1 Removal of Ti contamination 60
3.2.2 Synthesis of Ga-doped hydroxyapatite 60
3.2.2.1 HAp(Ga) by co-precipitation 60
3.2.2.2 HAp(Ga) by transformation 61
3.2.2.3 HAp(Ga) by ion-exchange 61
3.2.2.4 Amorphous gallium phosphate 61
3.2.3 Synthesis of functionalized Au nanoparticles on hydroxyapatite . . . 61
3.2.4 Synthesis of functionalized Au nanoparticles on Ga-doped hydroxyapatite 62
3.2.5 Synthesis of gallium nanoparticles on hydroxyapatite 62
3.2.5.1 The Ga@HAp16 nanocomposite 62
3.2.5.2 Other Ga@HAp nanocomposites 63
3.2.6 Synthesis of Ag@HAp nanocomposite 64
3.2.7 Synthesis of functionalized Ga/Au core/shell nanoparticles on hydroxyapatite 64
3.3 Characterization Methods 65
3.3.1 X-ray diffraction (XRD) analysis 65
3.3.1.1 Determination of Ca/P ratio in HAp 65
3.3.1.2 Estimation of crystallinity of HAp and HAp(Ga) 65
3.3.1.3 Au crystallite size determination 66
3.3.1.4 High-temperature XRD 67
3.3.2 Spectroscopic investigations 67
3.3.2.1 Fourier-Transform Infrared Spectroscopy 67
3.3.2.2 Nuclear magnetic resonance 67
3.3.2.3 UV-VIS spectroscopy 68
3.3.3 Microscopy 68
3.3.3.1 Transmission electron microscopy 68
3.3.3.2 Scanning electron microscopy 69
3.3.3.3 Optical microscopy 69

3.3.4 Thermogravimetric (TG) and differential scanning calorimetry (DSC) analyses . . . 69
3.3.5 Specific surface area determination . . . 69
3.3.6 Metal content determination . . . 70
3.3.6.1 Quantitative determination of Ga in the HAp(Ga) and Ga@HAp samples . . . 70
3.3.6.2 Quantitative determination of Ga, Au and Ag in the other samples . . . 70
3.3.7 *In-vitro* release of Ga^{3+} ions . . . 70
3.3.7.1 Method for *in-vitro* release of Ga(III) from HAp(Ga) . . . 70
3.3.7.1.1 Static ageing of HAp(Ga)IE16 in PBS, MH and LB media . . . 70
3.3.7.1.2 Ion release from HAp(Ga)CP, HAp(Ga)TR and HAp(Ga)IE16 in LB . . . 71
3.3.7.2 Method for *in-vitro* release of Ga(III) from Ga@HAp . . . 71
3.3.8 Antibacterial tests . . . 71
3.3.8.1 Disc diffusion antibiogram . . . 72
3.3.8.2 Microdilution antibiogram . . . 72
3.3.8.3 BacLight Live/Dead bacterial survivability assay . . . 72
3.3.9 *In vitro* cytocompatibility tests . . . 73
3.3.9.1 Cell viability by MTT test . . . 73
3.3.9.2 Measurement of generation of reactive oxygen species (ROS) 73

4 Results 75
4.1 Hydroxyapatite . . . 75
4.1.1 Characterisation . . . 75
4.1.2 Synthesis optimisation . . . 76
4.1.2.1 Synthesis upscale . . . 76
4.1.2.2 Ti contamination . . . 78
4.1.2.3 Avoiding long ultrasonication . . . 79
4.2 Incorporation of Ga(III) into Hydroxyapatite . . . 81
4.2.1 Analysis of phase composition, thermal and surface properties . . . 81
4.2.2 Morphological characteristics . . . 85
4.2.3 Spectroscopic analysis . . . 89
4.3 Functionalized Gold Nanoparticles on Ga(III)-Containing Hydroxyapatite . 94
4.4 Ga@HAp Nanocomposite . . . 99
4.4.1 Optimization of the synthesis . . . 99
4.4.2 Characterization of the Ga@HAp16 nanocomposite . . . 102
4.4.3 Other Ga@HAp nanocomposites . . . 106
4.4.4 Ag@HAp reference . . . 109
4.5 Composite of Functionalized Ga/Au Core/Shell Nanoparticles and Hydroxyapatite . . . 110
4.6 Influence of the *In-vitro* Exposure of the Materials to Different Physiological Media . . . 119
4.6.1 HAp(Ga) . . . 119
4.6.2 Ga@HAp . . . 121
4.6.3 Ga/Au@HAp and Ga/Au/Arg@HAp . . . 122
4.7 Antibacterial Action Against *P. aeruginosa*, *E. coli* and *S. epidermidis* . . . 123
4.7.1 Antibacterial properties of HAp(Ga) . . . 123
4.7.2 Antibacterial action of Au/Arg@HAp(Ga) . . . 129
4.7.3 Antibacterial action of Ga@HAp nanocomposites . . . 132

4.7.3.1 Antibacterial action of Ga@HAp16 against *P. aeruginosa* . 132
4.7.3.2 Antibacterial action of other Ga@HAp nanocomposites against *P. aeruginosa* . . . 137
4.7.3.3 Antibacterial action of Ga@HAp16 against *E. coli* 139
4.7.4 Ga/Au/Arg@HAp 140
4.8 *In vitro* Cytotoxicity 142
4.8.1 HAp(Ga) 142
4.8.2 Au/Arg@HAp(Ga) nanocomposite 144
4.8.3 Ga@HAp nanocomposite 145
4.8.4 Cytotoxicity of Ga/Au core-shell nanoparticles on hydroxyapatite . . 148

5 Discussion 149
5.1 Core-Shell Structure of the Hydroxyapatite 149
5.2 Influence of Ga^{3+} Ions on the Formation and Properties of HAp(Ga) 150
5.2.1 HAp(Ga) by co-precipitation 152
5.2.2 HAp(Ga) by transformation 152
5.2.3 HAp(Ga) by ion exchange 153
5.2.4 Disordered surface layer as a drug delivery system 154
5.3 Ga@HAp 155
5.3.1 Top-down or bottom-up approach? 155
5.3.2 Biomedical properties 159
5.4 Attachment of Nanoparticles or Ion Incorporation? 162
5.5 Nanocomposites Combining Hydroxyapatite, Gallium and Gold 163
5.5.1 Au/Arg nanoparticles on HAp(Ga) 163
5.5.2 Ga/Au/Arg core-shell nanoparticles on hydroxyapatite 164
5.6 Metal ions, nanotechnology and other new or renewed trends to combat the antibiotic resistance 170

6 Conclusions 173

Appendix A Mie Scattering Theory and Surface Plasmon Resonance 175
A.1 Metallic Nanoparticles 175
A.2 Core/Shell Nanoparticles 180
A.2.1 Dielectric-metal core/shell NPs 182
A.2.1.1 Small shell thickness 182
A.2.1.2 Large shell thickness 182
A.2.2 Metal-dielectric core-shell NPs 183
A.2.3 Metal-metal core-shell NPs 183

Appendix B Reference X-Ray Diffraction Patterns of Hydroxyapatite and Ga Nanoparticles 185

Appendix C Fourier Transform Infrared (FT-IR) Spectroscopy of Hydroxyapatite 187

Appendix D Solid-State NMR of Hydroxyapatite 189
D.1 ^{1}H NMR 189
D.1.1 Bulk hydroxyapatite 189
D.1.2 Nanocrystalline hydroxyapatite 189
D.2 ^{31}P NMR 190
D.3 NMR Investigation of HAp(Ga) 191
D.4 Amorphous $GaPO_4$ Hydrate 191

Appendix E Phase Diagram of the Ga and Au Mixture **193**

References **195**

Bibliography **231**

Biography **233**

List of Figures

Figure 1.1: The antibiotic resistance problem. 2
Figure 1.2: Declining of new antibiotic development. 2
Figure 1.3: A timeline of new antibiotic discoveries and first appearances of the resistant strains. 3
Figure 1.4: Various possibilities of gaining antibiotic resistance. 4
Figure 1.5: Hard-soft acid base (HSAB) theory can predict the selectivity of metal ions for biological donor ligands. 7
Figure 1.6: Antibacterial mechanisms of metal ion toxicity. 9
Figure 1.7: Mechanisms of antibacterial activity of nanoparticles. 15
Figure 1.8: Schematic of the known pathways for intracellular uptake of nanoparticles. 19
Figure 1.9: Calculated Ga(III) speciation as a function of pH. 22
Figure 1.10: Gallium phase diagram. 25
Figure 1.11: Properties of Ga NPs. 28
Figure 1.12: Oxide shell on Ga NPs. 29
Figure 1.13: Ga nanoparticles prepared by physical methods. 29
Figure 1.14: Ga NPs prepared by chemical methods. 31
Figure 1.15: Dependence of solubility of different calcium orthophosphates on pH. . 43
Figure 1.16: Crystal structure of hydroxyapatite. 44
Figure 1.17: Morphology of hydroxyapatite. 44
Figure 1.18: The core-shell model of the nano-hydroxyapatite. 45

Figure 2.1: Schematic illustration of the materials investigated in the thesis. 54

Figure 3.1: Scheme of the synthesis of hydroxyapatite. 59
Figure 3.2: Synthesis of different HAp(Ga) materials. 60
Figure 3.3: Schematic representation of the synthesis of an Au/Arg@HAp(Ga) nanocomposite. 62
Figure 3.4: Illustration of the synthesis of the Ga@HAp nanocomposite. 63
Figure 3.5: Determination of crystallinity index (CI) from the X-ray diffractogram of hydroxyapatite. 66
Figure 3.6: Determination of splitting factor (SF) and C/P ratio from the IR spectrum of hydroxyapatite. 68
Figure 3.7: Calibration line of external standards for the $GaCl_4^-$–Rhodamine B spectrophotometric method. 70

Figure 4.1: Structural and morphological characteristics of the hydroxyapatite reference. 76
Figure 4.2: XRD patterns of products after two different scale-up approaches to the synthesis of HAp. 77
Figure 4.3: Morphology of HAp by (a) upscaled synthesis (2× volume at the same concentrations) and (b) the usual synthesis. 77

Figure 4.4: Erosion of Ti tip. 78
Figure 4.5: Contamination of HAp with Ti. 78
Figure 4.6: Removal of Ti from HAp 79
Figure 4.7: XRD patterns of hydroxyapatite by (a) 3-hour precipitation under reflux at 100 °C+15-min ultrasonication and (b) precipitation under 3-hour ultrasonication at 80 °C+15-hour ageing. 79
Figure 4.8: Comparison of HAp prepared by different methods. 80
Figure 4.9: Addition of Ga(III) to HAp. 81
Figure 4.10: X-ray diffraction pattern of the amorphous gallium phosphate hydrate. 82
Figure 4.11: X-ray diffractograms of (a) HAp and HAp(Ga) obtained by (b) co-precipitation (c) transformation and (d) ion exchange. 84
Figure 4.12: Thermal characteristics (TGA and DSC curves) of HAp and HAp(Ga). 85
Figure 4.13: Morphological characteristics of HAp(Ga) materials. 87
Figure 4.14: Electron microscopy analysis of HAp(Ga)IE and HAp(Ga)TR. 88
Figure 4.15: Locating Ga(III) in HAp(Ga) by TEM. 88
Figure 4.16: FTIR spectra of HAp and HAp(Ga). 89
Figure 4.17: ^{31}P MAS NMR spectra of HAp and HAp(Ga). 90
Figure 4.18: ^{31}P MAS NMR spectra with fitted Voigt profiles. 91
Figure 4.19: ^{1}H MAS NMR spectra of HAp and HAp(Ga). 93
Figure 4.20: ^{1}H–^{31}P CP-HETCOR NMR spectrum of HAp(Ga)IE with 16 wt % of Ga. 93
Figure 4.21: Characterisation of the Au/Arg@HAp(Ga)IE8 nanocomposite created from HAp(Ga)IE8. 95
Figure 4.22: Electron microscopy characterization of the Au/Arg@HAp(Ga)IE nanocomposite created from HAp(Ga)IE8. 96
Figure 4.23: TEM image of the Au/Arg@HAp(Ga)TR (left) and size distribution (right) of Au/Arg NPs in it, based on 400 Au NPs in a TEM image. . . 97
Figure 4.24: High magnification TEM images of Au/Arg NPs on HAp(Ga)IE8 (left) and HAp(Ga)TR (right). 97
Figure 4.25: Morphology of the Au/Arg@HAp. 98
Figure 4.26: X-ray diffractograms of Ga@HAp nanocomposites prepared by ultrasonic emulsification in different media. 99
Figure 4.27: Synthesis of Ga@HAp in water. 100
Figure 4.28: Morphology of Ga@HAp after sonication in EG. 101
Figure 4.29: Separation of the large and small Ga particles by centrifugation. 101
Figure 4.30: Electron microscopy analysis of Ga NPs and Ga@HAp nanocomposite prepared by ultrasonic emulsification method without surfactant. 104
Figure 4.31: Characterization of the Ga@HAp16 nanocomposite. 105
Figure 4.32: TEM size distribution of Ga NPs in different Ga@HAp nanocomposites. 107
Figure 4.33: Electron microscopy analysis of the Ga/OA NPs (prepared by thermal decomposition and with surfactants) and Ga/OA@HAp nanocomposite. 108
Figure 4.34: X-ray diffraction pattern of the Ag@HAp nanocomposite reference. . . 109
Figure 4.35: Image of the Ag@HAp nanocomposite under a scanning electron microscope (a) and a transmission electron microscope (b). 109
Figure 4.36: XRD patterns of the dried materials after mixing Ga micro- and submicro-droplets with $HAuCl_4$ in ethylene glycol. 110
Figure 4.37: XRD analysis of different nanocomposites by mixing Ga@HAp with $HAuCl_4$ in water. 111
Figure 4.38: SEM and EDXS analysis of the Ga/Au sample that contained no $AuGa_2$ phase. 112

Figure 4.39: Mixing of Ga@HAp from ethylene glycol with $HAuCl_4$ on ice bath. . . 113
Figure 4.40: Morphology of Ga/Au/Arg@HAp formed by ultrasonication of Ga@HAp + $HAuCl_4$ + Arg in water. 113
Figure 4.41: Morphology of Ga/Au/Arg@HAp formed by mixing of Ga@HAp with an aqueous solution of $HAuCl_4$+Arg on an ice bath. 114
Figure 4.42: Morphology of Ga/Au/Arg@HAp formed by titration of a $HAuCl_4$ solution with NaOH to pH 7, addition of an aqueous solution of arginine and dropwise addition of the mixture to an ethyleneglycolic suspension of Ga@HAp on ice. 115
Figure 4.43: TEM EDXS analysis of a Ga/Au/Arg nanoparticle in a Ga/Au/Arg@HAp nanocomposite. 115
Figure 4.44: Morphology (under TEM) of Ga/Arg/Au/Arg@HAp obtained by dispersing Ga onto HAp in the presence of Arg in ethylene glycol, then mixing with HAuCl4+Arg+NaOH to pH 7 on ice bath. 116
Figure 4.45: TEM EDXS analyses on the different types of Ga/Au/Arg NPs found in the Ga/Arg/Au/Arg@HAp nanocomposite. 117
Figure 4.46: Spectroscopic analysis of Ga/Au/Arg@HAp. 118
Figure 4.47: Ion release from HAp(Ga)IE16. 119
Figure 4.48: Comparison of XRD patterns of HAp(Ga)IE16 before and after ageing in PBS with pH 5.4. 120
Figure 4.49: Release of Ga^{3+} ions from HAp(Ga) in LB. 120
Figure 4.50: Ion release from Ga@HAp. 122
Figure 4.51: Disc diffusion antibacterial test of HAp and the HAp(Ga) against *P. aeruginosa*. 123
Figure 4.52: Microdilution antibiograms of different HAp(Ga)IE materials. 124
Figure 4.53: Microdilution antibacterial test against *P. aeruginosa* for the HAp(Ga) obtained by (a) co-precipitation and (b) transformation. 125
Figure 4.54: Antibacterial activity of HAp(Ga) against *P. aeruginosa*. 125
Figure 4.55: Morphology of *P. aeruginosa* bacteria exposed to HAp and HAp(Ga)IE16. 126
Figure 4.56: Microdilution antibiogram against *P. aeruginosa* of HAp(Ga)IE14 in M9 medium. 126
Figure 4.57: Antibacterial activity (against *P. aeruginosa* MW1) of (a) $Ga(NO_3)_3$, (b) amorphous $GaPO_4$ hydrate and (c) the supernatant after 1-day ageing of HAp(Ga)IE16 in PBS. 127
Figure 4.58: Antibacterial properties of HAp(Ga)IE against *E. coli*. 128
Figure 4.59: Disc diffusion antibiogram of HAp(Ga)IE5 against (a) *S. epidermidis* and (b) *P. aeruginosa*. 128
Figure 4.60: Disc diffusion antibiogram against *P. aeruginosa*: Au/Arg@HAp (left) and Au/Arg@HAp(Ga)IE (right). 129
Figure 4.61: Dilution antibiogram assay of Au/Arg@HAp and Au/Arg@HAp(Ga) against *P. aeruginosa* MW1. 130
Figure 4.62: Disc diffusion antibiogram of (a) Au/Arg@HAp(Ga)TR and (b) Au/Arg@HAp14 against *E. coli*. 130
Figure 4.63: Diffusion antibiogram assay against *S. epidermidis*: Au/Arg@HAp, Au/Arg@HAp(Ga)TR and Au/Arg@HAp(Ga)IE4. 131
Figure 4.64: Antibacterial properties of the Ga@HAp nanocomposite against *P. aeruginosa* MW1. 132
Figure 4.65: Dilution antibiogram assay of (a) Ga@HAp and (b) Ag@HAp nanocomposite against *P. aeruginosa* MW1. 133

Figure 4.66: Colony counting after dilution antibiograms of HAp and Ga@HAp against *P. aeruginosa*. 134
Figure 4.67: Survivability of *P. aeruginosa* MW1 in the presence of Ga@HAp. . . . 135
Figure 4.68: Bacterial morphology after 24-hour incubation with HAp or Ga@HAp. 135
Figure 4.69: Microdilution antibiogram of Ga@HAp16 against PAMW1 in M9 medium. 136
Figure 4.70: Microdilution antibiogram of liquids after 1-day ageing of Ga@HAp16. . 136
Figure 4.71: Antibacterial action of the released Ga^{3+} ions. 137
Figure 4.72: Disc diffusion antibiogram of (a) Ga/OA@HAp nanocomposite against *P. aeruginosa* with (b) HAp as the negative control. 137
Figure 4.73: Microdilution antibiograms of other Ga@HAp. 138
Figure 4.74: Microdilution antibiogram of Ga@HAp against PAO1. 139
Figure 4.75: Antibacterial activity of Ga@HAp16 against *E. coli*: (a) disc diffusion antibiogram, (b) microdilution antibiogram. 139
Figure 4.76: Diffusion antibiogram of Ga/Au/Arg@HAp nanocomposite against *E. coli* and *P. aeruginosa*. 140
Figure 4.77: Microdilution antibiogram of Ga/Au/Arg@HAp (a) and Ga/Au@HAp (b) against *P. aeruginosa*. 141
Figure 4.78: Diffusion antibiogram (a) and microdilution antibiogram (b) for the Ga/Arg/Au/Arg@HAp nanocomposite against *E. coli*. 141
Figure 4.79: Cytotoxicity of HAp(Ga) with respect to L929 mouse fibroblasts. 142
Figure 4.80: Cytotoxicity of HAp(Ga)IE, $Ga(NO_3)_3$ and amorphous $GaPO_4$ hydrate. 143
Figure 4.81: Cytotoxicity of the released Ga(III) from the HAp(Ga)IE. 143
Figure 4.82: Cell viability of L929 in dependence of Au/Arg@HAp or Au/Arg@HAp(Ga) concentration. 144
Figure 4.83: Cytotoxicity assays on the HAp, Ga@HAp16 and Ag@HAp. 145
Figure 4.84: Generation of reactive oxygen species (ROS) in L929 fibroblasts after incubation with HAp or Ga@HAp. 146
Figure 4.85: Generation of reactive oxygen species (ROS) in L929 fibroblasts after incubation with HAp, Ga@HAp or Ag@HAp. 147
Figure 4.86: Dimensions of cells counted in the flow cytometer. 147
Figure 4.87: L929 cell viability in the presence of Ga@HAp nanocomposites. 148
Figure 4.88: L929 cell viability in the presence of Ga/Au@HAp and Ga/Au/Arg@HAp nanocomposite, respectively. Hydroxyapatite is the negative control. . . 148

Figure 5.1: (a) Illustration of the structure of HAp(Ga) obtained by co-precipitation, transformation and ion exchange with Ga^{3+} ions and (b) the mechanism of formation of HAp(Ga)CP nanocrystals. 150
Figure 5.2: Graphical presentation of the Ga(III) incorporation into HAp and its influence on the biological properties of the HAp(Ga) biomaterial. . . . 156
Figure 5.3: A graphical summary of the diverse properties of the Ga@HAp biomaterial and the proposed sources of its antibacterial action. 159
Figure 5.4: A graphical overview of the useful properties of the Au/Arg@HAp(Ga)TR nanocomposite. 164

Figure A.1: A schematic of the system solved by Mie with notations used in the text. 179
Figure A.2: Calculated UV-VIS spectra of different Au nanoparticles (left) and Ga nanoparticles (right). 181
Figure A.3: Calculated spectra of AuAg nanoalloys and Ag/Au core/shell NPs from the literature. 184
Figure A.4: My calculations of UV-VIS spectra of Ag/Au core-shell nanoparticles. . 184

Figure B.1: Indexed XRD pattern of hydroxyapatite (PDF number 01-089-6438). . 185
Figure B.2: X-ray diffractogram of 24-nm and 46-nm Ga NPs from the work of Yarema *et al.* 186

Figure C.1: IR spectra of HAp from the literature. 187

Figure D.1: Comparison of NMR spectra of nanocrystalline and a highly crystalline HAp sample. 190
Figure D.2: NMR spectra of HAp(Ga) from the literature. 192

Figure E.1: Gallium-gold bulk phase diagram. 193

List of Tables

Table 1.1: Ga(III)-based antimicrobials. 34
Table 1.2: Ga(III) cytotoxicity *in vitro* 39

Table 4.1: Crystallinity determined from the XRD patterns. 83
Table 4.2: Composition, surface and thermal characteristics of HAp and HAp(Ga). 86
Table 4.3: Peaks determined by fitting the ^{31}P NMR spectra of HAp and HAp(Ga). 92
Table 4.4: Synthesis parameters and composition of different Au/Arg@HAp and Au/Arg@HAp(Ga) nanocomposites examined throughout the thesis. . . 94
Table 4.5: Synthesis parameters and composition of different Ga@HAp nanocomposites examined throughout the thesis. 106

Table 5.1: Comparison of two methods for creating the Ga@HAp nanocomposite. . 157

Table C.1: FT-IR band positions and explanations for hydroxyapatite. 188

Abbreviations

a. u.	... arbitrary units
abs	... absorbance
ACP	... amorphous calcium phosphate
ADP	... adenosine diphosphate
Arg	... arginine
ATP	... adenosine triphosphate
BET	... Brunauer–Emmett–Teller
CDP	... cytidine diphosphate
CLD	... chemical liquid deposition
CFU	... colony forming units
CP	... co-precipitation
CP-HETCOR	... cross-polarisation–heteronuclear correlation
cts	... counts
DCPD	... dicalcium phosphate dihydrate
DFOB	... desferrioxamine B
DRIFT	... diffuse reflectance infrared Fourier transform
DMSO	... dimethyl sulfoxide
DNA	... deoxyribonucleic acid
DSC	... differential scanning calorimetry
DTA	... differential thermal analysis
EDXS, EDS	... energy-dispersive X-ray spectroscopy
EG	... ethylene glycol
FEG	... field emission gun
FWHM	... full width at half maximum of a peak
JSI	... Jožef Stefan Institute
IPS	... International Postgraduate School
FTIR	... Fourier-Transform Infrared
HAp	... hydroxyapatite
ICP-AES	... inductively coupled plasma atomic emission spectroscopy
IE	... ion exchange
LB	... Luria-Bretani
MAS	... magic angle spinning
MBC	... minimal bactericidal concentration
MBE	... molecular beam epitaxy
MEM	... minimum essential medium
MH	... Mueller-Hinton
MIC	... minimal inhibitory concentration
MIR	... mid infrared
MRSA	... methicilin-resistant *Staphylococcus aureus*
NAD, NADH	... nicotinamide adenine dinucleotide
NADP	... nicotinamide adenine dinucleotide phosphate

NIR	...	near infrared
NMR	...	nuclear magnetic resonance
norm.	...	normalised
NP	...	nanoparticle
OA	...	oleic acid
OCP	...	octacalcium phosphate
OD	...	optical density
PBS	...	phosphate buffered saline
PDF	...	powder diffraction file
RNA	...	ribonucleic acid
ROS	...	reactive oxygen species
SAED	...	selected-area electron diffraction
SEM	...	scanning electron microscope/microscopy
SF	...	splitting factor
SPR	...	surface plasmon resonance
TC_{50}	...	toxic concentration that kills 50 % of cells
TCP	...	tricalcium phosphate
TE	...	transverse electric
TEM	...	transmission electron microscope/microscopy
TGA	...	thermogravimetric analysis
THF	...	tetrahydrofuran
TM	...	transverse magnetic
TR	...	transformation
UV-VIS	...	ultraviolet-visible (light)
wt	...	weight
XPS	...	X-ray photoelectron spectroscopy
XRD	...	X-ray diffraction

Symbols

A ... area under a curve, integrated X-ray diffractogram
a_L ... coefficient of the transverse magnetic modes in the vector harmonic expansion
B ... integral breadth
$\mathbf{B}$ ... magnetic induction
b_L ... coefficient of the transverse electric modes in the vector harmonic expansion
c ... concentration
d ... thickness of the shell in a core-shell sphere
$\mathbf{D}$ ... electric displacement field (electrical flux density)
δ ... chemical shift in a NMR spectrum
$\mathbf{E}$ ... electric field
$E^{\varnothing}$... standard reduction potential in aqueous solution at 25 °C
E_0 ... magnitude of electric field
ε ... dielectric constant (permittivity)
$\tilde{\varepsilon}$ ... complex dielectric function
ε_0 ... vacuum permittivity
η ... viscosity
$\mathbf{F}$ ... force
γ ... surface tension
γ_{ij} ... interfacial tension between the liquid being emulsified and the dispersing medium
$\dot{\gamma}$ ... shear rate
h ... Planck's constant
h ... height of a peak in a spectrum/diffractogram
$\mathbf{H}$ ... magnetic field
$h_L^{(1)}$... Hankel function of the first order
χ ... susceptibility
χ_m... magnetic susceptibility
$I_{A(\mathrm{hkl})}$ integrated intensity (area) of a (hkl) X-ray diffraction maximum of substance A
$\mathbf{J}$ ... current density
j_L ... Bessel function of the first order
k ... angular wavenumber
κ ... extinction coefficient
K_n... equilibrium constant of n-th step of hydrolysis
K_S... Scherrer constant
l ... length of the light path through the sample
L ... crystallite size
λ ... wavelength
m ... mass (of a sample, substance)
$\mathbf{M}$ ... magnetisation
M_i... molecular/molar mass of a substance i
μ ... permeability

μ_0 ... vacuum permeability
n ... (real) refractive index
$\tilde{n}$ ... complex refractive index
N ... number of particles
N_j ... number of electron dipoles
ν ... frequency
ω ... angular frequency
$\mathbf{P}$ ... polarisation
$\mathbf{p}_j$ ... dipole moment
P_L^m ... associated Legendre polynomial
q_j ... charge
r ... radius of a sphere
R ... reflectance
R ... radius of the core in a core-shell sphere
ρ ... charge density
σ ... optical conductivity
σ_{ext} ... extinction cross section
T ... transmittance
θ ... incidence angle of the X-ray beam in a XRD experiment
V ... volume
V_a ... volume of an aliquot
w_i ... mass fraction of a substance i in a mixture/composite/compound/material
y_L ... Bessel function of the second order (Neumann function)
z_L ... spherical Bessel function

Chapter 1

Introduction

1.1 The Antibiotic Resistance Problem

Resistance of bacteria to antibiotics is becoming more and more an urgent problem of the humanity. The most serious threat comes from vancomycin-resistant ***E****nterococcus* (VRE, mainly *E. faecium*), methicilin-resistant ***S****taphylococcus aureus* (MRSA), ***K****lebsiella* (especially *K. pneumoniae*), ***A****cinetobacter baumanii*, ***P****seudomonas aeruginosa*, ***E****nterobacter* and *Escherichia coli* (the so-called "ESKAPE" pathogens[1], [2], among which the first two are Gram-positive and the other five Gram-negative), Gram-positive *Mycobacterium tuberculosis* and some other Gram-negative bacteria [3], [4]. Soon there will be no available antibiotics to treat infections with these pathogens.

Antibiotics were able to eliminate many bacterial diseases very efficiently without doing any harm to human cells, that is why their use has grown rife and has become uncontrolled. Many people take antibiotics without any proven bacterial infection, often even because their doctor recommends it [5]. On the other hand, even if the use of an antibiotic is justified, patients often stop the treatment too soon. Antibiotics are also widely used in agriculture, stockbreeding and poultry breeding [6], [7]. Besides, sterile environment is necessary in hospitals as it enables operations, transplantations etc. Actually, it was exactly in the hospitals that the problem of overgrowth of resistant species appeared first.

Why do misuse and overuse of antibiotics lead to an increased number of resistant bacteria? The reason is quite obvious. In an environment, impregnated with antibiotic, only the resistant strains can survive. Since the competitors for resources were all wiped out by the antibiotic, all the food is left only for the resistant species, which can then rapidly multiply. On the other hand, in an environment without antibiotic, the non-resistant species have more chance for survival. However, some investigations have shown that if the antibiotic environment with a lack of non-resistant strains is maintained long enough, the resistant strains survive better also in the absence of the antibiotic [8], [9]! Moreover, we need to point out it is not only the overuse and misuse that speeds up the spread of the resistance. Some mechanisms of resistance do not destroy the antibiotic and leave it active in the environment. Thus they help themselves maintain the antibiotic environment, furthermore, the drug can be released into other environments and alter them [5], [10], [11], [12].

In the last decade, the use of antibiotics has been reduced due to many precautions against drug misuse and overuse, so that spreading of resistance slowed down, but it did not decrease (see Figure 1.1). We could get rid of the resistant strains with new antibiotics. Unfortunately, development of new antibiotics has almost ceased in the last decades [6], [13] (Figure 1.2).

Investments in research and development of new kinds of antibiotics were minimized

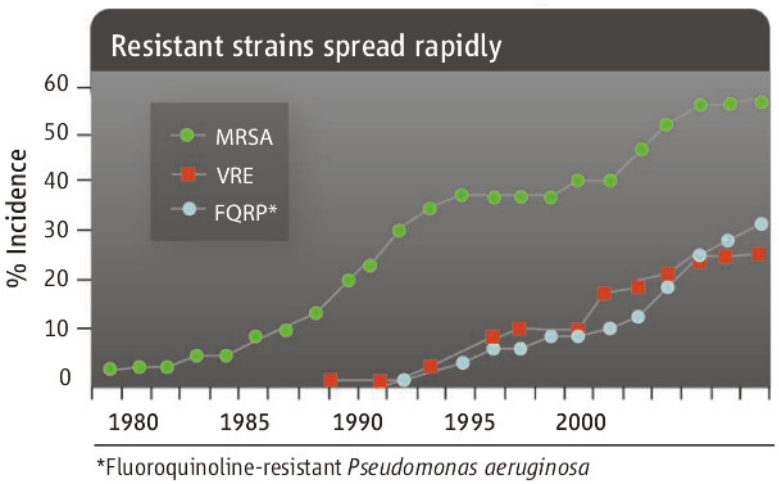


Figure 1.1: The antibiotic resistance problem. Curves are showing an increase of fraction of resistant strains for three different bacterial species (Source: Centers for Disease Control and Prevention) [14].

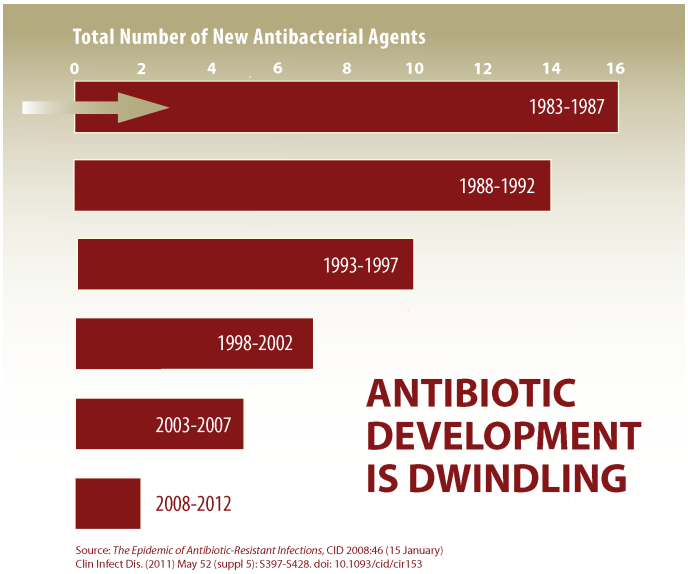


Figure 1.2: Declining of new antibiotic development. Decrease of the number of new antibiotics over years [15], [16].

due to their unprofitability [1], [6], [13]. Recent warnings of many health organizations, such as Interagency Task Force on Antimicrobial Resistance, Infectious Diseases Society of America (IDSA), Centers for Disease Control and Prevention (CDC), National Institutes of Health, National Institute of Allergy and Infectious Diseases (NIAID) etc., improved this situation a little. However, new antibiotics need to be more and more complex, so they require more time to be designed. Unfortunately, the available time is very short since bacteria obtain resistance to an antibiotic extremely fast. This is well evident in Figure 1.3, which presents a timeline of antibiotic discoveries and first appearances of resistant strains.

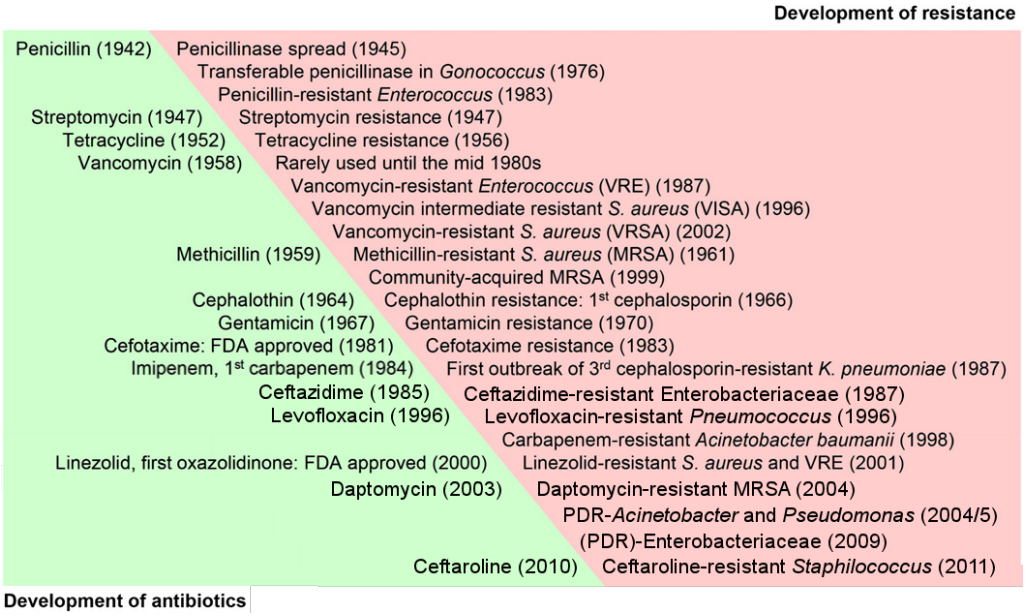


Figure 1.3: A timeline of new antibiotic discoveries and first appearances of the resistant strains [17].

How can bacteria gain resistance so fast? There are three main facts that can explain it:

1. Genes for resistance to all currently used and probably for many later discovered antibiotics already exist in some bacterial strains in the nature [7], [18], [19]. Bacteria had fought antibiotics far before we first used them against pathogenic bacteria [6].

2. Pathogenic strains can obtain these genes in many different ways, shown in Figure 1.4: transduction, transposition, recombination, transformation, conjugation, mutation [5], [7], [9], [11].

3. Bacteria proliferate extremely fast.

These are in fact the main causes of the resistance problem.

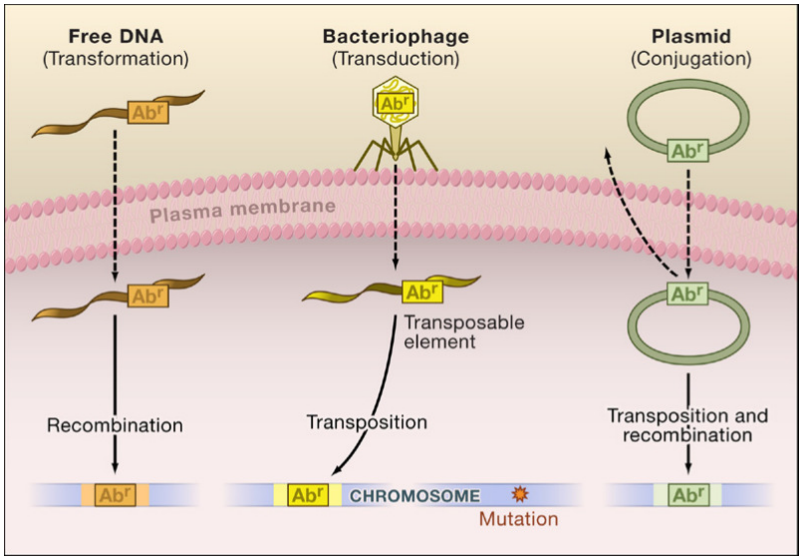


Figure 1.4: Various possibilities of gaining antibiotic resistance [11].

What can we deduce from all these facts? Instead of focusing only on the development of new antibiotics, which will sooner or later create resistance, we should focus on preventing the resistance itself. We need to find an alternative to antibiotics. One option is to go back to the antimicrobials that were used before the discovery of antibiotics: metals and metal ions. The new knowledge gained by the emergence and progress of biomaterials science and nanotechnology can enable:

(i) local, targeted action with minimised side effects,

(ii) improved transport towards and eased penetration into the pathogenic species, leading to higher efficiency,

(iii) unique opportunity for the development of more effective medicines.

For treatment with nanoparticles and antibacterial ions to be as efficient as treatments with antibiotics once were, especially the following must be ensured:

(a) Nanoparticles must effectively destroy the bacteria.

(b) Their action must not affect the eukaryotic cells.

In the next sections I will present what progress scientific research has made so far in ensuring these two conditions. To better understand how the antibacterial action of ions and nanoparticles differs from the action of the antibiotics, let us first briefly summarize the latter.

1.1.1 Antibacterial action of antibiotics

The main antibiotics currently in use involve the following mechanisms [10], [20]:

(a) inhibition of bacterial cell-wall biosynthesis [β-lactam antibiotics (penicillins, cephalosporins), vancomycin],

(b) inhibition of bacterial DNA replication and repair [quinolones],

(c) inhibition of bacterial translation [aminoglycoside antibiotics (streptomycin), macrolides (erythromycin), tetracyclines, chloramphenicol, oxazolidinones],

(d) inhibition of bacterial transcription [actinomycin],

(e) inhibition of bacterial processes that require growth factors [growth factor analogues (sulfa drugs)].

The most important feature of antibiotic antibacterial mechanism is that each kind of antibiotic binds on one specific target.

1.2 Antibacterial Inorganic Ions

1.2.1 Categorization and the main representatives

Antibacterial metal ions can be classified by the three important properties that determine their toxicity [21], [22]:

1. **Donor atom selectivity.** A central metal ion binds to the atoms of donor ligands – such as O, N and S – through interactions that are often strong and selective [21]. There are two most widely accepted classifications of metal ions for their interactions with biological ligands:

   (a) *Irving–Williams series of divalent metal ion ligand affinities.* This series clearly demonstrates the affinity of biological molecules for first-row transition metals, which increases in the order: Ca^{2+}, Mg^{2+}, Mn^{2+}, Fe^{2+}, Co^{2+}, Ni^{2+}, Cu^{2+}, Zn^{2+}. The ions more on the right can displace the ions more on the left of the series from the biological molecules.

   (b) *Hard–soft acid base (HSAB) theory or Pearson's acid base theory.* This is classification of metals into Lewis acids and has been determined empirically. It provides an ordering of transition metals according to their preferences for specific organic ligands that are regarded as Lewis bases (see Figure 1.5). Hard acids and bases tend to have a smaller ionic radius, a high oxidation state and weak polarizability. By contrast, soft species tend to have a large ionic radius, a low oxidation state and strong polarizability. Hard acids react preferentially with hard bases, and soft acids with soft bases. The affinity of a hard acid for a hard base is mostly ionic in nature, whereas the interaction between a soft acid and soft base is mostly covalent. Acids and bases that have an intermediate character between hard and soft are classified as borderline (intermediate). Examples of hard Lewis acids are Ca^{2+}, Mg^{2+} or Ga^{3+} and hard bases are oxygen-containing ligands (see the left part of the Figure 1.6). Soft Lewis acids are e.g. Hg^{2+}, Cu^{+}, Ag^{+} and Cd^{2+}, while soft Lewis bases are primarily sulphur and nitrogen ligands: thiol (R-SH) groups that are found in proteins (cysteine) and nitrogen imidazoles (Figure 1.6). Consequently, the toxicity of these metals is approximately proportional to their affinity for S. Intermediate (borderline) Lewis acids, such as Co^{2+}, Ni^{2+}, Cu^{2+} and Zn^{2+}, will relatively stably coordinate to hard and soft donor ligands. Among the most toxic metal ions soft Lewis acids largely prevail.

2. **Reduction potential.** Redox reactions occur in many intracellular processes. Therefore, the ability of a metal ion to gain/lose an electron importantly affects its biological role and toxicity. Reduction potential is a measure of the reactivity of metal ions. Redox-active metal ions, such as copper, chromium, iron and vanadium, can

be involved in one-electron transfer reactions and consequent free radical generation leading to oxidation of biomolecules and cellular damage due to oxidative stress (more in Section 1.2.2.1). On the other hand, redox-inactive metallic ions can also generate oxidative stress, so that they bind to and inactivate thiol-containing molecules that would normally reduce the oxidative stress (more in Section 1.2.2.2). Several researchers have noted that the toxicity of many redox-active metal ions roughly correlates with their standard electrode potentials [21], [23], [24].

3. **Speciation.** In biological media, metals can exist as multiple different chemical species (different oxidation states and different soluble and insoluble forms); which of these species are present, and in what proportion, is determined by several factors, including pH, reduction potential, ionic strength and temperature. Essential metals are never free inside a cell, and an intricate network of transporters, metalloregulatory sensors and metallochaperones restricts metal speciation and guides metal atoms to specific enzymes, structural and storage proteins. Parameters that affect the oxidation state of metals can also vary between subcellular compartments. For instance, in Gram-negative bacteria, the cytoplasm is a strong reducing environment relative to the periplasm, and this can affect the oxidation state of a metal and thereby change its speciation. Because the chemical form of a metal determines its reactivity and solubility, the speciation of a metal (rather than its total concentration) is key to understanding its toxicity, as this influences its bioavailability [21].

The first ions that regained interest as antimicrobials were the ones that had been invaluable for centuries/millennia in treatments of infections before antibiotics were discovered: Ag^{+}, Cu^{+}/Cu^{2+} and Zn^{2+}.

The resurgence of silver occurred already before the antibiotic resistance alarm by showing its favourability over antibiotics in treatment of burn wounds and post-burn infections in 1965 [25]. It started with a 0.5 wt % $AgNO_3$ solution and was later developed into silver sulfadiazine (a combination of $AgNO_3$ with a sulpha drug, usually applied as an ointment or a hydrophilic cream) to solve the toxicity of $AgNO_3$ and resistance of *P. aeruginosa* [25], [26], [27]. Many other ionic silver drugs emerged, but silver sulfadiazine has remained the most widely used, although it delays the wound healing process [27], [28]. In the last decade, antibacterial properties of ionic silver were observed in a wide variety of bacteria and fungi. A table of antimicrobial minimal inhibitory concentrations and toxic concentrations for eukaryotic cells can be found in ref. [29].

Zn^{2+} has also obtained an important role in the treatment of skin wounds, but due to skin and hair promoting rather than antimicrobial properties. The antibacterial properties of Zn^{2+} ions are exploited especially in oral healthcare for the prevention of caries, gingivitis and periodontitis. Zinc salts are used in mouthwashes, either alone or in combinations with different antibacterial agents and detergents [30]. They are also added to toothpastes, commonly as zinc citrate [31]. The effect of Zn^{2+} ions is most probably only bacteriostatic, so oral-care products are designed for frequent use, while bactericidal action can be obtained in combinations with fluoride or Triclosan [31], [32], [33], [34].

Copper has made its comeback in the control of *Legionella* and other bacteria in hospital water distribution systems using the method of copper and silver ionization [35], [36]. Copper compounds (especially copper sulphate) have also been widely used in agriculture as antimicrobial, algicidal, pesticidal and antifungal agents, but also as animal feed additives, wood preservatives and in antifouling paints [22]. Due to environmental toxicity, copper compounds are being substituted by chelated forms of ionic copper or (elemental) copper surfaces that enable "contact killing" of microbes [30], [35], [36], [37], [38]. In 2008 the US Environmental Protection Agency (EPA) proclaimed copper surfaces as efficient antimicrobials [36]. Copper is the first metal to be awarded such a status [36].

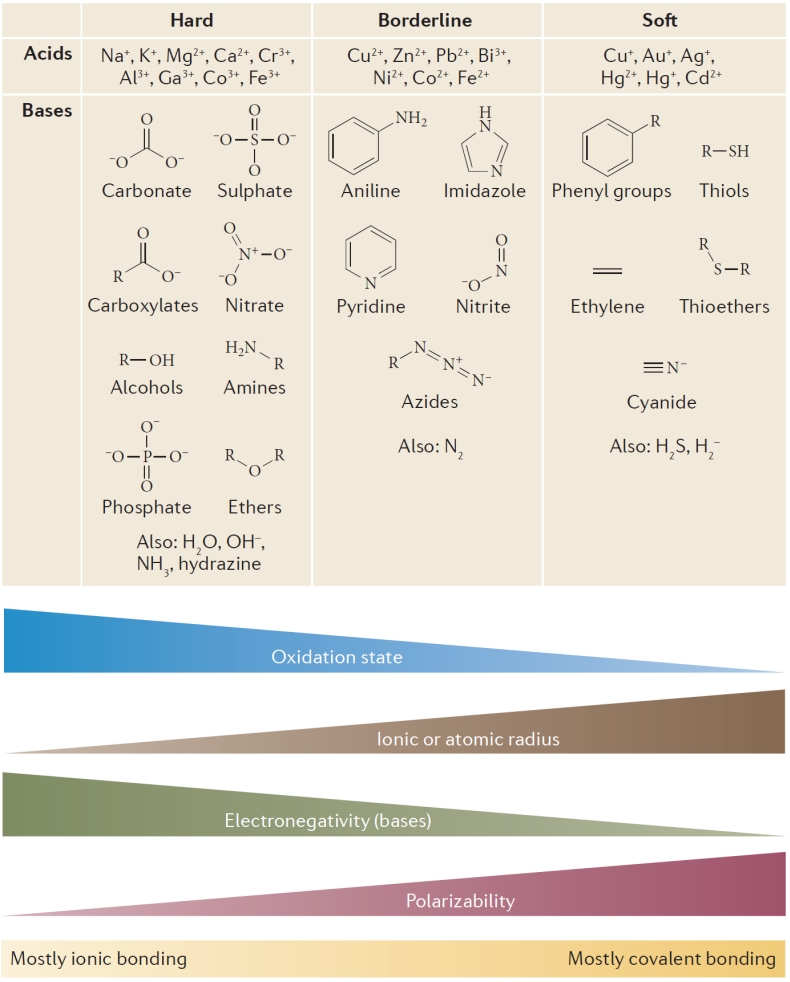


Figure 1.5: Hard-soft acid base (HSAB) theory can predict the selectivity of metal ions for biological donor ligands. This classification scheme is qualitative and can be used to predict the binding preferences of metals even in complex mixtures of donor ligands [21].

Further development of silver-, zinc- and copper-based medical applications was triggered by the warnings of bacterial antibiotic resistance and has gone in two directions:

(a) using the materials engineering and biomaterials knowledge to create systems for controlled delivery of antimicrobial ions (zeolites, polymers), metal-ion-impregnated textiles and polymers, such as wound dressings, clothing, mattress covers, gloves, mask filters, catheters etc, or metal-ion-containing antibacterial coatings and biomaterials (bioactive ceramics, glasses) [30], [35], [39];

(b) using nanotechnology to create Ag, Cu/CuO or ZnO nanoparticles for antibacterial protection. More information about this is provided in Section 1.3.

1.2.2 Antibacterial mechanisms

Antibacterial ions are much less specific than antibiotics and each ion has many different targets. Mechanisms of metal toxicity are generally agreed to be a consequence of metal ion affinity for cellular components and biomolecules, or the stability of metal-biomolecule complexes formed, although the consequences are varied [21], [22], [40]. Inorganic (metal) ions can exert toxic effects in a number of different ways, which are depicted in Figure 1.6 and explained in detail in the subsequent sections.

1.2.2.1 Reactive oxygen species

Reactive oxygen species (ROS) are highly reactive, cytotoxic molecules formed by the incomplete, one-electron reduction of O. ROS include the superoxide anion ($O_2^{\bullet -}$), peroxides (such as H_2O_2), the hydroxyl radical ($OH^{\bullet}$) and hypochlorite (HOCl). They are able to react with the components of the membrane and cell wall of bacteria, as well as other cell components (e.g., mitochondria), causing irreversible changes in their structure and thus the death of the bacterial cell. ROS are generated by the Fenton reactions of the Fe(III)/Fa(II) redox pair [41], [42]. Any other ion that forms a redox pair of two relatively stable oxidation states, e.g. Cu(II)/Cu(I), can undergo Fenton-type reactions (Eq. (1.1)) as well [43], [44]:

$$Cu^{+} + H_2O_2 \longrightarrow Cu^{2+} + OH^{-} + OH^{\bullet} \tag{1.1}$$

The hydroxyl radical is the most powerful oxidizing radical likely to arise in biological systems [45]. It (and also other reactive oxygen species) can cause oxidative damage to proteins, nucleic acids and lipids, which leads to cell death [21]. Cu(II) can be reduced to Cu(I) by many reducents inside the cells (see Section 1.2.2.2 and Eq. (1.6)) or by a superoxide anion (eq (1.2)) [45]:

$${O_2}^{\bullet -} + Cu^{2+} \longrightarrow O_2 + Cu^{+} \tag{1.2}$$

In this way, the Cu(II)/Cu(I) redox pair acts as a catalyser of the Haber-Weiss reaction (Eq. (1.3)) [21], [45]:

$${O_2}^{\bullet -} + H_2O_2 \longrightarrow O_2 + OH^{-} + OH^{\bullet} \tag{1.3}$$

The relevance of this antibacterial mechanism is still debatable, since cells tend to keep the H_2O_2 levels low [22]. One possibility for obtaining H_2O_2 is the following reaction (Eq. (1.4)):

$$2\,Cu^{+} + 2\,H^{+} + O_2 \longrightarrow 2\,Cu^{2+} + H_2O_2 \tag{1.4}$$

In many bacteria, also the enzyme superoxide dismutase (SOD) can create H_2O_2 from the superoxide ions (Eq. (1.5)), which can be generated by incomplete oxygen reduction during aerobic cellular respiration [43], [46]:

$$2\,{O_2}^{\bullet -} + 2\,H^{+} \xrightarrow{\text{SOD}} H_2{O_2}^{+}O_2 \tag{1.5}$$

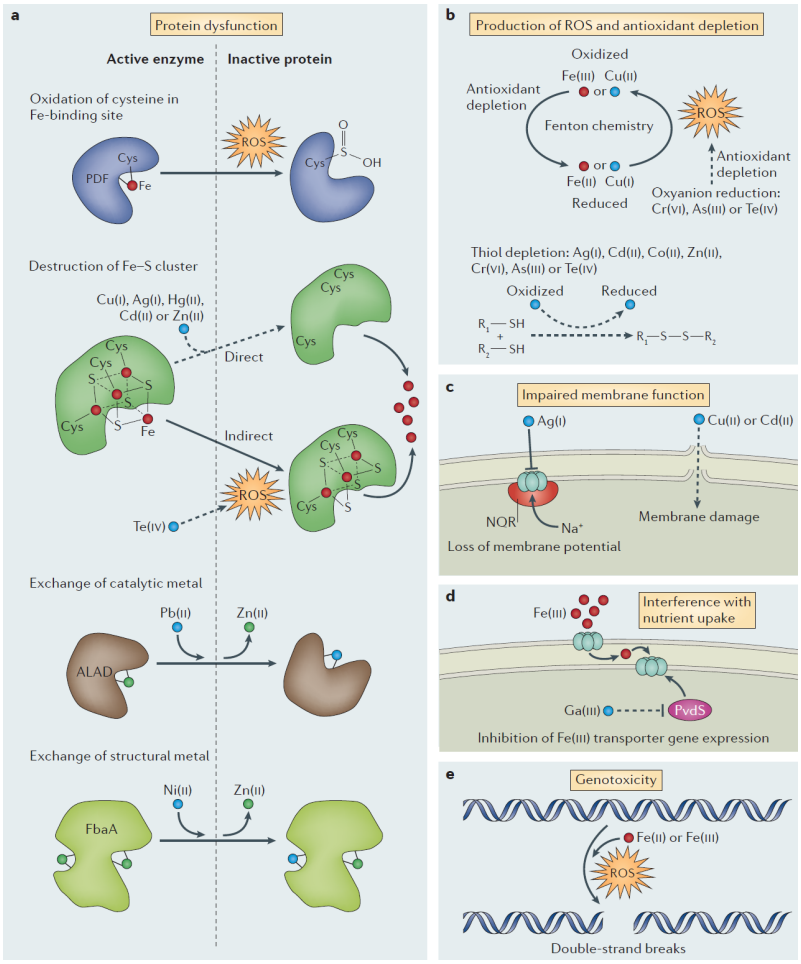


Figure 1.6: Antibacterial mechanisms of metal ion toxicity. a) Protein dysfunction. b)Production of reactive oxygen species (ROS) and depletion of antioxidants. c) Impairing membrane function. d) Interference with nutrient assimilation. e) Genotoxicity. Solid arrows represent pathways in which the underlying biochemistry has been elucidated, whereas dashed arrows represent a route of toxicity for which the underlying biochemical mechanism is unclear. ALAD, δ-aminolevulinic acid dehydratase; FbaA, fructose-1,6-bisphosphate aldolase; NQR, NADH:quinone oxidoreductase; PDF, peptide deformylase; PvdS, a σ-factor (σ^{24}) from *Pseudomonas aeruginosa* [21].

1.2.2.2 Antioxidant inactivation

Antioxidants that are most commonly inactivated are the ones that contain thiol (-SH) groups, the so-called cellular "thiol pool" [21], [44]. Soft acids, such as Ag^+ (or Cu^+), react with thiols to form covalent Ag–S (or Cu–S) bonds. This thiol depletion decreases the amount of available antioxidants that normally control the ROS level. Hence, a consequence of this effect is increased production of ROS. The importance of this mechanism for Ag^+ can be seen in the observation that Ag^+ ions often have a stronger antibacterial effect under aerobic than under anaerobic conditions [41], [42]. On the other hand, Zn^{2+} as a borderline acid can bind directly to the thiol groups but also to a binding site close to the -SH groups or to another site of the protein resulting in a conformational change of the protein. Any of these bindings results in a decreased reactivity of thiol groups [43]. It is interesting that such binding of Zn^{2+} is actually its antioxidant property and gives protection of the thiol-containing biomolecule against free radical attack and oxidation [43]. Zn(II) is considered a major antioxidant for humans and other animals [34]. However, the protection of a biomolecule that regulates the ROS level can have the opposite effect. In case of $Cu^{2+/+}$, which forms a redox pair, there is also the possibility of antioxidant inactivation by redox reaction (Cu^{2+} + reduced antioxidant $\rightarrow$ Cu^+ + oxidized antioxidant). Such reaction with thiol groups can be expressed as [21], [44]:

$$2\,Cu^{2+} + 2\,RSH \longrightarrow 2\,Cu^{+} + RSSR + 2\,H^{+} \tag{1.6}$$

1.2.2.3 Protein dysfunction and loss of enzyme activity

Protein dysfunction and loss of enzyme activity occurs by binding to or blocking functional groups in biological molecules. There are many ways of inhibition but three of them are particularly important:

(a) Inactivation of thiols: inactivation of thiols occurs in a similar way as explained in Section 1.2.2.2, but the proteins do not necessarily act as antioxidants. The role of thiol could also be in the formation of the substrate binding site of an enzyme or simply maintaining the tertiary and quaternary protein structure.

(b) Displacing essential metal ions in enzymes: many important enzymes require metal ions as cofactors and if such ions are substituted by another ion that cannot provide the same function, the enzyme's action is hindered. A typical example of this mechanism is Zn^{2+} ion, which can substitute Mg^{2+}, Fe^{2+} or Cu^{2+} ions (see the Irving-Williams series). The latter two replacements are especially important in the enzymes of the respiratory chain, where the redox activity of these ions is required. Since Zn^{2+} cannot undergo a one-electron reduction/oxidation, the action of the enzymes is stopped and cellular respiration is inhibited [43]. This can reduce the production of the reactive oxygen species. However, in bacteria that lack catalase or superoxide dismutase, such inhibition of NADH oxidase can have the opposite effect of decreased protection against the H_2O_2 that comes from the environment [34]. Similarly, Ga^{3+} ions can substitute Fe^{3+} ions. More about this will be discussed in Section 1.4.4.

(c) Destruction of [4Fe–4S] clusters: [4Fe–4S] clusters are very important parts of many enzymes and they can be destroyed either by substitution of Fe (e.g., by Zn^{2+} or Ga^{3+}) or bonding to S (e.g., Ag^+), or indirectly by ROS. In this way, $Cu^{+/2+}$ inactivates Fe–S dehydratases, the cytoplasmic enzymes needed to make branched-chain amino acids [21], [36].

A consequence of protein dysfunction by metal ions can be an increased production of ROS, if certain enzymes of the respiratory chain are inhibited or if [4Fe–4S] clusters are

destroyed to release additional Fenton-active Fe into the cytoplasm [21]. The antibacterial action of zinc ions is mainly a consequence of the inhibition of enzymes [30], [31], [32], [33]. Competitive inhibition and reaction of Zn(II) with sulfhydryl groups are the currently known ways of inhibition by Zn^{2+} [31], [32], [33].

1.2.2.4 Impaired membrane function

Impaired membrane function is associated with the accumulation of ions in the cell membranes of bacteria, and thus with changes in their permeability by gradual release of proteins and lipopolysaccharides. The transportation of protons and/or other important ions through the cell membrane is prevented or out of control, which consequently leads to the destruction of the cell membrane and the death of the bacterial cell. An example of such mechanism is Ag^{+}, which can enter the bacterial cells through ion channels and disrupt the transport of other ions through these channels [47]. Additionally, inactivation of the respiratory and transport proteins in the cell membrane by reaction of Ag^{+} ions with their thiol (–SH) groups disrupts the membrane potential and permeability and leads to proton leakage and eventually to the detachment of the cytoplasm membrane from the cell walls [22], [30], [42], [48].

Similarly, binding of Zn(II) to the membrane inhibits membrane-associated enzymes, impairs calcium uptake and changes the fluidity of the membrane leading to increased permeability of cells to protons [30], [31]. Moreover, this binding may also reduce bacterial adhesion, colonization and subsequent plaque maturation due to modified cell surface properties of individual plaque bacteria [49]. Zinc may alter the cell surface proteins or simply reduce the net negative charge on the cell surface, which increases the co-aggregation [49].

1.2.2.5 Interference with nutrient assimilation

A typical example of this mechanism are Ga^{3+} ions, which interfere with the iron uptake. More on this topic in Section 1.4.4.

Zn^{2+} ions inhibit the utilisation of the bacterial carbon source. They can disrupt the metabolism of sugars (inhibition of acid production by dental plaque [31], [32]) as well as the amino acid metabolism (inhibition of alkali production from urea by dental plaque [31]). This consequently reduces the amount of ATP.

1.2.2.6 Effect on nucleic acids

By affecting the production of intracellular ATP, the ions disrupt the process of DNA replication. Inability of ATP synthesis could also be a consequence of the inhibited cellular respiration as in the case of Ag^{+} [22], [30], [42]. Apart from this indirect effect, metal ions can affect the nucleic acids also directly:

(a) Dysfunction: this involves effects on the secondary structure of nucleic acids. Ag^{+} ions can form complexes with the nucleobases of DNA and RNA. Such complexation can lead to DNA condensation and loss of replication ability (DNA needs to be unfoiled for the replication) [30], [42], [50]. However, some intracellular proteins might protect DNA from these interactions [51]. Intracellular Ag^{+} can also inhibit expression of the ribosomal 30S subunit protein S2, which leads to denaturation of the ribosome and inhibition of translation [51], [52].

By cross-linking within and between strands of DNA, copper may cause helical structure disorders and DNA denaturation [35], [53]. However, some studies have shown that H_2O_2 was required for the DNA breakage, which questions the relevance of this mechanism [35].

(b) Genotoxicity: this involves effects on the primary structure of nucleic acids (mutations). It is associated with Mn(II), Cr(VI), Co(II), Cd(II), Mo(IV), Sb(III) and As(III), as well as some organomercury complexes. However, ROS can damage the nucleic acids as well.

1.2.3 Bacterial resistance to metal ions

Since one antibacterial ion acts by several aforementioned mechanisms at the same time, bacterial resistance to antibacterial ions is not as prominent as in the case of antibiotics. Nevertheless, bacteria have found many ways to cope with the toxicity of metal ions. As copper and zinc are essential micronutrients required by a variety of enzymes [30], [40], [43], [44], [54], [55], systems for controlling their intracellular concentration exist in almost all organisms. A range of mechanisms for protection against the toxic effects of the excess copper or zinc ions can be found in bacteria [35], [44], [56], [57]:

(a) exclusion by a permeability barrier (relative impermeability of the outer and inner bacterial membranes to copper/zinc ions);

(b) intra- and extra-cellular sequestration of ions by cell envelopes and metallothionein-like proteins in the cytoplasm and periplasm;

(c) active transport membrane efflux pumps;

(d) reduction in the sensitivity of cellular targets to copper/zinc ions;

(e) extracellular chelation or precipitation of ions by secreted metabolites; and

(f) adaptation and tolerance via up-regulation/down-regulation of necessary genes in the presence of copper/zinc.

Such mechanisms have been observed in Gram-positive as well as Gram-negative bacteria and genes for the efflux pumps, ion scavengers and other related proteins can be encoded in chromosome or plasmid DNA [22], [44], [57]. Bacterial resistance to copper is relatively low, as compared to the resistance to antibiotics demonstrated by some microorganisms (i.e., 10-fold lower sensitivity to copper as opposed to 1000-fold less sensitivity to methicillin, for example by methicillin resistant *S. aureus*). Thus, in contrast to the highly resistant microbes that have evolved to antibiotics in less than 50 years of use, tolerant microbes to copper are extremely rare even though copper has been a part of the earth for millions of years. Above a certain threshold and time of exposure, which differs among the microorganisms, they eventually cannot deal with the copper overload and die [35]. Moreover, complete degradation of DNA occurs, so that the transmission of any resistant genes is prevented [36], [44]. A recent study compared the Cu and Zn resistance of MRSA and methicilin-susceptible *S. aureus* in a global collection of species [58]. While there was no difference in their Cu susceptibility, there were significantly more zinc-resistant MRSA strains, which also had an encoded zinc resistance [58].

Bacteria are able to develop resistance also to silver ions if they are applied at minimum inhibitory concentration (MIC) (2–4 mg Ag^+/l) or sub-MIC levels [28], and the genes for this resistance are in certain cases the same as the ones for the antibiotic resistance [22]. There are two forms of resistance: complexation of Ag^+ inside cells or reduced permeability to silver combined with an upgraded active efflux mechanism to pump silver out of the cell [28]. Several Gram-negative and Gram-positive bacteria have been reported to be silver resistant, including *Pseudomonas aeruginosa*, *Pseudomonas stutzeri*, members of the *Enterobacteriaceae* and *Citrobacter* spp. [30]. Resistance is mainly encoded in plasmid, but sometimes (e.g., in *E. coli* strains) also in the chromosome instead [22], [39], [42].

It seems that the bacterial resistance is an important issue also with antibacterial metal ions. Nevertheless, the antibiotic resistant bacteria are usually not resistant also to antibacterial ions, even though copper and silver resistance genes have been found associated with the antibiotic resistance genes in a few cases [22].

1.2.4 Cytotoxicity of metal ions

The mechanisms of antibacterial action of metal ions are not as specific as the mechanisms of antibiotics, so their toxicity is not selective and affects eukaryotic cells in a similar way. Many studies that compared the *in-vitro* cytotoxicity of different ions found out that Ag^{+} ions were among the most toxic ions towards fibroblast and osteoblast cells [59], [60], [61], [62]. Their TC_{50} (molar concentration) values were at least 10 times (up to 500 times) lower than TC_{50} values of Cu^{2+}, Zn^{2+} or Ga^{3+} ions. A review through the minimal inhibitory, bactericidal and cytotoxic concentrations from the vast literature of experiments on Ag^{+} has revealed a very narrow therapeutic window, in which ionic silver is efficient antimicrobial with low toxicity for eukaryotic cells [29]. It is well known that certain thiol-containing molecules (such as cysteine, glutathione or sodium thioglycolate), which can be present in the serum, reduce the *in-vivo* toxicity of silver ions [42], [63], [64]. However, it has been recently shown that the toxic values of silver nitrate and commercial silver-containing wound dressings for *P. aeruginosa, E. coli, S. aureus* and human fibroblasts are very similar under similar conditions and that thiol-containing molecules reduce their toxicity towards both prokaryotes and eukaryotes [64]. Moreover, the reaction of Ag^{+} with certain biomolecules leads to permanent accumulation of insoluble silver sulfide or silver selenide precipitates inside the cells, which is expressed as argyria (silver in the dermis; skin discoloration) and argyrosis (silver in cornea, conjunctiva, eye lens, and/or periocular regions; discoloration of eyes) [65]. Although so far argyria has not been shown to present a threat for the human life or the function of the organs and tissues and some scientists consider it a rather cosmetical and psychological problem, it is undisputedly a clear evidence of a problem in excretion of silver from the human body. In spite of insufficient and contradictory information about harmfulness of silver to human and environment, silver-based products have flooded the market recently [28], [29].

Copper ions are also toxic to both prokaryotes and eukaryotes at higher cellular concentrations [22], [66]. The risk of adverse reactions due to dermal contact with copper surface is considered extremely low. However, ionic copper is not appropriate for treatment of systemic infections, mainly because once copper is ingested it readily interacts with transport proteins as well as small molecular weight ligands, making it unavailable as an antimicrobial. Furthermore, in cases where no efficacious copper metabolism occurs, the unligated free copper in the body may be involved in disease pathogenesis, such as in Alzheimer's disease [35], [43]. It has also been observed that DNA oxidative damage by copper ions *in vivo* can be much lower than *in vitro* because stronger competing ligands, such as glutathione and cysteine, may remove copper away from the DNA [35].

1.3 Antibacterial Action of Nanomaterials

1.3.1 Categorization and the main representatives

Many different kinds of inorganic nanoparticles have shown antibacterial properties. Reviews on the research of antimicrobial nanomaterials can be found in ref. [17], [67], [68]. They can be classified by various properties that determine their toxicity:

1. Nature/chemistry of nanomaterials: carbon, metallic or metal oxide nanoparticles;

2. Bulk/ionic antibacterial properties: metals or metal oxides that possess antibacterial properties already in their bulk/ionic form, such as Ag, Cu/CuO or Zn/ZnO, are generally more effective nano-antimicrobials than the ones that do not, e.g., MgO, Al_2O_3, Fe_3O_4, TiO_2 or SiO_2. Antibacterial properties of the first group are greatly enhanced by decreasing the size to nanoscale to very strong bactericidal properties, whereas nanoparticles of the second group affect the bacteria only at a very small size, high concentrations and/or certain modification (addition of an antibacterial component or excitation with light) [33], [69];

3. Size: the dependence of properties on the size is one of the main characteristics of nanomaterials. Many properties are size-dependent: reactivity, solubility, stability of nanoparticles, interactions with cells/biomolecules, penetration into cells etc. In general, smaller particles exhibit higher toxicity/antibacterial efficiency [33], [50], [70]. But usually a threshold size can be found, above which a certain property becomes size-independent.

4. Shape: in silver nanoparticles the dependence of the efficiency on the shape was observed to be falling in the order: triangular nanoplates, nanospheres, nanowires [71]. ZnO antibacterial properties are also morphology dependent as certain facets (111) are more active than others (100). Thus, ZnO nanorods are stronger antimicrobials than ZnO nanospheres and flower-shaped nanoparticles with exposed polar facets (that possess a high amount of oxygen vacancies) are even stronger [72]. On the other hand, spherical ZnO NPs are more soluble than nanorods, which was explained by their higher surface curvature [72].

5. Surface properties: these are very important due to the increased fraction of atoms at the surface in nanoparticles. Nanomaterials are often categorized by their surface charge (zeta potential), which is taken as a measure of interactions with bacterial cells. On the other hand, the chemistry of the atoms/ions/molecules on the surface can very much determine the antibacterial properties/toxicity of the nanoparticles. Increased antibacterial activity of nanomaterials with respect to their bulk properties is usually a consequence of increased fraction of atoms of the surface, low-coordination and high-energy sites (corners, edges, kinks etc.) [73]. Moreover, nanoparticles usually have a capping agent on their surface to prevent their agglomeration/coalescence/flocculation, which can notably change their antibacterial properties. If an appropriate capping agent/functionalization is chosen, the nanoparticles can be designed to possess greatly enhanced antibacterial activity. In this way, gold nanoparticles, which are not antibacterial but rather highly biocompatible, can act also bactericidally in combinations with photo-sensitisers, antibiotics or photothermally [69]. On the other hand, capping agents/surfactants can add to toxicity of nanoparticles also unintentionally, as was observed for Au nanorods, which can be cytotoxic if they are synthesised with CTAB [74].

The majority of research has been done on metallic and oxide materials, particularly on silver, copper, gold and zinc, iron, magnesium, aluminium, titanium and silicon oxide [33], [69]. Silver nanoparticles are currently the most powerful antimicrobials that exhibit bactericidal action to a large variety of (Gram + as well as Gram −) bacteria [33], [50], [70]. ZnO has so far been found the most effective metal oxide antimicrobial, with efficiency comparable to silver [33], [75].

1.3.2 Antibacterial mechanisms

Antibacterial action of inorganic nanomaterials differs considerably from the action of antibiotics but not so much from the antibacterial action of metal ions. By contrast to antibiotics and similar to inorganic ions, every kind of nanomaterial has several targets. Many unsolved questions remain regarding the mechanism of antibacterial action of nanoparticles. It is evidently different for different kinds of nanoparticles and there are many mechanisms proposed for each kind of nanoparticle. The main currently proposed mechanisms are shown in Figure 1.7 and explained in more detail further on.

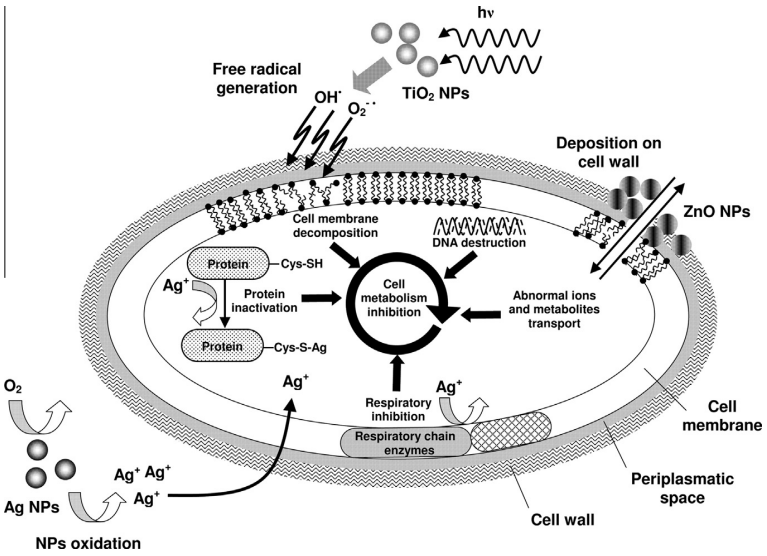


Figure 1.7: Mechanisms of antibacterial activity of nanoparticles [76].

1.3.2.1 Reactive oxygen species

The production of reactive oxygen species is an almost universal mechanism that can be encountered in all kinds of nanoparticles [33]. The effect of ROS was explained already in Section 1.2.2 about metal ions. However, while it was restricted only to redox pairs in the case of antibacterial ions, there are three important additional ways of direct ROS generation with nanomaterials:

1. Fenton-like oxidation of nanoparticles: A Fenton-like reaction (Eq. (1.7)) was suggested to account for the observed generation of $OH^\bullet$ radicals at pH below 7.4 [77]:

$$Ag + H_2O_2 + H^+ \longrightarrow Ag^+ + {}^\bullet OH + H_2O \tag{1.7}$$

   Free radicals are created at the surface of Ag nanoparticles and react with water and oxygen, which leads to the production of ROS, such as superoxide anion ($O_2^{\bullet -}$), hydroxyl radical ($OH^\bullet$) and singlet oxygen ($^1O_2$). These ROS damage the cell membrane. This event is more expressed in Gram-negative bacteria, which have a thinner peptidoglycan layer than Gram-positive bacteria [78].

2. Electron-hole pair in semiconductors (photocatalysis): If ZnO nanoparticles are shined with UV light, their antibacterial effect can become strongly bactericidal as a consequence of photocatalysis. ZnO is a semiconductor with a direct 3.3 eV band gap

[72]. Absorption of light with energy greater than 3.3 eV induces the electron transfer from the valence to the conduction band and a consequent separation of charge, generating a hole (h^+) in the valence band and an electron (e^-) in the conduction band [72], [79]:
$ZnO + h\nu \longrightarrow e^- + h^+$ (on the surface of ZnO particles).
At the surface of the excited ZnO particle, the valence band holes abstract electrons from water and/or hydroxide ions, generating $OH^\bullet$ radicals (Eq. (1.8)). In addition, electrons can reduce O_2 to produce the superoxide anion $O_2^{\bullet -}$ (Eq. (1.9)):

$$h^+ + H_2O \longrightarrow OH^\bullet + H^+ \tag{1.8}$$

$$e^- + O_2 \longrightarrow O_2^{\bullet -} \tag{1.9}$$

The obtained $OH^\bullet$ and $O_2^{\bullet -}$ can induce lipid peroxidation in membranes, DNA damage due to strand breakage or oxidized nucleotides and oxidation of amino acids and protein catalytic centers [79]. Some scientists pointed out that the negative charge prevents $O_2^{\bullet -}$ from passing through the membrane into the cell, so it can exert only outside damage. However, it can also combine with H^+ to create H_2O_2 (Eq. (1.10)), which can pass through into the cell and create internal damage that eventually leads to cell death [72]:

$$O_2^{\bullet -} + H^+ \longrightarrow HO_2^\bullet \tag{1.10a}$$

$$HO_2^\bullet + H^+ + e^- \longrightarrow H_2O_2 \tag{1.10b}$$

As in the case of ZnO nanoparticles, photocatalytic activity of TiO_2 nanoparticles can account for their antibacterial effect as a consequence of production of $OH^\bullet$ radicals. Of interest is metal doping (e.g., with Ag) of TiO_2, which can improve its antibacterial properties significantly, moreover, it can enable photocatalytic activity, induced by the visible light [17], [67].

3. Surface-generated ROS: it was observed that ZnO nanoparticles show bactericidal properties as well as ROS generation also in complete absence of light. This effect is tried to be explained by surface defects (nanosize potentiates the surface properties) and by a mechanism, in which oxygen or halogens adsorbed on the nanoparticle surfaces behave as oxidizers [32], [72]. Such a mechanism would be enhanced in an aerobic environment and it was observed that oxygen annealing and formation of nanoholes on the surface, which both stimulated a high amount of adsorbed oxygen atoms on the ZnO surface, increased the ROS production and enhanced the antibacterial properties [32], [72].

   In contrast to ZnO nanoparticles, TiO_2 nanoparticles do not possess any antibacterial properties in the absence of UV light. This has been explained by their weak interacting with bacterial surface due to their negative charge [75].

It is believed that the role of ROS in Cu NPs is much larger than in Ag nanoparticles, since they can be generated by Cu as well as the released Cu^+/Cu^{2+} ions by their dissolution [80] (see also Section 1.2.2.1). Both Cu and CuO antibacterial nanoparticles have been studied. They cause lipid peroxidation, cell wall and membrane damage and oxidative damage to DNA and they generate ROS already in the absence of any cells, in extracellular as well as intracellular environment.

1.3.2.2 Dissolution of nanoparticles and local release of antibacterial ions

Nanometals and metal-oxide nanomaterials possess all antibacterial characteristics of antibacterial ions, because of the ion release from the surface of these nanomaterials. Dissolution of silver nanoparticles is often considered to be the main mechanism of the antimicrobial activity of nanosilver [47], [81], [82]. In 2012, two important investigations on the mechanism of toxicity of Ag NPs were published and both brought out silver ions as the key mechanism of antibacterial action and cytotoxicity of Ag NPs [83], [84]. Singh and Ramarao showed that Ag ion-reactive weak antioxidants containing a large number of thiol groups (like N-acetylcysteine (NAC), methionine and cysteine) effectively reduced the toxicity of Ag NPs as well as the mytochondrial damage in the cells, whereas strong antioxidants and cell membrane ROS scavengers, which neutralize the external as well as internal ROS, did not reduce the cytotoxicity of the Ag NPs and the mytochondrial damage caused by Ag NPs to murine macrophages [83]. Since the main effect of such molecules is deactivation of Ag^+ ions and not deactivation of ROS, these results ruled out ROS as the main mechanism and proved a higher importance of the Ag^+ ions. Xiu *et al.* went even further and claimed that Ag^+ ions were the only active part of the Ag NPs and the contribution of nanoparticles was negligible [84]. They prepared and tested the nanoparticles under anaerobic conditions so that the ion release from them was negligible and the Ag NPs were ineffective against *E. coli* K12 under such conditions by contrast to the Ag^+ ions that remained antibacterial [84]. Moreover, if the Ag NPs were exposed to air prior to the antibacterial test under anaerobic conditions, so that a certain amount of ions was released from them, their antibacterial properties were enhanced and bacterial survivability dependence on the concentration of released ions matched its dependence when exposed to ionic solutions only [84]. In this way the authors have proven that only Ag^+ ions were active under anaerobic conditions.

However, I need to point out that under anaerobic conditions, bacteria do not use the aerobic cell respiration, which Ag nanoparticles could affect but it would not contribute to their toxicity under anaerobic conditions. Nevertheless, these studies have revealed the importance of the Ag^+ for the antibacterial action and cytotoxicity of Ag nanoparticles and the nanoparticulate form mainly contributes to enhanced transport of Ag^+ ions and local delivery. Whether it is only due to the enhanced transport of Ag^+ ions or there are additional important mechanisms, the amount of released ions from the Ag NPs at their minimal inhibitory concentration was always lower than the minimal inhibitory concentration of Ag^+ ions only and Ag NPs would need to be completely dissolved to obtain similar MIC of released ions and ionic solutions, while only a small fraction was dissolved in most extracellular or simulated intracellular media [47], [85], [86]. In 2013, Yu *et al.* found a way to separate Ag NPs and Ag^+ ions from the interior of the cells and thus determined the extent of intracellular dissolution of Ag NPs in HepG2 cells. Only 10 % of Ag NPs were dissolved after 24-hour exposure [87], which was two times larger than the extracellular dissolution, but still far from complete dissolution. On the other hand, a recent study observed (using the same technique of Ag NPs and Ag^+ separation after cell lysis) a 55 % dissolution of Ag NPs inside Chinese hamster ovary cell subclone K1 cells after only 1-hour incubation, which led to 80 % dissolution after 12 hours of incubation, which was much higher than the 5-7 % dissolution in cell growth media [85], [88]. The ion release from the Ag NPs is size-dependent. The highest concentration of released silver ions was observed in the case of the highest surface area of silver nanoparticles [86]. The lowest concentration of silver ions released was noted for silver nanoparticles with the lowest surface area, resulting in weak antimicrobial properties [86]. Nowadays, release of ions and their contribution to the antibacterial activity is considered important for Cu/CuO and ZnO NPs as well [33], [72].

1.3.2.3 Nanosize-specific mechanisms

Some mechanisms are characteristic for antibacterial nanomaterials and are very much related to their small size:

1. Interactions with cell wall/membrane: Adhesion of nanoparticles to the bacterial surface can alter the cell wall/membrane properties. The small size and extremely large surface area of nanoparticles enables them to make strong contact with the surface of a microorganism [47], [89], [90]. Nanoparticles with a more positive zeta-potential generally exhibit stronger interactions with bacteria since bacterial surface (cell wall) is negatively charged.

   Although the dissolution mechanism has been recognised as the most important for Ag NPs, certain investigations have highlighted the importance of their interactions with bacterial cells for their antibacterial action. Immobilised Ag NPs were more efficient than Ag^+ ion-releasing (Ag or AgCl) substrates as well as colloidal Ag NPs, even though they released a much lower amount of ions and the immobilised Ag NPs were not internalized [86], [91]. Moreover, while the toxicity of 20-80 nm Ag NPs follows the dissolution size-dependence and is mainly assigned to the released ions [86], the 10-nm Ag NPs are much more toxic, because at this size the interactions of nanoparticles with cell become much more important [86]. It has been observed that Ag nanoparticles attach to the cell wall/outer membrane and create holes ("pits") in it, which leads to the increase of the permeability of the membrane and leaking of intracellular components [51], [71], [73], [86], [92], [93].

   Interactions of Ag NPs with cell wall/membrane have been investigated in detail. For the sulfur-containing proteins it is not clear if they interact with nanoparticles, ions or both, and both can increase the trans/cis ratio of unsaturated membrane fatty acids, which can lead to the change of the membrane fluidity. Ag NPs can also change the lipid composition of the membrane, anchor and incorporate into the outer membrane. It is currently believed that the outer membrane damage is mainly "nano-specific" and not so much an action of the Ag^+ ions [86]. In this way, Ag NPs enhance the transport of Ag^+ ions into the cell.

   Likewise, it has been shown that the attachment of ZnO nanoparticles can damage the cellular membrane by changing the structure of proteins and phospholipids in the membrane (the ratio of β-sheets/α-helices decreases) and breaking the phosphodiester bond of L-α- Phosphatidyl-ethanolamine, which destroys their amphiphilic properties and bilayer structure [72], [75]. These effects have all been attributed to the small size of the particles, which enables more interactions with bacterial cell wall and membrane, and can lead similarly as in the case of Ag nanoparticles to disintegration of membrane and leaking, eventually causing cell death [72].

   Furthermore, Ag NPs affect also peptidoglycan [94], [95]. A change of secondary structure of the peptide branches and total configuration of peptidoglycan was observed after exposure to Ag NPs as well as release of muramic acid as an indication of fragmentation of glycan strands leading to "pits" in peptidoglycan/cell wall of Gram-positive bacteria [94].

2. Penetration into the cells: Peptidoglycan is permeable for particles with sizes up to 2 nm [75]. However, nanoparticles as large as 30 nm can usually be found inside bacteria, because the interactions with the cell wall ease the penetration of nanoparticles. Nevertheless, smaller particles (especially below 10 nm) penetrate more easily and are thus the first inside [95], whereas larger nanoparticles enter when the holes in the cell wall/membrane are large enough. Once inside, they affect the intracellular

components/processes as described before. However, accumulation of nanoparticles in certain intracellular areas (cytoplasm, periplasm) also changes their local environment and thus disrupts the cellular activities even if the nanoparticles do not directly interact with intracellular molecules [72]. By contrast to bacteria, eukaryotic cells offer several additional ways of entrance for nanoparticles, such as endocytosis and other active uptake mechanisms (see Figure 1.8). They often lead to accumulation of nanoparticles in particular organelles (lysosomes, phagolysosomes), which can consequently increase their toxicity due to increased release of ions under different (more acidic) conditions [96]. On the other hand, such trapping can also protect the other organelles, especially if the released ions are not very toxic.

Penetration into the cells presents another improvement in transport of antibacterial ions. Ag nanoparticles of less than 5 nm were more toxic than any other form of silver (silver ions, AgCl colloids), presumably due to easier transport through the cell wall/membrane of uncharged silver nanoparticles in comparison with charged silver ions [47], [97].

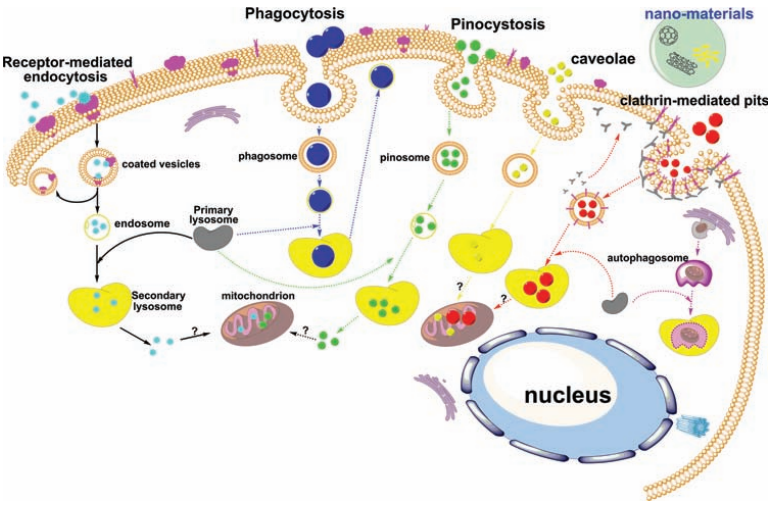


Figure 1.8: Schematic of the known pathways for intracellular uptake of nanoparticles [98].

1.3.3 Gold nanoparticles

Gold nanoparticles alone are considered biocompatible and bioinert [99], [100], [101]. Only Au NPs with size below 3 nm are cytotoxic due to their irreversible binding to key biopolymers [74], while cytotoxicity of Au NPs above 10 nm is usually not size-dependent [102]. Internalization of Au NPs into a eukaryotic cell is size-dependent (and shape-dependent) and differently sized nanoparticles enter the cell in different ways. Usually, the best and the fastest uptake was observed for 40–50 nm size [102] and it was higher for nanospheres vs nanorods [103]. The uptake of nanoparticles is also very much dependent on their charge (positively charged NPs generally penetrate more easily), the molecules on their surface and the cell type. Their ability to penetrate the tissue increases with decreasing size [104] and Au NPs with size above 15–20 nm cannot cross the blood-brain or the blood-retinal barrier [74], [99]. Au NPs can be used as antibacterial agents only if they are irradiated with NIR light (photothermal treatment) or if some antibacterial component is added to them [17], [67], [69]. Interestingly, some studies have shown also antibacterial activity of

gold nanoparticles with a non-antibacterial component added to them, like C/Au core-shell [105] or functionalized Au nanoparticles [106], [107]. The proposed mechanism of the latter is [106]:

(a) Au nanoparticles as carriers enable entry of the added molecules into bacterial cells, where they can directly affect some important molecules, otherwise protected by the cell wall and membrane;

(b) Concentration of otherwise inactive molecules on the surface of Au nanoparticle enables (or increases) some interactions that lead to bacterial death.

In this way, 4,6-Diamino-2-pyrimidinethiol, which does not act as an antibiotic, was able to chelate Mg^{2+} ions when attached to the Au nanoparticle [106]. This caused damage of the outer membrane (creation of vesicles), leading to increased permeability of the cellular membrane. This enabled entry of the nanoparticles inside, where chelation of Mg^{2+} and interaction of the particles with DNA resulted in inhibition of protein synthesis. Cell death followed as a consequence of leakage of intracellular content [106]. The antibacterial action of Au/4,6-Diamino-2-pyrimidinethiol NPs involves changing the membrane potential, inhibition of ATP synthase activities to decrease the ATP level and inhibition of the ribosome subunit for tRNA binding [108]. These gold NPs also enhance chemotaxis in the early-phase reaction, but do not induce any ROS-related process [108].

1.3.4 Multiple targets and cytotoxicity

Multiple targets were already recognised as an important characteristic of antimicrobial metal ions and are even more pronounced in nanomaterials. Nanomaterials have unique interactions with cell walls, membranes and intracellular components, which significantly reduces the possibilities of resistance. Moreover, metal and metal oxide nanoparticles can enhance the transport of the antibacterial ions into the cells, which could circumvent the bacterial resistance that involves efflux systems (see Section 1.2.3). However, Graves *et al.* demonstrated that *E. coli* bacteria can easily develop resistance to Ag NPs as well as Ag^{+} after 100-200 generations of exposure to Ag NPs [109] and several studies have shown low efficiency of Ag NPs against silver-resistant bacteria [47], [86].

Although a large number of targets is their major advantage over conventional antibiotics, the major problem of nanoparticles is the non-selectivity of their mechanisms for bacteria and consequent toxicity also for eukaryotic cells [17], [33]. Silver nanoparticles show similar cytotoxicity issues as Ag^{+} [29], whereas CuO nanoparticles are much more toxic to mammalian cells than Cu^{2+} ions and also much more cytotoxic than ZnO and TiO_2 nanoparticles [110].

Especially production of free radicals and reactive oxygen species already in the absence of any cells needs to be avoided. One of the rare nanomaterials that exhibited antibacterial activity without ROS generation are gold nanoparticles, which enable designed biomedical properties by functionalization. Nevertheless, the case of the Au nanorod cytotoxicity due to CTAB on their surface alarms that care should be taken about the surface properties of Au NPs as well. Moreover, although Au NPs generally exhibit great direct biocompatibility with mammalian cells, there are some difficulties with their excretion from the body. A similar accumulation to argyria can occur also with gold in the body and it is called chrysiasis, but it does not occur to such extent since Au is more bioinert and does not dissolve as easily as Ag in the body fluids [65]. Hence, it was observed only for continuous intraparenteral administration of Au(III) salts, while argyria was observed in all ways of administration and for Ag NPs as well. Silver and gold also have a similar mode of excretion, which goes mainly through the bile and then with the faeces, but for gold also

the routes through the skin, hair, nails, urine and breast milk are not negligible [65]. The most important cells for the removal of Au NPs from the body are believed to be macrophages in the liver (the so-called Kupffer cells), which help in transporting Au to the bile and the faeces, however, this removal appears to go very slowly [111], [112].

1.4 Gallium

1.4.1 Ionic gallium

Ga(III) is a hard Lewis acid (see Section 1.2, Figure 1.5). Therefore, aqueous solutions of its soluble salts (such as nitrate or chloride) have a low pH [113]:

$$Ga(H_2O)_6{}^{3+} + H_2O \rightleftharpoons Ga(OH)(H_2O)_5{}^{2+} + H_3O^+, \ \log K_1 = -2.6 \tag{1.11a}$$

$$Ga(OH)(H_2O)_5{}^{2+} + H_2O \rightleftharpoons Ga(OH)_2(H_2O)_4{}^{+} + H_3O^+, \ \log K_2 = -3.3 \tag{1.11b}$$

Maximum solubility is around 10^{-2} M (resulting in pH of approximately 2) [113], [114], above which an amorphous phase close to $Ga(OH)_3$ precipitates:

$$Ga(OH)_2(H_2O)_4{}^{+} + H_2O \rightleftharpoons Ga(OH)_3(\text{amorph}) + H_3O^+ + 3\,H_2O \tag{1.12}$$

The remaining gallium undergoes further hydrolysis:

$$Ga(OH)_2(H_2O)_4{}^{+} + H_2O \rightleftharpoons Ga(OH)_3(H_2O)_3 + H_3O^+, \ \log K_3 = -4.4 \tag{1.13}$$

Neutralisation of the acidic Ga(III) solutions leads to a decrease in solubility due to precipitation of amorphous $Ga(OH)_3$. This phase is, however, amphoteric, so minimal solubility (around $10^{-7.2}$M) is achieved at pH 5.2 [113]. Above this pH, the solubility starts increasing again due to the formation of soluble $Ga(OH)_4{}^-$ complex:

$$Ga(OH)_{3(aq)} + H_2O \rightleftharpoons Ga(OH)_4{}^- + H^+, \ \log K_4 = -6.3 \tag{1.14}$$

Hence, solubility of Ga(III) at pH 10 is $10^{-3.3}$ M [114]. The constants K_n in equations (1.11)–(1.14) are for water at 25 °C and zero ionic strength. The calculated distribution of Ga(III) forms in dependence of pH under such conditions is presented in Figure 1.9 (a) and precipitation of $Ga(OH)_3$ (Eq. (1.13)) is indicated with a dashed line. Experimentally, a clear solution is observed at pH $\leq$ 3 and pH $\geq$ 10 when a $Ga(NO_3)_3$ solution is titrated with a NaOH solution, but at pH $\leq$ 4 and pH $\geq$ 9 when $GaCl_3$ is titrated with NaOH [115], [116]. The Ga(III) speciation and $Ga(OH)_3$ precipitation range in the physiological saline (0.9 % NaCl) solution at 37 °C are very similar as in pure water at 25 °C [117]. However, they can be notably altered in more complex physiological media (such as cell growth media), in which other stable Ga(III) complexes can be formed and prevent the precipitation of $Ga(OH)_3$. Hence, the pH range, in which this phase precipitates, narrows down or even disappears (see Figure 1.9 b–d). As a hard Lewis acid Ga(III) tends to chelate via O atoms and to a certain extent also N atoms of the ligands [113]. Thus, amino acids and sugars in growth media extend the solubility of Ga(III) and prevent the $Ga(OH)_3$ precipitation below pH 6 (Figure 1.9). The presence of other complexants, such as citrate, can extend it even to and beyond pH 7 (Figure 1.9 (b), (d)). Moreover, in solutions containing very strong complexants, such as siderophores (desferrioxamine B), the precipitation of $Ga(OH)_3$ is completely prevented over the whole pH range (Figure 1.9 (c)). The affinity of Ga^{3+} ion for siderophores, transferrin, lactoferrin and other chelating molecules will be further discussed in Section 1.4.4. On the other hand, gallium phosphate also has a very low solubility (solubility product 10^{-21}), so in media with high concentration

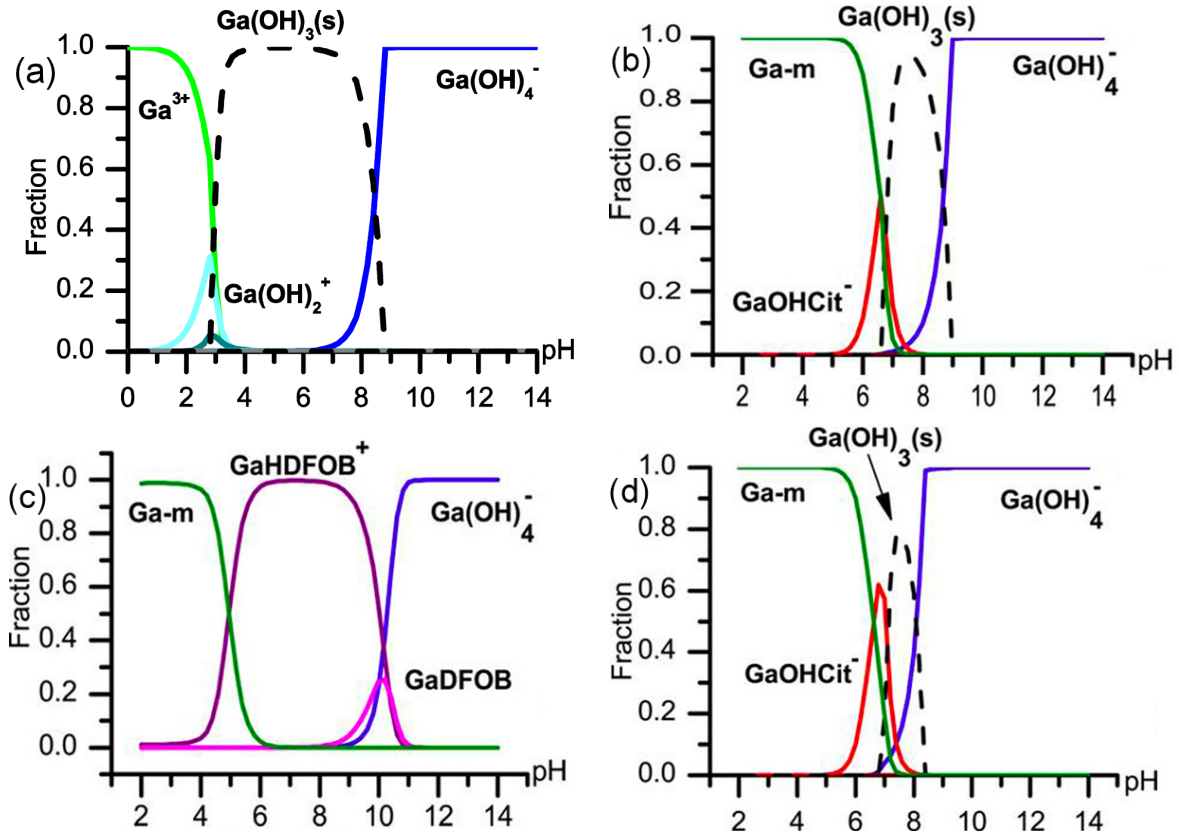


Figure 1.9: Calculated Ga(III) speciation as a function of pH in (a) a 20 μM aqueous solution of Ga(III); (b) 20% Iso-Sensitest medium with 20 μM Ga(III) and 50 μM citrate; (c) 20% Iso-Sensitest medium with 20 μM Ga(III) and 20 μM desferrioxamine B (DFOB); (d) 20% Iso-Sensitest medium with 5 μM Ga(III) and 50 μM citrate. Each line represents the fraction of the total amount of gallium in a specific complex in solution. Broken line represents precipitation of $Ga(OH)_3$. Ga-m denotes complexes of Ga(III) with medium components, such as amino acids or sugars. At lower total concentrations of Ga(III), the relative precipitation of $Ga(OH)_3$(s) is lower than at higher concentrations [118].

of phosphate ions (e.g., phosphate buffer), amorphous gallium phosphate can come out as the precipitate instead of amorphous $Ga(OH)_3$ [113], [114].

If amorphous $Ga(OH)_3$ precipitate is aged for 1 week at room T in the mother liquor, it transforms into a crystalline GaOOH phase [119]. The crystallisation is completed much faster (within less than one day) at pH 8-9 and temperature above 50 °C [116], [119], [120], [121], [122]. GaOOH can also be obtained directly (without intermediate amorphous $Ga(OH)_3$ precipitate) by hydrolysis of $Ga(NO_3)_3$ [123], [124] (but not $Ga(OH)_4^-$ [115], [116]) or elemental Ga under hydrothermal conditions (hydrothermal or sonochemical synthesis of GaOOH nanorods) [125], [126]. α-GaOOH has an orthorhombic Pbnm crystal structure with unit cell dimensions a=4.510 Å, b=9.750 Å and c=2.965 Å. Calcination of this compound leads to its conversion to Ga_2O_3. If it is done below 500 °C, GaOOH converts to α-Ga_2O_3, whereas above 500 °C the β-Ga_2O_3 phase is obtained [127], [128]. α-Ga_2O_3 has a hexagonal (rhombohedric) R-3c structure with unit cell dimensions a=b=4.979 Å and c=13.42 Å, whereas β-Ga_2O_3 has a monoclinic C2/m crystal structure with $\beta = 103.83°$, a=12.22 Å, b=3.038 Å and c=5.807 Å. At least two other polymorphs (γ, ϵ, probably also δ and κ) of Ga_2O_3 exist, which can be obtained after different calcinations of other Ga(III) precursors [127], [128]. However, they all convert to β-Ga_2O_3 above 900 °C. All gallium oxides are very insoluble in water and can be dissolved only in boiling concentrated strong acids or bases. GaOOH, on the other hand, dissolves also in diluted acids.

1.4.2 Elemental gallium

Gallium is a very peculiar metal. It has a low melting point (29.8 °C), a high boiling point (2200 °C), a very low vapour pressure, a descending solid-liquid isochore and expands during freezing like water (density near room T is 5.904 g·cm^{-3} and liquid density at melting point is 6.095 g·cm^{-3}) [129], [130], [131]. Being a stable liquid in a wide temperature range renders it useful for thermometers, its alloys are investigated in dentistry as substitutions for amalgams, for mirror surfaces, as a heat-transfer medium. It is already used as the focused ion beam source and for capturing solar neutrinos [129], [130], [132], [133].

Bulk crystalline gallium normally has an orthorhombic Cmca crystal structure (named α-Ga or Ga I) with a=4.520 Å, b=7.661 Å, c=4.526 Å unit cell dimensions and 4 atoms per unit cell. However, since each atom has only one nearest neighbour and its bonding has been recognised as covalent, this structure is often seen as a two times larger face-centred orthorhombic unit cell containing 4 Ga_2 dimers and very similar to the structure of solid iodine [134]. The partially covalent nature of this structure is responsible for many of the unusual properties of gallium, such as its large anisotropy of thermal and electric conductivity (being the lowest close to the direction of the dimers), a 2.3 eV wide pseudo-bandgap (large decrease in the electron density of states near the Fermi level) and lower conductivity in the solid than in the liquid state [134], which is why it is sometimes classified also as a semimetal [113], [132], [135], [136]. Phase diagram of the α-Ga solid phase, liquid Ga and Ga vapours is presented in Figure 1.10 (a). The prevalence of the liquid state is well evident, as well as the negligibility of the gas phase up to very high temperatures, solidification under vacuum and melting under increased pressure. However, the maximal decrease of the melting point of α-Ga by increasing the pressure is down to 2.4 °C (see Figure 1.10 (b)). Below this temperature, application of a high pressure (1.2 GPa or higher, depending on the temperature) leads to transformation into another solid allotropic modification, called Ga II [137]. Ga II has a body-centred-cubic cell with $a = 5.951 \pm 0.005$ Å (at 2.6 GPa and 313 K) and 6 atoms per unit cell [134], [138]. Its melting point increases with increasing pressure until 2.7 GPa (319.9 K), above which it is transformed on heating into another solid allotropic modification, Ga III, instead of liquid [137], [138], [139], [140].

At lower temperatures, the Ga II phase can be stable up to higher pressures. Thus, at room temperature, it is stable between about 2 and 15 GPa, above which it transforms into Ga III [140]. Ga III has a body-centred-tetragonal structure (similar to the structure of In at normal conditions [141]) with a = 2.813 ± 0.003 and c = 4.452 ± 0.005 Å at 2.8 GPa and 298 K [138]. It is stable up to 75–120 GPa, when it transforms to a face-centred cubic Ga IV crystal structure (similar to Al) [140], [141], [142]. Ga II, Ga III and Ga IV are stable only at high pressures. They can be super-decompressed though, but not below 0.2 GPa (2 kbar) [139].

Bulk liquid gallium can be supercooled down to −60 °C and the supercooled liquid crystallises (below 1.5 GPa) in another different allotropic modification, called β-gallium [143]. This phase is metastable and has a monoclinic C2/c crystal structure with unit cell characteristics: a= 2.766 ± 0.008, b= 8.053 ± 0.024, c= 3.332 ± 0.010 Å, $\beta = 92°02' \pm 05'$ [144]. Here, the gallium atoms are arranged in zigzag chains parallel to the [001] axis [144], [145]. The same phase is also obtained after heating amorphous solid Ga (obtained by freezing Ga vapours on helium-cooled quartz substrate at 4 K) above 15 K, but it transforms to α-Ga already at 70-80 K [143], [144], [146], [147]. On the other hand, β-Ga from the supercooled liquid does not convert to α-Ga and can exist at all temperatures up to its melting point (-16.3±0.02°C at 1 atm), above which it converts to liquid Ga [138], [139], [144]. This implies that there must be some close relation between the local structure of the β phase and the liquid phase. Indeed, the short range order (structure factor and pair correlation function) of liquid Ga, experimentally determined by neutron scattering experiments [148], [149] or calculated by molecular dynamics simulations [147], has revealed good agreement with the local structure of β-Ga, much better than with any other Ga crystalline form. β-Ga exhibits much more normal characteristics in comparison with α-Ga. It is metallic, it has a larger density than its melt and its melting point increases with increasing pressure [134], [148]. In fact, all phases mentioned so far, except α-Ga, display fully metallic properties, including liquid Ga [134], [150].

Similar metastability issues in crystallisation from the liquid Ga have been observed among the high-pressure phases as well. Cooling or compressing the liquid Ga gives Ga III instead of Ga II in the 2.5–5.4 GPa region and Ga II can be obtained only after sufficient supercooling (to 185–210 K) [137], [138], [140]. This has also been explained by greater similarity of Ga III than Ga II in the short range order to the liquid Ga [140].

Ga has a negative redox potential (Eq. (1.15)):

$$\mathrm{Ga^{3+}} + 3\,\mathrm{e^-} \rightleftharpoons \mathrm{Ga_{(s)}} \quad E^{\varnothing} = -0.56\mathrm{V} \tag{1.15}$$

However, it does not reduce water to hydrogen under normal conditions due to passivation with a thin oxide film. 2 ppm of oxygen and only a few minutes exposure to air are enough to establish the oxide film [152], [153], [154]. The oxide layer is dense and prevents further oxygen diffusion inside [155]. Thus, the oxidation is stopped within approximately 30 minutes (after only a few monolayers or about 1 nm of oxide layer) and the core remains elemental Ga [132], [156]. The oxide layer enables wetting of many materials, like our skin or glass, in spite of very high surface tension (735 N/m) of liquid gallium and increases the shear stress of the liquid gallium, which otherwise has a relatively low viscosity (1.894 cP) [129], [130], [131], [132], [154]. A sufficient increase in the shear rate can break the oxide film and re-establish the flow but also exposes the inner part to air, which further increases the shear stress with time due to oxidation [154].

The oxide layer makes gallium difficult for handling, fluidic applications and electrochemistry [156]. It also provides a physical, chemical, and electrical barrier that prevents the metal from making direct contact with its surroundings [156]. It seems that it is difficult to avoid the oxide film formation. Nevertheless, instead of all the effort to work in an

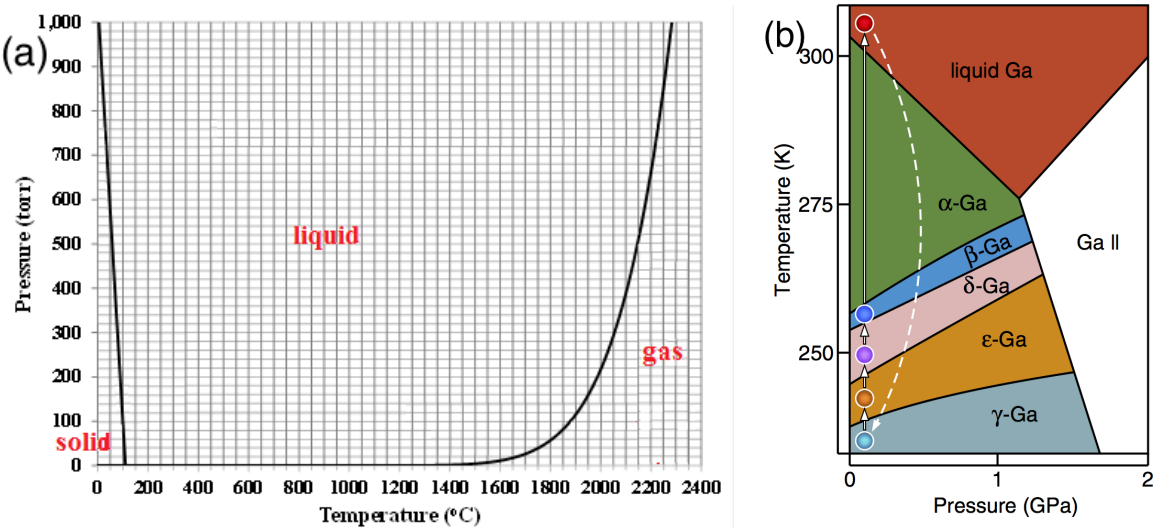


Figure 1.10: Gallium phase diagram: (a) Bulk α-gallium phase diagram from 0 to 2400 °C and 0 to 133.3 KPa. (b) A simplified phase diagram of gallium extended to lower temperatures (<0 °C) and higher pressures (up to 2 GPa). It combines (from right to left) a high-pressure Ga II phase, the metastable phases obtained by supercooling liquid Ga emulsions and the transformation sequence observed in Ga nanoparticles [138], [151].

inert atmosphere all the time and to avoid any contact with oxygen, the formation of the oxide layer can be prevented also using an acid bath [154], [157], [158]. Moreover, with this method also the already formed oxide layer can be removed (this occurs approximately 100 times faster than the formation of oxide layer in air [154]), whereas inert atmosphere can only prevent further oxidation [154]. The oxide layer can be completely dissolved in $>$ 0.2 M HCl solution or 10 % HCl in ethanol [153], while elemental gallium dissolves extremely slowly in these media [154]. The oxide layer can also be effectively removed by HCl vapours [159]. Moreover, a protective $GaCl_3$ film is created that slows down re-oxidation upon air exposure [157], [159]. This is probably the reason why HCl is preferred for oxide skin removal over dilute (1M) NaOH, which can also dissolve the oxide much faster than the elemental Ga underneath [156], [160], [161]. Another method of gallium oxide removal from the Ga droplets is Ar^+ ion bombardment for several minutes, which reduces the surface Ga_2O_3 to Ga [152], [162].

On the other hand, the oxide layer does not always need to be avoided as it can also give gallium some favourable properties. It mechanically stabilizes gallium in nonequilibrium and nonspherical shapes and enables good contacts with organic materials, such as plastics or biological materials [156]. Controlling the flow of liquid Ga by breaking and re-establishing the oxide skin enables filling of microchannels, metal patterning and printing [156], [160], [163]. Such properties, enabled by the surface oxide layer, are useful in microfluidic devices, soft electrodes and sensors, stretchable electronics, self-healing circuits, artificial electronic skins, or soft robotics [156].

1.4.3 Ga nanoparticles

1.4.3.1 Properties

Gallium nanoparticles (Ga NPs) possess many interesting properties:

1. Polymorphism:

When an emulsion of smaller (<100 but >1 μm) Ga droplets instead of bulk liquid gallium are supercooled, several additional (metastable) allotropic modifications can be obtained together with β-Ga and/or α-Ga. They are denoted γ, δ, ϵ etc. and are distinguished by their crystal structures and melting points (Figure 1.10). γ-Ga has a melting point at -35.6 °C and crystallises in the space group Cmcm with a= 10.593 ± 0.002, b= 13.523 ± 0.003 and c= 5.203 ± 0.001 Å. The unit cell contains 40 atoms in six independent special sites and grouped into pentagons and heptagons [139], [144], [164], [165]. δ-Ga has a melting point at –19.4°C and crystallises in the space group R-3m with a = 7.729 ± 0.004 Å and $\alpha = 72°02' \pm 03'$ at 191 ±2 K. The rhombohedral unit cell contains 22 atoms distributed on five independent special sites (five different coordination environments) [139], [145], [166]. ϵ-Ga has a melting point at –28.6 °C [139], [144]. These crystal structures also do not show the "anomalous" properties of α-Ga [145]. The prevailing allotropic modification after crystallisation has been found to depend on the temperature, the dispersing medium and the size of the Ga droplets [139], [167]. Thus, smaller supercooling (not below -50 °C), glycerol medium, absence of surface oxide layer and larger droplets favoured α-gallium, supercooling below -100 °C and silicone oil medium favoured the β phase, the presence of gallium oxide film and supercooling to between -60 and -100 °C favoured the γ phase, whereas the largest supercooling (to the lowest temperatures) and smaller droplets favoured the δ phase [139], [143], [144].

However, it has later been discovered that these phenomena are not restricted to emulsions only, but surface tension/interface energy is in fact the main factor influencing the supercooling as well as the predominant crystal phase. Thus, the investigation continued on sub-micrometre-sized Ga droplets and Ga nanoparticles and focused on the size dependence, irrespectively of the surrounding medium and the synthesis method of the nanodroplets. The following sequence according to the decreasing Ga droplet size has generally been found: α, β, γ, δ. α-Ga has never been observed at sizes <500 nm [167], [168], [169], [170], β-Ga comes out for particles with diameters above 60 and below 800 nm [167], [168], [169], [170], γ-Ga for diameters above 60 and below 600 nm (larger fraction at smaller diameters) [167], [168], [169], [170], nanoparticles with sizes between 12 and 60 nm crystallise solely as δ-Ga [145], [165], whereas Ga NPs with diameters smaller than 10 nm are liquid at all temperatures down to at least 90 K [145], [171]. Hysteresis between crystallization and melting is always observed, crystallisation occurs at temperatures lower than melting. Usually, α-Ga crystallises at 255 K and melts at 302.9 K, β-Ga crystallises at 235 K and melts at 258 K, γ-Ga crystallises at 193–205 K and melts at 238.7 K, whereas δ-Ga crystallises below 153 K and melts at 240–255 K [165], [167], [172].

2. Phase coexistence: Most of the data about the size and temperature dependence of the Ga polymorphism were obtained indirectly by DSC/DTA and temperature dependence of reflectivity. Usually, a Ga sample was a mixture of phases giving several successive "melting" peaks during heating and sometimes several successive "solidification" peaks, which were sometimes ascribed to solid-solid transformations as well. This raises the question whether liquid and solid Ga can coexist in a temperature interval between two melting temperatures or one phase is first transformed into another solid phase and then melted when the melting point of the most thermally stable polymorph for the given size is reached. Likewise, does liquid partially transform to one solid phase and the remaining part to another solid phase at lower temperature (liquid-liquid coexistence [173]) or does it first fully transform to one solid phase that converts to the other solid phase at the lower temperature? Moreover, the size range of certain polymorphs, especially β and γ widely overlaps implying a coexistence of

two solid phases as well. However, this might be attributed to the difficulty of the sample size controlling [172]. Many experiments on Ga particles with wide size distributions had shown the coexistence of β-Ga, γ-Ga and δ-Ga until the experiments on Ga NPs with sizes below 50 nm and very narrow size distributions clearly demonstrated that they crystallised only in δ solid phase below the δ-Ga freezing point and converted to liquid Ga above the δ-Ga melting point (see Figure 1.11) [165]. Nevertheless, most of the solid-solid transformation and coexistence phenomena have been shown for the γ phase, which might possess different properties. Thus, it can disappear below a certain temperature without reappearing upon heating [139], [143], [167], [168], undergo solid-solid $\gamma \rightarrow \epsilon \rightarrow \delta \rightarrow \beta$ transformation in a single 100-nm nanoparticle during heating with the help of laser pulses [174] and stable coexistence with liquid Ga in a solid/liquid core-shell form on a sapphire substrate from 180 K to 800 K [175]. Moreover, the solid–liquid coexistence is still likely to occur also for β and δ-Ga at temperatures near but below the melting point or close to but above the freezing point and it can be reversibly controlled in such temperature intervals by either electron or laser beam pulses [151], [174], [176], [177], [178].

3. Extreme supercooling:
   By decreasing the Ga droplet size to and below μm, supercooling was extended down to 150 K (-123 °C), which was explained by reduced probability of a nucleation site in each Ga droplet if they are small enough (below 100 μm) and well separated, while the critical temperature (150 K) was considered the temperature of homogeneous nucleation [143], [179] or the metastability limit, below which the liquid state becomes unstable with respect to infinitesimal fluctuations [180]. However, extreme undercooling down to at least 90 K has been proven for Ga nanoparticles with a diameter $\leq$10 nm [145], [171]. Decrease of melting point is manifested as the absence of α-Ga phase <500 nm, further absence of β or γ-Ga in nanoparticles $\leq$60 nm and absence of any solid phase for Ga nanoparticles with a diameter $\leq$10 nm. Thus, the melting point is decreased from 303 K to around 258 K below 500 nm size, then to 240–255 K below 60 nm and further to less than 90 K below 10 nm size. Size dependence of the melting and freezing point has been revealed also for different sizes within these ranges. 46-nm Ga NPs crystallised at 143–148 K and melted at 253–255 K, whereas 24-nm Ga NPs crystallised at 140–145 K melted at 240–245 K [165]. Interestingly, melting temperatures well above the bulk melting point have been shown for very small Ga clusters (<50 atoms) [171], [181].

4. Surface Plasmon Resonance:
   Due to the metallic properties of the liquid Ga, which is the state found under normal conditions, Ga NPs exhibit surface plasmon resonance (see Figure 1.12 and Appendix A). It appears in the ultraviolet region (mainly between 200 and 400 nm, i.e., 3–6 eV) and is size- and shape-dependent [155], [165], [182], [183], [184], [185]. Ga nanoparticles have been considered very attractive as plasmonics due to their high bulk plasmon energy of 13.9 eV, good chemical stability, size-tunable liquid state and broad temperature range of the stability of the plasmon resonance from -80 to 600 °C [165], [184]. They have been intensively investigated in 10–300 nm range and their surface plasmon resonance has been further extended into the visible region either by changing their shape to anisotropic truncated spheres on bulk substrates [155], [183], [184], [186], [187], [188] or by creating separated chains/arrays of nanoparticles on a GaN substrate [189]. Like bulk Ga, Ga nanoparticles get easily passivated by a thin amorphous surface oxide layer. The thickness of this layer has been estimated by HRTEM, X-ray scattering and X-ray photoelectron spectroscopy to 0.5–3 nm [165].

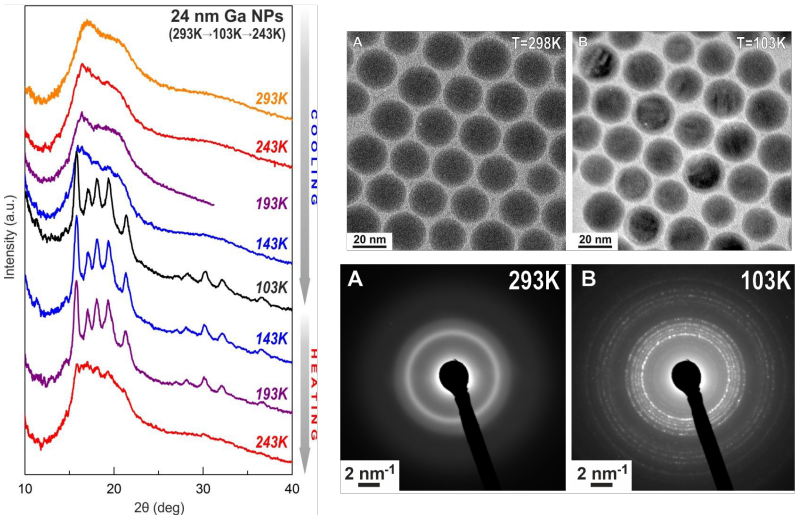


Figure 1.11: Properties of Ga NPs. *Left:* X-ray diffraction patterns of monodisperse Ga NPs with a diameter of 24 nm in dependence of temperature during a cooling and a heating cycle [165]. *Right:* TEM image and SAED pattern of the same 24-nm Ga nanoparticles in their liquid state at 293 K (A) and in their solid δ-Ga state at 103 K (B).

It remains constant over extended storage under ambient conditions as well as after more than 1 hour exposure to oxygen-argon plasma [165]. The formation of the oxide layer on the surface of Ga NPs results in a red shift of ∼0.5 eV (20–40 nm, depending on the size of the nanoparticles) in the SPR peak (Figure 1.12 (a)) [165], [187], [188]. So far, Ga nanoparticles without an oxide shell were created only under ultrahigh vacuum [187], [188], [190], [191] or in inert (nitrogen, argon) atmosphere with oxygen-free non-polar solvents [192]. The surface oxide can be dissolved by 50 mM HCl, but it causes immediate coalescence of nanoparticles into bulk droplets [193]. However, the native oxide layer is actually considered rather beneficial for Ga NPs. It prevents coalescence of Ga nanoparticles and in a sense makes the colloidal solutions of Ga nanoparticles possible [193]. It is non-permeable for oxygen, chemically inert, and stable also on the non-planar surface [165]. As it prevents further oxidation and does not shift the SPR peak by a very large extent, it makes Ga NPs much more stable plasmonics in comparison with Mg, Al and also Ag and Cu [155], [165], [188].

1.4.3.2 Synthesis

Not many articles can be found describing syntheses of gallium nanoparticles. Nevertheless, like with the Ga-based antibacterial nanomaterials (see Section 1.4.5) and characterization of Ga(III)-containing hydroxyapatite (see Section 1.5.2.2), a large progress has occurred in the field of synthesis and characterization of Ga NPs during my PhD study. Syntheses of Ga NPs can be classified as physical or chemical methods, of which the physical methods prevail. The following physical methods have been reported so far:

1. Evaporation of Ga and condensation of its vapours (the high temperature and ultra-high vacuum method, chemical liquid deposition, CLD): since gallium boiling point is at around 2000 °C, this method needs to be carried out in a sufficient vacuum so that the boiling point is decreased (10^{-5} mbar leads to about 1300 °C [194]). Ga vapours are then condensed into Ga NPs either on a bulk (e.g. sapphire) substrate [145], [171], [195] or together with a solvent (acetone, THF or 2-propanol) at 77 K

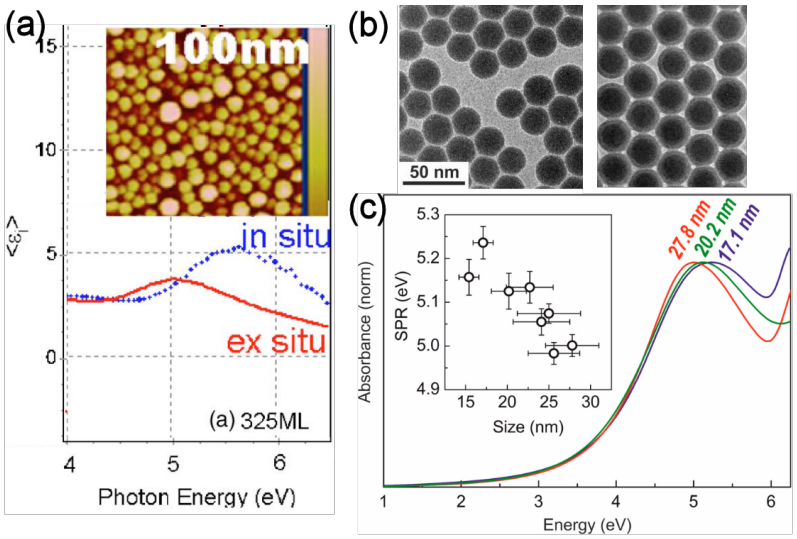


Figure 1.12: Oxide shell on Ga NPs. (a) A red shift in the surface plasmon resonance of Ga NPs due to the formation of the surface oxide layer [187]. The annotation *in situ* refers to the Ga NPs under vacuum without exposure to oxygen and the annotation *ex situ* refers to the same Ga NPs after weeks and months of exposure to air [187]; (b) Gallium oxide shell as observed under TEM. Ga NPs before (left) and after (right) a 10-min exposure to 25 % O_2+75 % Ar plasma are compared [165]; (c) Size dependence of the surface plasma resonance peak for the Ga nanoparticles covered with the oxide shell [165].

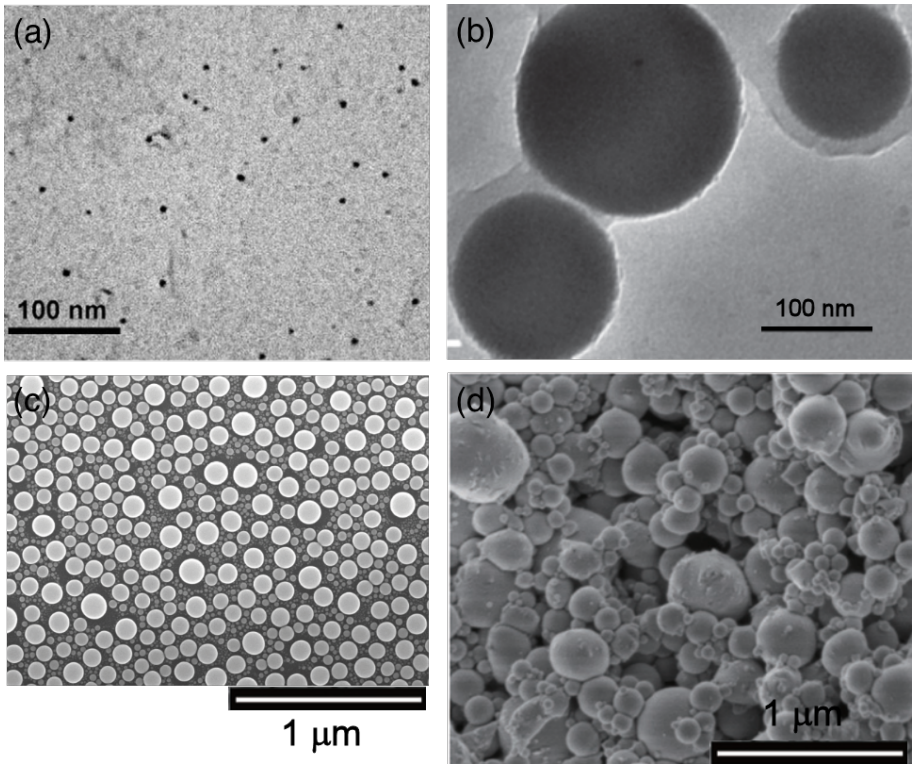


Figure 1.13: Ga nanoparticles prepared by physical methods: a) CLD in 2-propanol [191], b) ultrasonic emulsification in dodecane without a surfactant [192], c) MBE on Si substrate [185], d) ultrasonic dispersion in 2-propanol in the presence of dodecanethiol as a surfactant [193].

[191] to obtain a colloidal solution of gallium nanoparticles (Figure 1.13 (a)). Depositions on bulk substrate (usually sapphire) by beams of atoms, such as molecular beam epitaxy (MBE), also belong to this kind of synthesis (Figure 1.13 (c)). MBE is actually the most frequently used method for synthesis of Ga NPs [155], [183], [184], [185], [187]. Ga atoms have been deposited also on a very narrow silica optical fibre tip [174], [176], [177].

2. Emulsification of liquid gallium into nanodroplets [192], [193], [196], [197] and cooling below melting point, which does not require high temperature, sensitive reagents or ultrahigh vacuum. This method exploits the low melting point of gallium to get gallium nanoparticles by dispersing liquid gallium into small nanodroplets. It has been known already since the 1960s, but has reached the nanoscale only recently. A lot has been said about Ga phases derived from emulsions in Section 1.4.3.1. Gallium microparticles were created in silicone oil [139], [170], [197], glycerol [139], ethanol [143], [180] etc. using various methods of emulsification and with or without surfactants, such as sodium oleate [143]. Later the ultrasonication was established as the best emulsification method that could produce gallium particles with sizes below 1 μm [170], [192] and even below 100 nm without using a surfactant [193]. Moreover, Ga droplets were dispersed in resins and polymers, such as poly(methyl methacrylate) and polystyrene, to obtain nanocomposites [167], [168], [170], in which Ga particles could be separated by size to a certain extent. Nevertheless, the wide distribution of particle size remains the main problem of this synthesis. In 2015, Yamaguchi *et al.* published an investigation about ultrasonic dispersion of Ga in 2-propanol [193]. They studied the influence of the synthesis parameters (ultrasonication power, time, temperature and surfactant concentration) on the mean diameter of the resulting Ga NPs. They discovered that the dependence on power and time was exponential, so that above a certain power and after sufficient time the mean size could not be further reduced by greater ultrasound power or longer sonication [193]. On the other hand, higher temperature (50 °C vs 20 °C) increased the final mean diameter but it did not have any influence if the Ga NPs had already reached the minimal size before the ultrasonication [193]. Moreover, the surfactant did not have any influence on the mean diameter as the surface oxide layer was already sufficient protection against coalescence [193]. However, the surfactant (dodecanethiol) could prevent the size increase in the presence of 50 mM HCl that dissolved the protective oxide layer. 290 mM C12SH successfully prevented coalescence by ultrasonication at 50 °C and 50 mM HCl, while 100 mM C12SH enabled reversible increase/decrease of the mean size by changing the temperature of ultrasonication in the presence of 50 mM HCl [193]. Although this study was very interesting and useful, I must point out that the size distribution of Ga NPs was still very wide (from 10 to 500 nm) with a non-negligible fraction of particles with a diameter above 200 nm (see Figure 1.13 (b),(d)).

These methods use bulk elemental gallium to create nanoparticles (the top-down approach). Chemical methods, on the other hand, use Ga(III) precursors to create Ga(0) nanoparticles (bottom-up approach). The following chemical methods can be found in the literature:

1. Reduction with strong reducents, very sensitive to oxygen and water: the negative redox potential of gallium requires the use of strong reducents, like alkalides in dimethylether [152] or Mg at high temperature (1300–1400 °C) and vacuum [198]. This method was used for obtaining gallium nanoparticles from $GaCl_3$ with alkalides in dimethylether [152], but the authors did not show or report about the size distribution of the Ga particles. Nanosized gallium was also created inside MgO nanotubes

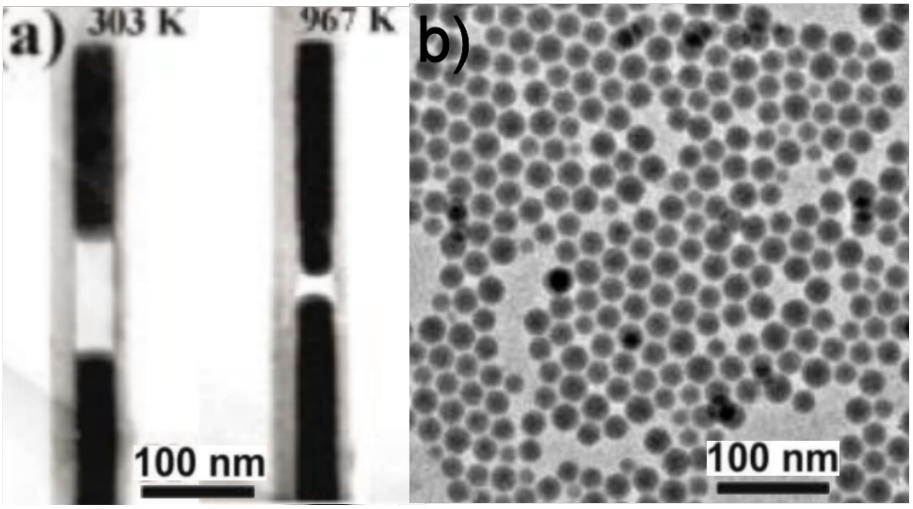


Figure 1.14: Ga NPs prepared by chemical methods: a) Ga nano-thermomether in MgO nanotubes, high-temperature reduction of Ga_2O_3 with Mg [198]; b) monodisperse Ga/OA nanoparticles in hexane, thermal decomposition of $Ga_2N(Me_2)_6$ [165].

by the reduction of Ga_2O_3 with Mg at high temperature (1300-1400 °C) and vacuum [198] (see Figure 1.14 a)).

2. Thermal decomposition of tris(dimethylamino)gallium dimer ($Ga_2N(Me_2)_6$) [165]: this method creates Ga nanoparticles with tunable size between 12 and 46 nm and very narrow size distribution (see Figure 1.14 b).

With these syntheses colloidal suspensions of gallium nanoparticles, polymer nanocomposites or gallium nanoparticles on a bulk substrate have been created. In the attempt of making a nanocomposite with hydroxyapatite and retaining its bioactive properties (see Section 1.5.1), the ultrasonic emulsification seems the only option for a single-step synthesis. This method is the least demanding, but its main drawback is the wide size distribution. Another possibility is a two-step method by first creating a colloidal solution of Ga NPs and then joining them with HAp.

1.4.4 Biomedical properties of Gallium(III)

1.4.4.1 From diagnostic and anticancer to antimicrobial agent

Since gallium was not discovered before the end of the 19th century, it was not used as antimicrobial before the discovery of antibiotics [199]. Antibacterial properties of gallium were first mentioned in 1931 [199], which is around the time of the discovery of penicillin and ten years before the first application of penicillin. Early research on gallium was primarily addressed to its adsorption, tissue distribution, metabolism, and toxicity [199]. In the 1970s, the use of radioactive isotope ^{67}Ga in medical imaging was brought out to locate tumor, inflammation, and infection sites [199]. ^{67}Ga-scans are particularly sensitive to lymphomas, sarcomas, bone tumors, and hepatocellular carcinoma. ^{67}Ga scanning is still used today in the diagnosis and staging of lymphomas [200], [201]. The success of the cancer diagnosis led to investigations of Ga(III) as an anticancer agent. $Ga(NO_3)_3$ has demonstrated clinical efficacy in multiple myeloma, bladder cancer, lymphoma, ovarian cancer, and hepatocellular carcinoma [113], [201]. Only few investigations on gallium antimicrobial properties were conducted in that time and before the year 2000 [113], [201].

In 2003, a pharmaceutical formulation of citrate-buffered $Ga(NO_3)_3$ (sold as the trademark Ganite) was approved by the US Food and Drug Administration (FDA) for treatment of malignancy-associated hypercalcaemia. This and perhaps the warnings about the antibiotic resistance problem led to a much more intensive research of Ga(III) as an antibacterial agent in the 2000s. These investigations have revealed great efficacy of gallium nitrate against *M. tuberculosis*, even inside the macrophages [202], and against *P. aeruginosa* [203], to which gallium maltolate was effective too [204]. Ga^{3+} has shown many favourable antibacterial properties [118], [203]:

(a) it can stop the growth of bacteria;

(b) at sufficiently high concentrations it can kill the bacteria;

(c) much (5X) higher concentration of Fe(III) is needed for the number of bacteria to start increasing again;

(d) it prevents biofouling, a common feature of pathogens;

(e) only much (10X) higher concentration of Fe(III) can restart biofouling;

(f) it can destroy also already built biofilms and bacteria in the inner part of the biofilm are even more affected (lack of Fe in that part boosts the effectiveness of Ga even more);

(g) subinhibitory concentrations of Ga prevent biofilm formation even during the early stages of attachment;

(h) antibiotic-resistant organisms (even those with multidrug resistance) are generally sensitive to Ga.

The greatest success of Ga(III) as an antibacterial agent so far has been achieved in the treatment of tuberculosis, cystic fibrosis and burn wounds. A recent study has shown that $Ga(NO_3)_3$ at safe therapeutic dosage (10 mg/kg) protects mice from *M. tuberculosis* infection [205]. A Phase-1 clinical study is being conducted in the United States since 2010, which tests Ganite administration in human patients suffering from cystic fibrosis, and chronically infected by *P. aeruginosa* [199], [201], [206]. Current results show that intravenous Ganite infusion for 5 days decreases the amount of *P. aeruginosa* in the lung without any serious adverse effect [199], [206]. Thus, so far, Ganite seems a promising novel therapeutic agent for the treatment of chronic lung infection by *P. aeruginosa* in cystic fibrosis patients. Then, subcutaneous application of gallium maltolate was effective in reducing *S. aureus*, *A. baumannii* and *P. aeruginosa* colonization in burn wounds of thermally injured mouse model [204]. These data support a potential use of gallium maltolate *in vivo*, especially in topical administration for the prevention and treatment of wound infections. It is interesting that this *in vivo* treatment was also effective against *S. aureus*, although *in-vitro* tests of Ga(III)-citrate and Ga(III)-maltolate against *Staphylococcus* spp. revealed very high (millimolar) inhibitory concentrations [199]. Beside $Ga(NO_3)_3$ and Ga-maltolate some other forms of Ga(III) have also been used, i.e., chloride [207], citrate [118], desferrioxamine B and other complexes [118], [208], and they were tested against other bacterial species too [199], [209]. Antibacterial properties of a variety of Ga(III)-based antimicrobials *in-vitro* against *E. coli* and *P. aeruginosa* are given in Table 1.1. Considerable progress has been recently made in the development of Ga delivery technologies, developing materials like gallium-doped phosphate-based glasses [210], [211], [212], gallium-carboxymethyl cellulose [213], gallium-incorporated mesoporous bioactive glass scaffolds [214], Ga-containing

phosphosilicate glasses [215], [216] and Ga grafted titanium implants [217]. Such novel materials may eventually be used in other clinical applications, for example to coat catheters and medical prosthetic devices [201]. Recently, three reviews have been written on the gallium antibacterial topic [135], [199], [209].

1.4.4.2 Mechanisms of antibacterial action

The following is currently known about the mechanism of antibacterial action of Ga^{3+} ions:

1. Ga^{3+} and Fe^{3+} ions have a remarkably similar ionic radii, electronegativities, electron affinities, ligand affinities and coordination geometries, and consequently similar binding to chelates and proteins [113]. This allows Ga^{3+} to follow many of the uptake and transport pathways for Fe^{3+}. It is the differences between Ga^{3+} and Fe^{3+}, however, that are responsible for gallium's therapeutic effects. In contrast to Fe(III), Ga(III) cannot be reduced to the oxidation state (+2) under physiological conditions. Furthermore, Ga(III) can exist also in the form of gallate $Ga(OH)_4{}^-$. Hence, at pH 7.4 and 25°C, Ga^{3+} has a solubility of about 1 mM (98.4 % as $[Ga(OH)_4]^-$ and 1.6% as $Ga(OH)_3$) whereas Fe^{3+} has a solubility of only about 10^{-18} M. Thus, small amounts of nonprotein-bound gallium can exist in a solution at physiological conditions, versus insignificant amounts of nonprotein-bound Fe^{3+}, permitting biological interactions for Ga^{3+} that would not be possible for Fe^{3+} [113], [199], [200], [222]. Ga(III) can bind to transferrin, the protein for iron transport, which still has a lot of binding sites unoccupied by Fe(III). In addition to binding to transferrin, Ga(III) binds even more avidly to the related protein lactoferrin as well as to the iron storage protein ferritin [200].

2. Most bacteria require iron for growth. Pathogens can obtain it after entering the host with the help of the so-called siderophores, which can take Fe^{3+} away from transferrin, as the amount of free Fe in the host cells is very low (approximately 10^{-18} M) [20], [203]. In addition to self-produced siderophores, bacteria can also acquire iron through surface receptors for xenosiderophores (i.e., siderophores produced by other bacteria or fungi), or other iron chelators, including citrate, heme, and hemoproteins (e.g., hemoglobin), and host's iron-binding proteins (i.e., transferrin and lactoferrin) [199]. Hence, if bacteria "grab" gallium instead of iron, it will, according to the further described mechanisms, prevent their multiplication inside the host, which is crucial for harming the organism. The substitution of Ga^{3+} for Fe^{3+} was observed in bacterial ferric-binding protein (FbpA), an iron transporter in the same protein superfamily as transferrin. Ga^{3+} can also substitute Fe^{3+} in non-ribosomal peptide microbial siderophores [200]. Gallium acquisition was best studied in *Pseudomonas aeruginosa*. There are more than 30 possible siderophore uptake systems in *Pseudomonas spp.*, and among these, there are two well-defined uptake systems for pyoverdine and pyochelin [118]. They can also utilize exogenous iron chelators like citrate and desferrioxamine B (DFOB), which is a hydroxamate-based siderophore [118]. It has been shown that pyochelin siderophore is very important for Ga^{3+}

[1] medium developed by Hussain, Hastings and White

[2] 0.1 to 0.15 mM dypridyl was added for iron restriction

[3] a minimal medium consisting of 40 mM K_2HPO_4, 22 mM KH_2PO_4, 7 mM $(NH_4)_2SO_4$, 34 mM succinic acid, 0.1 % casamino acids and 1 mM MgSO4 adjusted to pH 7

[4] tryptic soy broth

[5] Deferrated Casamino Acids medium

[6] Roswell Park Memorial Institute medium, usually used for culturing mammalian cells

Table 1.1: Ga(III)-based antimicrobials [135], [209]. Chemically defined media are marked with a ∗.

Effect on	microorganism	Ga(III) compound	growth condition (medium)	Ga(III) inhibitory concentration [μM]	reference
Planktonic growth	*Escherichia coli*	Ga(III)–Cit, DFOB–Ga(III)	Iso-Sensitest	IC_{90} = 2560–5120	[118]
		Ga(III)–Cit, DFOB–Ga(III)	HHW*[1]	IC_{90} = 1280–5120	[118]
		$GaCl_3$	LB	MIC >800	[208]
		Ga(III)–PPIX	nutrient broth+dipyridyl[2]	MIC <0.8	[208]
	Pseudomonas aeruginosa	$Ga(NO_3)_3$	BM2 succinate*[3]	IC_{90} = 1–40	[203]
			unknown medium	MIC = 6–59	[209]
			minimal medium without iron*	MIC = 62.5	[218]
		$GaCl_3$, DFOB–Ga(III)	1% TSB[4]	MIC = 32	[207]
		Ga(III)–Cit	HHW*	IC_{90} = 20–40	[118]
			Iso-Sensitest	IC_{90} = 80–640	[118]
		DFOB–Ga(III)	HHW*	IC_{90} = 40–640	[118]
			Iso-Sensitest	IC_{90} = 160–1280	[118]
		Ga(III)–Cit	Iso-Sensitest	IC_{90} = 200	[219]
			Fe-free (chelated) Iso-Sensitest	IC_{90} = 200	[219]
		Ga(III)–salicylidene acylhydrazide	Iso-Sensitest	IC_{90} = 200	[219]
			20% Iso-Sensitest	IC_{90} = 50	[219]
			Fe-free (chelated) Iso-Sensitest	IC_{90} = 100	[219]
		Ga(III)-staphyloferrin A	unknown medium	820	[209]
		Ga(III)-cepaciachelin	unknown medium	29	[209]
		Ga(III)-2,3-dihydroxybenzoyl-serine	unknown medium	57	[209]
		Ga(III)–mesoporphyrin IX, Ga(III)–PPIX	0.3 g/L TSB	2	[220]
		$Ga(NO_3)_3$	iron-depleted medium (DCAA[5])*	12.5-25	[136]
	Staphylococcus epidermidis	Ga(III)–Cit	HHW*	IC_{90} = 1280–2560	[29]
			Iso-Sensitest	IC_{90} = 2560–5120	[118]
		DFOB–Ga(III)	HHW*	IC_{90} = 640–2560	[118]
			Iso-Sensitest	IC_{90} = 1280–5120	[118]
		GaM	RPMI*[6]	MIC = 225–450	[221]
		Ga(III)–mesoporphyrin IX, Ga(III)–PPIX	0.3 g/L TSB	2	[220]
Biofilm	*P. aeruginosa*	$Ga(NO_3)_3$	Flow cells (1% TSB)	BIC = 0.5 BBC = 100	[203]
		$GaCl_3$, DFOB–Ga(III)	Flow cells (1% TSB)	BIC = 1	[207]
		DFOB–Ga(III)	Flow cells (1% TSB)	BBC = 1000	[207]
		Ga(III)–Cit	Microtitre plates (20% Iso-Sensitest)	MBIC = 10–25	[118], [219]
		Ga(III)–salicylidene acylhydrazide	Microtitre plates (20% Iso-Sensitest)	MBIC = 3	[219]
	S. epidermidis	GaM	Microtitre plates (RPMI)	MBIC = 211–6741	[221]

entrance into the *P. aeruginosa* bacterium and its consequent antibacterial action [136]. However, Ga was also taken up by a *P. aeruginosa* mutant defective for both pyochelin and pyoverdine pathways as well as by a mutant with a mutation of the ferric citrate uptake system [118], [203]. HitAB Fe transport system (Fe(III) transport system of the cytoplasmic membrane) is also involved in Ga(III) uptake by *P. aeruginosa* [199], [223]. There are most probably many more, undiscovered ways for bacterial uptake of ionic gallium.

3. Ga(III) can affect the synthesis of siderophores by regulation of gene expression [203]. Ga treatment can induce the expression of pyochelin biosynthetic genes [203]. By contrast, exposure to Ga(III) can abolish the increased pyoverdine biosynthesis and pyoverdine gene expression that normally occurs during Fe limitation [203]. Ga(III) represses the transcriptional regulator pvdS and genes under its control [203]. The pvdS regulator controls genes involved in the synthesis of pyoverdine, the pyoverdine receptor, and other Fe-responsive genes [203]. This leads to the shortage of Fe inside the cell and consequent inhibition of many iron-requiring enzymes.

4. The presence of Ga(III) results in inhibition of many enzymes, but it is not yet clear for all of them whether this is a direct inhibition, a consequence of the Fe shortage inside the cell or both. This most probably also depends on the situation, whether Ga(III) entered the cell or not, which is connected to the Ga(III) concentration [224]. The following enzymes are known to be affected by Ga(III):

   (a) Ribonucleotide reductase, which requires Fe^{3+} ion as a cofactor for proper activity [205], [222]. This enzyme catalyzes conversion of ribonucleotides into deoxyribonucleotides, a reaction that enables the synthesis of DNA. It consists of two dimeric subunits termed R1 and R2. The R1 subunit contains substrate and effector-binding sites, while the R2 subunit contains an essential binuclear iron center and a tyrosyl free radical. The activity of the R2 subunit increases as cells enter S phase, but since the R2 subunit has a half-life of 3–4 h, a continuous supply of iron is needed for its activity to support DNA synthesis. Disruption of the flow of iron to the R2 subunit diminishes ribonucleotide reductase activity. Hence, inhibition of cellular iron uptake by Ga(III) results in inhibition of the activity of the R2 subunit and a block in ribonucleotide reductase [225]. In this way, Ga^{3+} prevents the synthesis of DNA in the cell. Cellular iron deprivation does not appear to be the sole mechanism by which gallium blocks ribonucleotide reductase activity. Gallium nitrate was shown to block the enzymatic activities of CDP and ADP reductase in a cell-free assay system, suggesting that Ga(III) can also directly inhibit the activity of ribonucleotide reductase. Although the mechanism by which this occurs has not been elucidated, it is hypothesized that gallium disrupts the iron center of the R2 subunit leading to the loss of enzymatic activity. Hence, gallium inhibits ribonucleotide reductase through both an indirect (blockade of cellular iron uptake) and a direct action [225].

   (b) Ga(III) inhibits Fe-containing catalase and Fe-cofactored superoxide dismutase and decreases the iron content in catalase [226], [227]. Although also an increased superoxide dismutase activity in response to Ga(III) exposure has been observed [227].

   (c) Gallium disrupts also the cellular respiration, in which iron has a very important role. Ga(III) inhibits enzymes of the electron transport chain, such as complex I, II, which contain Fe–S clusters, and IV, which contains heme groups [228]. This results in decreased oxidative phosphorylation and ATP production [228].

Ga(III) can also inhibit enzymes of the citric acid cycle, such as aconitase, succinate dehydrogenase and fumarase A, which all contain Fe–S clusters [205], [228]. Furthermore, a decreased expression of the latter two enzymes was also observed as a consequence of Ga(III) [228]. However, while the Fe–S clusters participate in redox reactions in the other enzymes, their role in aconitase and fumarase A is different. Therefore, enzyme inactivation by Ga(III) is not only due to its redox inability but also via some other mechanism. Since it was observed that Ga(III) also decreased the amount of Fe–S clusters, it is believed that it destroys them [228].

5. Destruction of Fe–S clusters can lead to increased amounts of Fenton-active Fe, which can create reactive oxygen species [21]. They can further damage the proteins, DNA, lipids, as already discussed. In fact, they can destroy the Fe–S clusters. Increase in oxidized lipids and proteins and increased production of H_2O_2 was noticed due to Ga^{3+} antibacterial action [227]. However, Ga^{3+} quenches the superoxide ion signal rather than generates it [227]. It is not yet clear whether the ROS are the main reason for the bactericidal activity or only a consequence of the Ga^{3+} antibacterial action.

6. Metabolic profile of bacteria is altered in the presence of gallium due to altered expression of genes involved in carbon utilization and reduced expression of ribosomal genes [118], [203]. This effect differs depending on the carbon sources used by bacteria [118]. Concentrations of amino acids and many other metabolites (such as glucose) can be decreased due to the effect of Ga(III) on their biosynthesis. This is usually in agreement with the decreased transcription of genes for their transport and metabolism [118], [203]. However, concentrations of pyroglutamic and glutamic acids were decreased the most in *P. aeruginosa*, even though gene expression related to glutamate biogenesis or utilization has been reported to be unchanged in the presence of gallium [118], [203]. Glutamate is one of the central metabolites in *P. aeruginosa*, and its concentration has been shown to change in response to different carbon sources. Moreover, glutamate is a starting point for heme biosynthesis [118]. One possible explanation is that Ga might trigger bacteria to adjust their enzymatic reactions in a more favorable way with regard to energy acquisition and to avoid Fe-consuming pathways. Some carbon sources induce expression of Fe-demanding pathways, and since Fe is not available, these pathways become costly for the cell and inhibit growth. Strong growth inhibition of *P. aeruginosa* by Ga-Citrate was observed on Casamino Acids, and it implies that during infections when amino acids are the preferred carbon source, Ga could have a more potent effect [118].

1.4.4.3 Bacterial resistance to Ga(III)

Evidently, gallium affects many different processes. This large number of targets is promising as it might avoid the resistance problem. Furthermore, since gallium is not an essential nutrient, there are no systems for monitoring its homeostasis as in the Zn or Cu case and it is also not as abundant and long-used as silver, so that such systems would have emerged. Because bacteria cannot discriminate between Fe(III) and Ga(III), they will not sense an increase of Ga^{3+} concentration and a decrease of Fe^{3+} inside to trigger the iron/gallium efflux. However, since Ga(III) enters microbial cells by exploiting specific Fe(III)-uptake mechanisms, mutations in these pathways could block gallium from reaching its cellular targets, ultimately making bacteria less susceptible to gallium inhibitory activity, as it has been observed in laboratory studies of Ga(III) antibacterial mechanism, in which resistant strains were created by genetic modification of *P. aeruginosa*. Examples of such targeted

mutation (gene modification) that led to resistance are making pvdS insensitive to Ga(III) [203], deleting genes for the HitAB transporter [223] and deleting genes connected with pyochelin biosynthesis or uptake [136]. Nevertheless, such mutations could never completely prevent Ga^{3+} entrance into bacterial cells and only 2–4 times higher Ga(III) concentrations were already effective against the resistant strains. Besides, it is not known whether such mutations could spontaneously occur as a response to the constant Ga(III) exposure.

A more dangerous possible type of resistance is that bacteria start utilizing Fe(II) instead of Fe(III). Some bacteria can indeed secrete heme-sequestering proteins, called hemophores, which scavenge heme from various hemoproteins and deliver it to bacterial cells [229], in a way that resembles the siderophores. Moreover, under microaerophilic or anaerobic conditions, the soluble ferrous ion (Fe^{2+}) predominates over insoluble Fe^{3+}, and several bacteria also possess specific transporters on the cytoplasmic membrane to directly acquire Fe(II) [199], [230]. Recently, a spontaneous mutant of *P. aeruginosa* with 12-fold increased resistance to Ga(III) has been obtained *in vitro* through sequential subculturing in the presence of an inhibitory concentration of $Ga(NO_3)_3$ [223]. Genome sequencing revealed 64 nonsilent point mutations in this mutant, mostly occurring in genes involved in metabolism, membrane transport, cell division, DNA recombination/repair, signal transduction, energy production and synthesis of siderophores and phenazines [223]. Among the latter, the most evident was pyocyanin overexpression. Pyocyanin most likely protected the bacteria due to its capacity to catalyze the reduction of either free or protein bound Fe(III) to Fe(II), which would not be affected by Ga(III) competition [223]. Accordingly, lower concentrations of Fe(II) than of Fe(III) are needed to protect the cells against Ga [231]. Nonetheless, the mutation rate at which these Ga(III)-resistant strains arise has neither been evaluated nor compared with the frequency of antibiotic resistance. Furthermore, the fitness cost associated with the development of resistance to Ga(III) should also be determined, and compared with the cost of resistance to conventional antibiotics [199]. In fact, such study was published in 2014 soon after the demonstration of this spontaneous mutant resistance and it revealed much faster and larger evolution of resistance against conventional antibiotic treatments in comparison with gallium treatments [224]. The authors in this study also considered several possible scenarios by which resistance to Ga(III) could emerge and found out that switching of bacteria to another siderophore, xenosiderophores or other iron chelators would not lead to the spread of the resistance since all these events are already occurring, cannot escape gallium and are available to all bacteria (they are "public goods"). Furthermore, upregulated production of reducing agents (such as pyocyanin) to extracellularly reduce Fe^{3+} to Fe^{2+} and switch to Fe(II) uptake is also unlikely to cause the resistance to spread, because of the large fitness costs connected with the increased production of a metabolite (pyocyanin), which would again be a shared trait/public good [224]. However, what remains concerning is the possibility of emergence of a special Ga(III) efflux pump that was suggested due to observed mutations in the transport proteins, the multidrug efflux pump and permease [223], but its importance for resistance to Ga(III) still needs to be confirmed. Anyway, since several cellular processes were found to be involved in adaptation/resistance to Ga(III), this probably means that such resistance would be costly and unlikely to spread [135]. It is also very important and promising that so far no connection between the antibiotic and Ga(III) resistance has been found.

Some bacterial strains are able to cope with the Ga stress also by employing enzymes that do not require iron to restore their metabolism. Such effect was studied in detail in *P. fluorescens* strain, which can tolerate Ga(III) concentrations above 1 mM [227], [228]. It was found that they overcome the Ga(III) inhibition of fumarase A and iron deprivation and re-activate the citric acid cycle by expressing the iron-independent fumarase C [228].

They also fight the increased oxidative stress by expressing an H_2O-forming NADH oxidase to convert NADH to NAD^+ and enzymes involved in producing NADPH from NAD (NAD^+ kinase converts NAD^+ to $NADP^+$, while NADP-dependent isocitrate dehydrogenase and glucose-6-phosphate dehydrogenase create NADPH from $NADP^+$) [227], [228], [232]. Moreover, enzymes like aspartate transaminase and malate dehydrogenase that play a critical role in the production of aspartate are upregulated [232]. In this way, *P. fluorescens* treated with Ga elaborates a hydroxyaspartate containing metabolite, which can chelate Ga(III) [232].

1.4.4.4 Cytotoxicity and medical applicability of Ga(III)

As already mentioned, gallium was first employed as an anticancer drug and as such obviously revealed cytotoxic properties. One possible selectivity might arise due to Ga(III) quenching of bacterial siderophores without entrance into the cells at lower concentrations that are not cytotoxic [224]. Nevertheless, apart from siderophore quenching and inhibition of specific bacterial enzymes, Ga^{3+} ions have a non-selective effect and act similarly on both prokaryotic and eukaryotic cells. Ga(III) hinders the uptake of Fe through receptors for transferrin and endosomal release of iron from transferrin to the cytoplasma. This leads to inhibition of iron-dependent enzymes inside the cells, especially ribonucleotide reductase, and disruption of cellular respiration in mitochondria (and consequently increased intracellular ROS [233]). Different studies on the antineoplastic activity of Ga(III) showed that additional cellular processes, unrelated to iron homeostasis, may be altered by Ga(III). These alterations include: (i) inhibition of human tyrosine-specific protein phosphatase by a yet unknown mechanism, (ii) dose-dependent inhibition of magnesium-dependent ATPase through competition with magnesium, (iii) interference with DNA polymerase, and (iv) competition with magnesium for DNA binding and destabilization of the DNA helix [199]. So, how can Ga(III) then be useful if it is toxic to both bacteria and eukaryotic cells? Yes, it can be useful, like it can be useful in cancer treatment, because the requirement for iron of these cells is different. Cancer cells have a greater requirement for iron than normal cells; certain cancer cells display increased transferrin receptors, increased ferritin (iron storage protein) levels, and decreased ferroportin (iron efflux protein) levels [225]. These changes enable malignant cells to acquire increased amounts of iron to support their proliferation relative to nonmalignant cells. Cellular gallium uptake occurs mainly via the binding of gallium to transferrin and its incorporation into cells via transferrin receptor-mediated endocytosis of transferrin-gallium [225]. Since transferrin receptors are present in high numbers on cancer cells, they uptake more gallium than normal cells, ribonucleotide reductase is inhibited, cancer cells are consequently unable to make DNA and multiply and ultimately undergo apoptosis [200]. Similarly, bacterial cells proliferate very fast and since they do not have iron storage facilities like eukaryotic cells, they constantly require iron. On the other hand, healthy eukaryotic cells generally do not take up significant amounts of gallium [200]. Hence, it is expected that gallium selectivity will come out when bacteria and mammalian cells are exposed to Ga(III) simultaneously. Interestingly, even healthy eukaryotic cells that are rapidly proliferating are not affected much by gallium. The inability of Ga to enter heme likely accounts for its lack of accumulation in healthy proliferating hematopoietic cells of the bone marrow. The reasons for the low Ga-avidity of other proliferating healthy cells, such as gastrointestinal mucosal cells and the transient cells of hair follicles, are not known, but may be due to efficient local iron recycling [200]. There are also other properties of gallium that make it a promising non-cytotoxic antimicrobial. By being irreducible under physiological conditions, gallium cannot participate in redox reactions, such as the Fenton-type reactions that make free iron (mainly as Fe^{2+} in solution) highly toxic. Ga(III) is also not observed to enter Fe(II)-bearing molecules such as heme,

and thus avoids toxicity due to interference with oxygen transport (via hemoglobin) or with cytochrome-mediated reactions [201], [225]. An overview of *in-vitro* cytotoxicity of Ga(III) most relevant to my doctoral thesis is given in Table 1.2.

Table 1.2: Ga(III) cytotoxicity *in vitro*

cell line	Ga(III) compound	toxicity assay	TC_{50} [μM]	reference
L929[1]	$Ga(NO_3)_3$	MTT	> 1000	[234]
L929	$Ga(NO_3)_3$	MTT	TC_{70} = 1434	[235]
L929	$GaCl_3$	MTT	1530	[60]
L929	$GaCl_3$	3H-thymidine incorporation	53	[61]
L929	$GaCl_3$	clonogenic assay	36	[62]
L929	Ga^{3+} released from SiO_2-CaO-Ga_2O_3 glass-ceramics	MTT	> 800	[236]
L929	Ga(III)–salicylidene acylhydrazide	Alamar Blue	> 200	[219]
L929, BEAS-2B[2], A549[3], J774[4]	Ga(III)–Cit	Alamar Blue	> 640	[118]
L929, BEAS-2B, A549, J774	DFO–Ga(III)	Alamar Blue	> 640	[118]
BEAS-2B	Ga(III)–salicylidene	Alamar Blue	> 200	[219]
A549	acylhydrazide	Alamar Blue	> 200	[219]
Kidney epithelial cells	$GaCl_3$	MTT	2140	[60]
Human gingival fibroblasts	$GaCl_3$	3H-thymidine incorporation	41	[61]
Balb/c 3T3 mouse fibroblasts	Ga^{3+} atomic absorption standard solution	MTT	200	[59]
		MTT	29 (24h), 10 (48h), 5.7 (72h)	[237][5]
		total protein mass	458	[59][6]
		3H-Leu incorporation	143	[59]
		3H-Tdr incorporation	65	[59]
		3H-Tdr incorporation	14 (24h), 8.6 (48h), 7.1 (72h)	[237]
primary human fibroblasts (MRC-5)	Ga(III)–PPIX	cell proliferation kit II (XTT) and LDH release	>160	[208]
U2-OS	Ga^{3+} released from Mg-Ga alloy	MTT	> 9.2 (2 days), 4.4–9.2 (5 days)	[238]
osteoclasts	$Ga(NO_3)_3$	trypane blue exclusion	> 100	[239]
osteoclasts, osteoblasts	$Ga(NO_3)_3$	cell tracker green staining, MTT	> 100	[240]
mouse osteoblasts MC3T3-E1	$GaCl_3$	clonogenic assay	25.3	[62]

[1] mouse fibroblast cells

[2] human bronchial epithelial cells

[3] human alveolar epithelial cells

[4] mouse monocyte-macrophage cell line

[5] Ga^{3+} ions were added to cells immediately and then cells were incubated in the presence of ions for 24, 48 or 72 hours

[6] Ga^{3+} ions were added to cells after 24-hour incubation and the cells were further incubated in the presence of ions for 24 hours

Similarly to bacteria, cancer cells can also gain resistance to Ga(III). Gallium-resistant CCRF-CEM cells display a decrease in gallium and iron transferrin receptor-mediated uptake, an increase in the mRNA-binding activity of iron regulatory protein, and a decrease in the content of ferritin. The growth of CCRF-CEM cells resistant to gallium nitrate can still be inhibited by gallium maltolate, a compound that can be incorporated into cells independent of the transferrin–transferrin receptor pathway [225]. Some studies also revealed that exposure of CCRF-CEM cells to gallium nitrate produces an increase in ROS, a decrease in glutathione within 1–4 h, and a subsequent increase in metallothionein-2A and heme oxygenase-1 gene expression. Cells exposed to gallium initially generate a cytoprotective response by elevating metallothionein and heme oxygenase-1 levels in response to ROS; however, cell death eventually ensues when this response is overwhelmed [225], [233].

The use of gallium compounds for medical purposes is very welcomed. Beside the FDA-approved intravenous injecting of citrate-buffered $Ga(NO_3)_3$ with trademark Ganite, some other gallium compounds are already in clinical use, e.g., as a diagnostic for the localization of malignant cells and inflammatory lesions, or as a therapeutic for the treatment of cancer, autoimmune diseases and bone resorption disorders [135], [199], [222]. Currently, gallium compounds reported to have been tested in humans are citrated gallium nitrate for injection (Ganite; approved for use in the USA to treat cancer-related hypercalcemia); gallium maltolate for oral administration (Phase I trials); gallium 8-quinolinolate for oral administration (Phase I trials); and gallium chloride for oral administration (in a few cancer patients) [200].

By contrast to silver or gold, with gallium there are no problems with permanent accumulation in the body and it is effectively excreted also with urine [241]. It does accumulate particularly at sites of inflammation, infections and tumor cells, as there are a lot of receptors for transferrin, and at sites of bone formation, but it is almost exclusively bound to transferrin, and as such it is progressively removed through the bile and then with the faeces [242]. Otherwise, if concentration of gallium becomes too high or its intake is fast, the gallate ($Ga(OH)_4^-$) form prevails, which is excreted rapidly through the kidneys with urine [113], [222], [242].

1.4.5 Gallium-containing nanoparticles for biomedical applications

At the beginning of my PhD study, I could find only one report about Ga-based antibacterial nanoparticles, i.e., Ga_2O_3 nanoparticles. Murthy *et al.* have demonstrated antibiofouling properties of Ga_2O_3 nanoparticles (with average size of ≈100 nm) against *E. coli* and *S. aureus* [243]. However, concentrations up to 25 mg/L (133 μM) exhibited only very weak (towards *S. aureus*) or no inhibition (towards *E. coli*) of planktonic growth. The exploration of antibacterial properties continued in 2014 with a paper by Girija *et al.*, who demonstrated the antibacterial action of Ga_2O_3 nanorods (50×200 nm) against *E. coli* and *S. aureus* by a well diffusion test [244]. The nanorods created an inhibition zone in *E. coli* already at 25 mg/L concentration, whereas at least 50 mg/L concentration was needed for an inhibition zone in *S. aureus*. By contrast, bulk Ga_2O_3 did not create any inhibition zone. They also presented good photocatalytic properties of this semiconductor with a band gap of 4.9 eV, but photocatalysis was not responsible for the observed antibacterial action, since the test was performed in dark and Ga_2O_3 nanoparticles can create reactive oxygen species (only $OH^\bullet$ radicals) only under direct visible light illumination, as shown by Tzitrinovich *et al.* in 2013 [245]. In 2013, also an article about antibacterial activity of GaN nanoparticles (with average size of 50 nm) by Sahoo *et al.* was published [246]. They used confocal raman spectroscopy, a not so common and relatively new but more and more powerful method, to investigate the mechanism for the observed antibiofouling properties

of GaN nanoparticles towards *S. aureus*, *E. coli*, *P. aeruginosa*, and *Pseudomonas putida*. They explained their mechanism by local damage of the cell wall, caused by nanoparticles, which led to the leakage of intracellular components, and a possible release of Ga^{3+} ions inside the bacterial cells [246]. In the same year, another study about a new Ga(III) delivery system in the form of KGa[Fe(CN)6]/PVP NPs (average size of 15 nm) was published, which demonstrated their very good biocompatibility with HeLa cells until at least 1.1 mM concentration, their most probably endocytotic penetration into the cells and untargeted distribution in the cytoplasm, and *in-vitro* exchange of Ga(III) by Fe(III) from Fe(II) suggesting their ability to sequester Fe(II) and consequently release Ga(III) [247]. A very recent study on eutectic GaIn alloy nanoparticles (average size around 100 nm) has also shown their low *in vitro* cytotoxicity against HeLa cells for at least 21 mg/L (0.2 mM Ga) concentration and endocytosis, fusion and degradation of the eutectic GaIn nanoparticles with a release of Ga^{3+} ions inside HeLa cells [248]. The *in vivo* injection of these nanoparticles into mice caused no tissue damage, no allergic reaction, exhibited very low acute toxicity (maximum tolerated dose of 700 mg/kg), while Ga and In were excreted with both faeces and urine [248]. Furthermore, an *in vivo* study, performed on gallium phosphide nanowires (80 nm diameter, 4 μm length), confirmed their non-toxic influence to fruit fly *Drosophila melanogaster* [249]. However, the antibacterial properties of GaP, KGa[Fe(CN)6]/PVP and eutectic GaIn alloy nanoparticles have not been evaluated. On the other hand, Narayanasamy *et al.* incorporated Ga(III)-tetraphenyl porphyrin into polymer nanoparticles (average size of 300 nm) and demonstrated their efficiency against *Mycobacterium smegmatis* as well as against HIV in macrophages, and did not show any sign of cytotoxicity for macrophages even at 2 mM concentrations despite internalization of the nanoparticles into all compartments of the cells [250]. Another way for the local delivery of Ga(III)-tetraphenyl porphyrin was by its conjugation to Pt nanoparticles (average size around 30 nm) [251]. Bactericidal properties against *S. aureus* were demonstrated under visual light illumination. However, the non-conjugated Pt nanoparticles were not tested, so it is not clear how large their contribution was and to what extent they were only deliverers of Ga(III)-tetraphenyl porphyrin.

1.5 Antibacterial Materials for Bone/Tooth Replacement and Repair

Bacterial resistance to antibiotics presents a very serious problem for infections during the insertion of materials into the body/implantation. Even today these infections are mostly prevented and treated by several weeks or even months of oral or parenteral administration of high doses of strong antibiotics, which due to systemic distribution throughout the whole body have to be much larger than the bactericidal concentration to achieve a high enough concentration at the site of infection [252], [253], [254]. A newer method for the prevention of such infections is based on implants with a system for local drug delivery on the surface, which works as a kind of reservoir of encapsulated antibiotic and enables local release of the drug in dependence of solubility, diffusion coefficient and encapsulation efficiency, as well as in relation to biodegradability/bioresorption of the drug carrier [255], [256]. Hence, with this kind of implants, the antibiotic is present locally, which significantly reduces the required concentration of the drug and bypasses the systemic distribution. However, this does not solve the problem of bacterial resistance to antibiotics, since in the last phase of the release the antibiotic is released in low concentrations, which is ideal for the prevalence of resistant bacteria [257], [258], [259]. New ways for the local antibacterial protection of the implants, which can be brought by nanotechnology, are therefore very welcome.

1.5.1 Hydroxyapatite and other calcium orthophosphates

There are many kinds of calcium orthophosphates. They are classified by their Ca/P molar ratio [260]:

- 0.5: monocalcium phosphate (anhydrous form MCPA ($Ca(H_2PO_4)_2$) or monohydrate MCPM ($Ca(H_2PO_4)_2 \cdot H_2O$))
- 1.0: dicalcium phosphate (anhydrous form DCPA ($CaHPO_4$), also called monetite, or dihydrate DCPD ($CaHPO_4 \cdot 2\,H_2O$), also called brushite)
- 1.5: tricalcium phosphate (two different crystal structures of $Ca_3(PO_4)_2$, α and β-TCP)
- 2.0: tetracalcium phosphate (TTCP ($Ca_4(PO_4)_2O$), also called hilgenstockite)
- 1.33: octacalcium phosphate (OCP, $Ca_8(HPO_4)_2(PO_4)_4 \cdot 5\,H_2O$)
- 1.67: hydroxyapatite (HAp, $Ca_{10}(PO_4)_6(OH)_2$)

Apart from these crystalline phases another calcium phosphate is also very important, i.e., amorphous calcium phosphate (ACP, $Ca_xH_y(PO_4)_z \cdot nH_2O$ with n=3-4.5; 15-20 % H_2O). It does not exhibit a long-range order and its structure is usually described as an aggregate of randomly distributed $Ca_9(PO_4)_6$ clusters (roughly spherical with 9.5 Å diameter, the so-called Posner's clusters) with water incorporated in between [260], [261]. The chemical composition of ACP strongly depends on the solution pH and the concentrations of the mixing solutions and its Ca/P ratio can thus range from 1.2 to 2.5 [260], [261]. However, Ca/P≈1.5 prevails, especially if the ACP is properly washed [261].

Calcium orthophosphates differ in thermodynamic stability and solubility, so they convert one to another in dependence of the temperature or in aqueous media in dependence of pH. Hydroxyapatite is the most insoluble calcium orthophosphate between pH 4 and 10 (see Figure 1.15). TCP and TTCP cannot be precipitated from aqueous solutions (they are prepared by thermal decompositions or solid state reactions at high temperatures) and MCP is stable only below pH 2 [260], [262], [263]. Hence, when preparing HAp by precipitation in aqueous media, the competing calcium phosphates we could end up with are brushite, OCP and ACP). Which one prevails depends on the synthesis conditions, among which Ca/P precursor ratio and pH are the most important. DCPD is stable from pH 2 to 6, OCP between pH 5.5 and 7, HAp (stoichiometric or non-stoichiometric) between 6.5 and 12 and ACP is metastable in the 5–12 pH range [260], [262], [263]. DCP, TCP, OCP and ACP tend to transform to HAp in aqueous media under physiological conditions (pH 7.2–7.4) [260], [262], [263]. Full hydrolysis of OCP to HAp occurs within 6 hours [260]. *In-vitro* HAp precipitation (as well as *in-vivo* formation of bone mineral) is currently understood as ACP→OCP→HAp transformation [260], [262]. Such transformation is accelerated at higher temperatures and goes to completion within a few hours of boiling [260], [262].

Another important property is the thermal stability of calcium orthophosphates. The ones with Ca/P ratio <1.5 are thermally unstable (they transform to pyrophosphate upon thermal dehydration), so they are usually not sintered for improvement of mechanical properties [263]. Stoichiometric hydroxyapatite (with Ca/P=1.67) is stable until 1350 °C, above which it decomposes to TTCP and α-TCP [266].

Calcium orthophosphates with Ca/P ratio between 1 and 2 are very useful for bone/tooth replacement and repair [260], [262], [263]. Hydroxyapatite is the most favourable material for bone/teeth implantation, bone fracture repair and tissue engineering [262], [267], [268], [269], as its high chemical and structural similarity with the biological calcified tissues

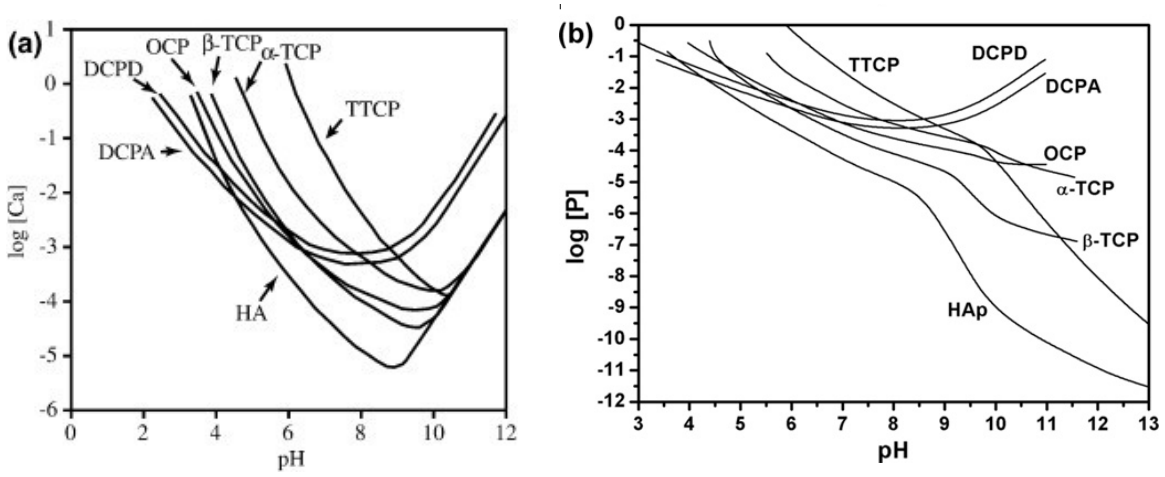


Figure 1.15: Dependence of solubility of different calcium orthophosphates on pH [264], [265], expressed as Ca^{2+} (a) or $PO_4{}^{3-}$ (b) concentration vs pH.

make it very biocompatible and bioactive [260]. Recently, it has been intensively explored also for drug delivery [270], [271].

Hydroxyapatite usually crystallizes in a hexagonal crystal system (a=b≠c, $\alpha = \beta = 90°$, $\gamma = 120°$) with a space group $P6_3/m$. The apatitic unit cell is often divided into four different types of crystallographic positions ("sites") [272] (see Figure 1.16):

1. tetrahedral sites for six P^{5+} ions, each in 4-fold coordination with oxygen,
2. Ca(I) sites for four of the Ca^{2+} ions,
3. Ca(II) sites for the six other Ca^{2+} ions (arranged in such a way that they form a channel along the c-axis), and
4. the channel site, which is typically occupied by two OH^- anions.

The "lath" or "plate" morphology (Figure 1.17), also a characteristic of the bone apatite, does not conform to the hexagonal symmetry of the crystal structure, which is an evidence that the formation of HAp by precipitation goes through an intermediate OCP phase [260], [262]. Stoichiometric hydroxyapatite is stable only between pH 9.5 and 12. At lower pH, PO_4 groups get protonated and the resulting more positive charge is compensated by Ca and OH deficiency. Thus, a calcium-deficient hydroxyapatite (CDHA) is formed with formula $Ca_{10-x}(HPO_4)_x(PO_4)_{6-x}(OH)_{2-x}$ ($0 < x < 1$)) and $1.5 < Ca/P < 1.67$. Stoichiometric hydroxyapatite does not exist in biological systems. Biological apatite is a calcium-deficient hydroxyapatite with different ions, such as Na^+, K^+, Mg^{2+}, Sr^{2+}, Zn^{2+}, $CO_3{}^{2-}$, F^-, Cl^-, $SiO_4{}^{4-}$, incorporated into its structure [260], [262], [274], [275]. Today the biological apatite is understood as a hydrated-hydroxylated calcium phosphate with a formula $Ca_{10-x}[(PO_4)_{6-x}(CO_3)_x][(OH)_{2-x-2y}(CO_3)_y] \cdot nH_2O$, where x>y and n≈1.5 [276]. Structural water resides in the c-axis ion channels, while structural carbonate primarily substitutes phosphate ions (B-type substitution) with up to 15 % substituting OH^- ions (A type substitution) inside the channels [272], [276], [277], [278]. B and AB-type carbonate substitution have an effect on the Ca/P ratio opposite to the protonation of $PO_4{}^{3-}$. Thus, carbonated hydroxyapatites can have the Ca/P ratio >1.67 [279], [280]. Any non-stoichiometry (Ca/P <1.67 or Ca/P>1.67) results in thermal conversion of hydroxyapatite to different biphasic, triphasic or multiphasic calcium phosphate mixtures between 700 and

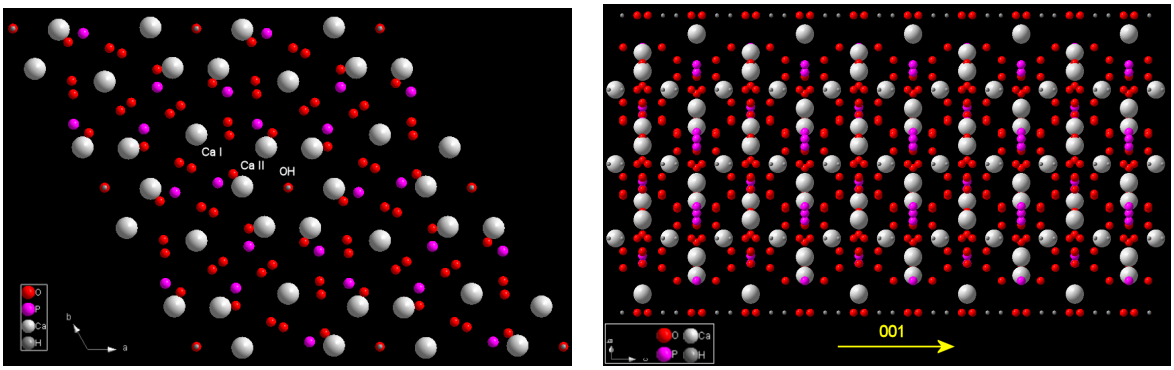


Figure 1.16: Crystal structure of hydroxyapatite. *Left*: crystal structure of hydroxyapatite (PDF number 01-089-6438) in the [001] (c-axis) direction. The characteristic 0.30–0.35 nm wide c-axis apatitic channel with six-fold symmetry, where OH^- ions are located, is clearly visible. *Right*: crystal structure of the same hydroxyapatite in the [1-10] direction, in which it is usually observed under TEM when the specific anisotropic morphology, shown in Figure 1.17, gives it preferential orientation.

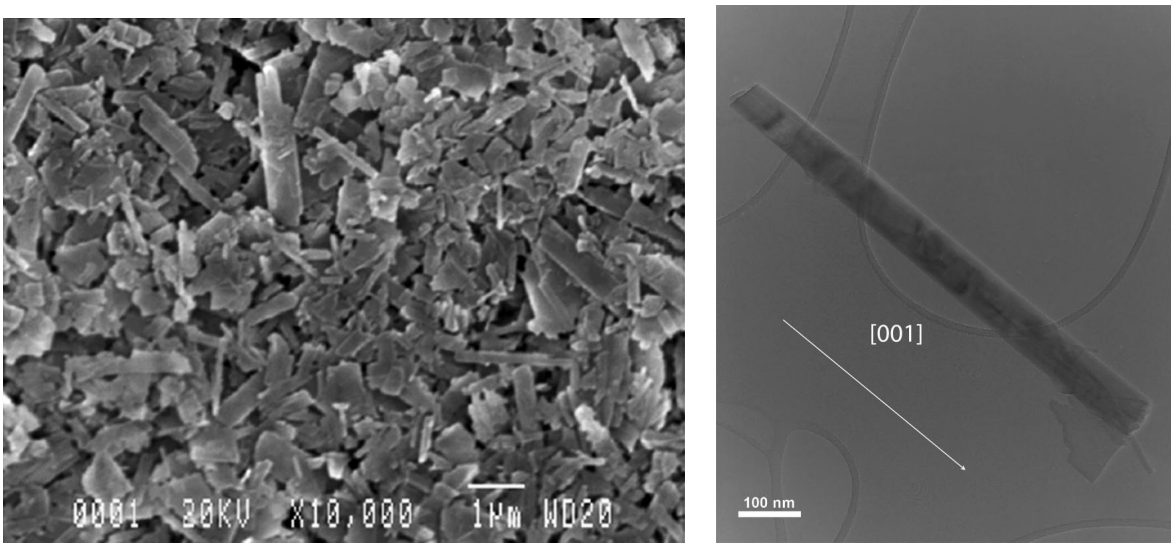


Figure 1.17: Morphology of hydroxyapatite, which is used as a reference and a bioactive carrier in the nanocomposites throughout this work. I will refer to such morphology as "submicrometer-sized laths" or "nanolaths" that join together laterally into plates [273]. Their largest dimension is in 001 direction, whereas the other two dimensions are really nano (<100 nm).

1300 °C [262], [263], [281]. Hydroxyapatite with 1.5< Ca/P <1.67 transforms above 700 °C to a mixture of β-TCP and stoichiometric HAp [282], [283], [284], [285]. Since β-TCP is thermally less stable than α-TCP, it transforms to α-TCP above 1125 °C [260], [262]. α-TCP is thermally stable until about 1430 °C, above which it transforms to α'-TCP [265]. On the other hand, HAp with Ca/P >1.67 transforms above 800 °C to a mixture of CaO and HAp [283].

Biological apatite is also nanodimensional. Biological apatite in bone is in the form of plate-like nanocrystals (elongated along the crystallographic c-axis) with 30–50 nm length, 15–30 nm width and 2–10 nm thickness (just a few unit cells thick) [260], [275]. Such nanocrystals fill the ∼40-nm gaps between the ∼67-nm collagen triple helices, which are self-assembled into collagen fibrils of 80–100 nm thickness and a length of a few to tens of microns [260], [275]. Thus, the apatite nanocrystals are nearly parallel to each other with their c-axes roughly parallel to the long axes of the collagen fibrils [260], [275]. Unlike bone, teeth consist of at least two different biominerals: enamel (a crown, the part above the gum line) and dentin (root, the part below the gum line). Enamel is almost entirely inorganic and consists of rod-like apatite crystals measuring 25–100 nm and an undetermined length of 100 nm to 100 μm or longer along the c-axis [260], [275]. On the other hand, dentin is very similar to bone in composition, hierarchical structure and dimensions of the apatite part (∼25 nm width, ∼4 nm thickness and ∼35 nm length) [260], [275]. Nanocrystalline HAp consists of a hydroxyapatitic crystalline core ($Ca_{10}(PO_4)_6(OH)_2$) and an outer disordered layer, which besides the phosphate ions contains also HPO_4^{2-} ions, carbonate and Ca^{2+} ions as well as structural and adsorbed water (see Figure 1.18). This disordered surface layer is very similar to the amorphous calcium phosphate (ACP) and enables adsorption of water, which is very important for the orientation of nanocrystallites [286]. NMR analyses have revealed that a HAp nanocrystallite with 10x10x30-50 nm dimensions has around 50 % of total P in the crystalline core in the form of PO_4^{3-} ions, while the remaining 50 % are in the outer, 1 nm thick layer in the form of PO_4^{3-} and HPO_4^{2-} ions [287].

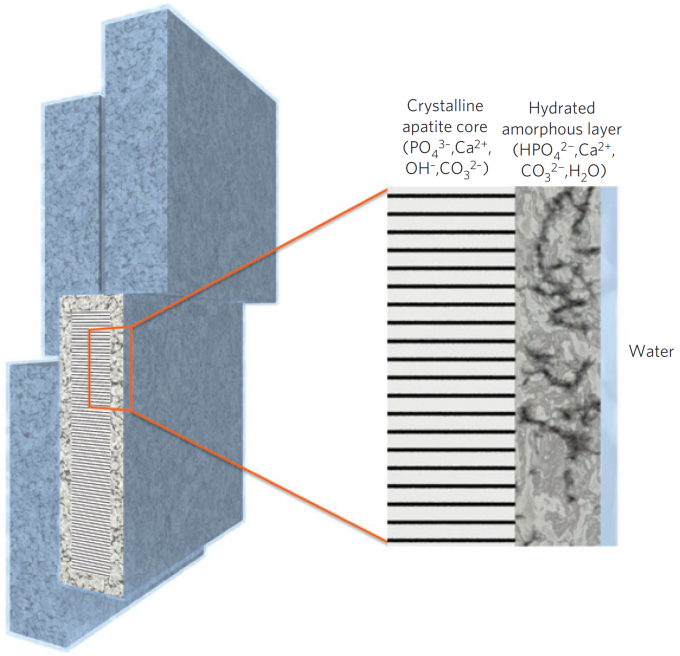


Figure 1.18: The core-shell model of the nano-hydroxyapatite. Apatitic core and ACP shell differ also in their composition [286].

1.5.2 Incorporation of antibacterial ions into hydroxyapatite

Hydroxyapatite has a remarkable capacity for ion incorporation and exchange. Moreover, the introduction of even small quantities of some ions may cause changes/improvements in biological, physicochemical, or mechanical properties [40]. Biological apatite also has different ions incorporated into its structure, as has already been mentioned above. These ions are usually added to the synthetic hydroxyapatite to enhance its bioactivity. Furthermore, other ions have also been tried (Mn^{2+}, Ag^{+}, Cu^{2+}, Ti^{4+}, Ce^{3+}, Eu^{3+}, SeO_3^{2-}), either for the same purpose of enhanced bioactivity or to add an antibacterial protection [40]. Hydroxyapatite materials with incorporated metal ions will be subsequently denoted HAp(M), where M is the symbol of the incorporated metal ion. It is very important and often difficult to achieve that the addition of antibacterial ions does not make the hydroxyapatite toxic also for the tissue cells. During the search through the literature about the hydroxyapatites with incorporated antibacterial ions I noticed an incredible inconsistency and incompleteness in the majority of published works. Thus, although antibacterial properties and cytotoxicity of Ag-doped hydroxyapatite are being explored for more than ten years, it is still not clear, for which Ag contents such materials are more toxic to bacteria than to eukaryotic cells, and if such contents even exist.

Substitution of Ca(II) by Ag(I) occurs in the HAp(Ag) materials and triggers charge compensation by OH depletion, so that the final chemical formula $Ca_{10-x}Ag_x(PO_4)_6(OH)_{2-x}$ was usually found. A number of studies investigated the antibacterial as well as cytotoxic properties for the same materials. Some HAp(Ag) materials enabled good survivability of mammalian cells and antibacterial protection [288], [289], [290], whereas some HAp(Ag) materials were antibacterial but also cytotoxic [289], [291], [292], [293], [294], [295]. It seems that the content of the antibacterial ions in the doped hydroxyapatite mainly determines the therapeutic window (concentration range of efficient antibacterial activity and low cytotoxicity). For HAp(Ag) materials, the limiting value, at which the material was equally or more toxic to eukaryotic cells than to bacteria, was usually found above 1 wt % ($x \approx 0.1$) [289], [292], [293], [294], [296], although lower (0.02–0.4 wt %) contents were also sometimes shown to be cytotoxic [291], [295], [297]. It is expected that HAp(Ag) materials with Ag contents below 1 wt % down to a certain Ag content would have a useful therapeutic window for certain bacterial strains and cell lines and an optimum Ag content providing the widest therapeutic window would be found. This value would vary for different strains and cell lines. However, the studies on HAp(Ag) materials so far contributed very little to finding the Ag contents with useful therapeutic windows. The cytotoxic concentration was often not found [290], [298], [299], [300], [301], [302], [303], while the concentration range in the cytotoxicity test was often below MIC [298], [301], [302]. On the other hand, if the antibacterial hydroxyapatite is in the form of a coating rather than suspension, we get a range of Ag contents that exhibit antibacterial properties and low toxicity instead of the therapeutic window of concentrations for each Ag content. In coatings, the minimal value of Ag^{+} content needed for antibacterial action was usually found in the range 1–2 wt % [289], [304], [305]. HAp(Ag) materials with such contents also delayed the bone healing and triggered mild inflammatory reaction in the early healing phase *in vivo*. However, there was no remarkable inflammatory reaction through 3 week healing periods and bone repair was successful [292], [293]. Another study revealed that already a 0.4 wt % Ag content ($x=0.04$) accelerated infection healing in mice from 7 days (HAp) to 48 h (HAp(Ag)) [306]. An important issue regarding the variation of antibacterial potency with different bacterial strains is the influence of the antibiotic resistance to the antibacterial performance of the doped hydroxyapatite materials and it has been addressed in a few investigations. One compared the HAp(Ag) antibacterial action towards antibiotic-resistant and susceptible *E. coli* and much lower inhibition was observed for the resistant strain, which implies that

the antibiotic resistance might have enabled also the resistance to Ag^{+} [300]. On the other hand, another study observed strong antibacterial action of a HAp(Ag) coating on Ti towards both antibiotic-susceptible *S. aureus* and MRSA [304].

Even though many more studies are needed to confirm this, it seems so far that a Cu content providing a useful therapeutic window will not be found since the non-toxic HAp(Cu) were usually found below 0.3 wt % (x= 0.05) content [290], [307], [308], [309], while their antibacterial properties were very weak even for the 0.66 wt % (x= 0.1) content, which already exhibited strong cytotoxicity [307]. Even less is known about the therapeutic window of concentrations for the HAp(Zn) materials. It seems that quite high Zn contents and HAp(Zn) concentrations are usually antibacterial [308], [310], which might be toxic to tissue cells as well, but these materials need much more investigation before drawing any conclusions. An interesting observation was that the antibacterial properties of HAp(Zn) might come out only after a longer incubation. In this view, the HAp(Zn) with 1.6 wt % Zn, which was non-toxic to human adipose-derived MSCs, had no inhibitory effect on the growth of *S. aureus* after 1 day but exhibited strong bactericidal properties after 6 days [311].

Apart from the content of the antibacterial ion, also the form, shape and size of the material contribute notably [292], [293]. Moreover, the antibacterial and cytotoxic properties of doped hydroxyapatites depend also on the location of antibacterial ions, whether they are preferentially in the internal lattice or in the hydrated surface layer [310]. I need to point out that the antibacterial and cytotoxicity tests were generally very different and predicting the outcome of the "fight for the surface" [312] based on these *in-vitro* tests should be taken with care. One study evaluated the antibacterial action against *S. aureus* and *S. epidermis* as well as cytotoxicity against osteoblasts in a similar way, in a kind of MTT assay (with WST 1 agent) [313]. Different Ag-doped calcium phosphate cements were compared, among them also HAp(Ag) with 0.75 wt % of Ag. HAp(Ag) was much more toxic to osteoblasts than to bacteria [313].

Some studies compared hydroxyapatite-based materials, doped with different antibacterial ions (Ag^{+}, Cu^{2+}, Zn^{2+}), for their antibacterial and biocompatible properties [291], [314]. HAp(Ag) was always found to be more antimicrobial but also more cytotoxic than HAp(Cu) or HAp(Zn) [291], [314], [315]. HAp(Zn) and HAp(Ag) coatings on Ti-6Al-4V with similar mass ion content (about 1.5 times higher molar ion content in HAp(Zn)) showed similar antibacterial activity against *S. mutans*, but HAp(Zn) was bioactive and enhanced the attachment and growth of fibroblasts while HAp(Ag) was cytotoxic (already for 10–100 times lower contents) [291]. Combined incorporation of two antibacterial ions was also tried. Addition of Ti^{4+} ions improved the antibacterial properties under UV illumination, which was especially evident for HAp(Cu) and HAp(Zn) [315]. Recently, a composite of 30 wt % HAp(Ag,Cu)+β-TCP(Ag,Cu) and 70 % bioactive glass has been created and tested against bacteria (*S. aureus, E. coli* and *P. aeruginosa*) and adipose-derived multipotent mesenchymal stromal cells (AD-MSCs) [316]. Different contents were tried and $0.05 \leq x_{Ag} \leq 0.1$ and $0.025 \leq x_{Cu} \leq 0.05$ contents were found to stimulate bone tissue repair while having satisfactory biocompatibility and antimicrobial properties [316]. The doped and non-doped composite materials were then also administered *in vivo* into rat bone defects aseptically and showed similar bone-healing effects [316].

Other antibacterial ions are also emerging, such as Se(IV), Se(VI) [317], [318], [319] and ions of the lanthanoid group, especially Ce^{3+} [320], [321], [322], [323].

Ga(III) incorporation into hydroxyapatite as well as β-TCP has been investigated (see Section 1.5.2.2 for further details), but the antibacterial properties of such materials have not been evaluated yet at the beginning of my doctoral study. We carried out such investigation in the framework of my PhD study and published the results against *P. aeruginosa*

and L929 mouse fibroblasts in 2016 [324].

1.5.2.1 Effect of ionic gallium on bone growth

The first studies on Ga-substituted hydroxyapatite were for the purpose of the explanation of the effects of gallium on bones. A two-week intraperitoneal administration of gallium nitrate into rats resulted in a bone with 0.05 wt% of Ga that consisted of larger and/or more perfect crystalls, had an increased Ca and P content, lower CO_3/PO_4 ratio and lower solubility [325]. For three different types of *in-vitro* hydroxyapatite formation at 37 °C and pH 7.4 (direct precipitation, transformation of ACP to HAp, and seeded crystal growth), gallium ions in the 0.01–1 mM range decreased the rate of formation in a dose-related manner [326], [327]. Solubility of HAp at pH 5.0 was decreased in the presence of 0.1 and 0.4 mM Ga^{3+}. These studies have proven the adsorption of Ga^{3+} ions onto hydroxyapatite crystals, which inhibited their further growth, and suggested that Ga^{3+} could also incorporate into the early calcium phosphate precipitates during the formation of hydroxyapatite [326], [327].

Apart from their effect on the bone mineral, Ga^{3+} influence the bone growth also in another way. They hinder bone resorption in the body and stimulate new bone growth by inhibiting the action of the osteoclasts without affecting the osteoblasts [113], [240], [328].

1.5.2.2 Incorporation of gallium ions into calcium phosphates

It was evident that Ga^{3+} ions can adsorb on the already-formed HAp nuclei as well as on the nuclei in the process of formation, but the question remained whether they can also incorporate into the HAp in formation. Ga(III) ionic radius is 0.47 (for coordination number 4), 0.55 (coordination number 5) or 0.62 (coordination number 6), while the ionic radius of Ca(II) is 1.0 (coordination number 6) [329]. Ga ions are much smaller than Ca^{2+} ions, hence this substitution is not expected or it notably distorts the structure of hydroxyapatite if it occurs. Korbas *et al.* explained this in an X-ray absorption spectroscopy comparison of an in-vitro-grown bone mineral with different Ga-doped calcium phosphates (poorly crystalline hydroxyapatite, amorphous calcium phosphate and brushite), which revealed that gallium ions 6-60 μM can substitute Ca^{2+} ions in a noncrystalline $HPO_4{}^{2-}$ rich calcium phosphate precursor phase, which prevents further transformation of this precursor phase into the hydroxyapatite. This substitution of Ca^{2+} ions with Ga^{3+} ions resulted in a distorted brushite configuration with the local environment around Ga being similar to $GaPO_4 \cdot 2\,H_2O$ [330]. However, they cannot incorporate into the hydroxyapatite but can only adsorb to its surface, which results in the inhibition of the hydroxyapatite growth [330]. Hence, so far the doping of the hydroxyapatite lattice with gallium ions has not been observed and it is believed to be impossible. Nevertheless, interstitial Ga^{3+} incorporation without substituting Ca^{2+} ions remained possible. In 2009, Melnikov and colleagues came up with the idea of gallium-containing hydroxyapatite for local delivery of gallium ions. They claimed that Ga ions were intercalated into the interstitions of the hydroxyapatite lattice when it was formed by precipitation in the presence of 3 mM $Ga(NO_3)_3$ or 128 mM $NaGa(OH)_4$, without actually giving any proof for that [331]. On the other hand, the characteristic apatitic core and ACP-like shell structure of nanocrystalline hydroxyapatite (see Figure 1.18) offers another possibility for incorporation of Ga^{3+} ions within the disordered surface layer [287]. First publication about such incorporation was made as late as in 2015 by Mellier *et al.* explaining the Ga(III) incorporation by a precise NMR characterisation [114]. The investigation clearly showed that Ga^{3+} ions were incorporated only into the disordered surface layer and not into the apatitic core. They even created an injectable Ga-doped apatitic cement (with a bioactive amount of up to 0.3 wt.% of Ga)

and showed that its *in-vivo* injection into rabbit femurs resulted in successful bone healing without any side effects [114]. The same group of scientists also demonstrated in 2010 and 2011 that the calcination of a gallium-containing Ca-deficient nano-hydroxyapatite above 800 °C results in its conversion to a gallium-doped TCP with a fully controllable amount of gallium (formula $Ca_{10.5-1.5x}Ga_x(PO_4)_7$ with $< x < 0.75$) [332], [333]. Gallium-doped β-TCP can also be created by direct solid-state synthesis [332], [333].

1.5.3 Nanocomposites from antibacterial nanoparticles and hydroxyapatite

Another way of adding antibacterial properties by modification of hydroxyapatite is by exploiting nanotechnology and attaching antibacterial nanoparticles on the surface of hydroxyapatite. In this way, a nanocomposite material is created. This kind of modification of hydroxyapatite is newer than incorporation of antibacterial ions, hence the amount of articles on this topic is not so vast yet. For the nanocomposites, the N@HAp notation will be used throughout this work, where N is the chemical formula of the antibacterial nanomaterial in the nanocomposite. When going through the literature about antibacterial hydroxyapatite nanocomposites, I ran into similar inconsistency and incompleteness in the majority of works as in the case of hydroxyapatites doped with antibacterial ions. From the literature data on Ag@HAp nanocomposites we can conclude that at least 0.5–2 wt % Ag content is needed for the Ag@HAp nanocomposite to have antibacterial properties [68], [334], [335], [336], [337], [338], [339], [340], [341]. But which contents are non-cytotoxic at their antimicrobially efficient concentrations? Vukomanović *et al.* have clearly demonstrated recently that the Ag@HAp nanocomposite containing 10 wt % of Ag does not have any useful therapeutic window against *E. coli*, *S. aureus*, IMR-90 human lung fibroblasts and U2OS osteosarcoma, since its MIC is above TC_{50}. It is expected that the Ag content below 5 wt % content will enable a useful therapeutic window. Another way of reducing the cytotoxicity instead of reducing the Ag content is by adding growth promotors into the nanocomposite and changing the surface of the nanoparticles. In this way, nanocomposite coatings on Ti were prepared that consisted of bone morphology protein-2 (BMP-2) and Ag/chitosan nanoparticles and were not cytotoxic despite containing 15 wt % of Ag [342]. Both BMP-2 and chitosan contributed to lowering the cytotoxicity while the antibacterial properties were maintained. *In-vivo* implantation into rabbits was also performed and it showed promising results.

During the preparation of the Ag@HAp nanocomposites, an Ag_3PO_4 phase can also sometimes emerge [343]. Ag_3PO_4@HAp nanocomposites with different Ag_3PO_4 content (0.1–6 % Ag, it is not clear what the % means) have been tested for their antibacterial activity and cytotoxicity and turned out to be very efficient against *S. aureus* and *P. aeruginosa* but also highly toxic for human osteoblasts [344]. Surprisingly, the cytotoxicity of the 0.09 % sample was decreasing with incubation time, so that the survivability for the 48-hour incubation was already above 80 %. Another interesting type of silver-based antibacterial nanocomposites are the composites of hydroxyapatite and the AgX-coated TiO_2 nanoparticles (X= Cl, Br, I), which are strongly bactericidal for *E. coli* under visible light illumination [345], [346], [347]. While the AgX/TiO_2 nanoparticles are not active in the dark, the AgX/TiO_2@HAp nanocomposites have exhibited antibacterial activity also without visible light illumination. Wiglusz *et al.* compared the antibacterial action of HAp(Ag) and Ag@HAp against several bacterial strains and HAp(Ag) was found more efficient and bactericidal [303].

The effect of the size, the size distribution and the homogeneity of the distribution of the Ag NPs in the nanocomposites has not been evaluated yet. A study in this direction has, however, been done on the ZnO@HAp nanocomposites. ZnO@HAp nanocomposites

with different ZnO contents (2, 10, and 25 wt %), three different sizes of the ZnO particles (<1 μm, <100 nm and <50 nm) and two different sintering temperatures (830 or 1000 °C) were compared for their antibacterial properties against *S. aureus* and *E. coli*. Better antibacterial properties were observed for the lower sintering temperature and higher content of ZnO, but even 25 wt % did not completely inhibit the bacterial planktonic growth in any sample [348]. The ZnO@HAp nanocomposite with the smallest ZnO nanoparticles (<50 nm) was the strongest antimicrobial in both planktonic growth inhibition and prevention of bacterial attachment, whereas the <1 μm and <100 nm samples had similar growth-inhibiting activity but the <100 nm sample was evidently better in the prevention of bacterial attachment at 10 and 25 % content [348]. Research of ZnO@HAp nanocomposites has only started during my PhD study, so I found only one other article about such materials, which has shown inhibition zones against *E. coli* and *S. mutans* for ZnO@HAp materials with very high (> 80 wt %) ZnO contents [349]. The minimal ZnO content for antibacterial properties and cytotoxicity of ZnO@HAp nanocomposite remains unknown.

Vukomanović *et al.* have done a very interesting and precise investigation of Au@HAp nanocomposites with Au nanoparticles functionalized by amino acids [68], [107], [350], which set a new direction away from the strongest antibacterial nanoparticles towards modification of biocompatible nanoparticles to achieve targeted antibacterial action. Au/Arg@HAp, Au/Gly@HAp and Au/His@HAp were tested against *E. coli* and *S. aureus* by a disc diffusion antibiogram, standard dilution antibiogram, qualitative live/dead assay and bacterial morphology observation under SEM, and their cytotoxicity against U2OS osteosarcoma as well as IMR-90 human lung fibroblasts was examined by a quantitative live/dead assay in a flow cytometer [68], [350]. All three nanocomposites exhibited good antibacterial properties against both bacterial strains and stronger antibacterial action against *E. coli* than a comparable Ag@HAp nanocomposite (containing 10 wt %, which is roughly the same chemical amount of substance). MIC for the Ag@HAp was 0.56 mM (0.74 mM MBC) Ag against *E. coli* and 0.74 mM (MBC 1.16 mM) Ag against *S. aureus*, while TC_{50} values were 0.37 mM Ag for U2OS osteosarcoma and 0.23 mM Ag for IMR-90 human lung fibroblasts [68], [336]. On the other hand, Au/Arg@HAp had MIC values 0.32 mM (MBC >4 mM) Au against *E. coli* and 1.6 mM (MBC 4 mM) Au against *S. aureus*, but TC_{50} values above 1.6 mM Au [68], [350]. Non-functionalized Au@HAp nanocomposite and Arg+HAp did not show any antibacterial properties, so the nanocomposites really had a designed antibacterial activity. However, only arginine functionalization yielded a material with useful therapeutic window, whereas the use of other amino acids resulted in too toxic nanocomposites with MIC higher than TC_{50}. Au/Gly@HAp nanocomposite had MIC of 0.33 mM Au (MBC >5.5 mM) against *E. coli* and 4.4 mM Au (MBC=5.5 mM) against *S. aureus* but TC_{50} values at 0.27 mM Au [68]. Au/His@HAp had MIC of 0.45 mM Au (MBC >3.8 mM) for *E. coli* and 2.3 mM Au (MBC >3.8 mM) for *S. aureus* but TC_{50} of 0.15 mM Au for IMR-90 and 0.45 mM Au for U2OS [68]. The authors noticed the amphyphylic nature of the functionalized Au nanoparticles and its similarity to the structure of antibacterial peptides. The amphipathicity of these molecules enables them to cross the membrane and interact with both the hydrophobic and hydrophilic components of the membrane lipid bilayer [350]. Based on the similarity in structure, the observed shrinkage and wrapping of the cell wall of *E. coli*, selective toxicity (high biocompatibility and strong antibacterial activity) and more positive zeta potential, the authors gave a reasonable and attractive hypothesis that the mechanism of the antibacterial action of the Au/Arg@HAp is similar to the mechanism of the antibacterial peptides. Their antibacterial action is based on electrostatic interactions, the surface charge (caused by Arg) to "sense" the bacterial surface, to damage it and/or to cross it and get inside the cell, where they target various metabolic pathways that are essential for the microorganism's life [350]. The main

advantage of Au/Arg NPs over antibacterial peptides according to the authors is their better stability and resistance to enzymatic degradation or inactivation, better transport and targeting properties [350]. Nevertheless, the suggested "antimicrobial-peptide-mimicking" mechanism of Au/Arg NPs and Au/Arg@HAp nanocomposite has yet to be proven and needs to be further investigated in detail. Moreover, the toxicity of the Au/Arg@HAp nanocomposite on other strains and cell lines should also be checked. Apart from the amino-acid functionalized Au nanoparticles, antibacterial properties (against *Staphylococcus aureus, Streptococcus pyogenes* and *Pseudomonas aeruginosa*) were revealed also for the Au/PVA@HAp/PVA nanocomposite at very low (0.144 ppm) Au contents [351]. However, the cytotoxicity of this nanocomposite was not evaluated.

Another alternative for the toxic Ag nanoparticles are MgO nanoparticles. Pourdanesh *et al.* have created a nanocomposite from high density polyethylene (HDPE, 80 wt %), tricalcium phosphate (16 wt %), hydroxyapatite (4 wt %) and MgO nanoparticles (0.1 wt %) and demonstrated its antibacterial properties (disc diffusion inhibition zone) against *E. coli*, *S. aureus* and *P. aeruginosa* as well as low cytotoxicity for human osteoblasts. They further performed an *in-vivo* implantation of this nanocomposite into rabbits to test its biocompatibility (but not the prevention of bacterial infection) and it exhibited no increased inflammation and some favourable osteogenic properties in comparison with pure HDPE.

I found no gallium-based nanocomposites with hydroxyapatite or any other calcium phosphate at the beginning of my PhD study. This work will focus on exploring the Ga-based antibacterial protection of hydroxyapatite and combining two selective antibacterial agents (functionalized Au nanoparticles and Ga in ionic as well as nanoparticulate form) rather than broad-spectrum non-selective agents (such as Ag) to achieve a broad-spectrum antibacterial efficiency and retain the high biocompatibility, bioactivity and low cytotoxicity. Combinations of two different antibacterial agents, such as two different metal ions, can result in a synergistic or antagonistic effect, or both, depending on the concentrations of the two ions [30], [237]. The most desirable is the synergistic effect on antibacterial performance and antagonistic effect on cytotoxicity. Besides the synergistic or additive activity, a combination of drugs in general reduces the possibilities for drug resistance and decreases the required doses, reducing both cost and the chances of toxic side effects, or increases the spectrum of activity [38]. Several combinations of ions inside hydroxyapatite have already been tried, but I have not come across a combination of antibacterial ion-doping and attachment of antibacterial nanoparticles. In nanocomposites, only the addition of bioactive ions to reduce the cytotoxicity of the antibacterial nanoparticles has been done. Investigation of the combined effect of functionalized Au nanoparticles and Ga^{3+} ions is therefore interesting also from this point of view. During my doctoral work I have developed three new types of antibacterial nanocomposites: Ga NPs on HAp, functionalised Au NPs on HAp(Ga) and Ga/Au core-shell NPs on HAp. We have published the results about the first two [352], [353].

Chapter 2

Aims, Scope and Hypotheses

2.1 Aims

The aim of this doctoral dissertation is to create a new solution for antibacterial activity based on Ga, Au and HAp, which will manifest a very high level of novelty and originality, an important level of practical usefulness and a possibility for its transfer into the industry. To realize the scope of my doctoral thesis, I need to accomplish the following goals:

(a) investigation of the possibilities for antibacterial protection by using gallium and gold on hydroxyapatite with nanotechnology;

(b) development and optimization of the synthesis method of the Ga(III)-containing hydroxyapatite, Ga nanoparticles and functionalised Au nanoshells with Ga core (in terms of conditions, time, repeatability, yield, simplicity, price, etc.);

(c) selection of the most efficient functionalisation and developing method for the attachment of functional groups onto the surface of the nanostructures;

(d) ensurance of attachment of the antibacterial substance in the form of Ga nanoparticles, functionalised Au nanoparticles and functionalised Au nanoshells with Ga core onto the chosen bioactive carrier (hydroxyapatite or Ga-doped hydroxyapatite);

(e) determination of the mechanisms of material formation;

(f) comparison of Ga as antibacterial agent in the form of ions and nanoparticles; and

(g) comparison of Ga(III) drug delivery by hydroxyapatite, Ga nanoparticles and Au nanoshells.

Our intention is to develop materials with the specific design illustrated in Figure 2.1. The most important is the comparison of delivery of Ga as the antibacterial component into bacteria with Ga NPs, Ga/Au core-shell NPs or hydroxyapatite nanolaths. In the investigations I refer to the recently created material from hydroxyapatite and Au nanoparticles functionalized with arginine (Au/Arg@HAp) [68], [350].

2.2 Scope

The scope of this dissertation is:

(a) to obtain original scientific discoveries and new knowledge about not yet existing strategies for antibacterial protection with the use of nanotechnology, which will enable design and development of innovative effective antibacterial nanomaterials;

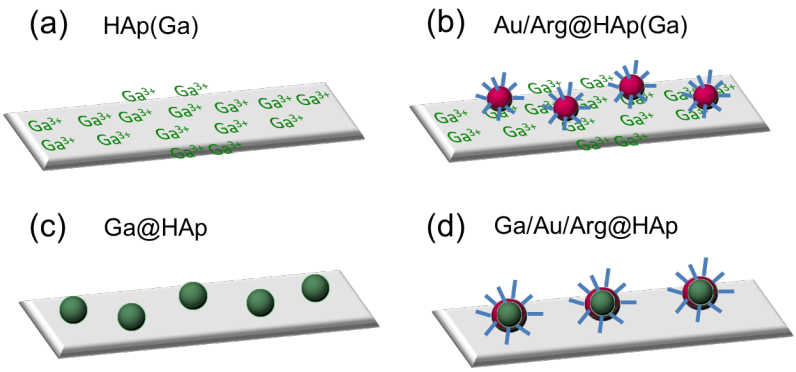


Figure 2.1: Schematic illustration of the materials investigated in the thesis: (a) Ga(III)-containing hydroxyapatite; (b) functionalized Au NPs on Ga(III)-containing hydroxyapatite; (c) Ga NPs on hydroxyapatite; (d) functionalised Ga/Au core-shell NPs on hydroxyapatite.

(b) to develop innovative strategies of antibacterial agents for future national and international scientific collaborations/projects;

(c) to precisely explore and objectively present different possibilities of antibacterial protection with low cytotoxicity based on gallium, gold and hydroxyapatite;

(d) to investigate the advantages and disadvantages of the new Ga- and Au-based antimicrobial strategies, and the usefulness and deficiencies of the developed materials for future biomedical applications.

The doctoral thesis involves the synthesis of several materials based on Ga, Au and hydroxyapatite (Figure 2.1):

1. hydroxyapatite that contains Ga^{3+} ions (HAp(Ga)) and releases them locally into the medium;
2. functionalized Au nanoparticles on HAp(Ga);
3. Ga nanoparticles on HAp; and
4. functionalized Ga/Au core-shell nanoparticles, attached to the surface of HAp.

The dissertation will explain the mechanism of incorporation of Ga ions, of the nanoparticle (Ga, Au in Ga/Au) formation, their functionalization with targeting groups (such as, amino acids) and creation of the composites with the carrier material (HAp or HAp(Ga)). An optimisation of the parameters in the syntheses of the new nanomaterials needs to be proposed and at the same time the antibacterial efficiency as well as cytotoxicity of the new materials need to be investigated in detail. Improved efficiency and selectivity in comparison with the recently designed Au/Arg@HAp composite nanomaterials [68], [107], [350] must be achieved.

2.3 Hypotheses

The following hypotheses regarding the HAp(Ga) material are proposed:

1. Ga^{3+} ions can be incorporated into calcium-deficient hydroxyapatite nanomaterial to obtain Ga(III)-containing hydroxyapatite.

2. Addition of Ga^{3+} into hydroxyapatite will give this biomaterial antibacterial properties against *P. aeruginosa*.

3. Ga^{3+} ions can be released from the hydroxyapatite in different physiological media and simulated body fluids.

The following hypotheses are proposed regarding the Ga@HAp material:

1. Nanoparticles of elemental gallium possess antibacterial properties.

2. It is possible to make a stable nanocomposite powder consisting of Ga NPs and hydroxyapatite.

3. By performing ultrasonication of liquid gallium in non-aqueous polar media or addition of a more volatile polar organic liquid to water, the sonochemical conversion of Ga to GaOOH can be prevented.

4. The Ga@HAp nanocomposite will exhibit effective antibacterial activity towards *P. aeruginosa*.

5. Antibacterial action of Ga NPs and hence of the Ga@HAp nanocomposite is connected with the release of antibacterial Ga^{3+} ions from the surface of the nanoparticles and their dissolution in physiological media and simulated body fluids.

6. Non-selective extracellular generation of reactive oxygen species does not contribute notably to the antibacterial action of the Ga@HAp nanocomposite and it will therefore have low cytotoxicity at concentrations that successfully inhibit bacterial proliferation.

7. Ga@HAp will have similar antibacterial properties as a comparable Ag@HAp nanocomposite, but lower cytotoxicity.

The following is hypothesised about the addition of the functionalised nanogold component to the HAp(Ga) and Ga@HAp materials:

1. Antibacterial activity of Au/Arg@HAp(Ga) will be a combination of the antibacterial action of Au/Arg NPs and Ga(III). Thus, this material will have a double antibacterial action: contact-based of Au nanoparticles and Fe(III) substitution by Ga(III).

2. The highly biocompatible Au/Arg@HAp nanocomposite exhibited effective antibacterial action especially towards *E. coli* and also towards *S. aureus*, to which Ga(III) ionic species in general show very high MIC values. Hence, combining the HAp(Ga) and Ga@HAp materials with Au/Arg nanoparticles would widen the antibacterial activity in terms of strain diversity but retain the selectivity in terms of eukaryotic vs prokaryotic cells.

3. Ga/Au core-shell nanoparticles can be formed by the galvanic method using Ga as the sacrificing core:

$$Ga + AuCl_4^- \longrightarrow Au + Ga^{3+} + 4\,Cl^-$$

   Ga has a negative redox potential, while the redox potential for the $AuCl_4^-$ reduction to Au is positive.

4. Functionalized Ga/Au core-shell nanoparticles are formed if $AuCl_4^-$ is reduced on the Ga NPs in the presence of amino acid.

Chapter 3

Experimental Work

3.1 Materials

3.1.1 Specifications of the reagents used for the syntheses

acetonitrile	gradient grade, for HPLC, ≥99.9%
$AgNO_3$	99+%, Alfa Aesar
L-arginine	98+%, Alfa Aesar
$Ca(NO_3)_2 \cdot 4H_2O$	99.98 % (metals basis), Alfa Aesar
chloroform	≥99.8%, stabilised with 0.5-1% ethanol
di-N-octylamine	97%
ethanol	absolute, anhydrous, ACS, for analysis, Carlo Erba reagents
ethylene glycol	spectrophotometric grade >99 %, Alfa Aesar
gallium	99.99 %, Acros Organics
$Ga(NO_3)_3 \cdot xH_2O$	99.9%, Sigma-Aldrich
$HAuCl_4 \cdot xH_2O$	99.99% (metals basis), Alfa Aesar
$NaBH_4$	p. a. (≥99%), Fluka
NaOH	ACS reagent, ≥97.0 %, pellet
$NH_4H_2PO_4$	≥99.99 % (metals basis), Sigma Aldrich
octadec-1-ene	technical grade (90%), ACROS Organics
oleic acid	technical grade (90%), Sigma Aldrich
propan-2-ol	anhydrous, 99.5%, Sigma Aldrich
tetrahydrofuran	anhydrous, ≥99.9%
tris(dimethylamido)gallium(III) dimer	99.9% (metals basis), Alfa Aesar
urea	solid crystalline, 99.3+%, Alfa Aesar
water	deionized by reverse osmosis and ion exchanger

The amount of water in the $Ga(NO_3)_3 \cdot xH_2O$ was determined by TGA analysis [354] to be x=5.5.

3.1.2 Specifications of the reagents and chemicals used for the analyses

benzene	spectrophotometric grade (99.5+ %), Alfa Aesar
$CaCl_2 \cdot 2\,H_2O$	≥99.0%, suitable for cell culturing
CM-H2DCFDA	Thermo Fisher
DMSO	99.9+%, ACS reagent, ACROS Organics
$FeSO_4 \cdot 7\,H_2O$	≥99.0%, suitable for cell culturing
gallium	99.99 %, Acros Organics
glutaraldehyde	25% aqueous solution, for electron microscopy, Agar scientific
HCl	37 %, for analysis, Carlo Erba reagents
HNO_3	65%, for analysis, EMD Millipore (Merck)
KBr	FT-IR grade, ≥99%
Luria-Bertani broth	microbiologically tested, Miller, Sigma-Aldrich
menadione	crystalline, Sigma Aldrich
$MgSO_4 \cdot 7\,H_2O$	≥99.5%, suitable for cell culturing
3-(4,5-dimethylthiazol-2-yl)-2,5-diphenyltetrazolium bromide (MTT)	for cell viability assays, Thermo Fisher
Mueller-Hinton broth	for microbiology, Sigma-Aldrich
NaCl	≥99.0%, crystalline, Fisher chemicals
phosphate buffered saline (PBS) tablet	Sigma-Aldrich
rhodamine B	Alfa Aesar
trisodium citrate dihydrate	99 %, Alfa Aesar

PBS tablet when dissolved in 200 mL of H_2O gives 10 mM (1.44 mg/mL) Na_2HPO_4, 1.8mM (0.24 mg/mL) KH_2PO_4, 2.7 mM (0.2 mg/mL) KCl and 137 mM (8 mg/mL) NaCl. M9PBS is an aqueous solution of Na_2HPO_4 (6 g/L), KH_2PO_4 (3 g/L), NaCl (0.5 g/L) and NH_4Cl (1 g/L).

Millonig phosphate buffer (pH 7.4) consists of $NaH_2PO_4 \cdot 2\,H_2O$ (1.8 g/L), $Na_2HPO_4 \cdot H_2O$ (23.25 g/L) and NaCl (5 g/L).

M9 consists of:

(a) the M9PBS solution, which is autoclaved;

(b) solution of $MgSO_4$ (final 1 mM), $CaCl_2$ (final 100 μM) and glucose (final 2 g/L), which is sterilised through a 100-nm filter;

(c) solution of micronutrients (3 μM $(NH_4)_6Mo_7O_{24}$, 0.4 mM H_3BO_3, 30 μM $CoCl_2$, 10 μM $CuSO_4$, 80 μM $MnCl_2$ and 10 μM $ZnSO_4$), which is prepared 1000X concentrated, filtered through the 100-nm filter and diluted during the M9 medium preparation;

(d) solution of $FeSO_4$ (final 1 μM), which is freshly prepared and sterilised through the filter.

Live/Dead® BacLight™Bacterial Viability Kit L7007 "for microscopy" from Molecular Probes was used for the fluorescence survivability assays.

3.1.3 Growth media and cells

agar	for microbiology, Sigma-Aldrich
fetal bovine serum	research grade, for cell culture, Sigma-Aldrich
L-glutamine	Invitrogen
Luria-Bertani broth	microbiologically tested, Miller, Sigma-Aldrich
McCoy's 5A medium	Sigma-Aldrich
Minimum Essential Medium (MEM) Eagle	with Earle's salts and without sodium bicarbonate, suitable for cell culture, Gibco
Mueller-Hinton (MH) broth	for microbiology, Sigma-Aldrich
penicillin	Invitrogen
streptomycin	Invitrogen

MH agar plate was prepared by mixing MH broth (to final concentration of 21 g/L) and agar (to final concentration of 17 g/L), heat to boiling, then autoclaving the solution for 15 min at 121 °C and pouring the solution into petri dishes after it cooled down to at least 60 °C. The poured solution was left to solidify at room T in the laminar flow cabinet.

M9 agar plate was prepared by mixing 50 mL of sterile M9 minimal medium with 200 mL of an autoclaved 2 (w/V) % solution of agar at 40 °C and solidification at room temperature in a laminar flow cabinet. Bacterial strains *P. aeruginosa* MW1 and PAO1(wild type) were a gift from Dr. Matej Butala from the Biotechnical Faculty of the University of Ljubljana. For further details on these two strains the reader may refer to [355]. *S. epidermidis* NCIMB 8853 (FDA strain PCI 1200) was purchased from ATCC (ATCC12228). Mouse fibroblasts L929 (NCTC) were purchased from the European Collection of Authenticated Cell Cultures (ECACC no. 85103115). The same holds true also for the human fetal lung fibroblast IMR-90 (ECCAC no. 85020204) and human osteosarcoma U2OS cell line (ECCAC no. 92022711).

3.2 Synthesis Methods

3.2.1 Synthesis of hydroxyapatite

Hydroxyapatite was synthesized by ultrasound-assisted homogenous precipitation using the thermal degradation and hydrolysis of urea [273], [356], [357], [358]. The process contains two stages: precipitation and transformation (Figure 3.1). During the precipitation stage,

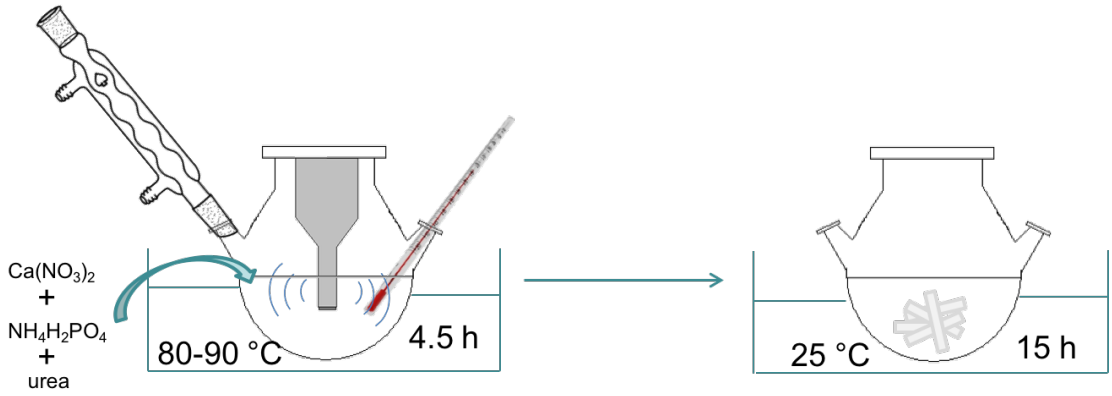


Figure 3.1: Scheme of the synthesis of hydroxyapatite: precipitation under ultrasonication at 80-90 °C (left), followed by ageing (transformation) at room temperature (right).

$Ca(NO_3)_2 \cdot 4\,H_2O$ was mixed with $NH_4H_2PO_4$ and heated to 80 °C. Then, an aqueous solution of urea was added to achieve a Ca: P: urea molar ratio of 2: 1: 5 and a 9 mM concentration of $NH_4H_2PO_4$ before sonication. This mixture was irradiated by ultrasound pulses of 2 s duration with 1 s breaks and 80 % amplitude for 3 hours of pulses, while the temperature was maintained at 80–90 °C. A 750 W sonochemical apparatus (Sonics & Materials) with a replaceable 13-mm tip was used as the ultrasound source. Then the transformation stage followed, during which the precipitate was aged in the precursor solution for 15 hours. After this, the precipitate was centrifuged, washed with water and dried at room temperature. If HAp was used for further modification (ion exchange or nanocomposite formation), it was not dried, but centrifuged after washing and resuspended in the required medium.

The syntheses without sonication were done by mixing the same amounts of reactants in the same volume as in the above-described synthesis, except that magnetic stirrer was used and an oil bath to keep the solution/suspension at boiling conditions. The volume of the reaction mixture was kept constant by a reflux with the use of an Allihn condenser. These syntheses did not include the transformation step either.

3.2.1.1 Removal of Ti contamination

Ti-contaminated HAp was suspended in ethylene glycol and centrifuged at 2000 rpm for 10 min to sediment Ti, then the supernatant was mixed with 10x volume of water in order to sediment hydroxyapatite. After the centrifugation for 15 min at 6500 rpm the cleaned HAp was resuspended in water or ethanol for drying.

3.2.2 Synthesis of Ga-doped hydroxyapatite

The syntheses of different HAp(Ga) materials are schematically presented in Figure 3.2. The pH at different stages of the syntheses was measured by an Eutech PC700 pH-meter.

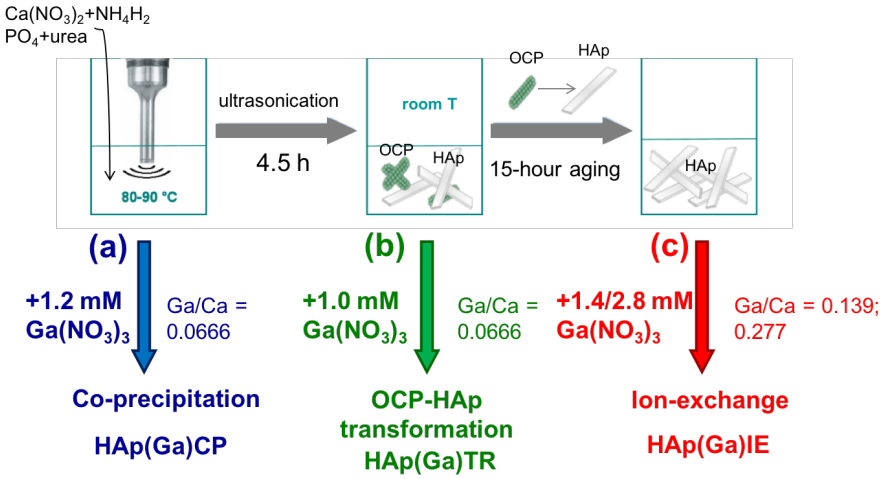


Figure 3.2: Synthesis of different HAp(Ga) materials by addition of Ga^{3+} ions at different stages of the HAp synthesis: (a) co-precipitation, (b) transformation, (c) ion exchange.

3.2.2.1 HAp(Ga) by co-precipitation

HAp(Ga)CP was created in the same way as HAp, but all the stages of the synthesis were done in the presence of Ga^{3+} ions (see Figure 3.2 (a)). Ga^{3+} ions were introduced into

the starting reaction mixture to a 1.2 mM concentration, so that the Ga/Ca molar ratio was 0.0666, while the amounts of the other reactants stayed the same. Then the synthesis continued in the same way as the synthesis of hydroxyapatite, so that after 3 hours of sonication at 80–90 °C the precipitated HAp(Ga)CP was also aged in the presence of Ga^{3+} ions.

3.2.2.2 HAp(Ga) by transformation

HAp(Ga)TR was created in the same way as HAp, but the transformation stage of the synthesis was done in the presence of Ga^{3+} ions (see Figure 3.2 (b)). After the sonochemical synthesis of HAp, an aqueous solution of $Ga(NO_3)_3$ was added to the reaction suspension to achieve a 1.0-mM Ga concentration and a Ga/Ca molar ratio of 0.0666. In this way the precipitated HAp (still containing some OCP and ACP) was aged in the presence of Ga^{3+} for 15 h to form HAp(Ga)TR.

3.2.2.3 HAp(Ga) by ion-exchange

HAp(Ga)IE was created by mixing an aqueous suspension of HAp (which was washed but not dried after the synthesis and re-suspended in water to a 1.5 g/L concentration) with an equal volume of an aqueous solution of $Ga(NO_3)_3$ for 24 hours (Figure 3.2 (c)). Four different concentrations of Ga^{3+} were used: 1.4 mM, 1.7 mM, 2.8 mM and 5.6 mM, while the starting Ga/Ca ratios calculated for the initial Ca molar mass used in the synthesis of HAp yielded 0.070, 0.085, 0.14 and 0.28, respectively. The Ga(III) solutions were two times diluted by mixing with HAp suspension.

The material with mixed octacalcium phosphate (OCP) and hydroxyapatite phase was prepared in the same way as hydroxyapatite (Section 3.2.1) but using two times higher concentrations of all the reagents. An aqueous suspension of this OCP/HAp (which was washed but not dried after the synthesis and re-suspended in water) was then mixed with an aqueous solution of $Ga(NO_3)_3$ (to obtain 1.4 mM Ga^{3+} and 0.139 Ga/Ca ratio) for 24 hours.

3.2.2.4 Amorphous gallium phosphate

Amorphous gallium phosphate hydrate was prepared by precipitation of $Ga(NO_3)_3$ with phosphate buffer [114]. A phosphate buffered saline tablet was dissolved in 200 mL of water and 25 mL of the resulting solution were mixed with 25 mg of $Ga(NO_3)_3 \cdot xH_2O$ for 1 day at 37 °C. The resulting precipitate was separated from the PBS solution by centrifugation, after which it was washed twice with water, resuspended in ethanol and dried at room temperature in a fume hood.

3.2.3 Synthesis of functionalized Au nanoparticles on hydroxyapatite

Synthesis of Au/Arg@HAp was done in a similar way as previously reported [68], [350]. 100 mL of aqueous suspension of hydroxyapatite ($\sim$ 0.75 g/L) were mixed with 50 mL of aqueous solution of arginine (2 g/L) and 1 mL of 2-propanol and ultrasonicated at 80 % amplitude for 10 min of pulses (2s duration, 1s breaks). Then, 50 mL of aqueous solution of $HAuCl_4$ (1 g/L) were added and another ultrasonication followed for 40 min of pulses (2s duration, 1s breaks). The synthesis was conducted in a water-jacketed glass vessel to maintain the room temperature inside the reaction mixture. The resulting suspension was centrifuged and dried at room T in a fume hood.

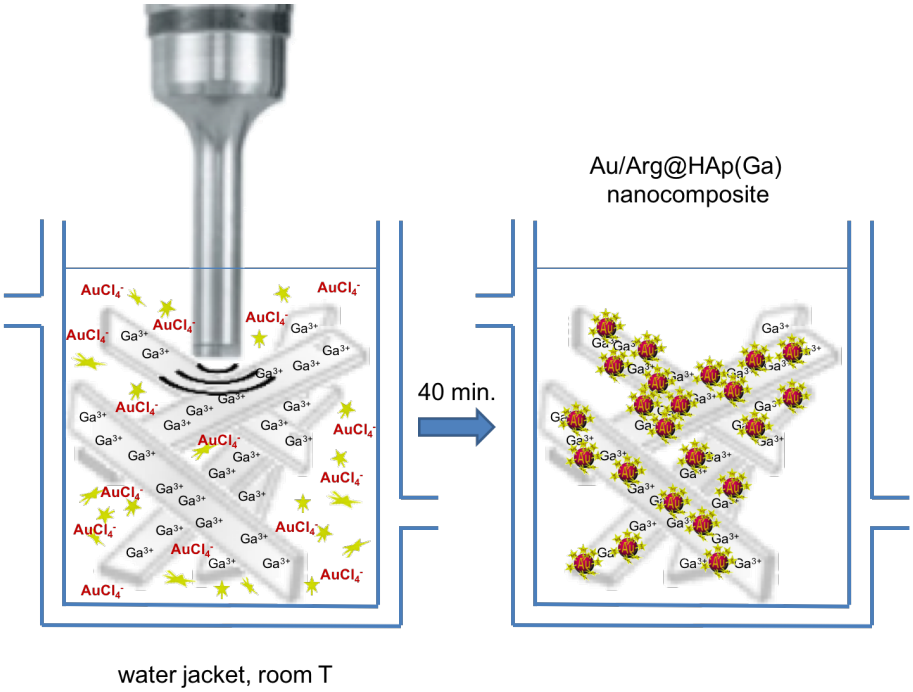


Figure 3.3: Schematic representation of the synthesis of an Au/Arg@HAp(Ga) nanocomposite.

3.2.4 Synthesis of functionalized Au nanoparticles on Ga-doped hydroxyapatite

Synthesis of Au/Arg@HAp(Ga) is depicted in Figure 3.3. 100 mL of aqueous suspension of HAp(Ga) (1.5 g/L) were mixed with 50 mL of aqueous solution of arginine (2 g/L) and 1 mL of 2-propanol and ultrasonicated at 80 % amplitude for 10 min of pulses (2s duration, 1s breaks). Then, 50 mL of aqueous solution of $HAuCl_4$ (1 g/L) were added and another ultrasonication followed for 40 min of pulses (2s duration, 1s breaks). The synthesis was conducted in a water-jacketed glass vessel to maintain the room temperature inside the reaction mixture. The HAp(Ga)IE suspension was used immediately after the 24-hour Ga(III) incorporation (see Section 3.2.2), whereas the HAp(Ga)TR suspension was centrifuged and resuspended in water before the synthesis of the Au/Arg@HAp(Ga)TR nanocomposite. The resulting suspension after the sonication was centrifuged and dried at room T in a fume hood.

3.2.5 Synthesis of gallium nanoparticles on hydroxyapatite

3.2.5.1 The Ga@HAp16 nanocomposite

The Ga@HAp16 nanocomposite was created by a low-temperature ultrasonic emulsification in a Suslick flask (Figure 3.4). Ga was liquefied by heating above 30 °C and weighed in the liquid state (50 mg). The surface oxide layer on the Ga droplet was removed by a quick washing with 20 μL of 1M HCl [154]. The wetting angle between the Ga droplet and the flask immediately increased. 50 mL of ethylene glycol (EG), purged with N_2, were added and ultrasound pulses were provided with a length of 2 s, 80 % amplitude and breaks of 1 s for 3 h in a N_2 atmosphere and reflux. A 750 W sonochemical apparatus (Sonics & Materials) with a replaceable 13 mm tip was used as the ultrasound source. The ultrasonic

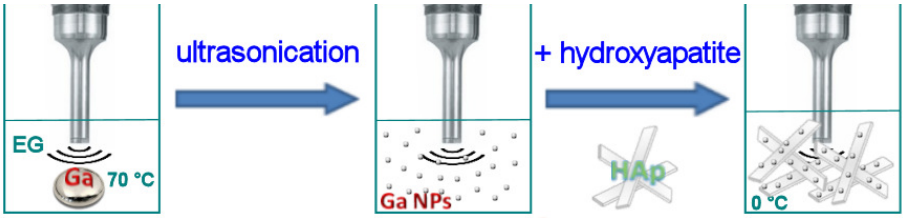


Figure 3.4: Illustration of the synthesis of the Ga@HAp nanocomposite.

horn was immersed 1.5 cm into the medium and the tip was 2.5 cm above the Ga droplet at the beginning. After 2 h of sonication, 10 mL of ethyleneglycolic suspension containing 70 mg of hydroxyapatite was added and the mixed suspension was further ultrasonicated with the same pulses. In the last 15 minutes of the sonication, the condenser was substituted with a pipe, connected to a rotary pump that created about 1 mbar pressure inside the reaction vessel. Under these conditions, the suspension was cooled to about 0 °C. The resulting suspension consisted of Ga particles with a wide size distribution from a few nm to 1 μm. However, the high viscosity of EG, stability of suspension of HAp nanorods in EG and absence of any interactions between large Ga particles and HAp nanorods enabled a separation of the Ga nanoparticles (diameter $<$ 100 nm), together with the HAp nanorods, from the larger Ga particles by centrifugation. Thus, the cold suspension was further cooled to -30 °C and then centrifuged at -9 °C and 5500 $\times$ g for 15 min. After such centrifugation, 80 % of HAp and the smallest Ga particles (20% of the starting Ga amount) remained in the supernatant. This supernatant was mixed with a three times larger volume of cold deionised water so that after centrifugation at 6300 $\times$ g for 15 min the Ga@HAp nanocomposite was sedimented. This sediment was re-suspended in 2-propanol, centrifuged and dried.

The HAp reference for Ga@HAp was prepared by mixing a hydroxyapatite suspension in EG with water, centrifuged and dried in the same way as the Ga@HAp.

Colloidal suspension of Ga NPs in EG was prepared by a 2-hour ultrasonication of 50 mg of liquid Ga in 50 mL of EG under the same conditions as in the synthesis of the Ga@HAp, followed by a 15-minute centrifugation at 5500 $\times$ g, after which the supernatant was retained and analysed.

3.2.5.2 Other Ga@HAp nanocomposites

Ga@HAp6-nano was created by the same procedure as Ga@HAp16 (Section 3.2.5.1) additional two centrifugations of the ethyleneglycolic supernatant (to obtain smaller particles) and mixing the remaining supernatant with a new aqueous HAp suspension (instead of pure water). Ga@HAp6 was made by the regular ultrasonic dispersion (Section 3.2.5.1) but using a 5 times lower amount of Ga and without separating the smaller Ga particles from the bigger by centrifugation. Ga@HAp32 was obtained by the regular ultrasonic dispersion method when HAp by reflux instead of sonochemical HAp was used. Ga/OA@HAp nanocomposite was created by ultrasonic dispersion and mixing of Ga/OA NPs with HAp in THF.

Ga/OA NPs were created by the thermal decomposition method as described in ref. [165]. 10$\times$ upscale of the synthesis was done and the synthesis was repeated twice from the same mixture of reactants. This mixture was prepared by weighing 1.100 g of $Ga_2(NMe_2)_6$ in a glovebox filled with N_2, dissolving it in 50 mL of water-free di-N-octylamine in a N_2 atmosphere on a Schlenk line and adding 82.5 mL of water-free octadecene in a N_2 atmosphere on a Schlenk line. Water (and other volatile impurities) was removed from di-

N-octylamine and octadecene by vacuum distillation on the Schlenk line. In the thermal decomposition procedure, 70 mL of water-free octadecene were heated on sand to 290 °C and then the reaction mixture (with room T) was quickly added, which decreased the temperature to 240 °C. The hot sand was substituted with a salty ice bath within 1 minute to immediately decrease the temperature below 200 °C and stop the thermal decomposition. The flask and the ice bath were further cooled with liquid nitrogen to reach the room temperature as soon as possible. The obtained brown suspension was then cleaned of precursors by repeated centrifugation and resuspension in a chloroform-oleic acid-ethanol mixture as described in ref. [165]. Thus, Ga/OA NPs in chloroform were obtained. They were centrifuged at $6300 \times g$ and the sediment was resuspended in tetrahydrofuran. The Ga/OA@HAp nanocomposite was then created by ultrasonicating (5 minutes of 2-s pulses with 1s breaks, 80 % amplitude) and mixing (5 hours in a sealed bottle) the suspension of Ga/OA NPs in THF (∼2.5 mg in 15 mL) with a HAp suspension in THF (50 mg in 50 mL). The final nanocomposite powder was obtained by centrifugation at $6300 \times g$ and -9 °C, resuspending in 2-propanol, another centrifugation at $6300 \times g$ and -9 °C, resuspending in 2-propanol and drying in a fume hood.

3.2.6 Synthesis of Ag@HAp nanocomposite

The nanocomposite of silver nanoparticles and hydroxyapatite (Ag@HAp) was created by the reduction of $AgNO_3$ with $NaBH_4$ in the presence of hydroxyapatite [339]. 30 mg of $AgNO_3$ were dissolved in 50 mL of water and mixed with 50 mL of an aqueous suspension of hydroxyapatite (70 mg). Then, 50 mL of an aqueous solution containing 80 mg of $NaBH_4$ were added and the mixing continued for 10 minutes. After this time, the suspension was centrifuged; the sediment was re-suspended in water, centrifuged again, re-suspended in ethanol and dried. The molar amount of $AgNO_3$ was the same as the molar amount of Ga in the Ga@HAp nanocomposite, so that 1 gram of Ag@HAp nanocomposite contained roughly the same chemical amount of antibacterial component (2 mmol of nanoparticles per g of composite) as 1 gram of the Ga@HAp nanocomposite. The 2 mmol/g (24 wt %) content of Ag in the Ag@HAp was confirmed by the ICP-AES analysis.

3.2.7 Synthesis of functionalized Ga/Au core/shell nanoparticles on hydroxyapatite

Ga/Au@HAp nanocomposite (without functionalisation) was created from the Ga@HAp16 nanocomposite by mixing the ethyleneglycolic supernatant (30 mL) after the 15-min centrifugation at -9 °C and $5500 \times g$ (see Section 3.2.5.1) with a cold aqueous solution (120 mL) of $HAuCl_4$ (40 mg) for 10 hours at 263–273 K. A centrifugation at $6300 \times g$ and 0 °C followed to sediment the Ga/Au@HAp nanocomposite, which was then washed with 2-propanol and dried in a fume hood at room T.

Ga/Au/Arg@HAp was created in a similar way, but a $HAuCl_4$ (40 mg)+arginine (50 mg) aqueous solution was used instead of only the $HAuCl_4$ solution. This solution was prepared by dissolving $HAuCl_4$ in 100 mL of water, titration with 0.1 M NaOH to pH 7, addition of 10 mL of arginine solution and filling with water to 120 mL.

Ga/Arg/Au/Arg@HAp was synthesised by the following procedure. 50 mg of liquid Ga were ultrasonicated for 15 min in 50 mL of solution of arginine (200 mg) in ethylene glycol with pulses of 2s duration, 1s breaks and 80 % amplitude. Then 50 mL of suspension of HAp (80 mg) in ethylene glycol were added and the suspension was further ultrasonicated with the same pulses for 1 hour. In the last 15 minutes of the sonication, the condenser was substituted with a pipe, connected to a rotary pump that created about 1 mbar pressure inside the reaction vessel. Under these conditions, the suspension was cooled to about 0

°C. 50 mL of the resulting Ga/Arg@HAp suspension were mixed at 0 °C with 200 mL of cold aqueous solution of $HAuCl_4$ (70 mg)+arginine (100 mg), pre-titrated with 1 M NaOH to pH 7. The final Ga/Arg/Au/Arg@HAp nanocomposite powder was obtained after a 15-min centrifugation at $6300 \times g$ and 0 °C, washing with 2-propanol and drying in a fume hood at room T.

3.3 Characterization Methods

3.3.1 X-ray diffraction (XRD) analysis

X-ray diffraction patterns in Figures 4.9 (c), 4.11, 4.21 (a) and 4.31 (a, b) were measured with an Empyrean X-ray diffractometer, from 4 to 70° (or 10 to 90°) with 100 s steps of 0.013° and Cu anode. Bruker AXS D4 Endeavor X-ray diffractometer was used for obtaining all the other XRD patterns with measurements from 2 to 70°, using 3 s steps of 0.02° and Cu anode.

3.3.1.1 Determination of Ca/P ratio in HAp

Ca/P ratio of HAp was determined by a quantitative XRD method based on the conversion of CDHA to biphasic mixture of HAp and β-TCP during calcination above 700 °C. In this method, the sample is calcined at 1000 °C for 15 h, after which its XRD is recorded and quantitative XRD analysis based on integration of particular peaks is conducted [283].

If $w_{TCP} < 80\%$, the following ratio of peak areas is taken (Eq. (3.1)):

$$\frac{I_{HAp(211)}}{I_{TCP(0210)}} \approx \frac{A_1 \cdot w_{HAp}}{B_1 - w_{HAp}} \tag{3.1}$$

If $w_{TCP} > 80\%$, the HAp 211 peak is too weak, so the 210 peak is used instead (Eq. (3.2)):

$$\frac{I_{TCP(0210)}}{I_{HAp(210)}} \approx \frac{A_2 \cdot w_{TCP}}{B_2 - w_{TCP}} \tag{3.2}$$

The constants A_1, A_2, B_1 and B_2 are obtained by a calibration curve of different standard stoichiometric HAp+β-TCP mixtures. Raynaud *et al.* obtained the following values [283]: $A_1 = 0.93 \pm 0.03$, $B_1 = 95.8 \pm 1.2$, $A_2 = 5.45 \pm 0.18$ and $B_2 = 92.7 \pm 0.5$. $w_{TCP} = 100 - w_{HAp}$ in % is then calculated from Eq. (3.1) or (3.2) and its value (in %) is used for the calculation of the Ca/P ratio according to Eq. (3.3):

$$\frac{Ca}{P} = \frac{\frac{10 \cdot (100 - w_{TCP})}{M_{HAp}} + \frac{3 \cdot w_{TCP}}{M_{TCP}}}{\frac{6 \cdot (100 - w_{TCP})}{M_{HAp}} + \frac{2 \cdot w_{TCP}}{M_{TCP}}}, \tag{3.3}$$

where $M_{HAp} = 1004.64$ and $M_{TCP} = 310.18$.

3.3.1.2 Estimation of crystallinity of HAp and HAp(Ga)

The percentage of crystallinity of HAp is usually determined from the ratio of the crystalline peak areas between 25° and 36° and the area of the amorphous hump of ACP at 2θ (29–31° [359]. However, the amorphous hump is difficult to fit and can appear also at larger 2θ values, depending on the chemical composition and preparation of ACP, so that it overlaps with the crystalline HAp peaks [261]. Thus, the % crystallinity was rather determined as the ratio of the crystalline peak areas and the whole area between 25° and 36° (Eq. (3.4)):

$$\%\ \text{crystallinity} = \frac{A(peaks)}{A(peaks + background)} \tag{3.4}$$

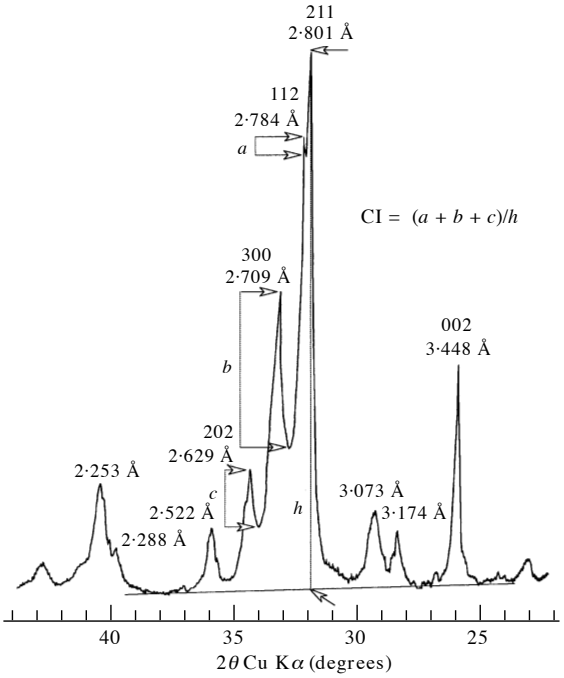


Figure 3.5: Determination of crystallinity index (CI) from the X-ray diffractogram of hydroxyapatite [361].

The degree of crystallinity X_C was determined from the height of the (300) peak (h_{300}) and the valley between the (300) and (112) peaks ($h_{112/300}$) [360] (Eq. (3.5)):

$$X_C = 1 - \frac{h_{112/300}}{h_{300}}. \tag{3.5}$$

The crystallinity index (CI) was determined from the heights of the peaks (211), (300), (112) and (202), and the valleys in between [361] (Eq. (3.6), see Figure 3.5 for a graphical explanation):

$$CI = \frac{h_{112} - h_{112/211} + h_{300} - h300/112 + h_{202} - h_{202/300}}{h_{211}}, \tag{3.6}$$

where h_{211}, h_{112}, h_{300} and h_{202} are the heights of the peaks and $h_{112/211}$, $h_{300/112}$ and $h_{202/300}$ the heights of the valleys in between.

3.3.1.3 Au crystallite size determination

Generally, broadening of XRD peaks due to small crystallite size is described by the Scherrer equation (Eq. (3.7)), which enables estimation of the crystallite size L from the width of the XRD maxima:

$$L = \frac{K_S \lambda}{B_{size} \cdot \cos\theta}, \tag{3.7}$$

where B_{size} is integral breadth (i.e., peak area/peak height ratio) in radians and K_S the so-called Scherrer constant or shaping factor, as its value depends on the shape of the crystallites and the definition of L[362]. For a cubic crystal with cube edge dimension L $K_S = 6h^3/[(h^2 + k^2 + l^2)^{1/2} \cdot (6h^2 - 2(k + l)h + kl)]$, where the indices h, k and l are to be interpreted as $|h|$, $|k|$ and $|l|$, and as arranged in the order $h \geq k \geq l$ [363]. B_{size} was

determined by fitting a pseudo-Voigt profile in the Highscore Plus Panalytical program and assuming the Lorentzian part as the size broadening [364] (Eq. (3.8)):

$$B_{size} = B_{Lorentz}(observed) - B_{Lorentz}(instrumental) \tag{3.8}$$

The default instrumental broadening in the program was used.

3.3.1.4 High-temperature XRD

In order to determine the thermal stability and phase composition after heating, the samples were heated up to 1200 °C inside an Empyrean X-ray diffractometer. A temperature program was set up so that an XRD measurement was made at room temperature, after which the sample was heated to 600 °C, held at this temperature for 30 minutes and measured. After the XRD measurement, the sample was further heated and measured in the same way after 30 minutes of calcination at 800 °C, 1000 °C, 1100 °C and 1200 °C. XRD patterns were measured from 10 to 90° with 100-s steps of 0.013°.

3.3.2 Spectroscopic investigations

3.3.2.1 Fourier-Transform Infrared Spectroscopy

FTIR analyses were performed on a Perkin Elmer Spectrum 400 MIR spectrophotometer in the DRIFT technique for a sample diluted with 70 mg of KBr. For white samples, such as HAp(Ga) and HAp, 5 mg of sample were used, whereas for non-white samples, such as Ga@HAp or Au/Arg@HAp(Ga) as well as their reference HAp, 2 mg of sample were used instead.

The splitting factor (SF) was determined by the method of Weiner and Bar-Yosef [365], which measures the heights of the absorption bands at 565 and 605 cm^{-1} and the height of the minimum trough between the split peaks [366]. The calculation is expressed in Eq. (3.9):

$$SF = \frac{h_{565} + h_{605}}{h_{590}} \tag{3.9}$$

The method of the SF measurement is also presented graphically in Figure 3.6. The carbonate content from the IR spectrum was expressed as a C/P ratio, calculated by Eq. (3.10) from the heights of the CO_3^{2-} band at 1422 cm^{-1} and the PO_4^{3-} band at 1035 cm^{-1} [366]:

$$C/P = h_{1415}/h_{1035} \tag{3.10}$$

The way the heights are determined is shown in Figure C.1.

3.3.2.2 Nuclear magnetic resonance

Solid-state magic angle spinning (MAS) NMR experiments were performed using a 3.2-mm Varian HX MAS probe on a narrow-bore 600-MHz (14.1 T) Varian NMR system, operating at a ^{1}H Larmor frequency of 599.54 MHz and a ^{31}P Larmor frequency of 242.69 MHz. The ^{1}H and ^{31}P chemical shifts were reported relative to the signals of tetramethylsilane and H_3PO_4, respectively. A sample spinning frequency of 20 kHz was used for all the experiments. The ^{31}P MAS spectra were recorded with a 90° excitation pulse of 1.8 μs and a single scan. A two-dimensional ^{1}H-^{31}P CP-HETCOR spectrum was obtained by first exciting the protons with a 90° pulse having a duration of 2.3 μs and letting the proton magnetization evolve in the absence of homo- and heteronuclear decoupling, after which the magnetization was transferred to the phosphorous nuclei with a 500-μs cross-polarization (CP) contact time. The number of increments along the indirectly detected

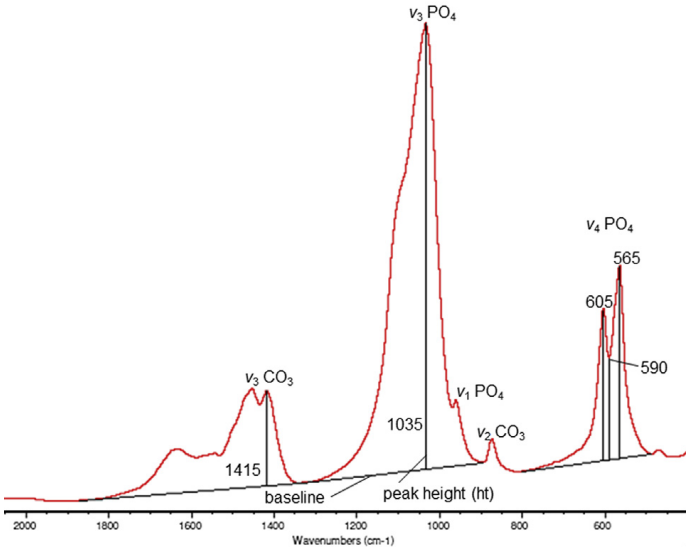


Figure 3.6: Determination of splitting factor (SF) and C/P ratio from the IR spectrum of hydroxyapatite[366].

dimension was 200, with each increment being measured with 128 scans and a repetition delay of 5 s.

^{1}H magic-angle spinning (MAS) NMR spectra were recorded on a 600 MHz (14.1 T) Varian NMR system using a 3.2 mm Varian HX MAS probe. A ^{1}H Larmor frequency of 599.54 MHz was reported relative to the proton signal of tetramethylsilane. A rotation-synchronized Hahn-echo pulse sequence was used with 90° and 180° pulse widths of 2.3 μs and 4.6 μs, respectively. The sample rotation frequency was 20 kHz, the repetition delay between consecutive scans was 30 s, and the number of scans was 4.

3.3.2.3 UV-VIS spectroscopy

For the UV-VIS spectroscopy a UV-Vis-NIR Spectrophotometer Shimadzu UV-3600 was used. For calculating the theoretical UV-VIS spectra of Ga and Au NPs, a MATLAB program (The Metal Nanoparticle (MNP) simulator) created by Guido Goldoni was used. It is based on the MATLAB programs written by Christian Mätzler [367] using the Mie scattering theory [368]. More details about the Mie theory are given in Appendix A. For the spectra of the core-shell NPs, i.e., Ga/Au and Au/Arg NPs, the MNP simulator was modified to use the MATLAB programs for a coated sphere, written by Christian Mätzler [367] using the Aden-Kerkel model [369]. The optical constants used for Ga and Au are given in Appendix. For Arg, a constant real refractive index of 1.664 was assumed [370].

3.3.3 Microscopy

3.3.3.1 Transmission electron microscopy

Transmission electron microscopy was done on a JEM2100 microscope with a LaB_6 electron source and Cu TEM grids with lacey carbon. The simulated electron diffraction patterns were calculated by the EMS software using parameters of the hexagonal P6/m hydroxyapatite (PDF number 01-089-6438) crystal structure and several Ga, Ga_2O_3 and GaOOH structures from the database. The size distribution of nanoparticles was determined by particle counting and measurement of their diameters based on the TEM images.

Histograms were then fitted with a Gaussian or a log-normal curve to obtain the most frequent (mode) size and the width of the size distribution. Polydispersity was calculated as the ratio between the standard deviation and the median of the size distribution [371], [372], expressed in %.

3.3.3.2 Scanning electron microscopy

Scanning electron microscopy was performed on a FEG SEM 7600F. The samples were dried on an Au-sputtered 100-nm hydrophilic polycarbonate isopore membrane filter (Merck Millipore VCTP02500), stuck on the carbon tape and coated with 5 nm of carbon before the analysis.

In order to observe the bacterial morphology under a scanning electron microscope, the bacterial cells had to be fixed, dehydrated and dried in a critical point dryer [373], [374]. 3 % glutaraldehyde in Millonig phosphate buffer (MPB) was used as a fixative. See Section 3.1.2 for details about MPB. Bacterial suspension after the microdilution antibiogram (all parallel samples were joined together to obtain a larger amount of bacteria in case of Ga@HAp or HAp(Ga)) was centrifuged at 1500×g, after which nearly all supernatant (growth medium) was removed and substituted with the fixative. After resuspending the bacteria in the fixative, a 100-nm hydrophilic polycarbonate isopore membrane filter (Merck Millipore VCTP02500) was added into the suspension and the samples were left in the refrigerator overnight. Next day, the bacteria collected on the membrane filter were dehydrated by moving the membrane gradually from the phosphate buffered to the pure ethanol media: MPB, MPB, MPB, 10 % ethanol in sterile water, 20 % ethanol in sterile water, 50 % ethanol in sterile water and 100 % ethanol. The membrane with bacteria was left for 15 minutes in each solution before moving it to the next one. Then the membrane was moved into a new 100 % ethanol medium for 1 hour before it was transferred to the critical point dryer (K850, Quorum Technologies). There the ethanol was substituted by liquid CO_2, which was led to supercritical conditions before it was removed. The membrane with the dried bacteria was stuck on the carbon tape and sputtered with 5 nm of Pt/Pd before the analysis.

3.3.3.3 Optical microscopy

Phase-contrast and fluorescence images were recorded on a Nikon Eclipse Ti-U inverted microscope. Excitation from 465 to 495 nm and emission from 515 to 555 nm were used for the green fluorescence images. Excitation from 532 to 587 nm and emission from 608 to 683 nm were used for the red fluorescence images.

3.3.4 Thermogravimetric (TG) and differential scanning calorimetry (DSC) analyses

Thermogravimetric analyses were performed on a Jupiter 449 simultaneous thermal analysis (STA) instrument coupled with a 403C Aëoloss mass spectrometer (MS) (Netzsch, Selb, Germany). The measurements were performed with a heating rate of 10 °C/min in an Ar atmosphere using a TG/DSC sample holder.

3.3.5 Specific surface area determination

The specific surface area was measured with the Brunauer–Emmett–Teller (BET) method using the Micromeritics Gemini II 2370 nitrogen-adsorption apparatus (Norcross, GA).

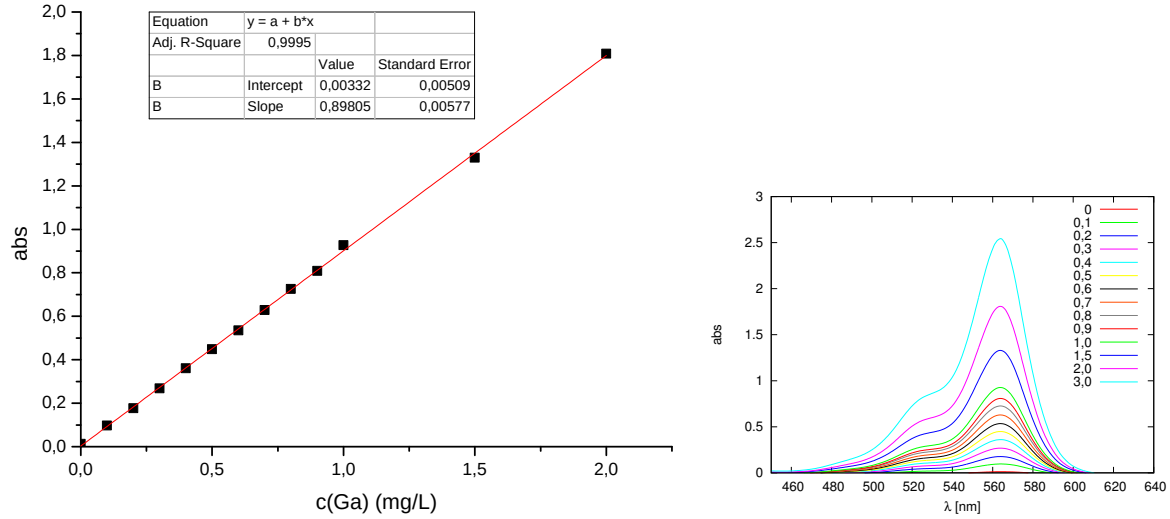


Figure 3.7: Calibration line of external standards for the $GaCl_4^-$–Rhodamine B spectrophotometric method (left) and the absorption spectra of the standards with well distinct maximum at 564 nm (right).

3.3.6 Metal content determination

3.3.6.1 Quantitative determination of Ga in the HAp(Ga) and Ga@HAp samples

The amount of Ga in the diluted sample was determined by a spectrophotometric method based on the absorbance of the $GaCl_4^-$–Rhodamine B complex [375], [376]. The complex was formed in 4 mL of NaCl-saturated sample solution with 0.1 wt % of Rhodamine B and extracted to 4 mL of benzene. The standards for a calibration curve from 0.1 to 2 mg/L Ga concentrations (see Figure 3.7) were obtained by dissolving a measured mass of Ga in aqua regia, evaporating to dryness and dissolving the obtained white powder in 6 M HCl. To determine the amount of Ga in the dried samples, 6 mg of a powder sample were dissolved in 6 mL of 6 M HCl and diluted 100–200 times with 6 M HCl. For the determination of the Ga concentration in the solutions from the ion-release study, 200 μL of solution were mixed with NaCl and 200 μL of 37 % HCl and diluted to 4 mL with 6 M HCl and the Rhodamine B solution. The concentration of Ga^{3+} in the liquids of the ion-release study was determined by first mixing equal volumes (100-200 μL) of the liquid and concentrated (37 %) HCl, supersaturating with NaCl and then diluting with 6 M HCl and the Rhodamine B solution to a volume of 4 mL and extracting to 4 mL of benzene.

3.3.6.2 Quantitative determination of Ga, Au and Ag in the other samples

Ga and Au content in the Au/Arg@HAp and Au/Arg@HAp(Ga) samples as well as Ag content in the Ag@HAp nanocomposite were determined by inductively coupled plasma atomic emission spectroscopy (ICP-AES).

3.3.7 *In-vitro* release of Ga^{3+} ions

3.3.7.1 Method for *in-vitro* release of Ga(III) from HAp(Ga)

3.3.7.1.1 Static ageing of HAp(Ga)IE16 in PBS, MH and LB media 5 mg of HAp(Ga)IE16 were suspended in 5 mL of medium (PBS, MH or LB) and the 1 g/L

suspension was subjected to linear shaking at 60 rpm and 37 °C in a shaking water bath (Memmert, WNB7–45, Germany) for a certain period of time (1, 2, 3, 4, 5 or 6 days), after which the sample was removed from the water bath and centrifuged at 6300×g for 15 min. The supernatant after this centrifugation was further centrifuged at 15348×g for 15 min and the final supernatant was analysed for the concentration of Ga^{3+} ions (by the procedure described in Section 3.3.6.1). The average values and standard errors for each ageing time were calculated from three parallel samples.

3.3.7.1.2 Ion release from HAp(Ga)CP, HAp(Ga)TR and HAp(Ga)IE16 in LB

The investigation of the release of Ga^{3+} ions from the HAp(Ga) was performed at pH 7.4 using a Miller Luria-Bertani (LB) medium. A total of 10 mg of each sample (HAp(Ga)CP, HAp(Ga)TR or HAp(Ga)IE) were dispersed in 10 mL of LB medium. The dynamic conditions (60 rpm) and constant temperature (37 °C) were ensured by the use of a shaking water bath (Memmert, WNB7–45, Germany). The three Ga(III)-containing materials were aged in simulated physiological conditions by constant shaking at 60 rpm and 37 °C for a period of 10 days. The total release of the Ga^{3+} ions was monitored during the ageing. A 1-mL aliquot of the liquid containing the released Ga^{3+} ions was taken out every two days and replaced with 1ml of fresh LB medium. The aliquot was then centrifuged at 15348×g for 15 min and the supernatant was analysed for the concentration of Ga^{3+} ions. The concentration of the released Ga^{3+} ions was measured using complexometric quantitative analysis (Section 3.3.6.1). The investigations were performed in three parallel measurements. Since a portion of the medium was substituted by fresh medium every 2 days, the concentrations were recalculated to account for the dilution using equation (3.11):

$$c^*(after\,2n\,days) = (\frac{10}{9})^{n-1} \cdot c_{2n}(measured). \tag{3.11}$$

Thus, if the Ga release stopped we would have a constant line instead of a descending line. Since the three materials contained different amounts of Ga, the amount of released Ga was also converted into the fraction of contained Ga using equation (3.12):

$$\frac{released\,Ga^{3+}}{contained\,Ga^{3+}} = \frac{c_{2n} \cdot V + \sum_{k=0}^{n-1}(c_{2k} \cdot V_a)}{w_{Ga} \cdot m}, \tag{3.12}$$

where V_a = 1 mL, V=10 mL and c are the measured concentrations.

3.3.7.2 Method for *in-vitro* release of Ga(III) from Ga@HAp

A 0.2 g/L and a 0.5 g/L suspension of Ga@HAp in Mueller-Hinton broth and 0.5 g/L suspensions of the same material in 0.9 % NaCl and PBS were prepared. All suspensions were orbitally shaken for 24 hours at 37 °C and 237 rpm. Then, the samples were centrifuged at 5500 × g for 15 minutes and the supernatants were further centrifuged at 9400 × g for 15 minutes, after which the supernatants were filtered through a 0.1 μm filter. Concentration of Ga^{3+} in the filtered liquids was determined by the spectrophotometric method (Section 3.3.6.1). The gallium content in the Ga@HAp before suspending in the media was also determined and the ratio of released/contained Ga was calculated as $\frac{m(Ga)released}{m(Ga)contained}[\%] = \frac{c(Ga)released}{w(Ga)\cdot c(Ga@HAp)}$. Thus, an average and standard deviation of this value was calculated from 3 parallel samples and 6 parallel samples in the case of the Mueller-Hinton medium (due to two different concentrations of Ga@HAp).

3.3.8 Antibacterial tests

All materials that underwent antibacterial tests were sterilised after weighing by adding a droplet of 2-propanol and drying inside a laminar flow cabinet under UV light.

3.3.8.1 Disc diffusion antibiogram

An overnight culture of *P. aeruginosa*, *E. coli* or *S. epidermidis* was grown in the LB medium at 37 °C and 237 rpm orbital shaking in a H1 Hybrid Multi-mode Microplate Reader (Synergy) until the end of the logarithmic phase (OD600≈1 or approx. 10^9 cfu/mL). Then it was diluted 100× with 0.9 % NaCl and 50 μL of the diluted culture were spread onto a Mueller-Hinton (MH) agar plate with a Drigalski spatula or a sterile swab to obtain a semi-confluent growth of bacteria. Then a disc with 6-mm (or 8-mm) diameter of the dried material sample (20 mg), which was made by pressing the material powder at 5 kN (2 kN for the Ga@HAp and Ga/Au@HAp materials), was put onto the MH agar plate with bacteria. The plate with the inoculum and the material disc was incubated for 24 h at 37 °C. Phase-contrast images were recorded on a Nikon Eclipse Ti-U inverted microscope.

3.3.8.2 Microdilution antibiogram

An overnight culture of *P. aeruginosa* (MW1 or PAO1) or *E. coli* was diluted 1000× with MH broth to obtain a concentration of 10^6 cfu/mL (between $2{\cdot}10^5$ and 10^6 cfu/mL) of bacterial culture. The dried material was suspended in MH broth and different dilutions were made in this medium from the stock suspension. Similarly, $Ga(NO_3)_3 \cdot 5.5\,H_2O$ was dissolved in the MH broth and filtered through a 0.1 μm filter, after which different dilutions were made with the sterile MH broth from the stock solution. 100 μL of the suspension (or solution) were mixed with 100 μL of bacterial culture in a microtiter well and the flat-bottom Brand 96-well plate was incubated with 237 rpm orbital shaking for 24 hours in a H1 Hybrid Multi-mode Microplate Reader (Synergy) while monitoring the absorbance (optical density) at 600 nm (OD600). Thus, the growth curves for all samples were obtained and compared for the determination of the minimal inhibitory concentration (MIC). To eliminate the influence of the absorption by the materials, the starting values of OD600 were subtracted from all the measurements and the absorbances of the corresponding sterile samples were subtracted from the signal of the samples with bacteria. An arithmetic average and standard deviation were calculated from 4 parallel samples for each OD600 value. To determine the bacterial concentration in the samples with OD600=0 after 24-hour growth, the liquids above the materials were diluted 1000× and 50 μL of each liquid was spread onto a new MH agar plate and incubated for 24 h at 37 °C, after which the number of grown colonies was counted. For the antibacterial action assay of the released Ga^{3+} ions, the filter-sterilized liquids were mixed in different ratios with an overnight culture of *P. aeruginosa* MW1 and Mueller-Hinton broth, so that the bacterial concentration in the samples was $5{\cdot}10^5$ cfu/mL. Then, a microdilution antibiogram was performed in the same way as for the material suspensions and $Ga(NO_3)_3$. The average OD600 values and standard deviations were calculated from 4 parallel samples.

3.3.8.3 BacLight Live/Dead bacterial survivability assay

The survivability of the bacteria after incubation with the material was analysed using a fluorescent dye live/dead assay, where SYTO 9 (green) and propidium iodide (red) fluorescence dyes were used for the staining. SYTO 9 permeates the cell membrane and binds to the nucleic acids of both the dead and live cells, while propidium iodide is impermeable to intact membranes, penetrates only the damaged membranes and binds to the nucleic acids of the dead bacteria [377]. Equal amounts of both fluorescent dyes were mixed and 1 μL of the mixture was added to 330 μL of bacterial suspension. The bacterial suspensions exposed to the Ga@HAp nanocomposite were pre-concentrated by centrifugation as they contained a much lower number of bacteria due to the inhibition of growth.

3.3.9 *In vitro* cytocompatibility tests

3.3.9.1 Cell viability by MTT test

Cytotoxicity of the materials was tested on human fetal lung fibroblasts IMR-90 (ECCAC no. 85020204) and mouse fibroblasts L929 (ECCAC no. 85103115), which were grown in MEM supplemented with 10 % fetal bovine serum, 2 mM L-glutamine, 100 units of penicillin and 100 μg of streptomycin per mL at 37 ^{o}C in a humidified 5 % CO_2 atmosphere. McCoy's 5A medium was used instead of MEM and 1.5 mM instead of 2 mM glutamine in case of the U2OS cells. Ten thousand cells per well were seeded on a 96-well plate and grown overnight, then the growth medium was replaced with fresh medium containing dispersed particles and incubated for 24h. To determine the remaining cell viability, growth medium was replaced with fresh medium containing 0.5 mg/mL 3-(4,5-dimethylthiazol-2-yl)-2,5-diphenyltetrazolium bromide (MTT) for two hours. The formed formazan crystals were solubilized in DMSO and transferred to a new transparent 96-well plate, where the absorbance at 570 nm was measured. Cell viability (%) was determined as the absorbance ratio between cells grown in the presence and absence of the materials. The average values and standard deviations were calculated from 6 parallel samples.

3.3.9.2 Measurement of generation of reactive oxygen species (ROS)

L929 cells were grown in a 12-well plate overnight, after which the medium was replaced with a fresh medium containing HAp (0.1 or 0.5 g/L concentration), Ga@HAp (0.1 or 0.5 g/L) or Ag@HAp (0.1 g/L) and a 16-hour incubation followed. As a positive control, a known ROS inducer menadione [378] was used at 75 μM concentration for 1h. After the incubation, the cells were washed with warm PBS and incubated with 5 μM CM-H2DCFDA (Thermo Fisher) in PBS for 15 minutes, followed by immediate FACS analysis using Ex/Em = 488/515-545 nm on a FACSCalubur flow cytometer (BD Biosciences). The chloromethyl group of the dye reacts with intracellular glutathione and other thiols, and the subsequent oxidation yields a fluorescent product. The fluorescence intensity plots were analysed using CellQuest acquisition software (BD Biosciences) and the mean fluorescence was determined. The average value of the mean fluorescence and its standard deviation were then calculated from 3 repetitions. The difference in the signals of the samples was statistically evaluated by a two-tailed Student's t test. The null hypothesis was that the ROS signal of the two compared samples was equal and this hypothesis was rejected if the probability $p<0.05$. In that case, the two samples were considered significantly different, otherwise their difference was not significant.

Chapter 4

Results

4.1 Hydroxyapatite

The common constituent (bioactive template) of all further presented materials is hydroxyapatite, which has also been used as a biocompatible and non-antimicrobial reference throughout my doctoral work. Its general characteristics have already been presented in Section 1.5.1, but here I will present my characterisation of this particular hydroxyapatite reference (synthesis details in Section 3.2.1) and some new discoveries regarding its synthesis that are important for its use as a constituent/precursor of the later developed materials.

4.1.1 Characterisation

Since the chosen synthesis method (relying on the thermal degradation of urea) precipitates the HAp at low pH (pH increases from 4.5 to 6.5 during ultrasonication and further to around 7 during OCP–HAp transformation), a Ca/P ratio <1.67 is expected. On the other hand, urea is also a source of carbonate ions, which can increase the Ca/P ratio by substituting the phosphate ions. Hence, I have investigated the thermal transformation of this HAp upon calcination at 1000 °C and determined the Ca/P ratio by the quantitative XRD method (described in Section 3.3.1). The HAp transformed into a mixture of β-TCP and HAp, which indicates its Ca deficiency, and the Ca/P ratio from the quantitative XRD was ∼1.54. A similar Ca/P (around 1.55) has been obtained by the EDS analysis as well. However, the reference XRD pattern that matched the powder pattern of the experimentally prepared hydroxyapatite in this work most strongly was hydroxyapatite with a reference code 01-089-6438, chemical formula $Ca_{9.868}(PO_4)_{5.586}(OH)_{4.006}$ (Ca/P=1.77) and cell parameters a = b = 9.4394 Å, c = 6.8861 Å (for indexed XRD pattern see Figure B.1 in the Appendix). Moreover, two stoichiometric hydroxyapatite references with formula $Ca_5(PO_4)_3(OH)$ and cell parameters a = b = 9.4320 Å, c = 6.8810 Å (PDF numbers 01-072-1243 and 01-073-0293) also matched the experimental XRD pattern very well and two other stoichiometric hydroxyapatite references with formula $Ca_{10}(PO_4)_6(OH)_2$ and cell parameters a = b = 9.4240 Å, c = 6.8790 Å (PDF numbers 01-074-0565 and 01-074-0566) as well. On the other hand, for the Ca-deficient HAp XRD reference patterns from the database as well as refined structures of Ca-deficient and non-stoichiometric carbonated hydroxyapatites from the literature [279], [379], [380], [381], the match was not as good as for the aforementioned reference patterns.

TEM and SAED analysis (Figure 4.1) has confirmed the crystallinity and the submicrometre lath/plate morphology with a typical elongation in the 001 crystallographic direction (see Section 1.5.1, Figures 1.16 and 1.17).

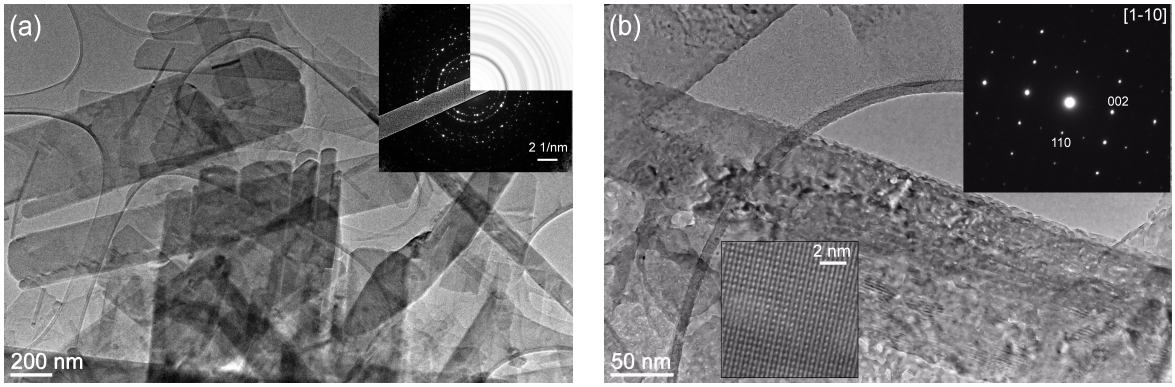


Figure 4.1: Structural and morphological characteristics of the hydroxyapatite reference: (a) TEM image of several laths crossed one over another and laterally joining into plates, with SAED (ring pattern and simulated pattern) inset top right; (b) TEM image of a HAp lath in [1-10] zone with a SAED spot pattern inset top right and a high magnification inset bottom left revealing crystal unit cells.

4.1.2 Synthesis optimisation

Although the established synthesis of hydroxyapatite is simple and gives fairly homogeneous sub-micrometer-sized HAp laths with desired biochemical characteristics, I have tried to make improvements to the hydroxyapatite synthesis since I have experienced several drawbacks during the preparations of many different modified hydroxyapatite materials. The standard synthesis has the following weak points:

1. the 19.5-hour synthesis (4.5-hour sonication+15-hour ageing) yields only about 150 mg of hydroxyapatite, which is enough for two nanocomposite/doped hydroxyapatite samples;

2. the long (4.5-hour) sonication in water erodes the Ti-Al-V tip, which contaminates the sample with Ti microparticles;

3. one Ti6-Al4-V tip (price 60 $) can be used only for one synthesis or for max. 4 syntheses if it is re-polished before each new synthesis (the polishing procedure lasts 3 hours minimally);

4. the long sonication at 80-90 °C is damaging to the machine (ultrasonicator) and can lead to more and more frequent overloads;

4.1.2.1 Synthesis upscale

First, I tried to upscale the synthesis by doubling the amount of reactants and thus their concentrations as well. However, this resulted in an unfinished conversion of OCP to HAp (Figure 4.2 (a)). Probably a longer synthesis time would be required to obtain only HAp. Hence, I have tried to double the volume as well so that the concentrations of reactants stayed the same. With this upscale the only obtained product was hydroxyapatite (Figure 4.2 (b)) and the amount of the product was twice the amount of the regular synthesis. Then I have also checked if the morphology has been retained by the upscale. A comparison of SEM images of the standard synthesis and the upscaled synthesis is presented in Figure 4.3. We can see that the morphology of HAp is not changed by the upscale. The 2X upscale reaches the maximal volume with the available ultrasonic equipment and for larger upscale a larger Suslick flask and a larger ultrasonic horn would be required.

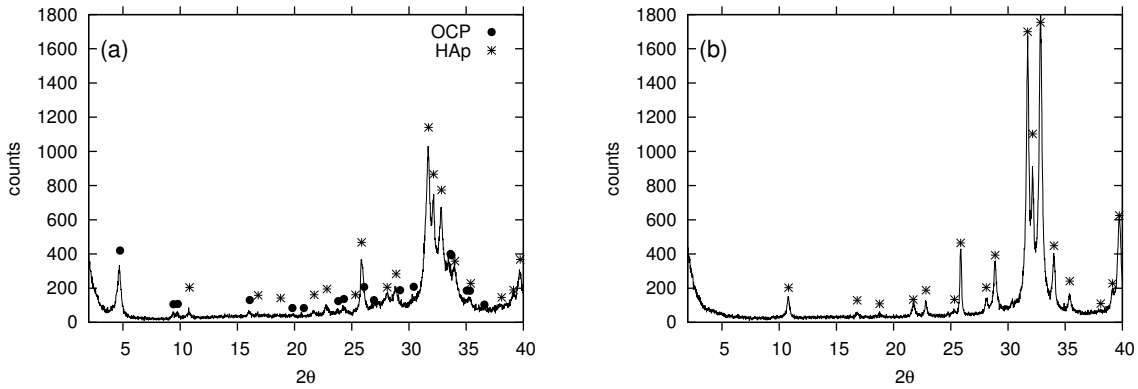


Figure 4.2: XRD patterns of products after two different scale-up approaches to the synthesis of HAp: (a) doubling the concentration of the reagents and (b) doubling the masses as well as the volume to keep the same concentrations. Peaks identified by the HAp reference (PDF number 01-089-6438) are marked with an asterisk (∗), whereas peaks identified with octacalcium phosphate reference (PDF number 01-079-0423) are marked with black circles (•).

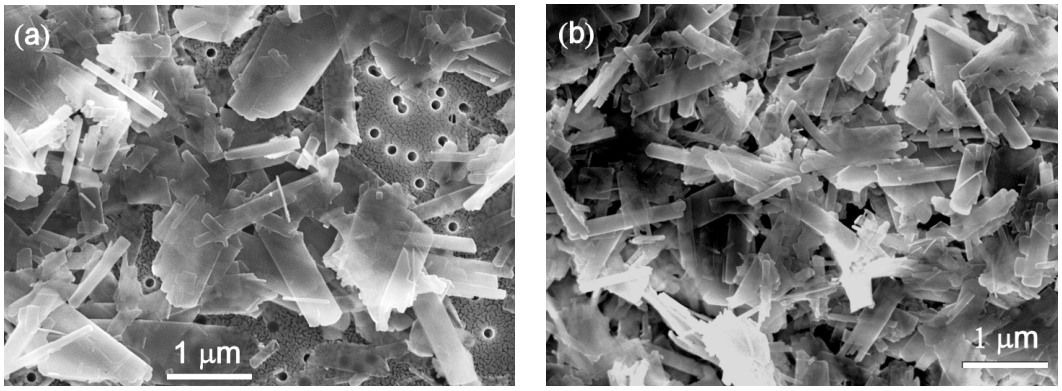


Figure 4.3: Morphology of HAp by (a) upscaled synthesis (2× volume at the same concentrations) and (b) the usual synthesis.

4.1.2.2 Ti contamination

No material has been found yet which could sustain the cavitation and extreme conditions at the collapse of the bubbles. That is why the tip of the titanium horn is eroded during the synthesis (Figure 4.4), especially in the aqueous media. Although the tip is replaceable



Figure 4.4: Erosion of Ti tip (source: Sonics & materials [382]).

and the Ti6-Al4-V a biocompatible alloy, it presents a contamination of the sample. Such a contamination is well evident. The HAp sample is grey instead of white (Figure 4.5 (a)), the Ti6-Al4-V microparticles can be seen on the sample under SEM (Figure 4.5 (b)) and Ti peaks are observed in the XRD pattern (Figure 4.6). I have noticed that the grey part of

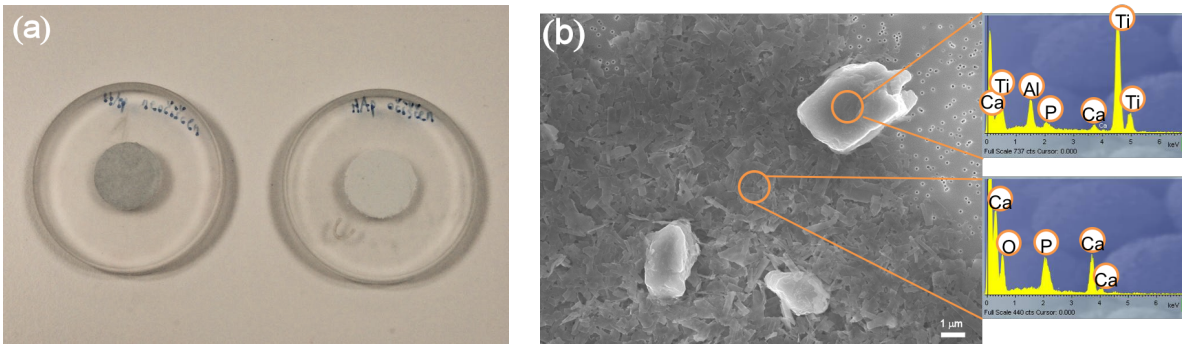


Figure 4.5: Contamination of HAp with Ti. (a) Due to the presence of Ti, hydroxyapatite powder gets a greyish colour. On the left the Ti-contaminated HAp is shown and on the right the whiter powder after the cleaning procedure; (b) SEM picture of Ti6-Al4-V microparticles on hydroxyapatite with EDS analysis confirming their Ti and Al content.

the sample (containing more Ti, see Figure 4.5 (a)) sedimented sooner than the white part (HAp) during the centrifugation. This difference was further enhanced in a more viscous medium, such as ethylene glycol. It has turned out that the HAp suspension in ethylene glycol was very stable during centrifugation. Thus, I have found a way to separate the Ti6-Al4-V microparticles from the HAp particles by centrifugation in EG. HAp was then sedimented from the supernatant simply by mixing it with water. I have noticed though that some ethylene glycol can stay attached to hydroxyapatite and can be seen in the FTIR spectrum. However, two additional washings with water are enough to get rid of the remaining ethylene glycol to such extent that it is not seen in the FTIR spectrum. The cleaned HAp powder is white (Figure 4.5) and exhibits no Ti phase in the XRD (Figure 4.6 left). I have also checked the sediment after washing it with 1M HCl, water, ethanol and drying. It clearly exhibited Ti peaks in the XRD (Figure 4.6 right) and I have also weighed the amount of Ti. HAp was contaminated with 12 mg of Ti during one synthesis, which agreed very well with the weight loss of the Ti tip during the synthesis.

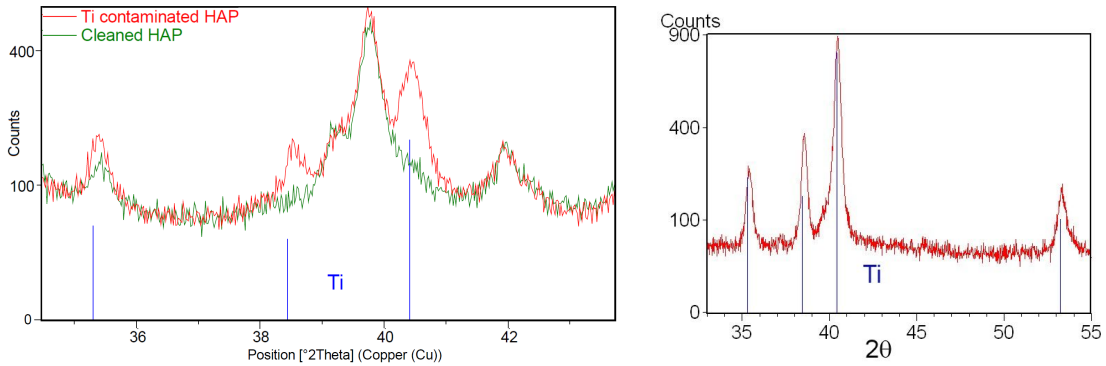


Figure 4.6: Removal of Ti from HAp. *Left:* XRD pattern of HAp before (red) and after (green) removal of Ti6-Al4-V microparticles showing the disappearance of the Ti phase; *Right:* XRD pattern of the Ti in the sediment after centrifugation.

4.1.2.3 Avoiding long ultrasonication

I further explored the possibility of completely avoiding the ultrasonication. Moreover, it is known that the conversion of ACP/OCP precursor to HAp is enhanced at boiling conditions [383], which cannot be achieved at the sonochemical synthesis as it is dangerous to the ultrasonic machine. Thus, I have investigated the synthesis of hydroxyapatite by precipitation under reflux at 100 °C. The products were pure HAp according to the XRD analysis, also after only 3 hours and without additional ageing (Figure 4.7). However, the

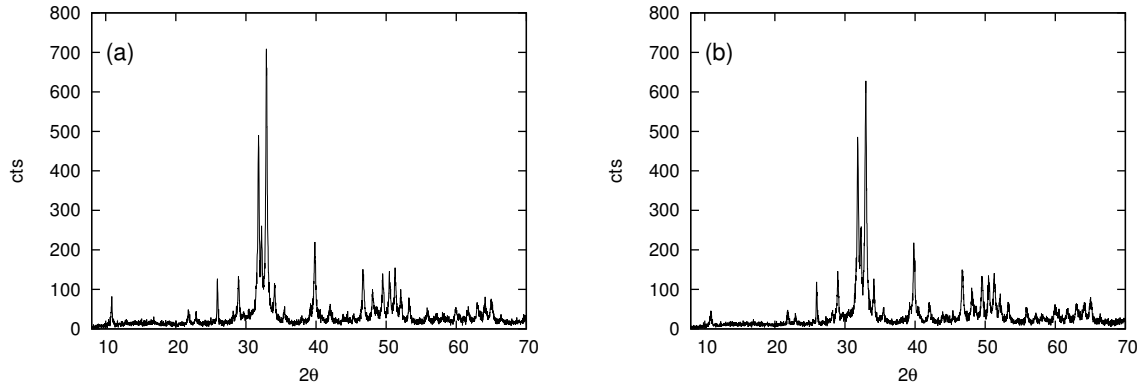


Figure 4.7: XRD patterns of hydroxyapatite by (a) 3-hour precipitation under reflux at 100 °C+15-min ultrasonication and (b) precipitation under 3-hour ultrasonication at 80 °C+15-hour ageing.

SEM analysis has revealed their slightly different morphology than that of the HAp laths prepared by ultrasonication (Figure 4.8). The HAp laths without sonication are longer and have sharper (cut) edges in comparison with the sonochemically prepared HAp laths, which exhibit rounder and torn edges and like to join by their side edges into a plate-like morphology. Hence, I have tried an additional 15-min (22.5-min lasting) ultrasonication immediately after the synthesis. As can be seen in Figure 4.8 (comparison of c and d), this was sufficient to break the long HAp laths into shorter ones and bring their morphology very close to the one of the sonochemically prepared HAp (comparison of Figure 4.8 e and f). Upscale of the synthesis without sonication is easy and a 5× upscale has been achieved

even with the additional 15-minute ultrasonication. These results show that the role of

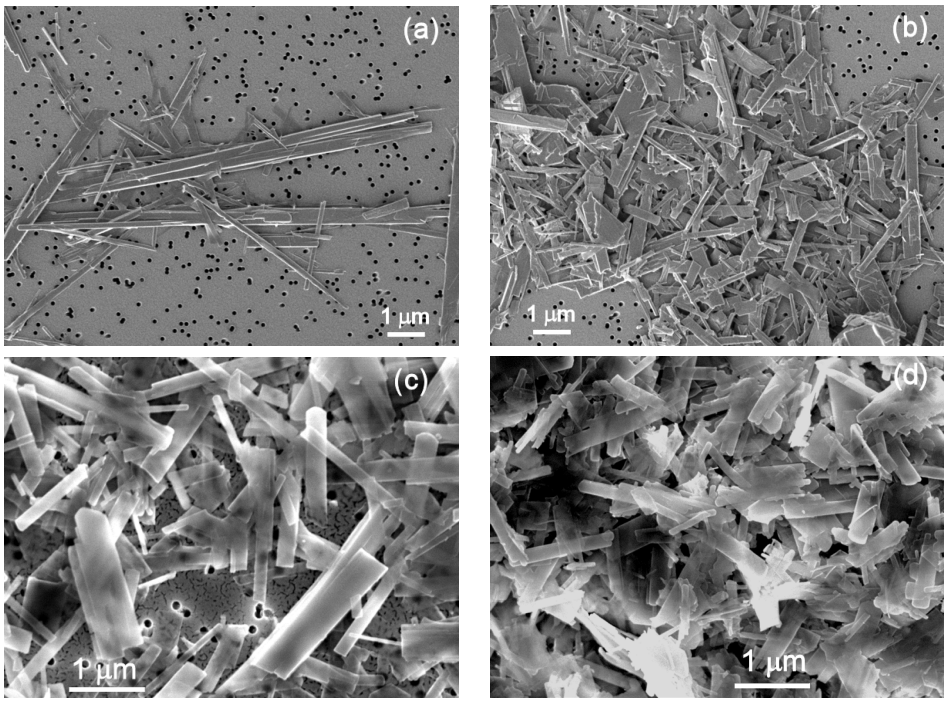


Figure 4.8: Comparison of HAp prepared by different methods: a) 3-hour precipitation at 100 °C in a flask under reflux; b), c) 3-hour precipitation at 100 °C under reflux and additional 15-min ultrasonication; d) regular sonochemical synthesis.

ultrasonication in the synthesis of hydroxyapatite is mainly in providing good mixing and affecting the morphology. Nevertheless, the 2× upscaled sonochemical synthesis was mostly used in preparation of modified hydroxyapatite materials throughout my doctoral work. As we shall see further on, this method was actually required to obtain certain HAp(Ga) and Ga@HAp materials. The samples derived from the 5× upscaled synthesis by the 3-hour precipitation and boiling under reflux+15-min ultrasonication will be explicitly specified.

4.2 Incorporation of Ga(III) into Hydroxyapatite

Most of the results presented in this section were published in our article about HAp(Ga) (see ref. [324]).

4.2.1 Analysis of phase composition, thermal and surface properties

The investigation of Ga(III) incorporation into the HAp began on the ion exchange by mixing the HAp with an aqueous solution of $Ga(NO_3)_3$ (see experimental details in Section 3.2.2). Ga(III) content in hydroxyapatite steadily increases for the first 10 hours and then slows down, so at least 24 hours of mixing are required to achieve the final Ga(III) content in the HAp(Ga) (Figure 4.9 (a)). It is interesting that the remaining solution after mixing

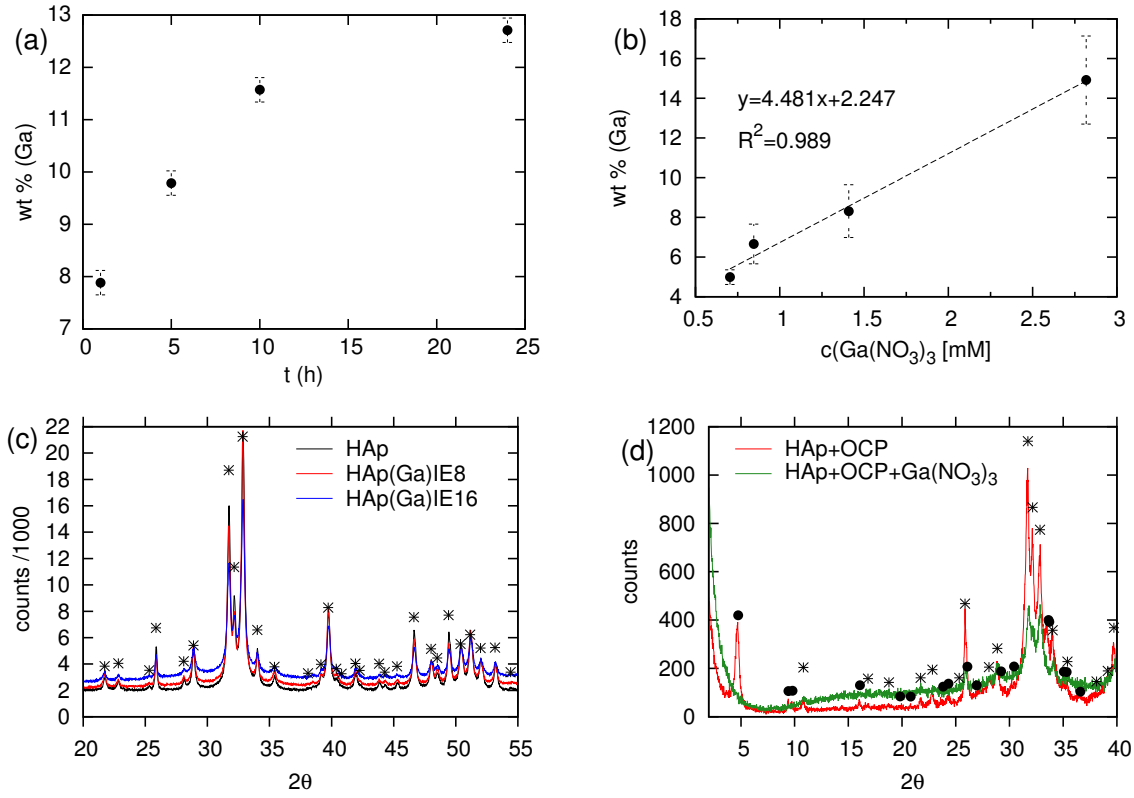


Figure 4.9: Addition of Ga(III) to HAp. (a) Amount of Ga in the HAp(Ga)IE material vs time of mixing with $Ga(NO_3)_3$; (b) Relation of the final Ga content to the concentration of $Ga(NO_3)_3$ used in the ion-exchange incorporation; (c) XRD patterns of HAp(Ga)IE materials with two different Ga(III) contents in comparison with pure HAp; (d) Disappearance of the OCP phase after mixing with $Ga(NO_3)_3$ as observed by the XRD analysis. Black circles (•) represent the OCP reference pattern (PDF number 00-026-1056) and asterisks (∗) represent the HAp reference pattern (01-089-6438).

contained virtually no (≤1 mg/L) Ga^{3+} ions, even though not all Ga(III) was incorporated into HAp at this concentration, which indicates that some amount of $Ga(NO_3)_3$ salt might have been adsorbed to the HAp and washed away during washing or adsorbed to the beaker used for mixing [326]. Different concentrations of $Ga(NO_3)_3$ resulted in different Ga(III) contents of HAp(Ga)IE and a linear fit for the Ga(III) content vs $Ga(NO_3)_3$ concentration dependence appeared very good in the studied concentration range (Figure 4.9 (b)). The

Ga(III) incorporation was first explored by the X-ray diffraction. No changes in the unit cell (no shift in the XRD patterns) were observed, only the background is increasing with the increasing Ga(III) content and the intensity of the HAp peaks is decreasing (Figure 4.9 (c)). When a HAp+OCP material instead of pure HAp was mixed with $Ga(NO_3)_3$, a disappearance of the OCP phase after mixing with $Ga(NO_3)_3$ was additionally observed (Figure 4.9 (d)). Since OCP is a HAp precursor phase during its synthesis, the addition of $Ga(NO_3)_3$ at different stages of the HAp synthesis was also further investigated. Thus, HAp(Ga) materials obtained during the co-precipitation (HAp(Ga)CP), transformation (HAp(Ga)TR) and ion exchange (HAp(Ga)IE) will be further compared using pure hydroxyapatite without any Ga^{3+} ions (HAp) as a reference. Since the addition of $Ga(NO_3)_3$ during the formation of HAp can result in precipitation of amorphous $GaPO_4$ (see Section 1.4.1), this species was also additionally prepared (see experimental details in Section 3.2.2). Figure 4.10 shows the XRD pattern of the prepared amorphous $GaPO_4$. The XRD

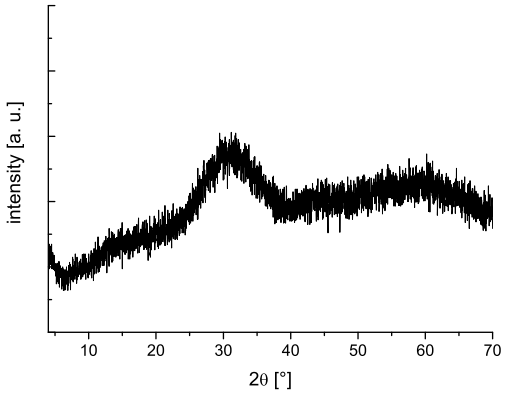


Figure 4.10: X-ray diffraction pattern of the amorphous gallium phosphate hydrate.

analysis (Figure 4.11) showed that all three investigated Ga(III)-containing apatites contained only one crystalline phase that was identified as hexagonal hydroxyapatite (reference PDF number 01-089-6438). In comparison with HAp, HAp(Ga)TR and HAp(Ga)IE, the diffraction maxima of the HAp(Ga)CP are much broader. This can either be an indication of a reduced crystallite size due to the influence of the Ga^{3+} ions on the growth of apatite crystals or a consequence of a change in the apatite structure by the incorporation of Ga^{3+} ions (Section 1.5.2.2). Crystallinity of the samples was compared by the methods of the XRD analysis relying on the separation of the HAp peaks between 30 and 35° 2θ or on the peaks/background ratio between 25° and 36° (see details in Section 3.3.1). The degree of crystallinity X_c and the crystallinity index were roughly the same for HAp, HAp(Ga)TR and HAp(Ga)IE. By contrast, the percentage of crystallinity exhibited a decreasing trend in the order HAp, HAp(Ga)TR, HAp(Ga)IE (Table 4.1). This implies that the crystallinity of the hydroxyapatite did not change after doping with Ga^{3+} and that HAp(Ga)IE might contain an extra amorphous phase. These parameters could not be extracted from the XRD pattern of HAp(Ga)CP due to high broadness of the peaks, yet four HAp peaks ((002), (112), (211), (300)) could still be well recognised. As indicated in Table 4.2, the chemical analysis confirmed the presence of Ga in all three apatites processed in the presence of Ga^{3+} ions. For comparison with HAp(Ga)TR and HAp(Ga)CP the HAp(Ga)IE with 16 wt % of Ga was mostly used, while the results from the other HAp(Ga)IE materials, when given, are always additionally marked with their Ga content to avoid any confusion. Thus, the amount of Ga(III) in the HAp(Ga)TR sample was four times lower

Table 4.1: Crystallinity determined from the XRD patterns. Details about calculation of these three quantities are given in Section 3.3.1.2.

sample	X_c [%] [360]	Crystallinity index [361]	% crystallinity
HAp	60	0.8	24
HAp(Ga)TR	58	0.8	22
HAp(Ga)IE16	62	1.0	18

than in HAp(Ga)IE, while the Ga(III) content in the HAp(Ga)CP sample was five times lower than in the HAp(Ga)IE. The influence of the Ga component on the structure of the apatites was analysed indirectly by an investigation of the materials' thermal stability and the changes in their surface properties. DSC and HT XRD analyses were used to monitor the decomposition and phase transformation of the Ga(III)-containing and pure apatites (Figures 4.11 and 4.12). The pure HAp went through the typical transformations of hydroxyapatite: loss of adsorbed water at 200 °C, loss of structural water at 600 °C, transformation of HAp into β-TCP at 800 °C, transformation of β-TCP to α-TCP at 1100 °C and conversion of α-TCP to α'-TCP at 1400 °C (Figure 2 a and Table 4.2) [266], [282], [284], [285]. The high-temperature (HT) XRD analysis of the pure hydroxyapatite confirmed its transformation to β-TCP above 800 °C and the further transformation of β-TCP to α-TCP above 1100 °C, so that at 1200 °C both HAp and α-TCP were present (Figure 4.11 a). On the other hand, in the case of the Ga(III)-containing apatites the transformation went from apatite to Ga(III)-doped β-TCP (β-TCP(Ga)). The HAp(Ga)CP exhibited the lowest thermal stability and it started transforming into β-TCP(Ga) already at 600 °C. The XRD maxima of the formed β-TCP(Ga) phase remained low and broad, even at higher temperatures (Figure 4.11 b). This and the DSC curve provide evidence that the HAp(Ga)CP sample is not ACP. Crystallisation of ACP is an exothermal process, which is manifested in a DTA/DSC curve as an exothermic peak between 500 and 700 °C [261], [384], [385]. During this process, ACP can be converted to a low-temperature α-TCP very similar to the phase that is otherwise stable only above 1100 °C [261], [384], [385]. Hence, the absence of any exothermic peaks in the DSC and no α-TCP in the HT XRD of HAp(Ga)CP are evidence of nanocrystallinity, rather than low crystallinity for this sample. While the conversion of HAp(Ga)CP and HAp(Ga)TR with 3–4 wt % of Ga into β-TCP(Ga) was almost quantitative, with a very small amount of Ga_2O_3 appearing above 1000 °C, HAp(Ga)IE with 16 wt % of Ga yielded one more phase at 800 °C, i.e., $GaPO_4$, which degraded into Ga_2O_3 above 1100 °C (Figure 4.11 c, d). We also observed that Ga-doped β-TCP, which is apparently more thermally stable than the non-doped β-TCP, does not convert to α-TCP and remained stable at 1200 °C. Above this temperature, in the systems with a smaller content of Ga^{3+} (HAp(Ga)CP and HAp(Ga)TR), the β-TCP(Ga) phase transforms into another phase (a sharp maximum at 1400 °C, Fig. 4.12 b,c). This event was not observed for the system with the highest content of Ga^{3+} (HAp(Ga)IE16, Fig. 2d). It seems that the high content of Ga^{3+} ions kept the thermal stability of the β-TCP(Ga) phase in the HAp(Ga)IE system and prevented its transformation into another phase, even at 1400 °C.

According to the TGA (Figure 4.12) we observed a larger mass loss for all three HAp(Ga) than for the pure HAp reference. The main loss occurred up to 550 °C, which is the region assigned to the loss of adsorbed and structural water [386]. Further mass loss is usually attributed to the release of CO_3^{2-} from the apatite as CO_2 [276], [279], [387]. It was interesting to observe the differences in the water loss among the Ga(III)-

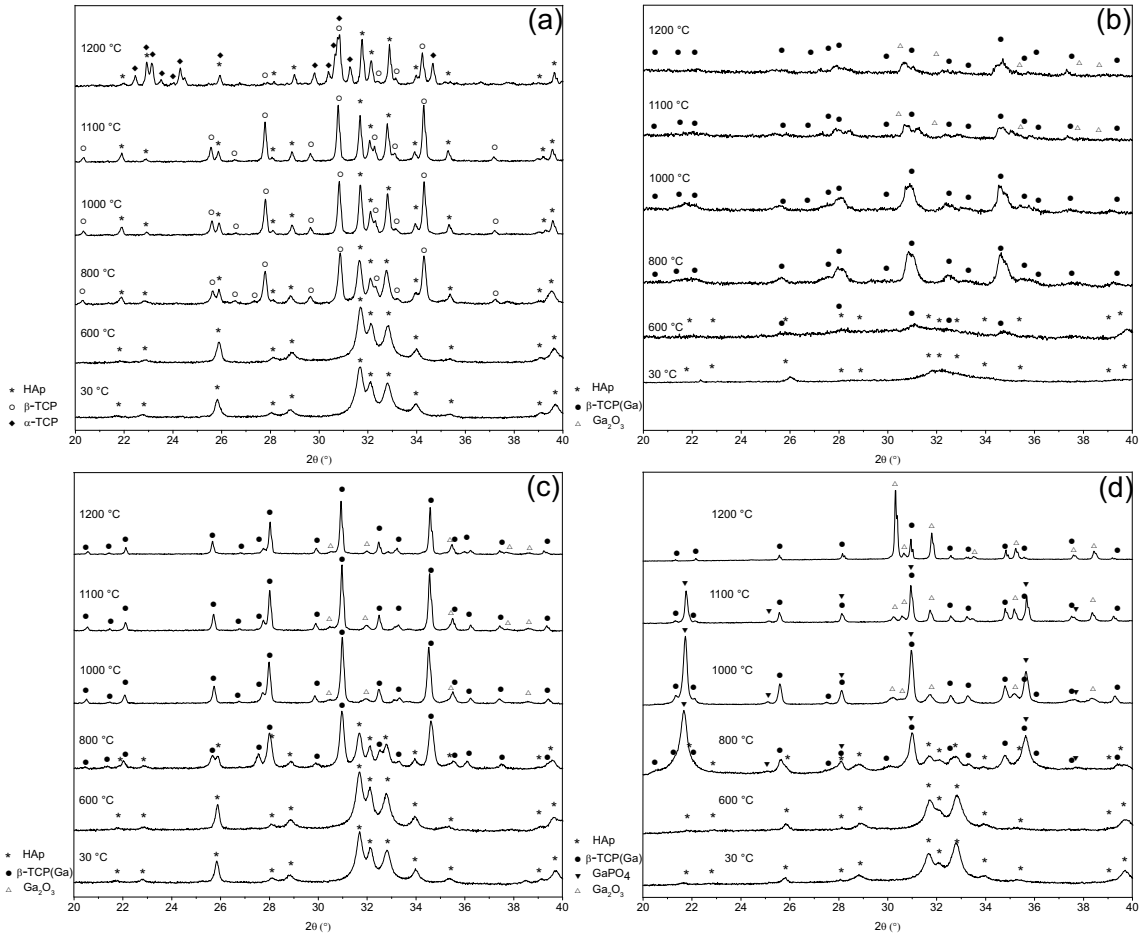


Figure 4.11: X-ray diffractograms of (a) HAp and HAp(Ga) obtained by (b) co-precipitation (c) transformation and (d) ion exchange (16 wt % Ga) at 30 °C, 600 °C, 800 °C, 1000 °C, 1100 °C and 1200 °C. Asterisks (∗) indicate peaks from HAp, empty circles (○) peaks from β-TCP, black diamonds (♦) peaks from α-TCP, black circles (●) peaks from Ga(III)-doped β-TCP, white triangles (△) peaks from Ga_2O_3 and black triangles (▼) peaks from $GaPO_4$. Figure published in ref. [324].

containing apatites. HAp(Ga)CP and HAp(Ga)IE exhibited a much larger mass loss than HAp(Ga)TR. They both contained about 7.5 % of adsorbed water (mass loss below 200 °C), but HAp(Ga)CP contained more structural water (5 % vs. 2.5 % mass loss between 200 and 550 °C).

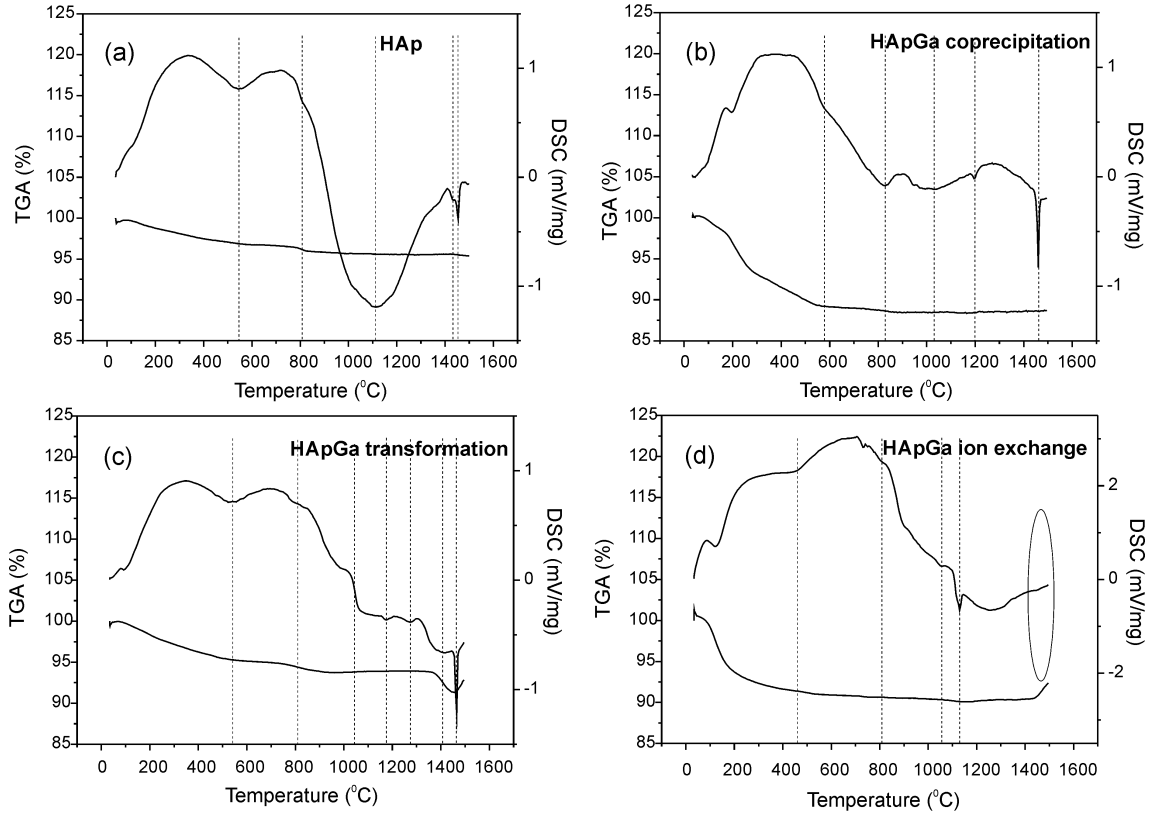


Figure 4.12: Thermal characteristics (TGA and DSC curves) of (a) HAp and HAp(Ga) obtained by (b) co-precipitation, (c) transformation and (d) ion exchange (16 wt % Ga). Figure published in ref. [324].

The investigation of the surface properties revealed an increased specific surface area for all three Ga(III)-containing apatites in comparison with the pure HAp reference (Table 4.2). This information explains the increased content of adsorbed water within these materials. The change was the most pronounced in the case of the HAp(Ga)CP material that had an eight times higher specific surface area than the pure HAp reference. On the other hand, the HAp(Ga)TR and HAp(Ga)IE had approximately two times larger specific surface areas in comparison with the pure HAp.

4.2.2 Morphological characteristics

Morphologically, the systems obtained by co-precipitation, transformation and ion exchange of apatite with Ga^{3+} ions show different characteristics (Figures 4.13 and 4.14). As expected, after the ion exchange of apatite with Ga^{3+} ions, its morphology of submicrometre-sized laths that join into plate-like structures, which is characteristic for sonochemically obtained apatite (see Sections 1.5.1 and 4.1), remained unchanged (Figures 4.13 e,f and 4.14 a). However, when apatite was co-precipitated with Ga^{3+} ions, the morphology of the obtained particles was changed into nanolaths with 30-nm lengths and 10-nm widths (Figure 4.13 a,b). The morphology of the HAp(Ga)TR was between these two cases

Table 4.2: Composition, surface and thermal characteristics of HAp and HAp(Ga) obtained by co-precipitation (CP), transformation (TR) and ion exchange (IE). The standard deviations were calculated from three batches (repeated syntheses) of each sample. Table published in ref. [324].

Sample	Ga content [wt %]	Specific surface area (BET) [m^2/g]	Phase transitions (TGA)				
			HAp→ β-TCP	HAp(Ga)→ β-TCP(Ga)	TCP $\beta \rightarrow \alpha$	TCP $\alpha \rightarrow \alpha'$	β-TCP(Ga) transf.
HAp	0	24±3	800 °C	-	1130 °C	1455 °C	-
HAp(Ga)CP	3.0±0.1	160±15	-	600 °C	-	-	1460 °C
HAp(Ga)TR	4.0±0.1	54±6	-	800 °C	-	-	1465 °C
HAp(Ga)IE	15±2	45±5	-	800 °C	-	-	-
	8.0±0.5	42±5					

and mainly contained sub-micrometre plate-like structures (Figures 4.13 c,d and 4.14 b). The results confirm the contribution of the Ga^{3+} ions to both stages that are significant for the synthesis of apatite crystals – the stage that includes the formation of the crystals and the next stage associated with the crystal growth and phase (OCP-HAp) transformation. EDS analyses (Figures 4.13 and 4.14) confirmed the presence of gallium and its uniform distribution (variation of 1 EDS wt %) throughout all three samples. Ga remained present all over the HAp even after washing with water for 6 times. The Ga EDS signal (EDS wt %) increased in the HAp(Ga)CP, HAp(Ga)TR, HAp(Ga)IE order and the Ca/P ratio of EDS signals decreased accordingly, which implies a substitution of Ca by Ga. The SAED analysis (Figures 4.13 b,d,f and 4.14) confirmed that the obtained Ga(III)-containing apatite laths are locally crystalline structures similar to the pure HAp reference (confront Figure 4.1) and did not reveal any distortion that could be assigned to the incorporation of the Ga^{3+} ions into the crystal lattice of the apatite. Similarly, well-ordered unit cells were observed under TEM at high magnifications for the systems obtained by transformation and ion exchange (Figure 4.13 d,f). These analyses revealed well-ordered, defect-free structures for the Ga(III)-containing lath/plate-like particles with preferential growth along the 001 crystallographic direction. There were, however, two differences with respect to the pure HAp TEM images. The crystalline structures of Ga(III)-containing apatites were coated with a few nm thick amorphous layer (Figure 4.15) and darker nanocircles/spots (with diameters around 2 nm) were seen on their surface (Figure 4.15). They were darker and more densely present on HAp(Ga)IE than on HAp(Ga)TR. However, their very small size and the extremely high sensitivity of HAp to electron beam prevented a local EDS on them, while the EDS analyses on the parts containing a larger number of spots did not reveal any higher Ga signal.

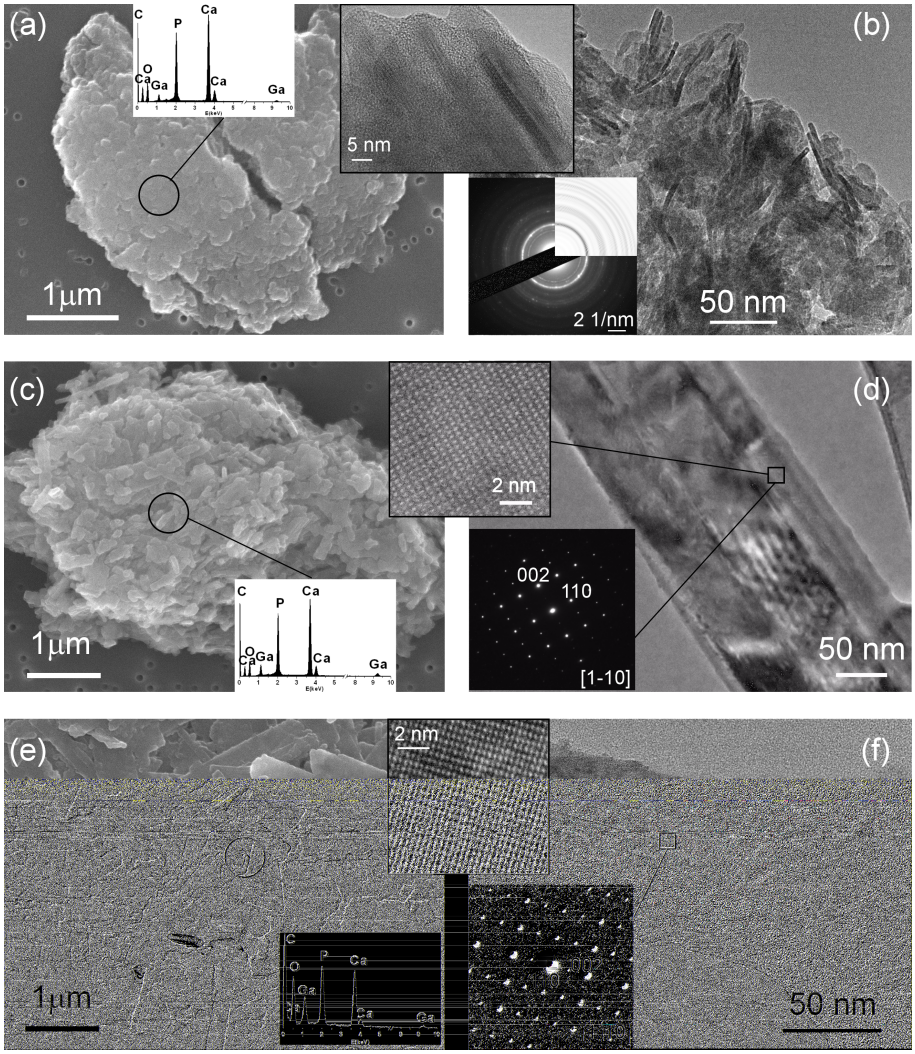


Figure 4.13: Morphological characteristics of HAp(Ga) materials obtained by co-precipitation (a, b), transformation (c, d) and ion exchange (e, f). Inset graphs in the left-hand (SEM) images are the SEM EDS analyses of the corresponding materials. Insets in the right-hand images are (b) ring electron-diffraction pattern with simulated hydroxyapatite pattern (white background) in the top-right quarter for the HAp(Ga)CP; (d, f) high-magnification TEM images and spot electron-diffraction patterns for the HAp(Ga)TR and HAp(Ga)IE materials. Figure published in ref. [324].

Figure 4.14: Electron microscopy analysis of HAp(Ga)IE and HAp(Ga)TR. (a) TEM image, SAED ring pattern (top left inset) and EDS analysis (bottom left inset) of HAp(Ga)IE16; (b) TEM image, SAED ring pattern (top left inset) and EDS analysis (top right inset) of HAp(Ga)TR. The small quarter insets (white background) in the SAED patterns are the simulated HAp electron ring di raction patterns.

Figure 4.15: Locating Ga(III) in HAp(Ga) by TEM. (a) High magni cation TEM image of HAp exhibiting a crystalline core and a thin amorphous surface layer; (b) high magni - cation TEM image of HAp(Ga)IE6 exhibiting a crystalline core and a thicker amorphous surface layer. Bottom: TEM images exhibiting darker nanocircles on the surface of (c) HAp(Ga)IE8 and (d) HAp(Ga)TR.

4.3 Functionalized Gold Nanoparticles on Ga(III)-Containing Hydroxyapatite

The HAp(Ga) materials were combined with Au/Arg functionalised NPs to obtain Au/Arg@HAp(Ga) nanocomposites. Most of the results presented in this section have also been published in our article about the Au/Arg@HAp(Ga) nanocomposite (see ref. [353]). Au/Arg NPs were created in the HAp(Ga) suspension by sonochemical reduction of $HAuCl_4$ in the presence of arginine (see Section 3.2.4 for experimental details). The primary reference for these nanocomposites were the Au/Arg@HAp nanocomposites (without Ga(III) incorporation) that were developed in the doctoral work of my supervisor [68], [350]. The Au/Arg@HAp and Au/Arg@HAp(Ga) nanocomposites that are going to be presented and their designations, by which they will be referred further on, are given in Table 4.4. When I was repeating the synthesis of Au/Arg@HAp, I noticed that it was difficult to control the room temperature in the reaction mixture by an ice bath. The ice melted quickly and the temperature could then soon increase up to 60 °C, which demanded constant renewal of the ice to maintain the temperature below 40 °C. Thus, I decided to use a continuous flow of water for cooling instead and the temperature could be kept at 20 °C in a water-jacketed vessel without any problems. However, as evident from Table 4.4, the decreased temperature slowed down the reduction of $HAuCl_4$ to Au NPs, which indicates an important contribution of heating caused by the ultrasonic horn. Larger Au content was obtained by longer ultrasonication. On the other hand, the reduction proceeded very well on the HAp(Ga) materials even at 20 °C (Table 4.4). The Au/Arg@HAp(Ga) nano-

Table 4.4: Synthesis parameters and composition of different Au/Arg@HAp and Au/Arg@HAp(Ga) nanocomposites examined throughout the thesis.

Sample	Temperature [°C]	Sonication time [min]	Ga content (wt %)	Au content (wt %)
Au/Arg@HAp10	>40	30	0	10.4
Au/Arg@HAp6	20	30	0	6.2
Au/Arg@HAp9	20	40	0	8.6
Au/Arg@HAp14	20	60	0	14.1
Au/Arg@HAp(Ga)IE4	20	40	4.3	/
Au/Arg@HAp(Ga)IE8	20	40	8.0	15.5
Au/Arg@HAp(Ga)IE16	20	40	15.6	10.6
Au/Arg@HAp(Ga)TR	20	40	3.5	14.7

composite consists of two crystalline phases (Figure 4.21 (a)): hexagonal hydroxyapatite and face-centered cubic gold. The wide X-ray diffraction maxima for Au indicate small (nanodimensional) crystallite size (9.0 nm for the (111) peak, 3.5 nm for the (200) peak and 4.7 nm for the (220) peak were calculated by the Scherrer equation, see Section 3.3.1.3).

The functionalization of Au nanoparticles with arginine is evident in the FT-IR spectrum (Figure 4.21 (b)). Bands at 3568, 1418, 1089, 1035, 964, 917, 874, 601 and 563 cm^{-1} come from the hydroxyapatite [273], while bands at 3331, 3194, 2939, 2873, 1663, 1636, 1454, 1385 and 1352 cm^{-1} belong to the vibrations of the bonds in the arginine (see annotations in Figure 4.21 (b)). Another evidence for the nanogold as well as its functionalisation is a surface plasmon resonance (SPR) peak in the UV-VIS spectrum at 527 nm (Figure 4.21 (c)). A well distinct peak implies a narrow size distribution of Au nanoparticles. The SPR peak is slightly shifted towards higher wavelength, which might be due to the functionalisation with arginine. Indeed, calculations of the UV-VIS spec-

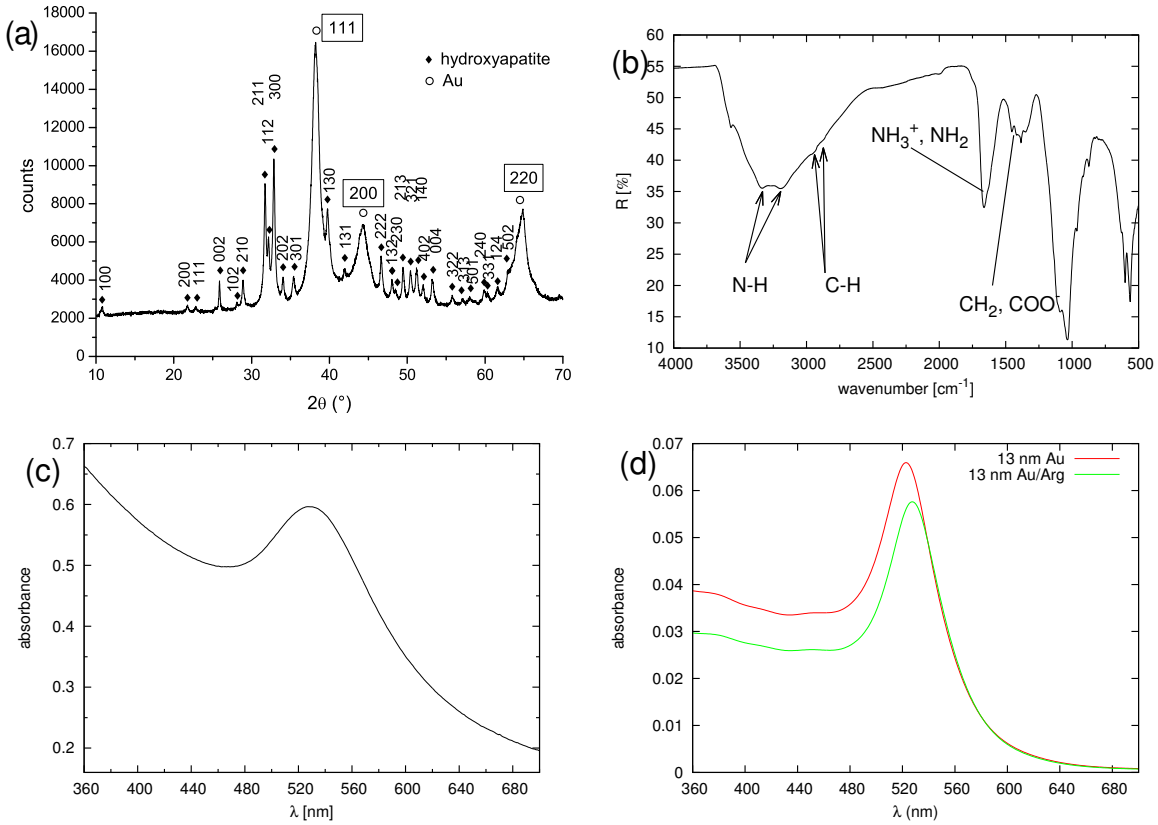


Figure 4.21: Characterisation of the Au/Arg@HAp(Ga)IE8 nanocomposite created from HAp(Ga)IE8: (a) X-ray diffractogram of the Au/Arg@HAp(Ga) nanocomposite; hkl indices for hydroxyapatite are vertical and rotated, while the indices for Au are horizontal and in rectangles; (b) FT-IR spectrum of the Au/Arg@HAp(Ga) nanocomposite; the bands that result from the arginine functionalization are marked on the graph; (c) UV-VIS spectrum of an aqueous suspension of the Au/Arg@HAp(Ga) nanocomposite; (d) calculated UV-VIS spectrum of 13-nm Au NPs and 13-nm Au NPs with a 0.8-nm thick Arg shell in water.

tra for spherical Au NPs with 13-nm diameter and Au/Arg core/shell NPs with a 13-nm core and a 0.8 nm shell (based on the length of an arginine molecule) have confirmed the slight red shift (from 523 to 527 nm) due to the amino acid attachment (Figure 4.21 (d)). An insight into the morphology of the Au/Arg@HAp(Ga)IE8 nanocomposite by electron

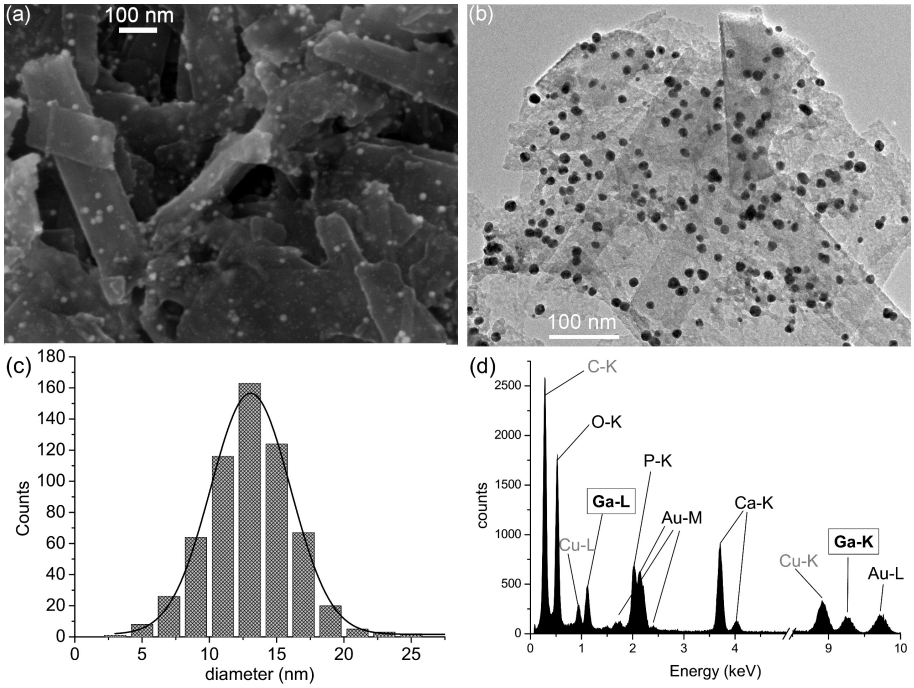


Figure 4.22: Electron microscopy characterization of the Au/Arg@HAp(Ga)IE nanocomposite created from HAp(Ga)IE8: (a) SEM, (b) TEM, (c) size distribution, based on 600 Au nanoparticles in a TEM image; (d) TEM EDS analysis. Figure published in ref. [353].

microscopy reveals that it consists of spherical gold nanoparticles that are attached to the hydroxyapatite lath/plate-like submicrometer-sized structures (Figure 4.22 a,b). The size distribution of the Au nanoparticles is narrow with the Gaussian fit yielding a 13±3 nm average size (Figure 4.22 (c)). The presence of Ga in the material was confirmed by the TEM EDXS analysis (Figure 4.22 (d)). A very similar morphology was observed for the Au/Arg@HAp(Ga)TR nanocomposite with the same mode size and slightly narrower size distribution of the Au NPs (13±2 nm, Figure 4.23). TEM investigation of Au/Arg NPs at high magnification (Figure 4.24) has confirmed their crystallinity. Moreover, it is clearly seen that the crystalline nanospheres are coated with a 0.8-nm thick, rather amorphous bright shell, which might be attributed to their functionalisation with arginine.

The morphology of the Au/Arg@HAp references is presented in Figure 4.25. It is similar to the morphology of the Au/Arg@HAp(Ga) but with slightly more irregularly shaped Au NPs that are less homogeneously distributed over the HAp laths. It seems that the increased specific surface area after Ga(III) incorporation enhances the reduction of Au as well as the attachment, separation and uniformity of Au/Arg NPs on the HAp.

Since higher temperature increased the yield of the sonochemical reaction, I have also investigated the synthesis of Au/Arg@HAp with regular stirring under reflux at 60 °C instead of ultrasonication. It yielded a similar morphology (spherical gold nanoparticles on the HAp submicrometer laths) under SEM, but a closer insight under TEM has revealed more coalesced Au NPs on the one hand and very small Au NPs on the other (Figure 4.25).

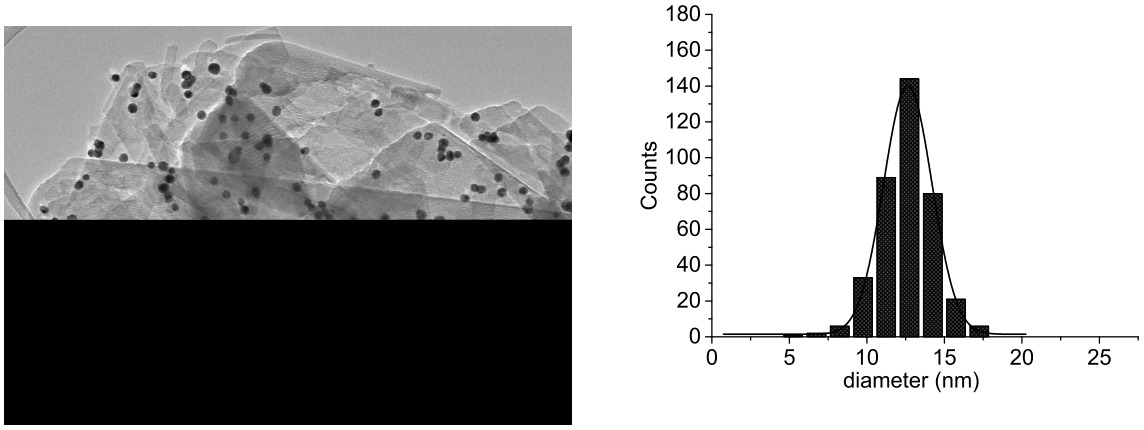


Figure 4.23: TEM image of the Au/Arg@HAp(Ga)TR (left) and size distribution (right) of Au/Arg NPs in it, based on 400 Au NPs in a TEM image.

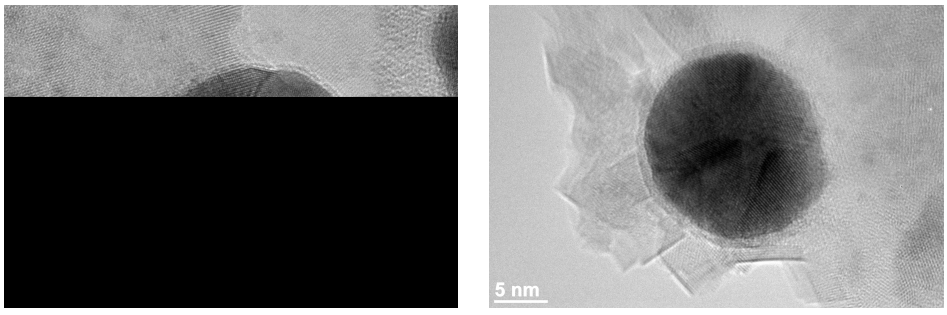


Figure 4.24: High magnification TEM images of Au/Arg NPs on HAp(Ga)IE8 (left) and HAp(Ga)TR (right).

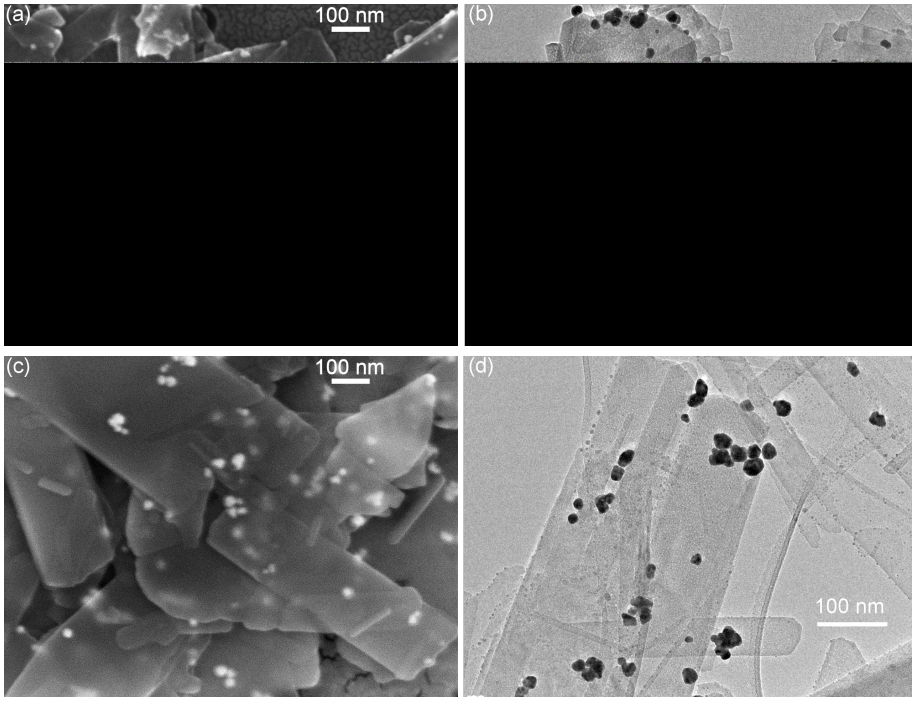


Figure 4.25: Morphology of the Au/Arg@HAp: (a) SEM image and (b) TEM image of the Au/Arg@HAp10 created by sonochemical synthesis; (c) SEM image and (d) TEM image of an Au/Arg@HAp created without sonication by mixing at 60 °C under reflux.

4.4 Ga@HAp Nanocomposite

4.4.1 Optimization of the synthesis

Among the synthesis methods listed in Section 1.4.3.2, the ultrasonic emulsification was my first choice. As already mentioned in Section 1.4.3.2, this method is simple and enables creation of Ga NPs in the presence of HAp to directly obtain a Ga@HAp nanocomposite, but its major disadvantage is the wide size distribution of the created Ga particles. I tended to avoid the high temperature, high vacuum and water-sensitive reducents to keep the desired properties of the hydroxyapatite, such as its nanocrystallinity, bioactivity, and the active surface for the attachment of nanoparticles. Thus, polar media that could mix with water were desired and the use of any surfactant was deliberately avoided. Aqueous

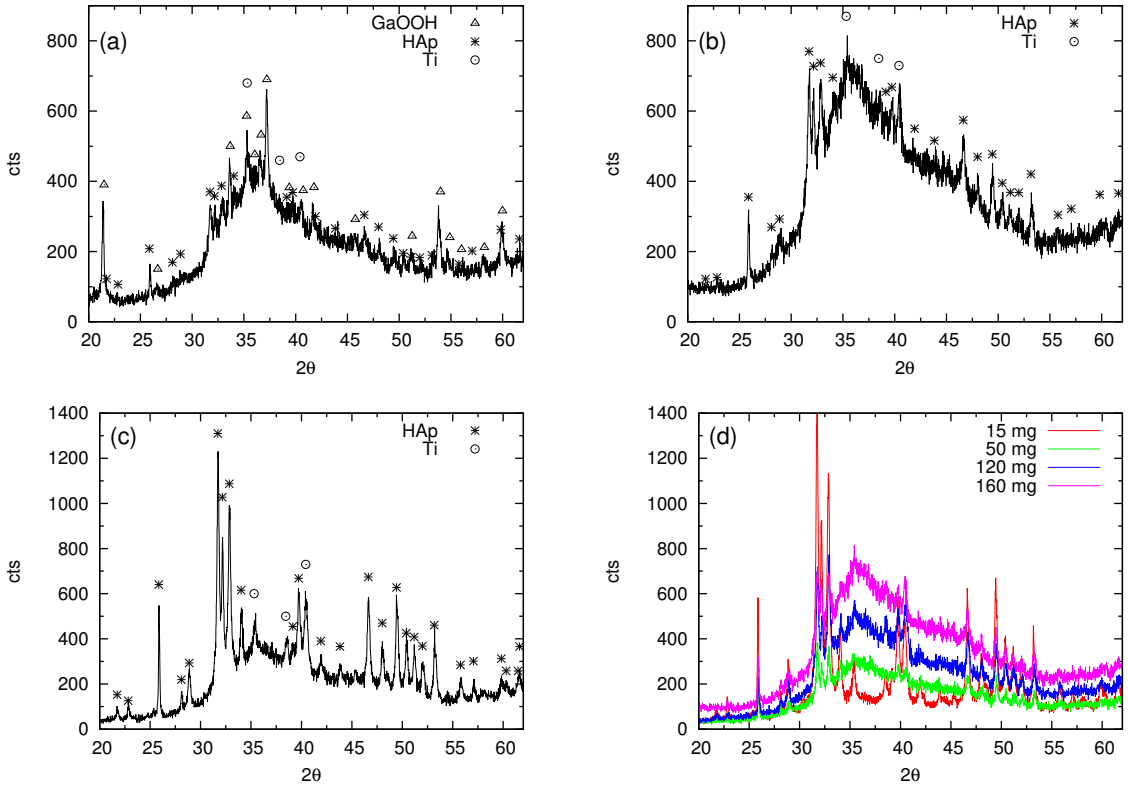


Figure 4.26: X-ray diffractograms of Ga@HAp nanocomposites prepared by ultrasonic emulsification in different media: (a) water, (b) water+acetonitrile (3:1), (c) ethylene glycol, (d) water+acetonitrile using different starting amounts of Ga (in mg) and the same starting amount of HAp. The reference patterns of the identified phases HAp (01-089-6438), Ti (00-001-1198) and GaOOH (00-006-0180) are marked by different points on the graphs.

medium would be preferred. However, water as the dispersing medium causes the sonochemical formation of GaOOH nanorods [192]. I have tested whether this sonochemical reaction occurs also in the presence of hydroxyapatite. XRD analysis (Figure 4.26 (a)) has confirmed that it does. I have then tried several other media and here I will focus on two of them: water+acetonitrile mixture and ethylene glycol. As seen in Figure 4.26 (b), the sonochemical reaction of Ga leading to GaOOH was completely prevented in a mixture of water and acetonitrile (3:1 or lower volume ratio). Likewise, there was no evidence of the GaOOH phase after ultrasonication in ethylene glycol (Figure 4.26 (c)). In

fact, no Ga crystalline phase could be detected. However, all diffractograms exhibited a high background (resembling two very broad peaks), which increased proportionally to the amount of Ga (Figure 4.26 (d)). Moreover, the location of the background matches the previously reported amorphous hump of liquid Ga NPs [165] (see Figure B.2 in the Appendix). An ultrasonic dispersion of Ga in water yielded mostly GaOOH nanorods and

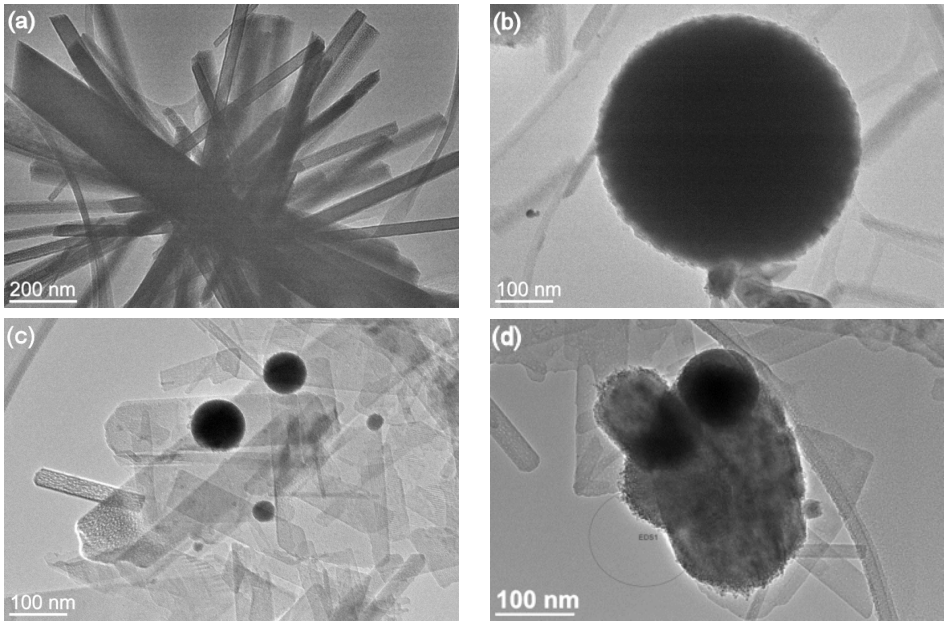


Figure 4.27: Synthesis of Ga@HAp in water. *Top:* Ultrasonication of molten Ga (without hydroxyapatite) in water, yielding GaOOH nanorods (a) and Ga submicrometer-sized spherical particles (b). *Bottom:* Ultrasonication of molten Ga in the presence of HAp, resulting in Ga nanospheres on the HAp laths (c) and shorter GaOOH nanorods on the HAp laths (d).

also submicrometer Ga particles (Figure 4.27 (a), (b)). However, in the presence of hydroxyapatite smaller Ga particles, among them many nanosized Ga particles, and shorter GaOOH nanorods were formed (Figure 4.27 (c), (d)). Nanosized Ga particles were obtained in the water + acetonitrile and the ethylene glycol medium as well. However, their size distribution was wide and even spheres of >0.5 μm were found on hydroxyapatite (Figure 4.28). Longer sonication did not significantly narrow the size distribution. Ethylene glycol medium offered an easy way for removing the large Ga particles by centrifugation in a similar way as Ti particles could be separated from hydroxyapatite (Section 4.1.2.2). The Ga@HAp nanocomposite can then be sedimented by centrifugation in EG-water mixture, which due to EG antifreeze properties can be cooled below the water freezing point. Obviously, the yield is decreased by the first centrifugation. About 80 % of HAp and about 20 % of Ga remained in the supernatant after centrifugation in ethylene glycol. Figure 4.29 (a) confirms that HAp and small Ga NPs are mainly retained in the supernatant, whereas the sediment consists mainly of larger Ga and Ti particles (Figure 4.29 (b)). Moreover, evident decrease of size could be obtained by centrifugation after ultrasonication also in the absence of HAp (Figure 4.29 c, d). Thus, a colloidal suspension of Ga NPs in EG was obtained.

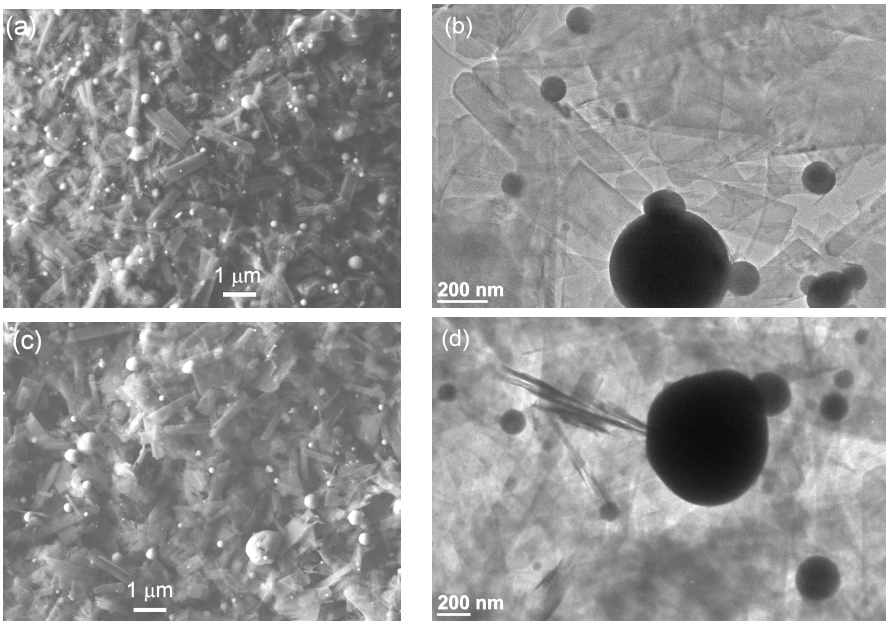


Figure 4.28: Morphology of Ga@HAp after sonication in EG: (a) SEM and (b) TEM image. Morphology of Ga@HAp after sonication in water+acetonitrile medium: (c) SEM and (d) TEM image.

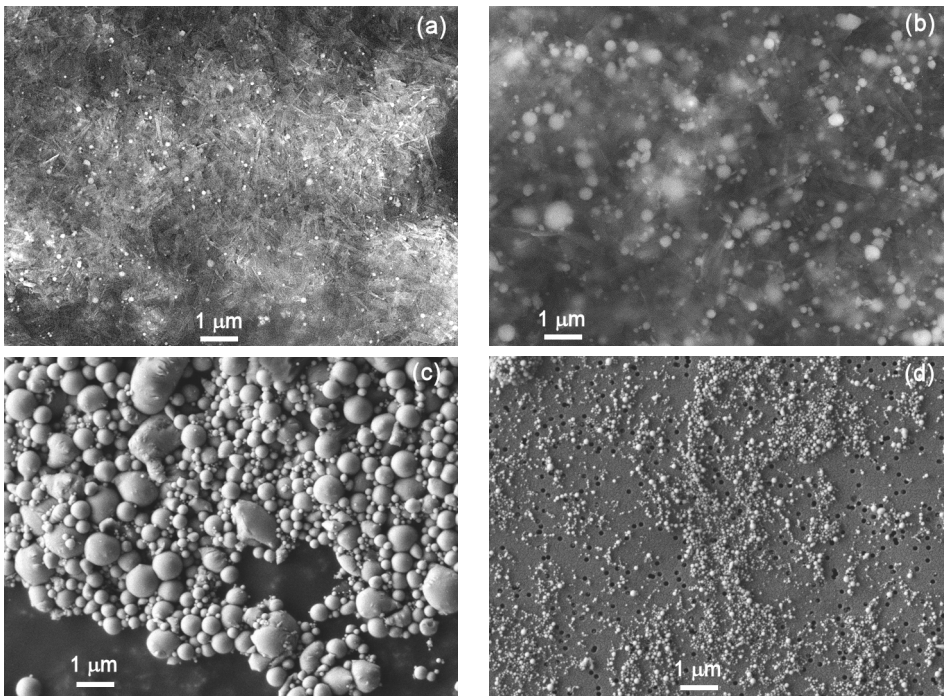


Figure 4.29: Separation of the large and small Ga particles by centrifugation: (a) Supernatant and (b) sediment after centrifugation in ethylene glycol; (c) Ga particles after 1 hour of sonication without centrifugation; (d) Ga nanoparticles in the supernatant after additional centrifugation.

4.4.2 Characterization of the Ga@HAp16 nanocomposite

Most of the analyses were done on this Ga@HAp nanocomposite and the results were also published [352]. The synthesis of the Ga@HAp16 nanocomposite was repeated several times and five batches contained on average 16 ± 2 wt % of Ga, which indicates a good repeatability of the synthesis.

Ultrasonication of Ga in the absence of HAp leads to a colloidal solution of Ga nanoparticles in EG. These particles are spherical (Figure 4.30 (a)–(c)) and have a unimodal size distribution with a peak at 24±2 nm and 40 % polydispersity (Figure 4.30 (b)). They exhibit a core-shell morphology, with a darker amorphous core and brighter amorphous shell (Figure 4.30 (c)). The EDS analysis on the Ga nanoparticles (Figure 4.30 (b), (c)) confirmed the Ga phase. The ratio of intensities between Ga (Lα_1, Kα_1) and O (Kα_1) peaks was compared with such intensity ratio of these two elements measured in GaOOH and amorphous gallium hydroxide samples of very similar size and thickness and under the same EDXS measurement conditions. I_{Ga}/I_O ratio for Ga NPs was 7 times larger than for amorphous gallium hydroxide and 6 times larger than for GaOOH, which implies that the Ga NPs are not made of gallium oxide or hydroxide but rather of elemental Ga. The small oxygen signal might have come from a thin amorphous oxide/hydroxide shell on the surface of the Ga NPs. Ga has a strong tendency to passivate with a thin oxide film [154]. Previous investigations [152], [165], [185], [187], [192] on Ga NPs have proven that the Ga core is covered with a thin oxide/hydroxide shell. The electron diffraction (SAED) pattern on the Ga NPs consists of a ring, a diffuse halo and a larger diffuse halo with very low intensity (Figure 4.30 (b), (d)). These three rings match the three most intensive rings of the polycrystalline monoclinic β-Ga electron diffraction pattern, whereas other Ga polymorphs, $Ga(OH)_3$, GaOOH or any Ga_2O_3 polymorph did not match well. This indicates that the nanoparticles are made of a disordered β-Ga, which is actually liquid Ga [147] (see sections 1.4.2 and 1.4.3.1). The SAED pattern is almost identical to the previously reported electron diffractions for liquid Ga nanoparticles [165], [171], [190].

Morphologically, the Ga@HAp16 nanocomposite consists of HAp nanorods and spherical Ga nanoparticles attached to their surface (Figure 4.30 (e)–(h)). The Ga nanoparticles in the dried nanocomposite are very similar to the colloidal Ga nanoparticles in EG. The size distribution of the Ga NPs in the Ga@HAp16 nanocomposite has a peak at 22±2 nm and 40 % polydispersity (Figure 4.30 (g)). The HAp does not influence the ultrasonic dispersion of the liquid Ga and the size distribution of the so-formed Ga nanoparticles. However, there is an important difference between the colloidal Ga NPs and the Ga NPs in the Ga@HAp16 nanocomposite. While the colloidal Ga NPs are obviously agglomerated, the Ga NPs in the Ga@HAp16 nanocomposite are attached to the HAp nanorods and well separated. Hence, hydroxyapatite hinders their coalescence and agglomeration after the ultrasonication most likely by some electrostatic interactions that stabilize the Ga nanoparticles and compensate their surface charge. High-magnification TEM image (Figure 4.30 (h)) reveals the crystallinity of the HAp nanorod and no crystallinity for the Ga particles. In the Ga@HAp16 nanocomposite, part of the oxide/hydroxide layer on the Ga NPs might have come from the hydroxyapatite, which can be concluded from the obvious wetting of the HAp surface by the Ga nanoparticle and the oxide layer deriving from the HAp.

The non-crystalline nature of Ga within the Ga@HAp16 nanocomposite was also confirmed by the XRD analysis. The diffractograms of both pure HAp and the Ga@HAp16 (Figure 4.31 (a), (b)) show the diffraction maxima typical for the structure of the hexagonal apatite (PDF number of the reference pattern 01-089-6438). There are no additional diffraction maxima that could be assigned to crystalline Ga, only an increased background between about 30 and 55° is observed for the Ga@HAp16 in comparison with the pure HAp. Based on our electron microscopy analysis and previous reports about the XRD of

the Ga NPs [165], [192] it is reasonable to explain the raised background as a consequence of the presence of liquid (amorphous) Ga NPs in the Ga@HAp16 nanocomposite.

I was searching for further evidence that the nanospheres were made of elemental Ga. Another evidence that Ga nanoparticles are made of elemental Ga is obtained from the optical properties. The UV-VIS spectrum of the colloidal solution of Ga NPs in EG contains a surface plasmon resonance (SPR) peak at about 250 nm (Figure 4.31 (c)). The SPR peak position (at $\sim$ 5.0 eV) agrees very well with a previous report [165] (see Section 1.4.3.1 and Figure 1.12), but is red-shifted in comparison with the calculated SPR peak by the Mie scattering theory [368] for 24-nm Ga NPs in a medium with a refractive index of 1.43 (ethylene glycol) and the optical constants for liquid gallium from the work of Knight *et al.* [185] (see Appendix A). This shift is attributed to the gallium oxide coating on Ga NPs (see Section 1.4.3.1). A similar peak can also be distinguished in the spectrum of the Ga@HAp16 nanocomposite as a shoulder superimposed on the absorbance curve of the HAp.

We investigated the type of interactions between the composite components by the FT-IR spectroscopy (Figure 4.31 (d)). The FT-IR spectrum of the pure HAp was compared to the spectrum of the Ga@HAp16 nanocomposite and both graphs are normalized to [0,1]. Both spectra show all the bands due to the characteristic vibrations of the phosphate and OH groups for hydroxyapatite [273]. No chemical shifts or disappearance of the fine structure were noticed in the Ga@HAp16 sample, so we can exclude any chemical interaction between the Ga NPs and the HAp. There is a decrease of the intensity of the peak at 3600 cm^{-1} (the ratio of heights of the OH (3570 cm^{-1}) vs the PO_4 (1032 cm^{-1}) peak was 4 times lower for the Ga@HAp16 in comparison with the HAp sample), which indicates existence of interactions that block the stretching mode of OH^- groups. Similar to our previous investigations on interactions between HAp and Ag nanoparticles [391], blocking OH^- vibrations could be assigned to physical interactions between Ga nanoparticles and HAp. These interactions stabilize the formed Ga nanoparticles within the Ga@HAp16 nanocomposite and control their aggregation and further growth by their attachment onto the surface of apatite mediated by the surface OH^- groups of HAp. From the XRD, electron microscopy and EDXS analyses we can conclude that Ga nanoparticles in the nanocomposite consist of a spherical amorphous Ga core and a thin amorphous gallium oxide shell. Although the raised background in the XRD pattern does not clearly explain what the Ga phase is, the undisputable proof that the nanospheres are elemental Ga comes from the SAED, EDXS and UV-VIS analyses.

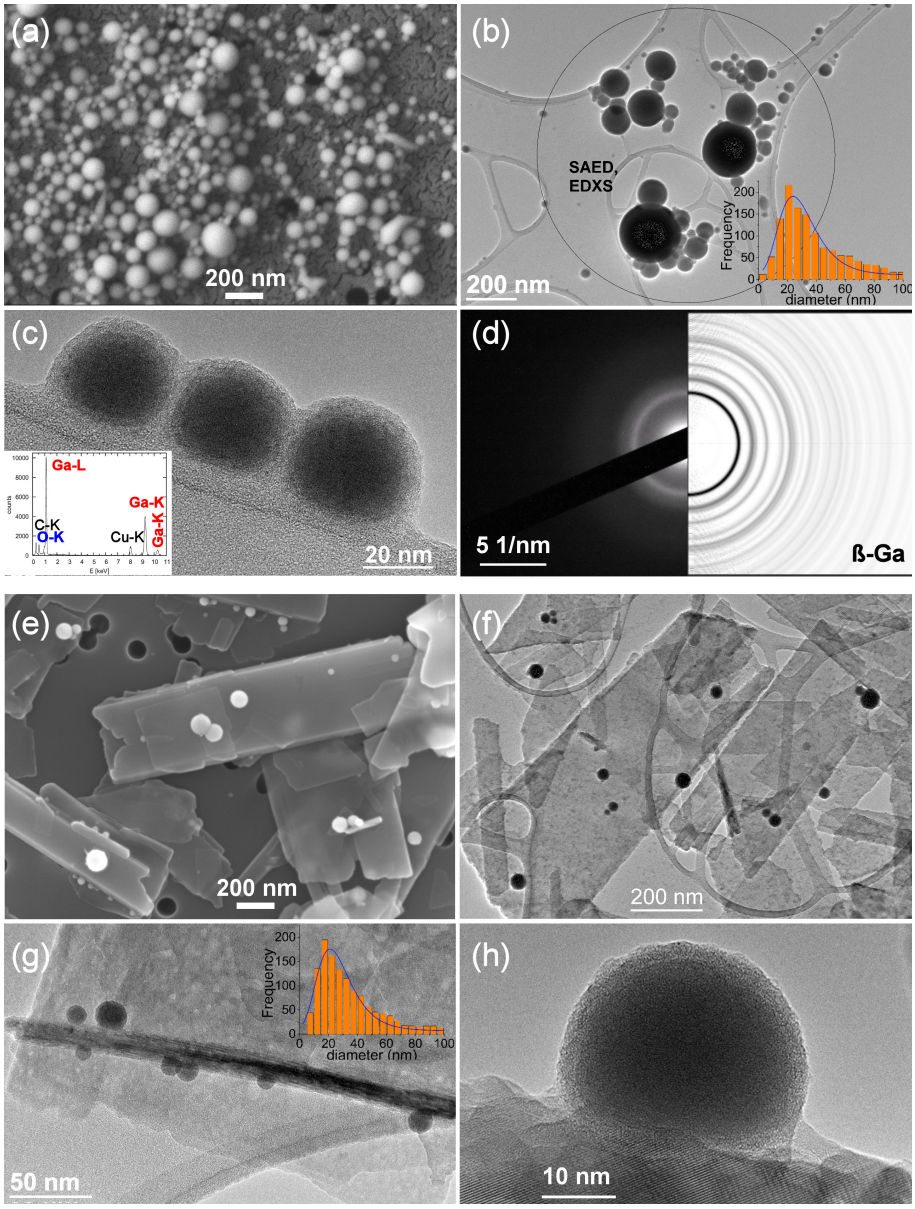


Figure 4.30: Electron microscopy analysis of Ga NPs and Ga@HAp nanocomposite prepared by ultrasonic emulsification method without surfactant. (a) SEM image of Ga nanoparticles (NPs) in ethylene glycol (EG); (b) TEM image of the Ga NPs, which were analysed by the EDXS and SAED, and the TEM size distribution of 1360 particles from the TEM images; (c) high magnification TEM of 3 Ga NPs in EG and EDXS analysis (inset); (d) SAED analysis of the Ga NPs with simulated electron-diffraction pattern for 24-nm β-Ga nanoparticles on the right-hand side (white background); (e) SEM image of the dried Ga@HAp16 nanocomposite; (f), (g) TEM images of the Ga@HAp16 nanocomposite; the inset in (g) shows the size distribution of 1338 Ga nanoparticles on HAp based on the contrast in the TEM images; (h) high magnification TEM of a Ga nanoparticle on hydroxyapatite. Figure published in ref. [352].

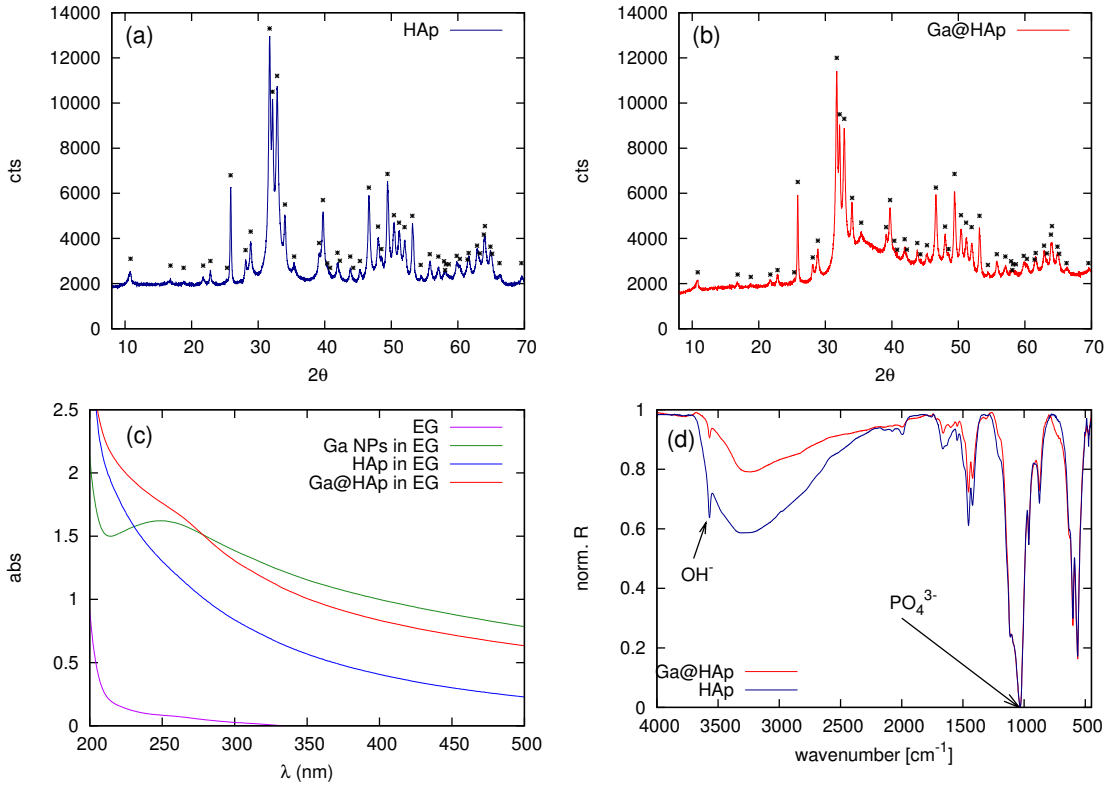


Figure 4.31: Characterization of the Ga@HAp16 nanocomposite. (a,b) X-ray diffractograms of (a) HAp and (b) Ga@HAp16. Asterisks (∗) denote hydroxyapatite hexagonal (P63/m) reference pattern with PDF number 01-089-6438; (c) UV-VIS spectra of ethylene glycol (EG), Ga NPs in EG, hydroxyapatite (HAp) and Ga@HAp16 nanocomposite in EG; (d) IR spectrum of Ga@HAp16 in comparison with pure HAp nanorods. Both curves are normalized to [0,1]. The peaks due to OH^- and PO_4^{3-} vibrations in hydroxyapatite that were used for calculation of the OH/PO4 ratio of heights are indicated with arrows. Figure published in ref. [352].

4.4.3 Other Ga@HAp nanocomposites

Although the synthesis of the Ga@HAp16 revealed very good repeatability, its dependence on the centrifugation and thus the specific HAp morphology is disadvantageous. Therefore, I further investigated options of

(a) leaving out the centrifugation step but using a proportionally smaller (20 %) starting amount of Ga, which resulted in Ga@HAp6 and Ga@HAp7 nanocomposites;

(b) using a different HAp (by precipitation under reflux at 100 °C, which resulted in the Ga@HAp32 nanocomposite;

(c) using sonication in the presence of HAp and centrifugation to obtain small Ga NPs, then mixing the colloidal Ga NPs with a new aqueous suspension of HAp, which resulted in Ga@HAp6-nano sample;

(d) using ultrasonication to deposit monodisperse Ga/OA NPs (prepared by thermal decomposition) onto HAp, which resulted in the Ga/OA@HAp nanocomposite.

The synthesis conditions and composition of the different Ga@HAp are summarised in Table 4.5. We can see that all syntheses create losses of Ga, which might occur during the removal of the oxide layer of the starting Ga droplet by HCl, during the ultrasonication and during centrifugation and resuspension. A comparison of data for the Ga@HAp16 and Ga@HAp32 also reveals that the ultrasonic+centrifugation method in ethylene glycol is not easily transferable to HAp with different morphology. Another interesting subject

Table 4.5: Synthesis parameters and composition of different Ga@HAp nanocomposites examined throughout the thesis.

Sample	hydroxyapatite	starting m(Ga)/m(HAp)	synthesis	Ga content (wt %)	final m(Ga)/m(HAp)
Ga@HAp16	sonochemical	0.67	ultrasonication + centrifugation (EG)	16	0.19
Ga@HAp6-nano	sonochemical	0.33	mixing colloidal Ga NPs (EG) with HAp (water)	6.3	0.067
Ga@HAp6	sonochemical	0.13	ultrasonication (EG)	6.4	0.068
Ga@HAp7	sonochemical	0.19	ultrasonication (water + acetonitrile)	7.0	0.075
Ga@HAp32	mixing at 100 °C	0.67	ultrasonication + centrifugation (EG)	32.4	0.48
Ga/OA@HAp	mixing at 100 °C	0.05	mixing/sonication of colloidal Ga/OA NPs with HAp (THF)	3.2	0.033

is the effect of these different synthesis conditions on the mean particle diameter and their size distribution. Ga@HAp6-nano had a 15-nm mode size and 70 % polydispersity, Ga@HAp6 22-nm mode size and 40 % polydispersity, Ga@HAp7 40-nm mode size and 70 % polydispersity, Ga@HAp32 33-nm mode size and 50 % polydispersity, whereas the size distribution of the Ga/OA@HAp was narrower (20 % polydispersity) with mode at 29

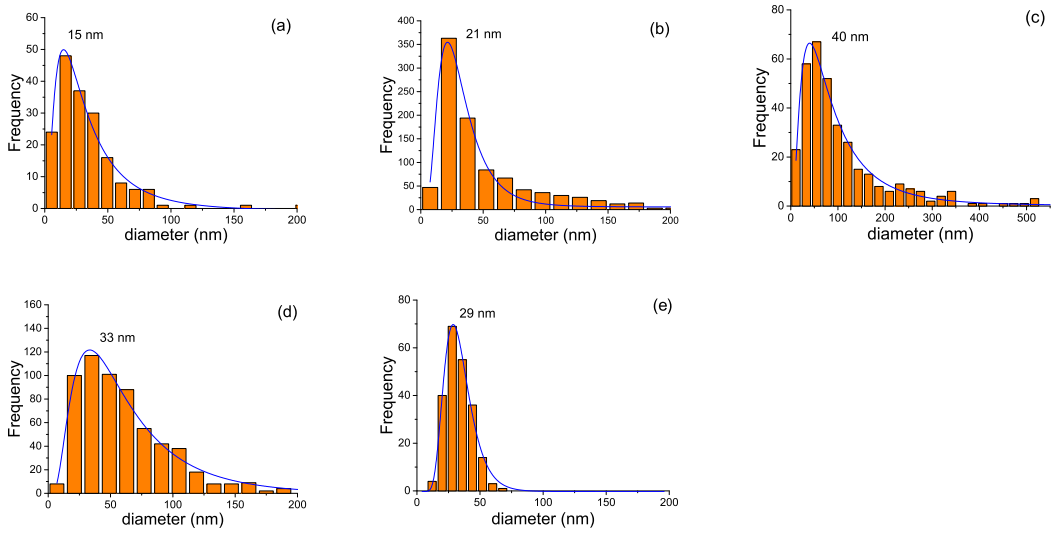


Figure 4.32: TEM size distribution of Ga NPs in different Ga@HAp nanocomposites: a) Ga@HAp6-nano, b) Ga@HAp6 without particle separation by centrifugation, e) Ga@HAp7 by ultrasonication in water:acetonitrile (2:1), d) Ga@HAp32 using HAp by precipitation under reflux+15-min ultrasonication instead of the sonochemical HAp, c) Ga/OA@HAp by dispersing Ga/OA NPs onto HAp. The size distributions were fitted with a log-normal function. See Table 4.5 and Section 3.2.5.2 for details about the preparation of these nanocomposites.

nm (the size distributions are presented in Figure 4.32). These results indicate that very similar size distribution of Ga NPs to that in Ga@HAp16 can be achieved in ethylene glycol even without centrifugation if a lower amount of Ga is used. On the other hand, different HAp resulted in a larger size and wider size distribution despite the use of centrifugation for size separation. In water+acetonitrile medium the average size of the Ga NPs is larger and the wide size distribution remained in spite of decreased Ga amount. A comparison of the narrow size distribution of the Ga/OA@HAp with the size distribution of the precursor colloidal Ga/OA NPs (Figure 4.33 (b)) reveals that the dispersion onto HAp did not change the mean size and the size distribution of the Ga/OA NPs. The morphology of the Ga/OA NPs and Ga/OA@HAp nanocomposite is presented in Figure 4.33. Unlike the Ga NPs in the Ga@HAp16 nanocomposite, the Ga/OA NPs in the Ga/OA@HAp nanocomposite were often found agglomerated and not well separated on the HAp.

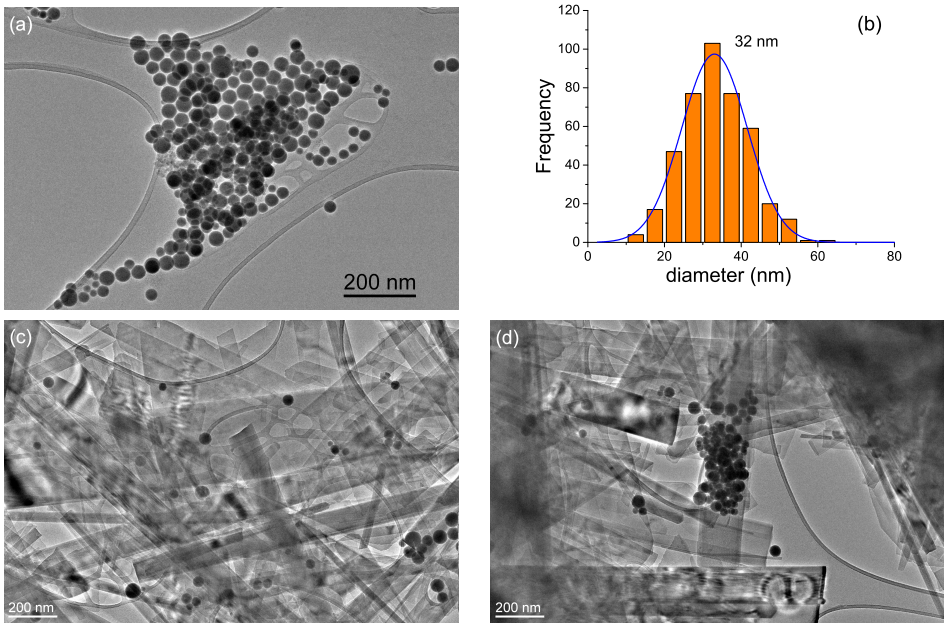


Figure 4.33: Electron microscopy analysis of the Ga/OA NPs (prepared by thermal decomposition and with surfactants) and Ga/OA@HAp nanocomposite. (a) TEM image of Ga/OA NPs in chloroform; (b) size distribution of Ga/OA NPs based on particles in the TEM images; (c) TEM image of the Ga/OA@HAp after dispersing Ga/OA NPs onto HAp by ultrasonication and mixing in THF; (d) TEM image of a part of the Ga/OA@HAp sample revealing agglomerated Ga/OA particles.

4.4.4 Ag@HAp reference

Ga@HAp16 nanocomposite will be additionally compared to a similar silver-based nanocomposite. The phase composition of the Ag@HAp nanocomposite (by XRD) is presented in Figure 4.34 and confirms the Ag and HAp constituents. It contained roughly the same chemical amount of metal component (2 mmol of nanoparticles per g of composite) as 1 gram of the Ga@HAp16 nanocomposite. The morphology of the Ag@HAp (Figure 4.35) was also very similar to the morphology of the Ga@HAp16 nanocomposite.

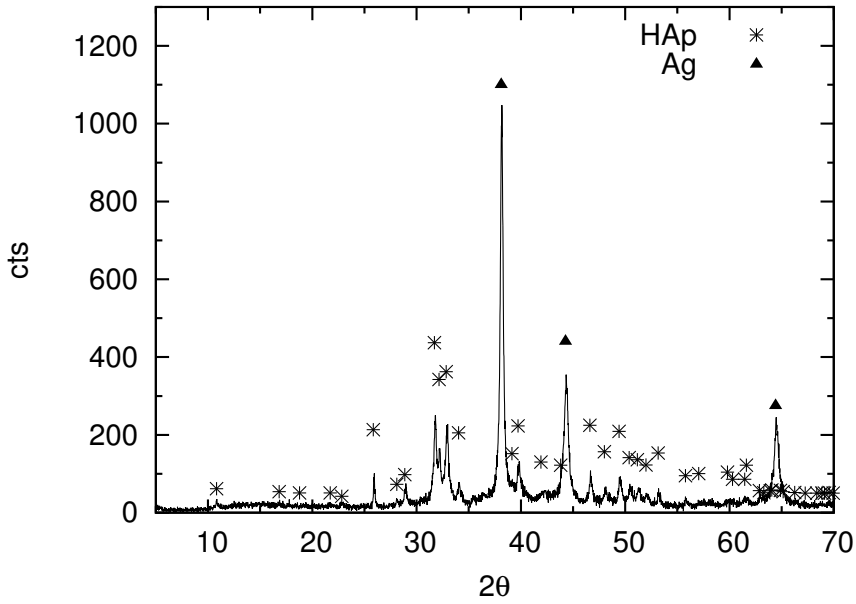


Figure 4.34: X-ray diffraction pattern of the Ag@HAp nanocomposite reference. Ag (00-004-0783) and HAp (01-089-6438) phases were identified.

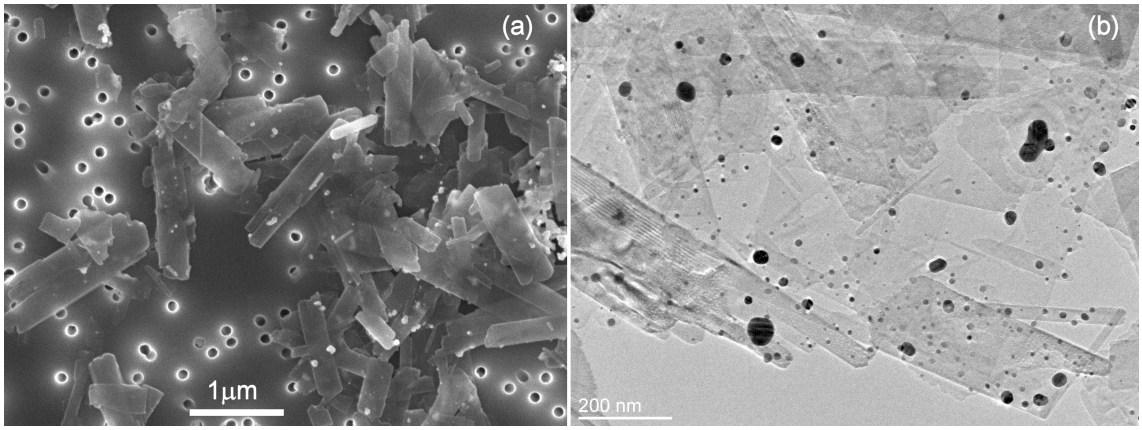


Figure 4.35: Image of the Ag@HAp nanocomposite under a scanning electron microscope (a) and a transmission electron microscope (b).

4.5 Composite of Functionalized Ga/Au Core/Shell Nanoparticles and Hydroxyapatite

Our hypothesis for creating Ga/Au core-shell nanoparticles was to use a gallium sacrificing core to grow the gold nanoshell on it. I have first tested this hypothesis on gallium μm and sub-μm droplets in ethylene glycol. $HAuCl_4$ solution in ethylene glycol was added to the gallium emulsion under a short ultrasonication. The creation of gold phase was confirmed by the XRD but it revealed also another phase, $AuGa_2$ (Figure 4.36 (a)). When a 6× lower mass of $HAuCl_4 \cdot xH_2O$ and mixing without ultrasonication was used, this phase was not obtained and the larger background between 30 and 50° indicates that a larger amount of gallium was retained (Figure 4.36 (b)). Several other conditions were then explored on

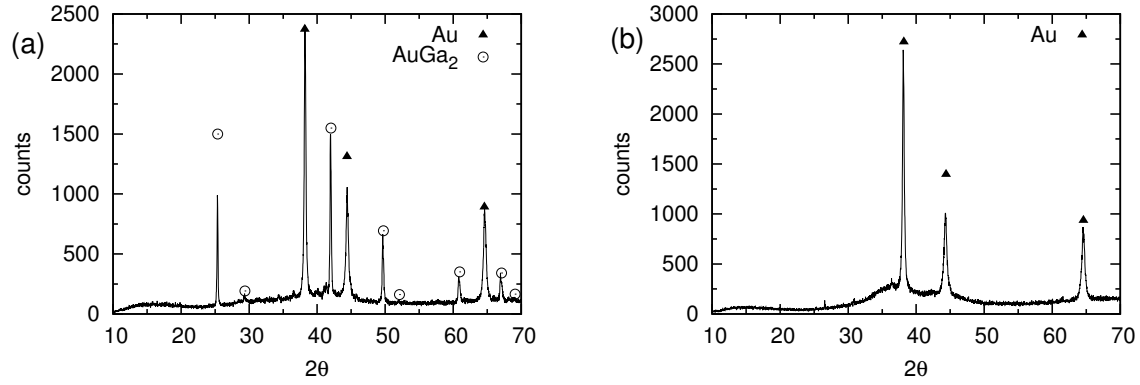


Figure 4.36: XRD patterns of the dried materials after mixing Ga micro- and sub-micro-droplets with $HAuCl_4$ in ethylene glycol: (a) 15-min ultrasonication at 50 % amplitude and room T with m(Ga)/m($HAuCl_4 \cdot xH_2O$)=0.25, (b) 4-hour mixing at room T with m(Ga)/m($HAuCl_4 \cdot xH_2O$)=1.6.

the Ga@HAp precursors. Comparison of two Ga/Au/Arg@HAp nanocomposites produced with the same concentrations of reagents but one with ultrasonication and the other without it gave no difference in the phase composition except for the additional Ti from the ultrasonic horn tip (Figure 4.37 (a) and (b)). Both contained also the $GaAu_2$ compound, which was observed after mixing in EG, EG+water, acetonitrile+water or water medium, in the presence or absence of arginine and even at a lower temperature (ice bath, see Figure 4.37 (c)) if the m(Ga)/m($HAuCl_4 \cdot xH_2O$)≤1. However, when the Ga surface was functionalised with arginine (by ultrasonication of Ga in a solution of Arg in ethylene glycol) and the $HAuCl_4$+Arg aqueous solution was neutralised to pH 7 by NaOH, the $AuGa_2$ was not formed even if the m(Ga)/m($HAuCl_4 \cdot xH_2O$)=0.7 (Figure 4.37 (d)). Investigation of the sample morphology with respect to the different synthesis conditions was then conducted with a particular interest in the Au shell and the local chemical composition of the Ga/Au particles. Herein, the EDXS analysis was employed. A SEM image with a linescan EDS analysis on a part of the Ga/Au sample that contained no $AuGa_2$ phase demonstrates that the Au phase is attached to the Ga droplet. A backscattered electron image of the same part of the sample provides a great contrast between the Ga and the Au part and matches very well the EDS analysis. This observation pointed out the usefulness of the backscattered electron imaging for analysing Ga/Au core-shell particles in a SEM. Figure 4.38 (c, d) provides a comparison with a secondary electron image, which reveals how the gold shell coverage of the Ga core can be immediately seen by switching to a backscattered mode. As we see, the Au phase is in the form of separated Au NPs that partially cover

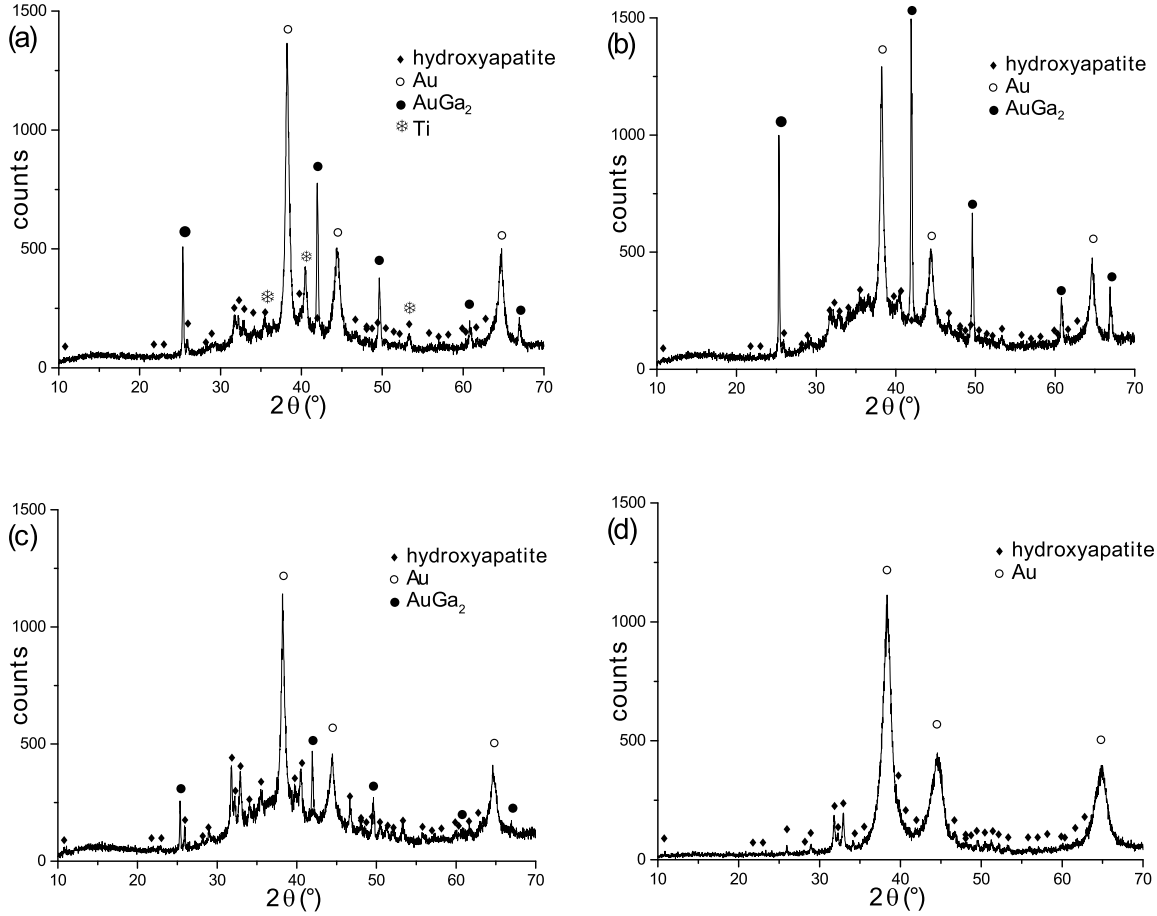


Figure 4.37: XRD analysis of different nanocomposites by mixing Ga@HAp with $HAuCl_4$ in water: a) Ga/Au/Arg@HAp by ultrasonication at room T and m(Ga)/m($HAuCl_4 \cdot xH_2O$)=1 b) Ga/Au/Arg@HAp by mixing at room T and m(Ga)/m($HAuCl_4 \cdot xH_2O$)=1, c) Ga/Au@HAp by mixing on an ice bath and m(Ga)/m($HAuCl_4 \cdot xH_2O$)=0.5, d) Ga/Au/Arg@HAp by mixing on an ice bath, m(Ga)/m($HAuCl_4 \cdot xH_2O$)=0.7, using Ga/Arg@HAp and $HAuCl_4$+Arg solution with pH 7.

the Ga surface rather than forming a continuous gold shell.

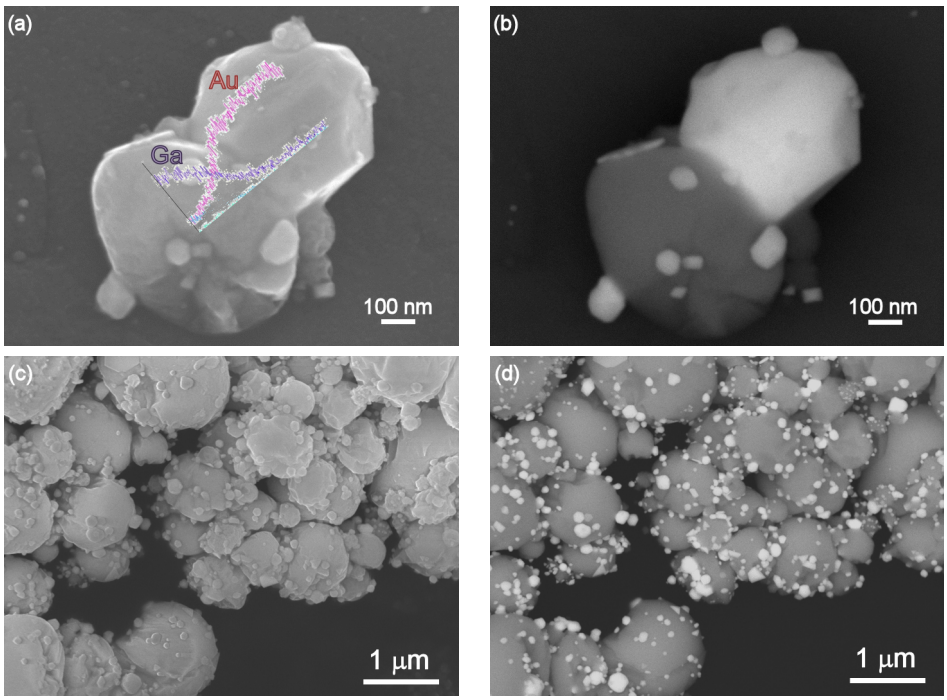


Figure 4.38: SEM and EDXS analysis of the Ga/Au sample that contained no $AuGa_2$ phase: (a) secondary electron image of a Ga/Au particle with a linescan EDXS analysis, (b) backscattered electron image of the same Ga/Au particle, (c) secondary electron image of the Ga/Au sample, (d) backscattered electron image of the same part of the Ga/Au sample as in (c).

Similar features were observed in the Ga/Au@HAp nanocomposite (formed by mixing Ga@HAp with an aqueous solution of $HAuCl_4$ on ice bath). The Ga/Au NPs were of a Janus "nanoraspberry" type [392], [393], [394] core-shell with white Au nanospheres attached to the darker Ga nanoparticles (Figure 4.39 a). The HAp laths are almost non-visible in a backscattered image, but are well evident in the TEM images. Due to the lower resolution of a SEM, the two phases composing a Ga/Au nanoparticle are better distinguished in a TEM, where the Au part is darker than the Ga part, which was confirmed by the EDS analysis (Figure 4.39 b, c).

Then the morphology of the nanocomposites aimed for an additional arginine functionalisation on the Au surface was examined. If the Ga/Au/Arg@HAp synthesis was done under ultrasonication at room T, the Au phase was in the form of a partial ring almost detached from the Ga core nanosphere (Figure 4.40). When mixing with $HAuCl_4$ and Arg solution on ice bath was used instead of the ultrasonication, the Ga/Au/Arg particle morphology changed to one very similar as in the Ga/Au@HAp nanocomposite (Figure 4.41). The ring-like Au was shortened to nanospheres and the attachment to the Ga surface was improved but the coverage was still only partial. However, if $HAuCl_4$ was titrated with NaOH to pH 7 before the Arg addition and mixing with Ga@HAp, the coverage was improved and a much more connected Au nanoshell was formed (Figure 4.42). The EDS analysis on such Ga/Au/Arg nanoparticle confirmed that the Ga core was retained (Figure 4.43).

Furthermore, if Ga surface was functionalised with Arg (by ultrasonicating Ga in the presence of Arg during the formation of the Ga@HAp) prior to mixing with the

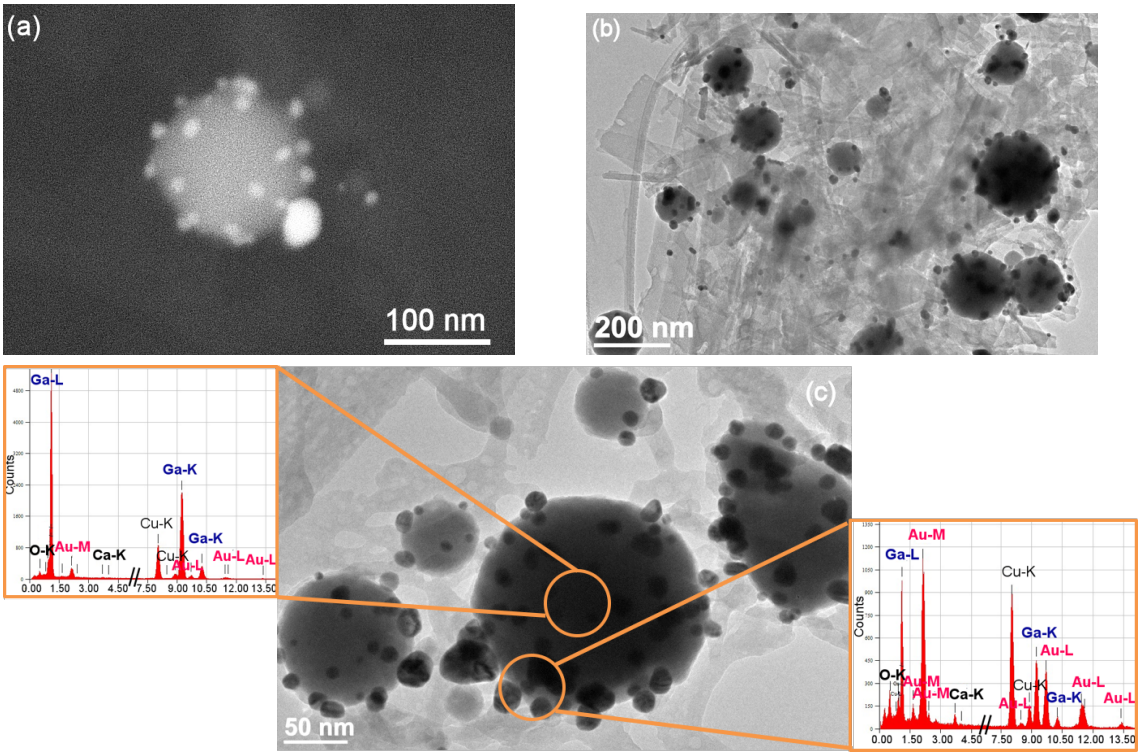


Figure 4.39: Mixing of Ga@HAp from ethylene glycol with $HAuCl_4$ on ice bath: (a) backscattered SEM image, (b) TEM image and (c) TEM image with EDXS analysis.

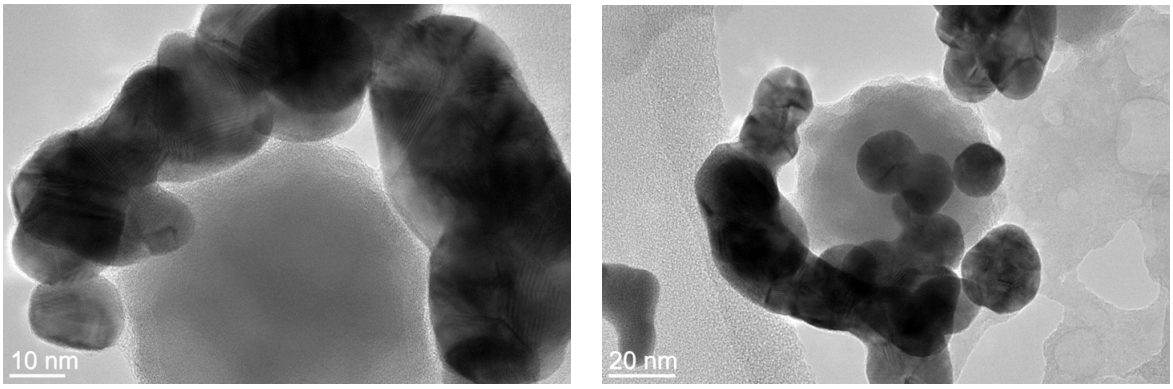


Figure 4.40: Morphology of Ga/Au/Arg@HAp formed by ultrasonication of Ga@HAp + $HAuCl_4$ + Arg in water.

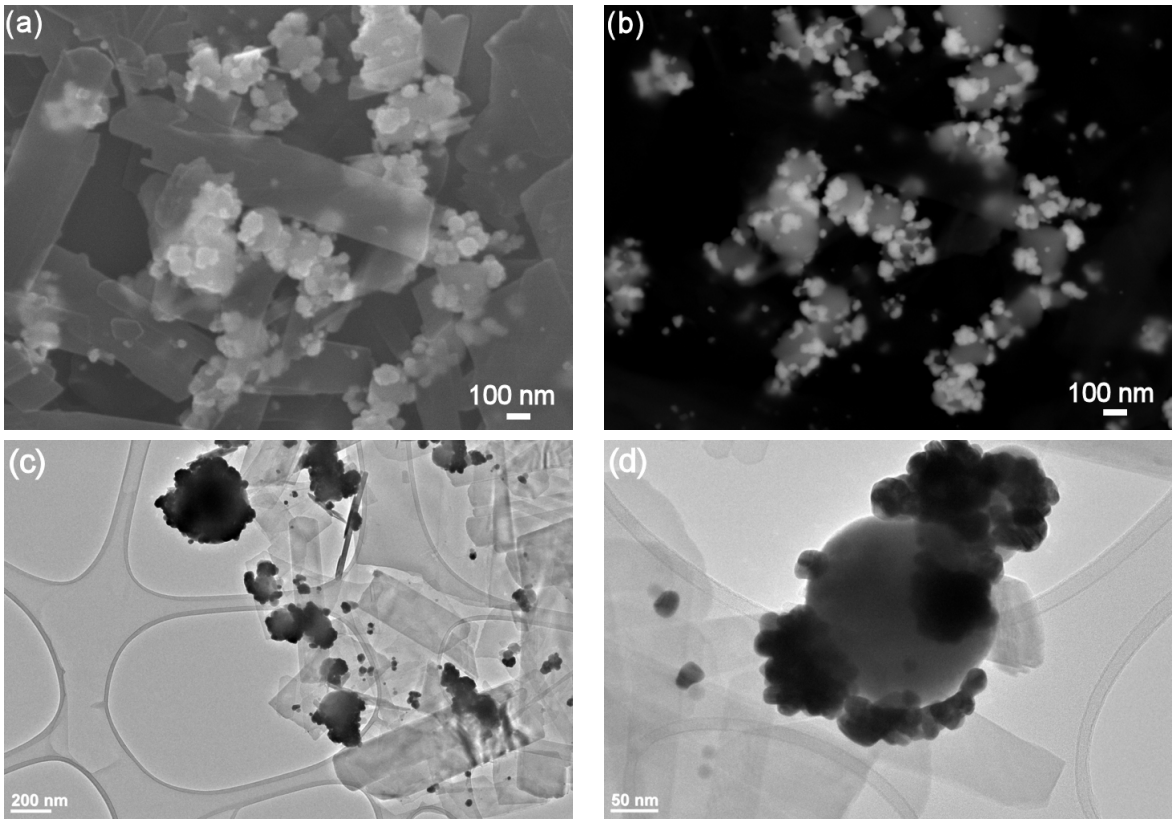


Figure 4.41: Morphology of Ga/Au/Arg@HAp formed by mixing of Ga@HAp with an aqueous solution of $HAuCl_4$+Arg on an ice bath: (a) secondary electron SEM image, (b) backscattered SEM image, (c, d) TEM images.

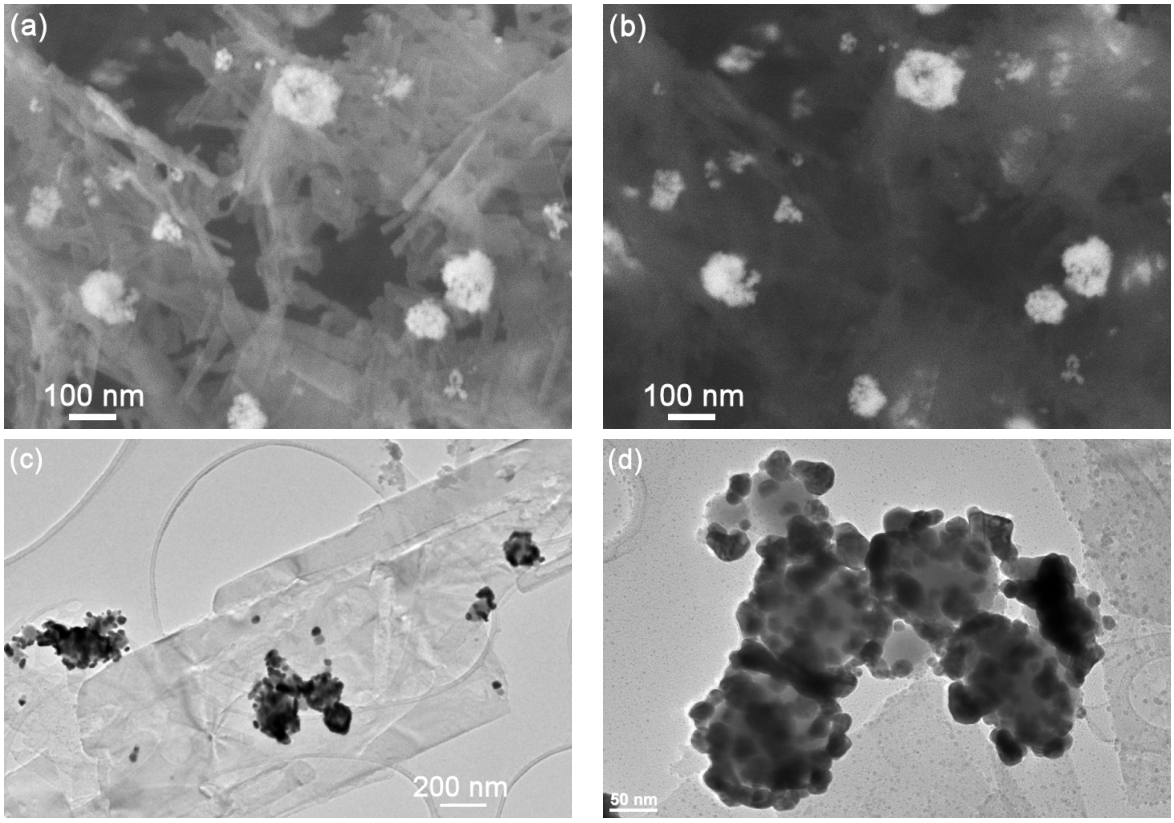


Figure 4.42: Morphology of Ga/Au/Arg@HAp formed by titration of a $HAuCl_4$ solution with NaOH to pH 7, addition of an aqueous solution of arginine and dropwise addition of the mixture to an ethyleneglycolic suspension of Ga@HAp on ice: (a) secondary electron SEM image, (b) backscattered SEM image, (c, d) TEM images.

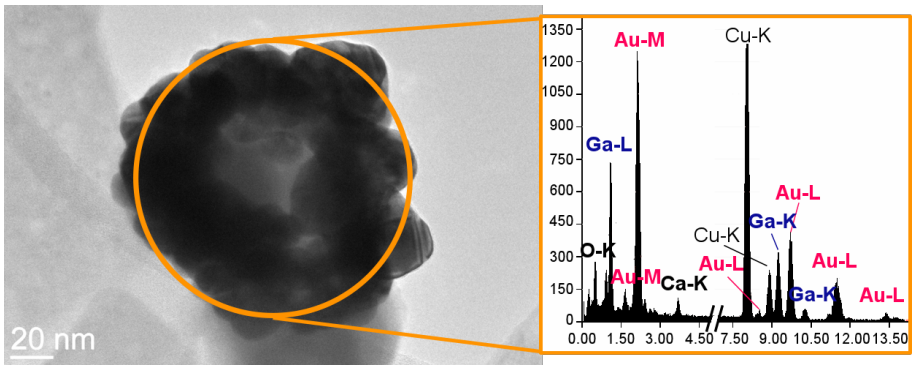


Figure 4.43: TEM EDXS analysis of a Ga/Au/Arg nanoparticle in a Ga/Au/Arg@HAp nanocomposite formed by titration of a $HAuCl_4$ solution with NaOH to pH 7, addition of an aqueous solution of arginine and dropwise addition of the mixture to an ethyleneglycolic suspension of Ga@HAp on ice.

$HAuCl_4$+Arg mixture (with pH 7), the Au shell was even finer and consisted of very small Au NPs (with diameters $\leq$ 5 nm, Figure 4.44).

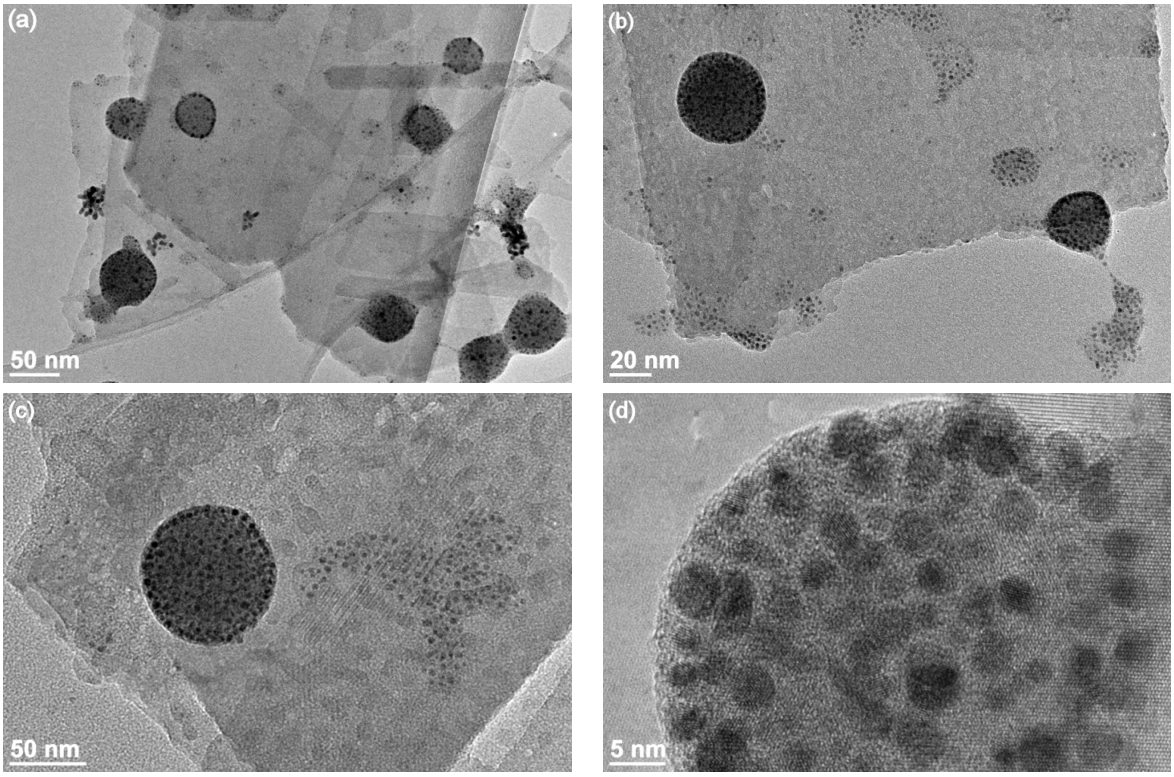


Figure 4.44: Morphology (under TEM) of Ga/Arg/Au/Arg@HAp obtained by dispersing Ga onto HAp in the presence of Arg in ethylene glycol, then mixing with HAuCl4+Arg+NaOH to pH 7 on ice bath. (a), (b) and (c) show the nanocomposite particles (core-shell nanospheres attached to HAp laths/plates) from different parts of the sample, whereas (d) presents a Ga/Arg/Au/Arg nanoparticle from the nanocomposite at a high magnification.

These Au NPs exhibited different connectivity leading to an Au shell with well distinct Au nanoparticles (and well-observed gallium core underneath, which still appeared covered with an oxide layer, Figure 4.44 d), a "broken shell" (Figure 4.45 (c)) or a continuous Au shell (Figure 4.45 (e)). The EDS analysis on these three types of Ga/Au particles revealed a decreasing Ga signal with increasing shell continuity, so that no Ga was detected on a Ga/Au particle with a continuous Au shell (Figure 4.45). I will further refer to such nanocomposite as Ga/Arg/Au/Arg@HAp to distinguish it from the Ga/Au/Arg@HAp nanocomposite without the functionalised Ga. If we compare the EDS analyses of Ga/Au@HAp, Ga/Au/Arg@HAp and Ga/Arg/Au/Arg@HAp, we can see that the Ga core was much more consumed in preparation of the core-shell nanoparticles in the Ga/Arg/Au/Arg@HAp nanocomposite than in the other two materials.

Coating of Ga NPs with an Au shell changes their optical properties (the surface plasmon resonance), as explained in Appendix A. This change is different for a core-shell structure, which retains the features of plasmonic peaks of both components but with much decreased intensity, in comparison with an alloy, which gives only one peak that is shifted with regards to the pure core SPR peak. Therefore, I have measured the UV-VIS spectrum of an aqueous suspension of Ga/Au/Arg@HAp nanocomposite (with the morphology presented in Figure 4.42) and compared it to the calculated Ga/Au spectra

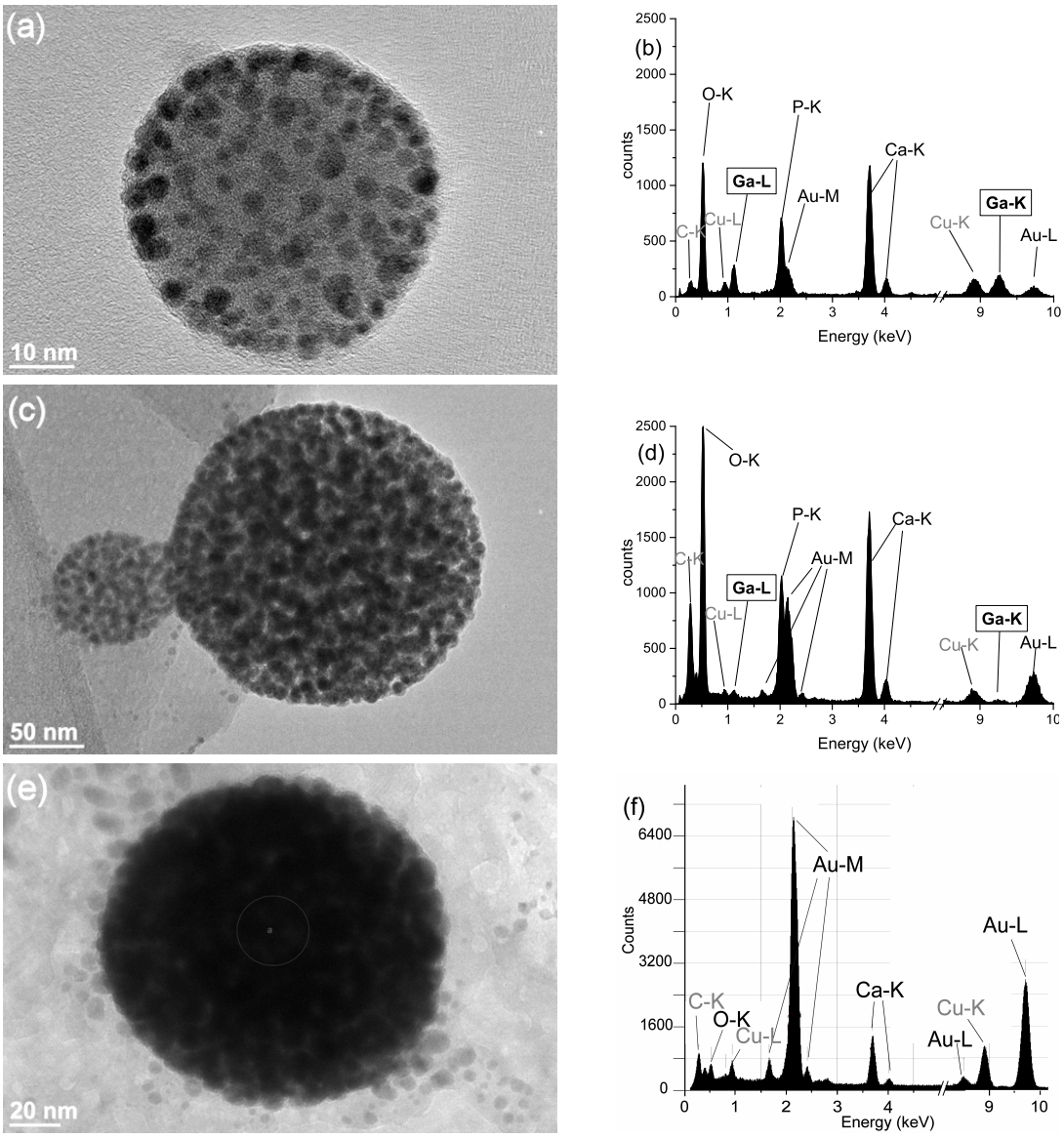


Figure 4.45: TEM EDXS analyses on the different types of Ga/Au/Arg NPs found in the Ga/Arg/Au/Arg@HAp nanocomposite: (a), (b) separated Au/Arg nanoparticles on the surface of a Ga nanosphere; (c), (d) cracked (discontinuous) Au shell on Ga nanospheres; and (e), (f) continuous Au shell on a Ga nanosphere.

(Figure 4.46 a, b). No well-distinct peaks were found except for a shoulder at around 520 nm and perhaps another very weak at around 265 nm, whereas the calculated spectrum predicted a peak at 290 nm due to Ga and another one at 505 nm due to Au. Both peaks are of very low intensity and the intensity of the Ga peak is further decreased with increasing Au shell thickness, whereas the Au peak experiences a gradual redshift and an intensity increase with increasing thickness in a similar way as observed in the Ag/Au system (see Figures A.3 and A.4 in the Appendix). Thus, the calculated spectrum for a 24-nm Ga core with 10-nm Au shell thickness is in fairly good agreement with the experimental spectrum, but the low intensity of the SPR and additional absorption by the HAp prevent more detailed conclusions.

As in the Au/Arg@HAp(Ga) nanocomposites, I sought out an evidence of functionalisation with arginine in the FTIR spectrum of the Ga/Au/Arg@HAp. The dark colour of the sample resulting in a large background (increasing with the increasing wavenumber) hindered the analysis in the functional group region (above 1000 cm^{-1}). Nevertheless, using background correction and comparison with the Ga/Au@HAp nanocomposite, the bands of the arginine functional groups could be identified in the Ga/Au/Arg@HAp nanocomposite (Figure 4.46 c, d).

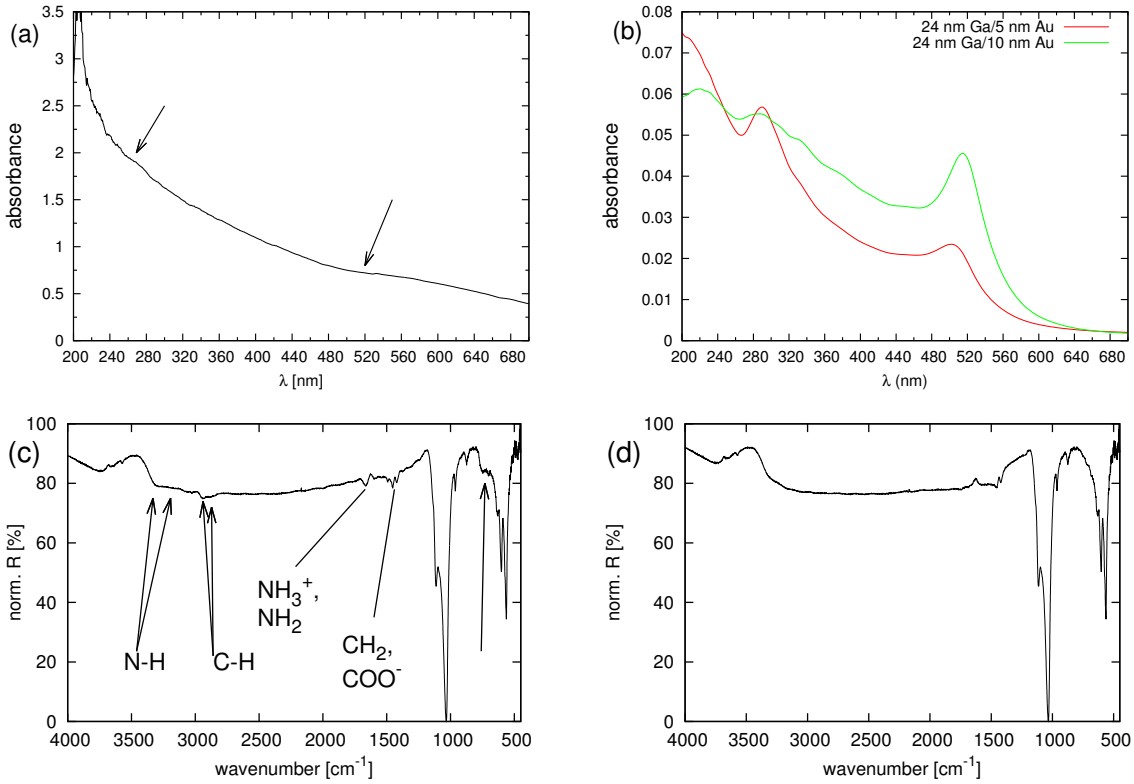


Figure 4.46: Spectroscopic analysis of Ga/Au/Arg@HAp. (a) UV-VIS spectrum of Ga/Au/Arg@HAp, (b) calculated UV-VIS spectrum of Ga/Au NPs, (c) FTIR spectrum of Ga/Au/Arg@HAp nanocomposite, (d) FTIR spectrum of Ga/Au@HAp nanocomposite.

4.6 Influence of the *In-vitro* Exposure of the Materials to Different Physiological Media

4.6.1 HAp(Ga)

Like in Section 4.2, the results of ion release during ageing in simulated physiological conditions will first be presented for the HAp(Ga)IE materials and then a comparison of HAp(Ga)CP, HAp(Ga)TR and HAp(Ga)IE will be made. I examined first the concentration of Ga^{3+} ions released from the HAp(Ga)IE16 after exposing it to two PBS media with different pH (7.4 and 5.4) for different periods of time. Values between 20 and 25 mg/L of Ga^{3+} were detected in PBS with pH 7.4 (Figure 4.47 (a)). Such concentrations were achieved already in the first day of ageing and did not increase after longer time exposure, which indicates that an equilibrium was reached within the first day already. Lower Ga^{3+} concentrations (10–15 mg/L) were detected at pH 5.4 and this ion release had an unusual characteristic. Concentration of Ga^{3+} after one day of exposure was roughly the same as at pH 7.4, whereas the values after longer ageing were lower, so that a different equilibrium was established after 2 days. This indicates conversion to a less soluble phase after 1 day. However, no change in material's phase composition was noticed by the XRD after 4 days of ageing (Figure 4.48). Nevertheless, the new phase might not be crystalline or its amount is below the detection limit of the XRD method. Perhaps the initially released ions precipitate with PBS after 1 day in the form of an amorphous gallium phosphate or additional adsorbed/released ions are incorporated into the HAp(Ga)IE at this lower pH in the same way as during its formation. The HAp crystalline signal did decrease after 4 days in PBS with pH 5.4. Ion release from HAp(Ga)IE16 has been tested in two bacterial growth media (Mueller-Hinton (MH) and Luria-Bertani (LB) broth) as well, where the ion release was increased up to 30 % of the contained Ga(III) (Figure 4.47 (b)). Both growth media have pH 7.4 but differ from the PBS in composition. The growth media contain amino acids, sugars, vitamins and micronutritions, whereas PBS consists only of Na/K phosphate and NaCl. The difference in composition of the two growth media is not so large. Hence, also the ion release is similar in both media.

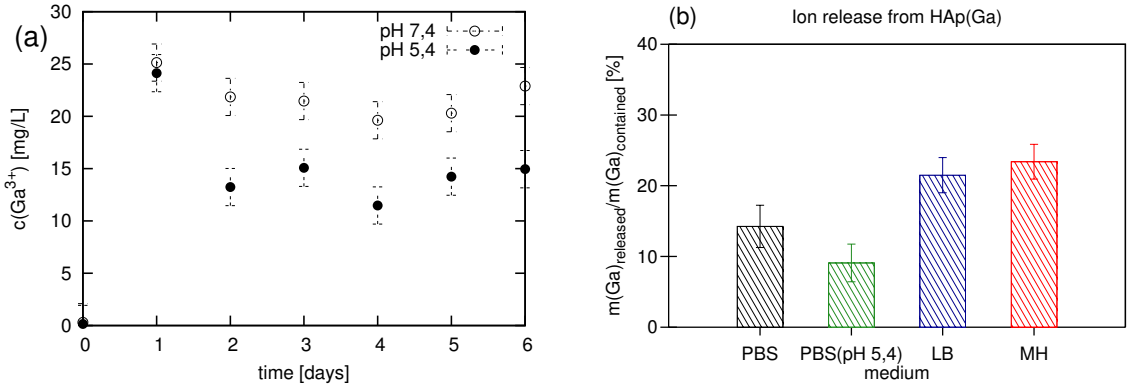


Figure 4.47: Ion release from HAp(Ga)IE16. (a) Concentration of Ga^{3+} released from 1 g/L HAp(Ga)IE16 in PBS with different pH in dependence of the time of the exposure to the medium. (b) Ion release from HAp(Ga)IE16 in different media after two-day ageings.

For comparison of HAp(Ga)CP, HAp(Ga)TR and HAp(Ga)IE, a more dynamic 10-day ion-release experiment in a Luria-Bretani growth medium (pH = 7.4) was conducted, which involved medium exchange during ageing. Ga^{3+} concentration in the medium above the

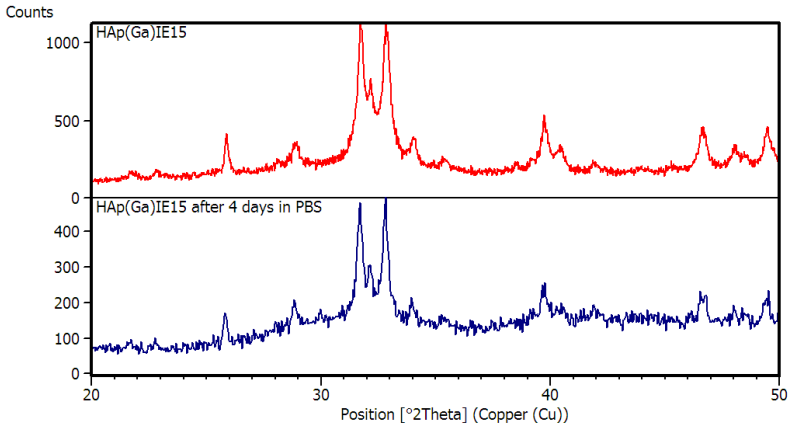


Figure 4.48: Comparison of XRD patterns of HAp(Ga)IE16 before and after ageing in PBS with pH 5.4.

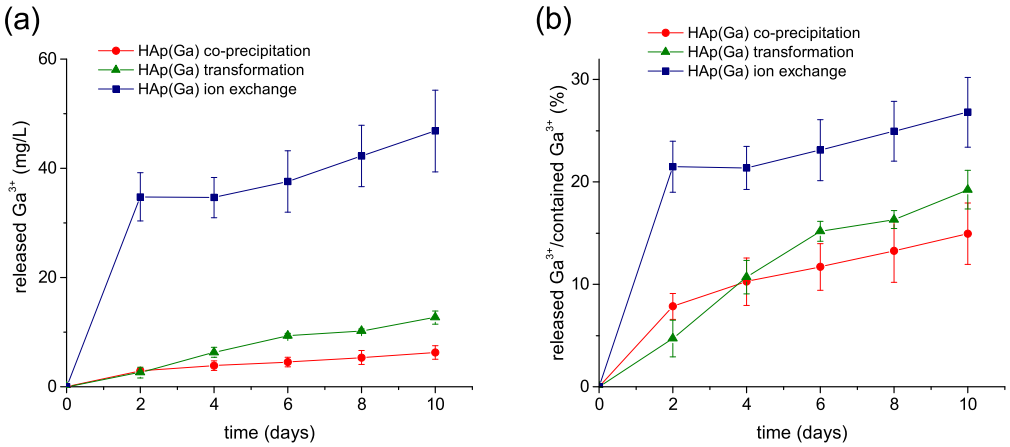


Figure 4.49: Release of Ga^{3+} ions from HAp(Ga) obtained by co-precipitation, transformation and ion exchange (16 wt % Ga) under simulated physiological conditions: (a) concentration of Ga^{3+} released during ageing of the 1 mg/mL suspensions of the three materials; (b) fraction of the contained Ga that was released into the LB growth medium.

same sample undergoing the ageing was checked every two days and fresh medium was added. The amount of released Ga^{3+} correlates with the total Ga content in the material and it increases from HAp(Ga)CP, over HAp(Ga)TR to HAp(Ga)IE. A large amount of Ga HAp(Ga)IE (with 16 wt % of Ga) was released already in the first 2 days, in contrast to the other two Ga-containing materials, which released about 7 times less Ga^{3+} ions in the same time period (Figure 4.49 a). After an initial burst release, the release of Ga^{3+} from the HAp(Ga)IE slowed down. However, it was still faster than from the HAp(Ga)CP and HAp(Ga)TR. Since the three samples contained different amounts of Ga, the kinetics of Ga release is better observed by comparing the fraction of the contained Ga(III) that is released (Figure 4.49 b). We can see that after the whole 10-day period 15–25 % of the contained Ga is released from all three materials. This occurs faster for the HAp(Ga)IE. It is interesting that HAp(Ga)CP releases more Ga than HAp(Ga)TR in the first 2 days, but then its release slows down, while for the HAp(Ga)TR it proceeds at the same rate for 6 days before slowing down, so that it reaches the same fraction as the HAp(Ga)CP in 4 days and surpasses it afterwards. In the last 4 days, the rate of Ga release is very similar for all three materials. The HAp(Ga)TR exhibits the optimum release kinetics without any initial burst release. It releases about 5 % of the initially contained Ga every two days until the sixth day and then about 5 % of the contained Ga during the next 4 days.

4.6.2 Ga@HAp

For Ga@HAp I have explored first the release of ions after mixing the EG suspension with 4 different media in 1:3 ratio (as in the sedimentation step of the synthesis but using other liquids instead of pure water). I was interested to what extent does the passivating oxide shell protect Ga NPs from dissolution in different media under physiological conditions and whether complexants of Ga(III), such as citrate, could increase the dissolution of Ga NPs in a similar way as they increase dissolution of amorphous gallium hydroxide (see Section 1.4.1). Indeed, the surface oxide layer protected well the Ga NPs against dissolution in physiological saline (9 g/L NaCl) and PBS solution, while the presence of 100 μM citrate triggered their dissolution (Figure 4.50). These results allude to a possibility of separating the released ion and nanoparticle effects during investigation of antibacterial performance of the Ga@HAp nanocomposite. Hence, in the attempt of finding a minimal growth medium, in which bacteria could grow but Ga(III) ion release would be minimised, I tested the release of Ga^{3+} ions after suspending the Ga@HAp16 powder in media with different combinations of components of the M9 minimal medium as well as in the M9 medium. This medium enables growth of bacteria but it contains only the minimal requirements for growth: glucose as the carbon source, phosphate buffer (M9PBS) for maintaining the neutral pH, essential metal ions (Na, K, Ca, Fe, Mg) and micronutrients (see Section 3.1.2 for its composition). However, the dried material revealed somewhat different results than the ethyleneglycolic suspension. The concentration of the released Ga^{3+} ions was higher (about 30 mg/L (30 % of all contained Ga) for different phosphate buffers) and no difference was observed between the PBS and the PBS+citrate medium. Therefore, I could not find a growth medium in which Ga@HAp16 would release negligible concentration of Ga^{3+} ions. Nevertheless, the ion release was still low in the NaCl (or NH_4Cl) solution and the presence of Mg^{2+} ions lowered the amount of released Ga(III). Thus, the ion release was lower (although still at 20 % of the contained Ga) in M9 medium, which is a combination of all these buffers, as well. By contrast, it was greatly increased in a MH medium reaching more than 50 % of all contained Ga.

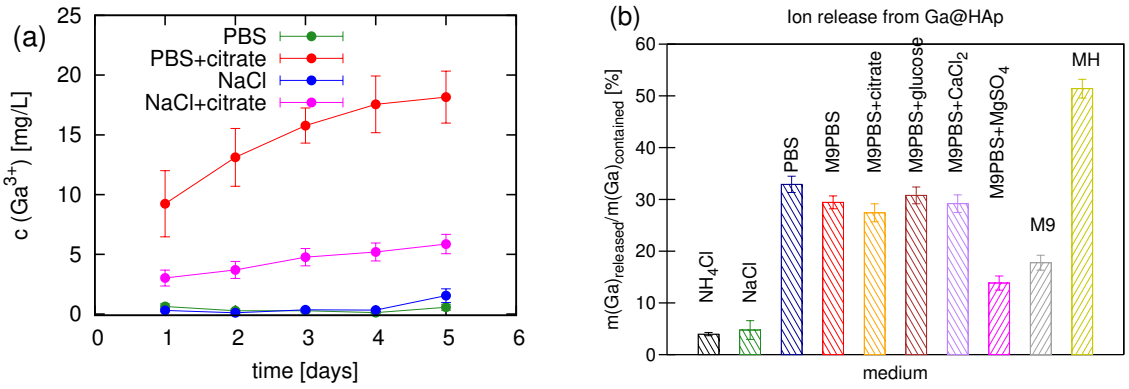


Figure 4.50: Ion release from Ga@HAp. (a) Release of Ga^{3+} from Ga@HAp by mixing the ethyleneglycolic suspension with different media; (b) Release of Ga^{3+} from Ga@HAp by resuspending the dried nanocomposite in different media.

4.6.3 Ga/Au@HAp and Ga/Au/Arg@HAp

I have compared the release of Ga^{3+} ions from the Ga/Au@HAp and the Ga/Au/Arg@HAp nanocomposite in Mueller-Hinton medium. This experiment revealed that virtually all Ga in both nanocomposites was dissolved and released as Ga^{3+} during a 24-hour shaking at 37 °C. A 0.3 g/L concentration of Ga/Au@HAp released 38.9±0.2 mg/L Ga(III), while the same concentration of Ga/Au/Arg@HAp released 43.1±0.3 mg/L Ga(III) within 24 hours of incubation. This represents 13.0 wt % of Ga/Au@HAp and 14.3 wt % of Ga/Au/Arg@HAp, or 81 % of the starting Ga content in case of Ga/Au@HAp and 89 % fraction of Ga in case of Ga/Au/Arg@HAp.

4.7 Antibacterial Action Against *P. aeruginosa*, *E. coli* and *S. epidermidis*

4.7.1 Antibacterial properties of HAp(Ga)

Most of the results presented in this section have been published in our article about HAp(Ga) [324] and some of them also in our article about Au/Arg@HAp(Ga) nanocomposite [353]. Let us first examine the antibacterial activity of the gallium-doped hydrox-

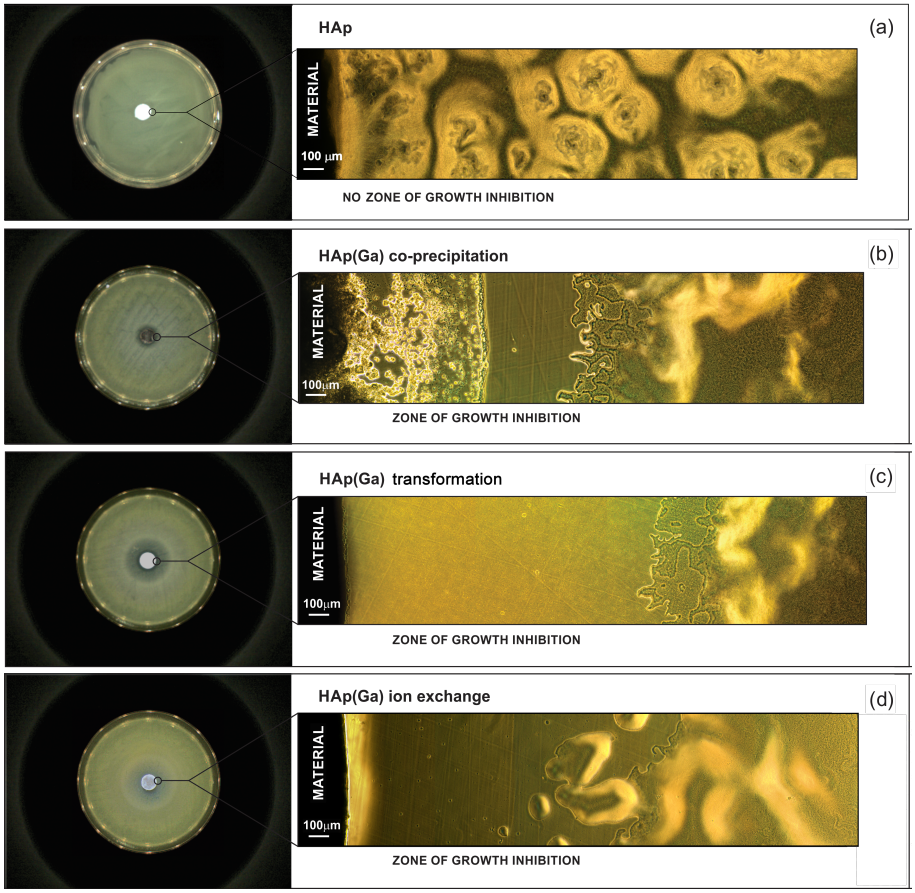


Figure 4.51: Disc diffusion antibacterial test against *P. aeruginosa* of (a) hydroxyapatite and the HAp(Ga) obtained by (b) co-precipitation, (c) transformation and (d) ion exchange, with zoomed zones of inhibition (on the right) as observed under a phase-contrast microscope.

yapatites towards the *P. aeruginosa* MW1 strain. All three materials created inhibition zones in the disc diffusion test (Figure 4.51) with the zone diameter increasing in the order HAp(Ga)CP < HAp(Ga)IE < HAp(Ga)TR, while the non-doped hydroxyapatite created no inhibition zone. The influence of the doped materials on the planktonic bacterial growth was quantified by a microdilution antibiogram assay. Whereas the non-doped hydroxyapatite enabled normal bacterial growth, exhibiting a typical growth curve, the doped materials slowed down the bacterial growth. The minimal inhibitory concentration (MIC) for HAp(Ga)IE decreased with increasing Ga(III) content from 0.3 g/L at 5 wt % Ga to 0.075 g/L at 16 wt % Ga (Figure 4.52). 0.3 g/L were found for the HAp(Ga)TR, while the HAp(Ga)CP exhibited a notably larger (0.9 g/L) MIC value (Figure 4.53). The minimal inhibitory concentrations in dependence on the Ga(III) content for all tested

HAp(Ga) materials are summarised in Figure 4.54 and seem to follow an exponential relationship. Colony counting was performed on a few higher concentrations of HAp(Ga)IE8 and HAp(Ga)IE16 that completely prevented bacterial growth and some bactericidal activity was observed (Figure 4.54), but none of the tested concentrations could be identified as a minimal bactericidal concentration (MBC). The bactericidal effect was manifested also in the morphology of some bacteria, which exhibited a deformed shape and holes in the cell wall/membrane (Figure 4.55). Such effect was not observed after the exposure to the HAp reference. I was wondering whether the bactericidal activity of the HAp(Ga)IE would be enhanced in a minimal growth medium. The results in Figure 4.56 indeed reveal a greatly decreased MIC to below 0.01 g/L for HAp(Ga)IE14 and a stronger bactericidal action leading to more than 1 logarithmic order of magnitude decrease in bacterial concentration at 0.4 g/L. Nevertheless, this concentration was still not MBC (leading to at least 3 logarithmic orders of magnitude decrease).

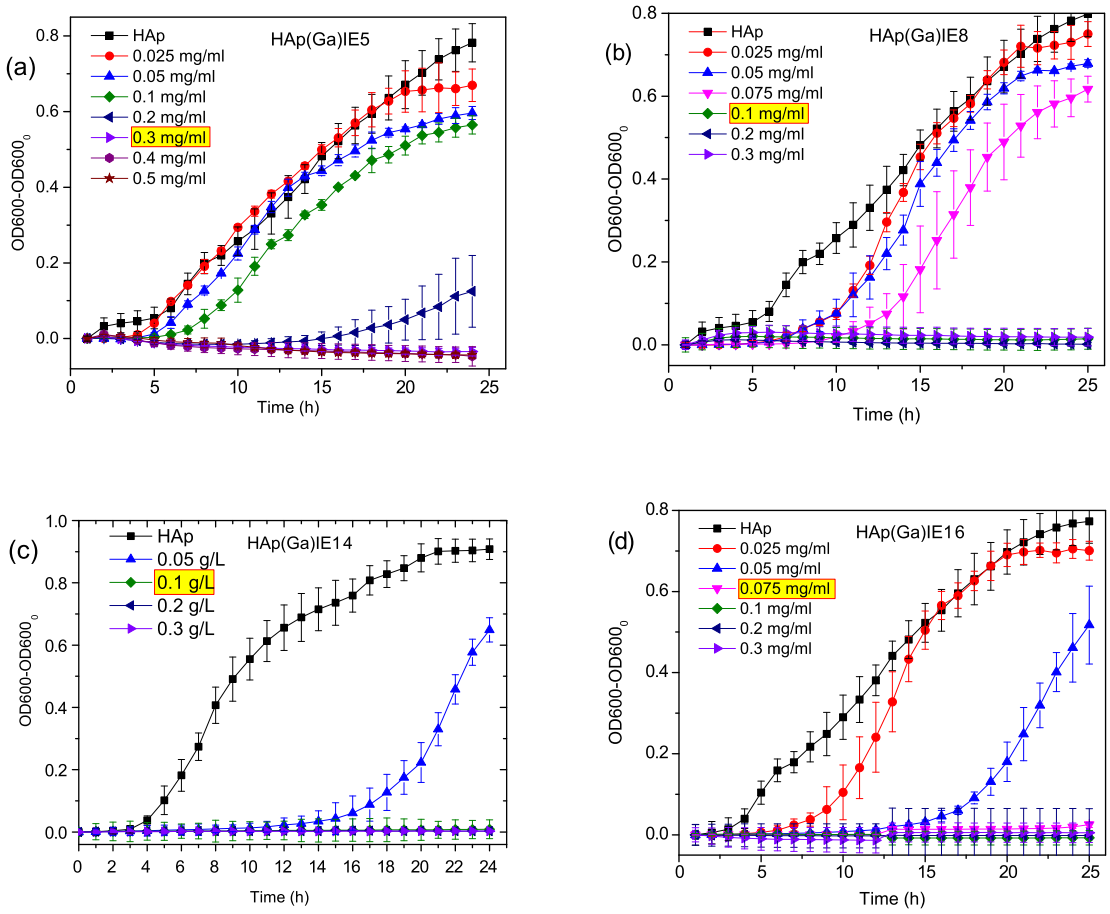


Figure 4.52: Microdilution antibiograms of different HAp(Ga)IE materials: (a) HAp(Ga)IE5, (b) HAp(Ga)IE8, (c) HAp(Ga)IE14, (d) HAp(Ga)IE16. 0.1 or 0.3 g/L HAp was the negative control. Minimal inhibitory concentrations in the legend are highlighted in yellow and surrounded by a red rectangle.

To better understand the importance of the released Ga^{3+} ions (investigated in Section 4.6.1) and the disordered Ga/Ca-phosphate surface layer (observed and characterised in Section 4.2), microdilution antibiograms were conducted also on the $Ga(NO_3)_3$·xH2O and

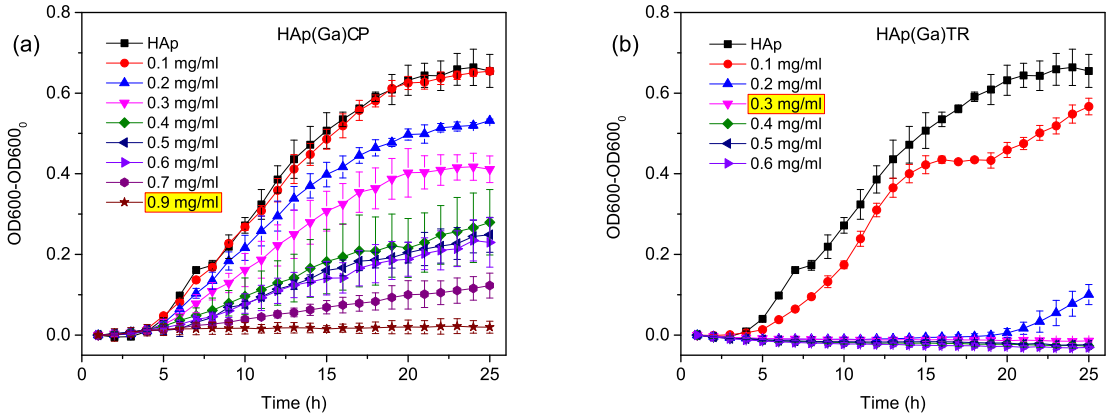


Figure 4.53: Microdilution antibacterial test against *P. aeruginosa* for the HAp(Ga) obtained by (a) co-precipitation and (b) transformation. Concentrations of the materials in the MH medium are given in the legends on the graphs. 0.3 g/L HAp was the negative control. Minimal inhibitory concentrations in the legend are highlighted in yellow and surrounded by a red rectangle.

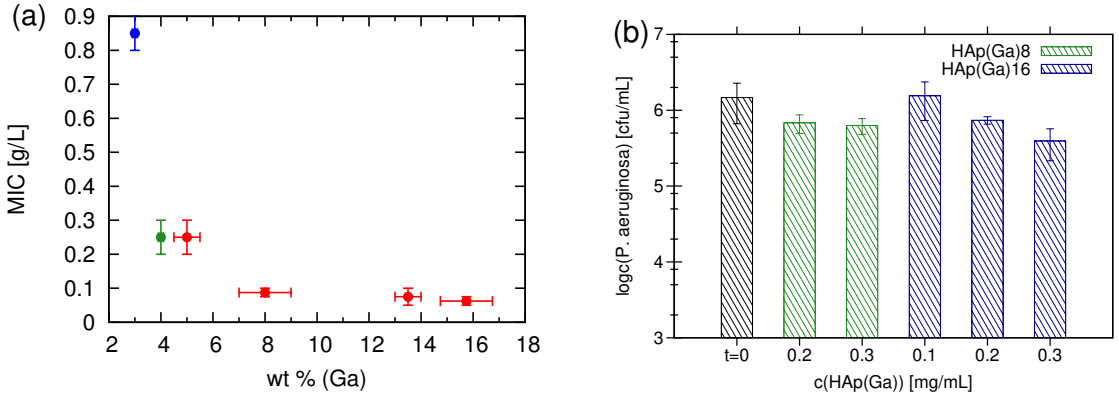


Figure 4.54: Antibacterial activity of HAp(Ga) against *P. aeruginosa*. (a) MIC in dependence of Ga(III) content. HAp(Ga)IE materials are marked red, HAp(Ga)TR green and HAp(Ga)CP blue; (b) Number of colonies after microdilution antibiograms by diluting the liquids above these samples after the 24-hour microdilution assay (Figure 4.52 (b), (d)) 10^3 times, smearing 50 μL onto the Mueller-Hinton (MH) agar plates and colony counting after incubation for 24 h. $t = 0$ represents the bacterial suspension in the beginning of the dilution antibiogram.

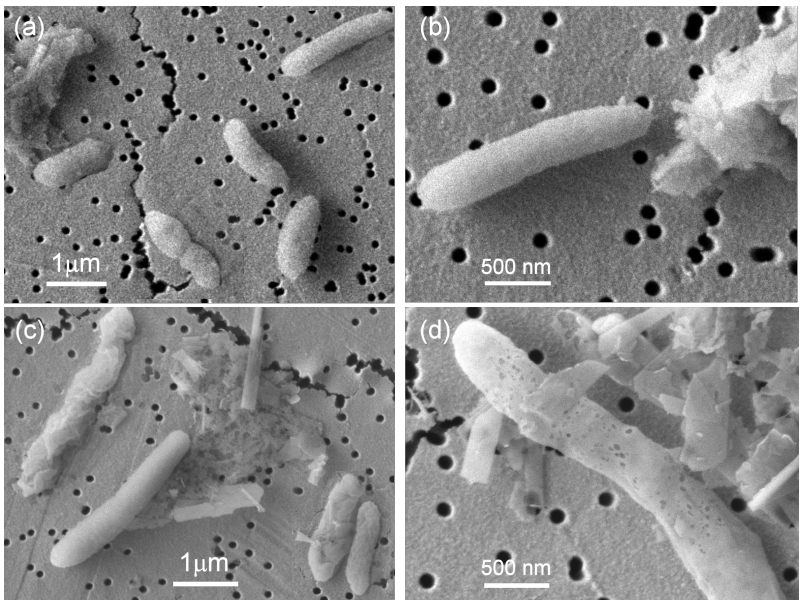


Figure 4.55: Morphology of *P. aeruginosa* bacteria exposed to (a, b) a 0.3 g/L concentration of HAp and (c, d) a 0.3 g/L concentration of HAp(Ga)IE16 material for 24 hours in a MH growth medium. 27 % of bacteria were damaged after exposure to HAp(Ga)IE16, based on examination of 190 bacteria under SEM.

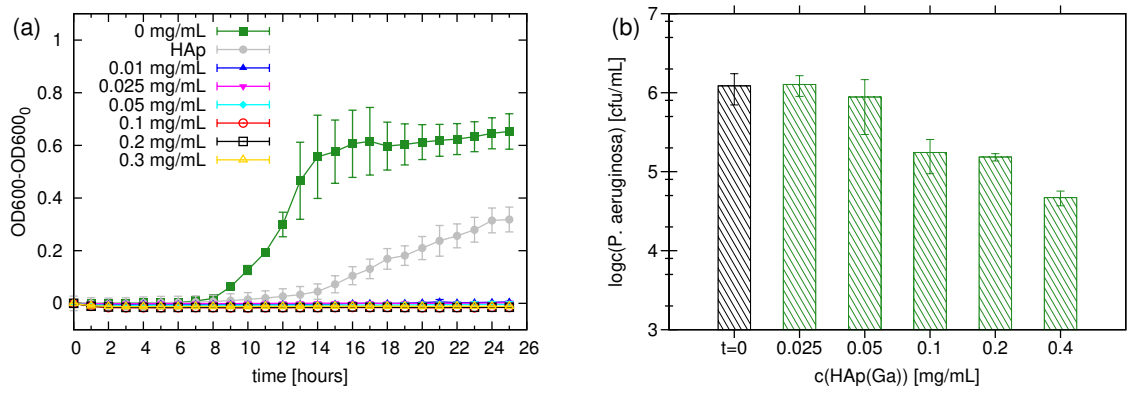


Figure 4.56: Microdilution antibiogram against *P. aeruginosa* of HAp(Ga)IE14 in M9 medium: (a) OD600 monitoring, (b) colony counting in the liquids above the material after the 24-hour microdilution antibiogram. $t = 0$ represents the starting bacterial suspension.

the amorphous $GaPO_4$, which was prepared by the precipitation of $Ga(NO_3)_3$ with a phosphate buffer (see Section 4.2 and 3.2.2). The molar concentrations were calculated by assuming $Ga(NO_3)_3 \cdot 5.5H_2O$ for gallium nitrate and $GaPO_4 \cdot 2H_2O$ for the amorphous phosphate. Gallium nitrate had a MIC at 0.075 g/L (211 μM, Figure 4.57 (a)) and gallium phosphate at 0.05 g/L (250 μM, Figure 4.57 (b)). Furthermore, the released ions from the HAp(Ga)IE16 in the PBS with pH 7.4 (Section 4.6.1) have also been tested against *P. aeruginosa* and had around 0.2 mM MIC (Figure 4.57 c).

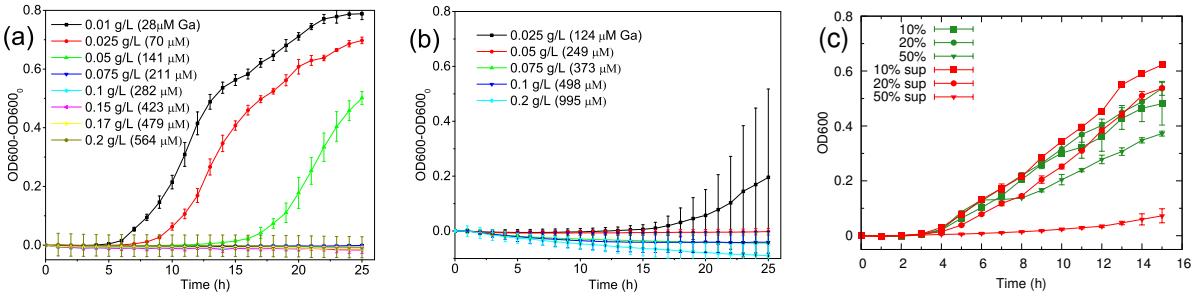


Figure 4.57: Antibacterial activity (against *P. aeruginosa* MW1) of (a) $Ga(NO_3)_3$, (b) amorphous $GaPO_4$ hydrate and (c) the supernatant after 1-day ageing of HAp(Ga)IE16 in PBS; 10 %, 20 % and 50 % volume ratio correspond to 36 μM, 72 μM and 181 μM Ga^{3+}, respectively.

After showing their antibacterial properties against *P. aeruginosa*, let us now examine the antibacterial activity of the HAp(Ga)IE materials against *E. coli*. As evident from Figure 4.58 (a, b), HAp(Ga)IE8 created no inhibition zone in a disc diffusion test against *E. coli* MG1655, not even on a minimal growth M9-agar plate. Furthermore, a microdilution assay of HAp(Ga)IE14 has revealed a very high MIC value (4 g/L), around 50 times higher than for the *P. aeruginosa* (Figure 4.58 (d)). On the other hand, $Ga(NO_3)_3$ created a wide inhibition zone also in *E. coli* (Figure 4.58 (c)), which indicates that this bacteria is sensitive to gallium but much higher concentrations are required for effective inhibition. I have also done a disc diffusion antibiogram of HAp(Ga)IE5 against *S. epidermidis* and no inhibition zone was observed, indicating that the antibacterial performance is low towards this type of bacteria as well (Figure 4.59 (a)). The same material created an inhibition zone against *P. aeruginosa* (Figure 4.59 (b)).

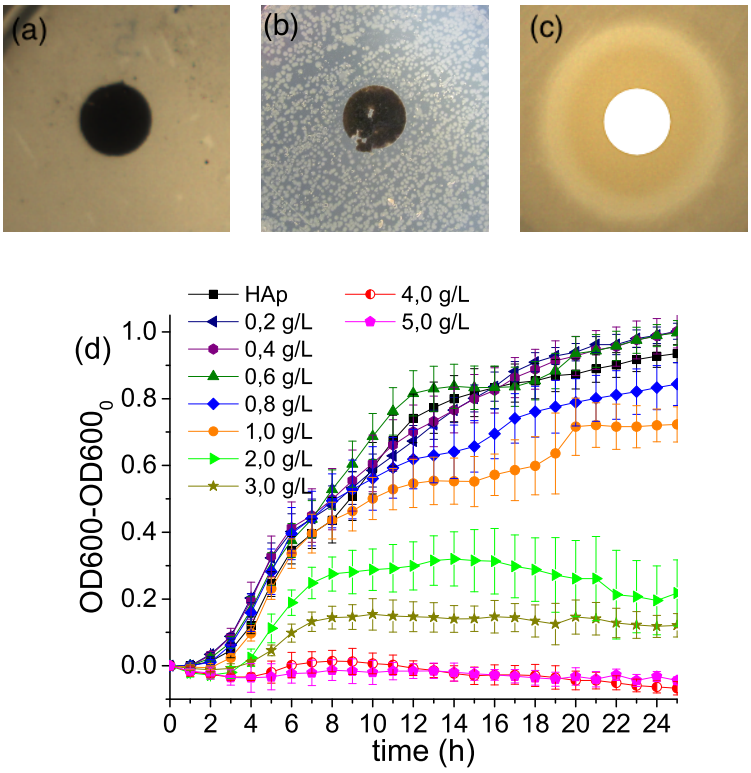


Figure 4.58: Antibacterial properties against *E. coli*: (a) disc diffusion antibiogram of HAp(Ga)IE8 on a MH-agar plate, (b) disc diffusion antibiogram of HAp(Ga)IE8 on a M9-agar plate, (c) disc diffusion test of $Ga(NO_3)_3 \cdot xH_2O$ on a MH-agar plate and (d) microdilution antibiogram of HAp(Ga)IE14 in MH broth.

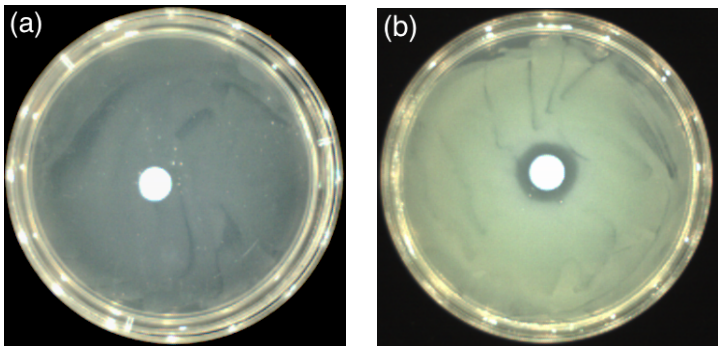


Figure 4.59: Disc diffusion antibiogram of HAp(Ga)IE5 against (a) *S. epidermidis* and (b) *P. aeruginosa*.

4.7.2 Antibacterial action of Au/Arg@HAp(Ga)

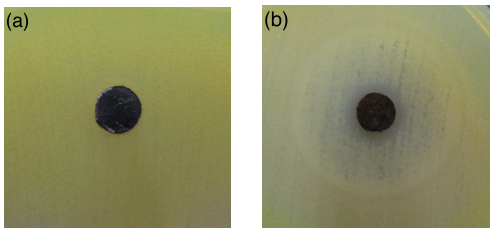


Figure 4.60: Disc diffusion antibiogram against *P. aeruginosa*: Au/Arg@HAp (left) and Au/Arg@HAp(Ga)IE (right).

As with the HAp(Ga) materials, I will first present the results of antibacterial tests for the Au/Arg@HAp and Au/Arg@HAp(Ga) materials with respect to the *P. aeruginosa* strain and then continue with the results on the other two types of bacteria. On the agar plate with *P. aeruginosa*, inhibition zones were observed in the case of Au/Arg@HAp(Ga) but not for the Au/Arg@HAp nanocomposite (Figure 4.60).

I further quantified the antibacterial action against *P. aeruginosa* by a microdilution antibiogram. Au/Arg@HAp(Ga) exhibited complete inhibition of growth above a certain concentration depending on their HAp(Ga) precursor (0.1 g/L for the Au/Arg@HAp(Ga)IE16, 0.3 g/L for the Au/Arg@HAp(Ga)IE4 and 0.2 g/L for the Au/Arg@HAp(Ga)TR), while even 1 mg/mL of Au/Arg@HAp (without gallium ions) could not completely prevent the growth of *P. aeruginosa* MW1 (Figure 4.61). The MIC values of the Au/Arg@HAp(Ga) nanocomposites are the same as for their corresponding HAp(Ga) materials, which indicates that the antibacterial action against *P. aeruginosa* mostly originates from the Ga(III) incorporation with little contribution of the functionalised Au NPs. By contrast, both the Au/Arg@HAp and the Au/Arg@HAp(Ga) nanocomposites created inhibition zones against *E. coli* as well as *S. epidermidis* (Figures 4.62 and 4.63). This implies that antibacterial action against these two types of bacteria comes primarily from the functionalised nanogold, since HAp(Ga) materials did not exhibit such action (Section 4.7.1). These interesting observations were presented to the scientific public in our article in 2017 [353].

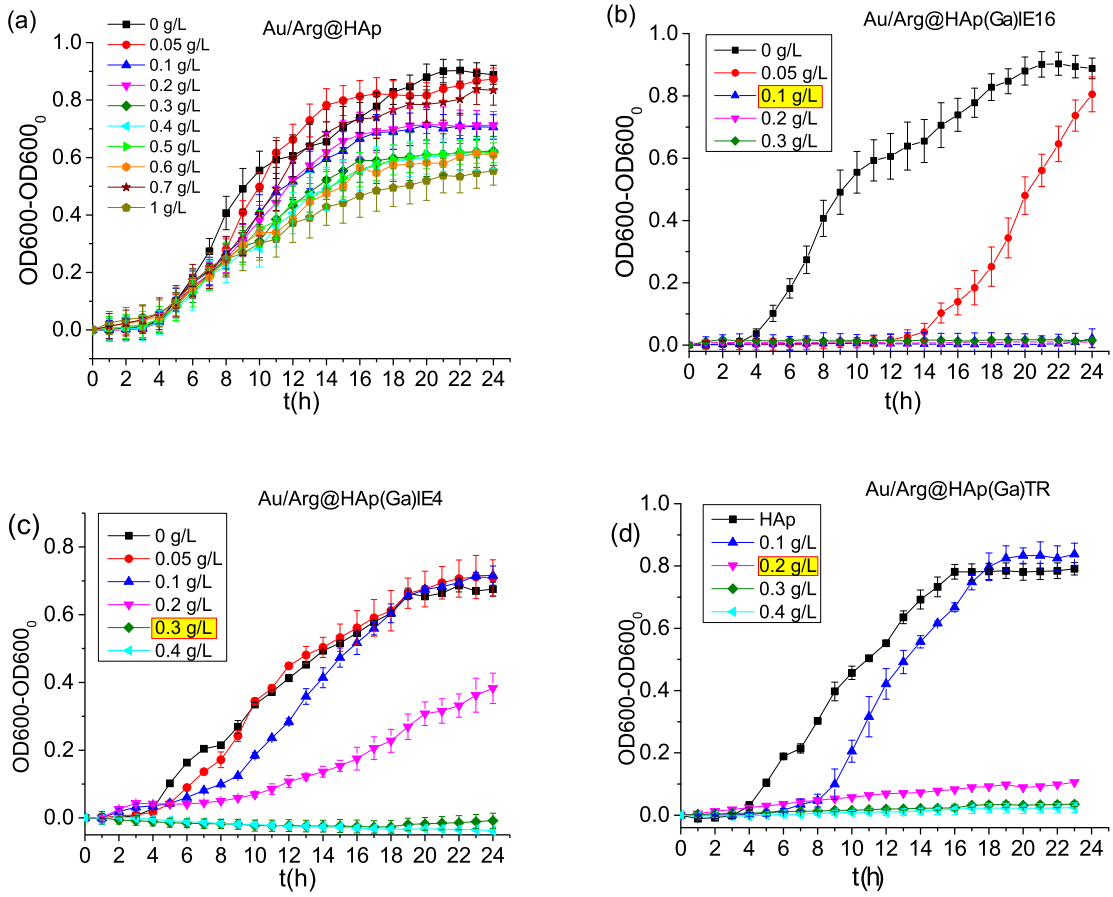


Figure 4.61: Dilution antibiogram assay against *P. aeruginosa* MW1: (a) Au/Arg@HAp14, (b) Au/Arg@HAp(Ga)IE16, (c) Au/Arg@HAp(Ga)IE4, (d) Au/Arg@HAp(Ga)TR. Minimal inhibitory concentrations in the legend are highlighted in yellow and surrounded by a red rectangle.

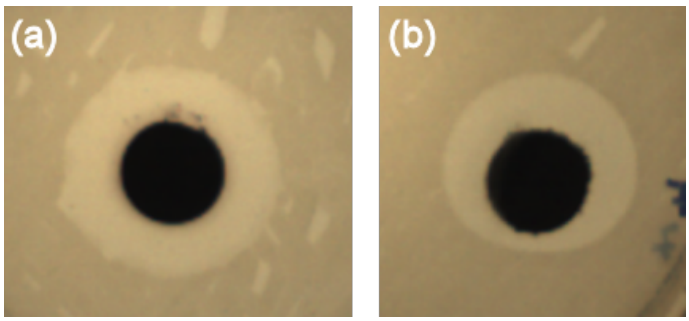


Figure 4.62: Disc diffusion antibiogram of (a) Au/Arg@HAp(Ga)TR and (b) Au/Arg@HAp14 against *E. coli*.

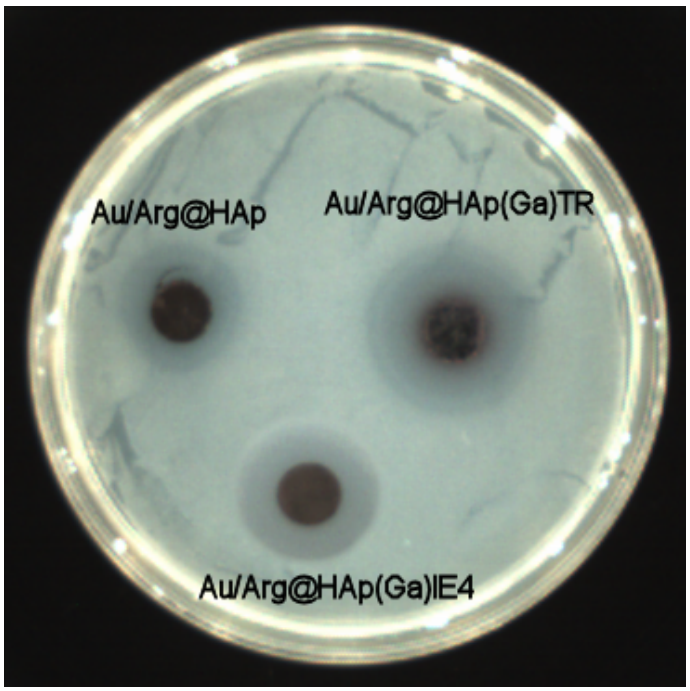


Figure 4.63: Diffusion antibiogram assay against *S. epidermidis*: Au/Arg@HAp, Au/Arg@HAp(Ga)TR and Au/Arg@HAp(Ga)IE4.

4.7.3 Antibacterial action of Ga@HAp nanocomposites

4.7.3.1 Antibacterial action of Ga@HAp16 against *P. aeruginosa*

The antibacterial properties of Ga nanoparticles on HAp were mainly tested on the *P. aeruginosa* MW1 strain and these results were published in 2016 [352]. In a disc diffusion test the Ga@HAp16 created an inhibition zone while the pure HAp reference did not (Figure 4.64 (a),(b)). A small section (3.4 × 0.6 mm) of the inhibition zone was further

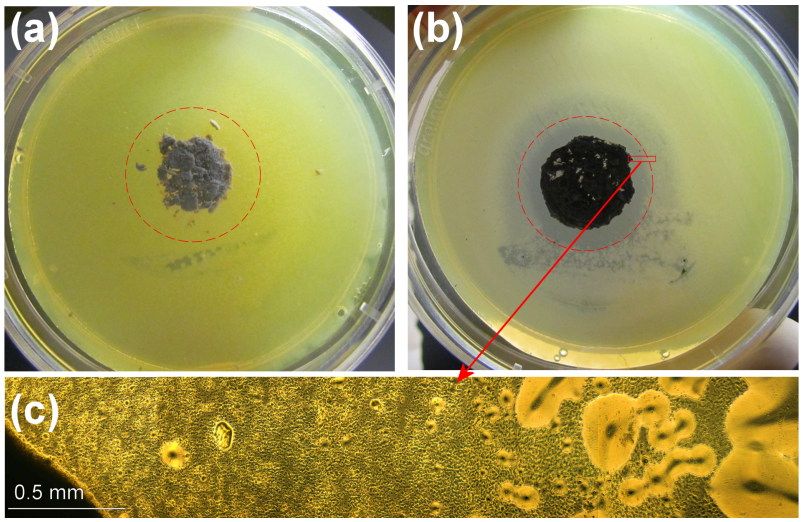


Figure 4.64: Antibacterial properties of the Ga@HAp nanocomposite against *P. aeruginosa* MW1. Diffusion antibiograms of (a) hydroxyapatite and (b) Ga@HAp; (c) phase-contrast micrograph of a small section (red rectangle in (b)) of the inhibition zone with Ga@HAp on the left-hand side (black) and bacterial colonies on the right-hand side.

observed under a phase-contrast microscope (Figure 4.64 (c)). It exhibits a gradual change of density for the bacterial colonies, induced by the material, starting from the almost clean region next to the material (black disc in Figure 4.64 (c)) over a few yellow circles (the material-influenced, non-grown colonies) to the dense vital bacterial colonies on the right-hand side of the figure, farthest away from the material.

The antibacterial action was quantified by a microdilution assay (Figure 4.65). The Ga@HAp16 was tested in the concentration range from 0.01 mg/mL to 1.0 mg/mL with the pure MH growth medium and a 0.5 g/L HAp suspension as negative controls. The growth medium with no material, the HAp and Ga@HAp16 concentrations below 0.1 mg/mL show a distinct growth curve, while the absence of such curve at higher concentrations represents a complete inhibition of growth (Figure 4.65 (a)). Hence, the minimal inhibitory concentration (MIC) is at 0.1 mg/mL for the Ga@HAp16. For comparison, a nanocomposite of silver nanoparticles and hydroxyapatite (Ag@HAp; see Section 4.4.4) was also tested on the same bacteria and in the same conditions (Figure 4.65 (b)). The obtained MIC value for Ag@HAp (0.2 g/L or 0.4 mM Ag) was higher than the MIC value of Ga@HAp16 (0.1 g/L or 0.2 mM Ga). The 1000x diluted bacterial suspensions above the sedimented Ga@HAp16 samples after the microdilution test were spread onto a Mueller-Hinton agar plate and the grown colonies after a 24-hour incubation at 37 °C were counted. A bactericidal effect was observed above the MIC value with a significant (1000x) reduction in the number of bacteria above 0.5 mg/mL (Figure 4.66).

The survivability of the bacteria after incubation with the material (growth medium without material and the HAp were negative controls) was additionally analysed using a

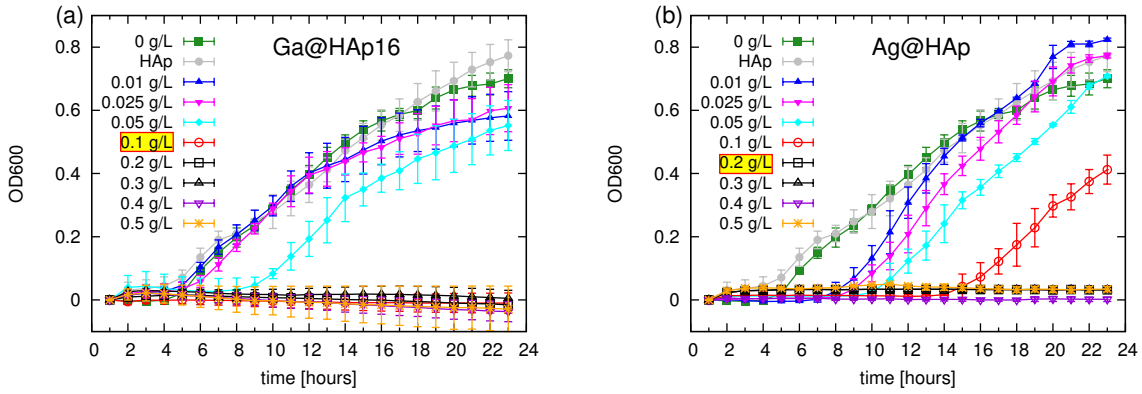


Figure 4.65: Dilution antibiogram assay of (a) Ga@HAp and (b) Ag@HAp nanocomposite against *P. aeruginosa* MW1. Mueller-Hinton (MH) growth medium without any material (0 mg/mL) and 0.1 mg/mL HAp were taken as the controls. Minimal inhibitory concentrations in the legend are highlighted in yellow and surrounded by a red rectangle.

fluorescent dye live/dead assay that stained all cells (live and dead) green and dead cells red. In the growth medium without any material, or with the HAp, many more bacteria grew and the majority of them were alive (Figure 4.67 (a)-(c)), while in the presence of the Ga@HAp16 some bactericidal effect could be observed resulting in clusters of dead bacteria (Figure 4.67 (d)-(f)).

The morphological characteristics of the bacteria after a 24-hour incubation with HAp and with Ga@HAp16 were examined under a scanning electron microscope (Figure 4.68). The presence of the Ga@HAp16 during the bacterial growth led to a much lower number of bacterial cells and a decreased amount of well-preserved cells in comparison with the HAp (a negative control). In addition, a change in the structure of the dead bacteria was noticed. The dead bacteria that were exposed to the Ga@HAp16 exhibited holes in their cell wall and total rupture of the outer membrane. Such damage in bacteria was not observed if they were exposed to the HAp material (Figure 4.68).

Even though the ion release was diminished in the minimal M9 medium (see Section 4.6.2), the antibacterial performance of the Ga@HAp16 nanocomposite in this medium was enhanced (Figure 4.69). Nevertheless, the bactericidal effect was very similar as in the MH medium.

So far, I have presented only the results pointing out the antibacterial action that seems not to be related to the release of ions. However, as we have seen in Section 4.6.2, more than 50 % of the contained Ga is released already in a 24-hour incubation. To evaluate the contribution of the released Ga^{3+} ions to the antibacterial effect of the Ga@HAp16, I have conducted additional antibacterial tests on the liquids containing the released ions. Microdilution antibiograms for the media based on the PBS of the M9 growth medium are shown in Figure 4.70. All 5 media (M9PBS, M9PBS+citrate, M9PBS+$CaCl_2$, M9PBS+glucose and M9PBS+$MgSO_4$) by themselves caused no inhibition while the supernatants containing Ga ions inhibited the growth of *P. aeruginosa* at 20-50% already. By considering the concentration of Ga^{3+} ions in these media, we arrive at 0.2 mM MIC for the M9PBS and M9PBS+$CaCl_2$, and around 0.1 mM MIC for the M9PBS+citrate, M9PBS+glucose and M9PBS+$MgSO_4$. These results stress the importance of the dissolution of the Ga NPs and the Ga^{3+} ion release for the antibacterial action of the Ga@HAp nanocomposite. Nevertheless, the dilution antibiogram of the released ions in the MH medium showed weaker antibacterial action in comparison with the released ions in the

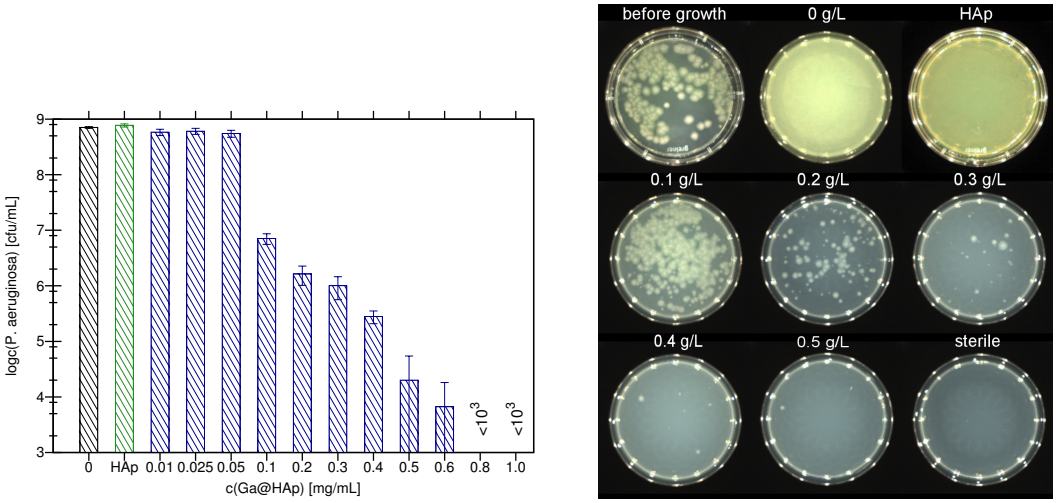


Figure 4.66: Colony counting after dilution antibiograms. Bacterial concentrations on the left-hand image for the growth medium without any material (0), HAp and Ga@HAp concentrations below 0.1 mg/mL were calculated by multiplying the OD600 values with $1{\cdot}10^9$ cfu/mL. For higher Ga@HAp concentrations the bacterial concentration was obtained by diluting the liquids above these samples after the 24-hour microdilution assay (Figure 4.65 (a)) 10^3 times, smearing 50 μL onto the Mueller-Hinton (MH) agar plates and colony counting after incubation for 24 h. The representative agar plates with colonies are shown in the right-hand image. Sterile MH growth medium (sterile), growth medium with *P. aeruginosa* and without material (0 g/L) before ($5{\cdot}10^5$ cfu/mL) and after the microdilution antibiogram, and 0.5 g/L HAp are put for comparison.

phosphate buffered media and these ions could not completely inhibit the growth of *P. aerugnosa* even at 218 μM concentration (Figure 4.71 (a)). Moreover, if we compare the growth curve of the Ga@HAp16 MIC with the corresponding curves for the released ions in the MH medium and $Ga(NO_3)_3$ (at concentrations similar to the concentration of Ga^{3+} released from the 0.1 g/L Ga@HAp16), we clearly see that the antibacterial action of the Ga@HAp16 is not only a consequence of the released ions and nanoparticles are required to achieve the high efficiency of the Ga@HAp16 (Figure 4.71 (b)).

Figure 4.67: Survivability of P. aeruginosa MW1. (a)-(c): uorescence (green (b) and red (c) and phase-contrast (a) microscope analysis of bacterial survival in the absence of any material; (d)-(f): uorescence (green (e) and red (f)) and phase-contrast (d) microscope analysis of bacterial survival after 24-hour incubation with 0.2 mg/mL of Ga@HAp.

Figure 4.68: Bacterial morphology. (a), (b), (c) SEM image of P. aeruginosa MW1 after 24-hour incubation in growth medium with 0.5 mg/mL hydroxyapatite; (d), (e), (f) SEM image of P. aeruginosa MW1 after 24-hour incubation in growth medium with 0.1 mg/mL of Ga@HAp. 51 % of the observed bacteria after exposure to Ga@HAp exhibited destroyed cell wall, according to the examination of 130 bacteria under a SEM.

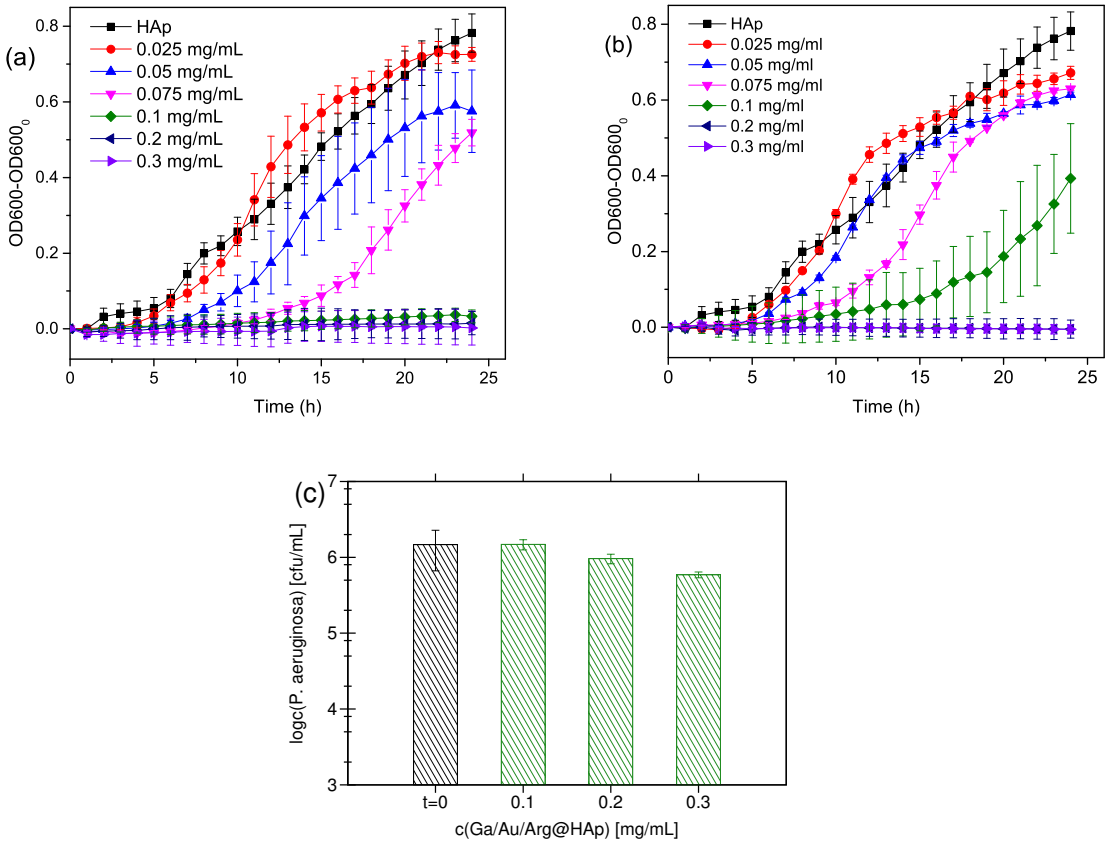


Figure 4.77: Microdilution antibiogram of Ga/Au/Arg@HAp (a) and Ga/Au@HAp (b) against *P. aeruginosa*; (c) colony counting in the liquids above the Ga/Au/Arg@HAp material after the 24-hour microdilution antibiogram. $t = 0$ represents the starting bacterial suspension.

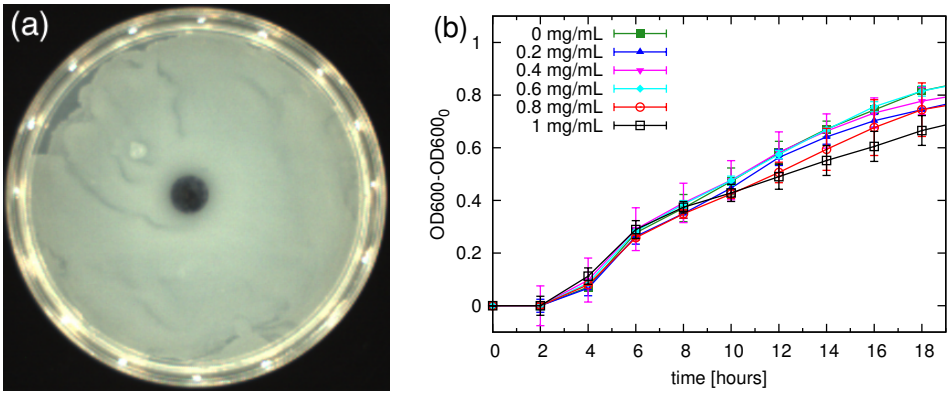


Figure 4.78: Diffusion antibiogram (a) and microdilution antibiogram (b) for the Ga/Arg/Au/Arg@HAp nanocomposite against *E. coli*.

4.8 *In vitro* Cytotoxicity

4.8.1 HAp(Ga)

Since the HAp(Ga)TR and HAp(Ga)IE materials were the most efficient in terms of antibacterial action, they were further investigated for toxicity against mammalian cells. The cytotoxicity of HAp(Ga)TR and HAp(Ga)IE (8 wt % Ga) in comparison with the non-doped HAp was examined against the mouse fibroblast cell line (L929) in the concentration range 0–1 g/L. Both HAp(Ga) materials enabled good cell survivability at MIC for *P. aeruginosa* (Figure 4.79 a). For HAp(Ga)TR the concentration of the material that stopped the growth of *P. aeruginosa* resulted in more than 80 % of surviving fibroblast cells, while for the HAp(Ga)IE8 it was above 70 %. However, HAp(Ga)IE exhibited rapidly increasing toxicity above MIC leading to a less than 50 % survival at concentrations of about four times MIC, while HAp(Ga)TR enabled a survivability comparable to HAp across the whole studied concentration range. Moreover, HAp(Ga)IE material with larger Ga content (14 wt %) was toxic already below MIC (less than 40 % survivability at 0.05 g/L concentration, Figure 4.79 b). Nevertheless, a study of the influence of the Ga content in the HAp(Ga)IE material on its cytotoxicity (Figure 4.79 b) shows that with decreasing Ga(III) content also the toxicity of a HAp(Ga)IE material is decreasing. However, as seen in Section 4.7.1, the antibacterial efficiency is decreasing with decreasing Ga(III) content as well. It seems that these properties are decreasing in a similar trend so that the thera-

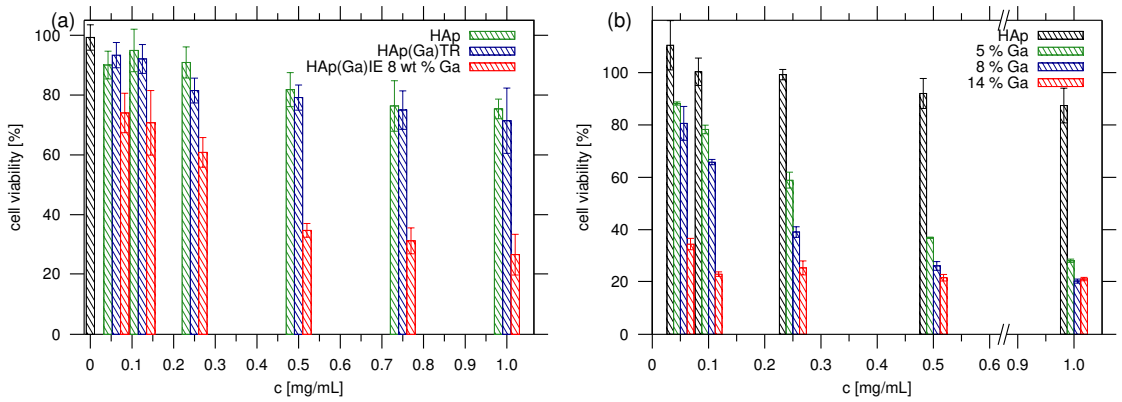


Figure 4.79: Cytotoxicity with respect to L929 mouse fibroblasts: (a) HAp(Ga)TR (MIC=0.3 g/L) in comparison with HAp(Ga)IE that contained 8 wt % Ga (MIC=0.1 g/L); (b) comparison of three HAp(Ga)IE with different Ga contents: 5 wt % (MIC=0.3 g/L), 8 wt % (MIC=0.1 g/L) and 14 wt % Ga (MIC=0.1 g/L). HAp was the negative control.

peutic window of HAp(Ga)IE remains narrow even at lower Ga(III) contents. The toxicity of HAp(Ga)IE8 and HAp(Ga)IE14 to mammalian cells was confirmed also in U2OS human osteosarcoma cells (Figure 4.80 (a)). While the survivability of these cells in the presence of the HAp(Ga)IE8 material was still good at its MIC value (0.1 g/L), it dropped to 50 % at 0.5 g/L. On the other hand, it was as low as 30 % already at the MIC value in case of HAp(Ga)IE14.

In order to explore the source of increased toxicity in the HAp(Ga)IE system, additional investigation of the contribution of the higher concentration of released Ga^{3+} ions as well as the contribution of an additional surface amorphous $GaPO_4$ phase present in the HAp(Ga)IE was performed. The amorphous gallium phosphate was more toxic than the gallium nitrate, so that at a 500-μM concentration only about 40 % of the cells were

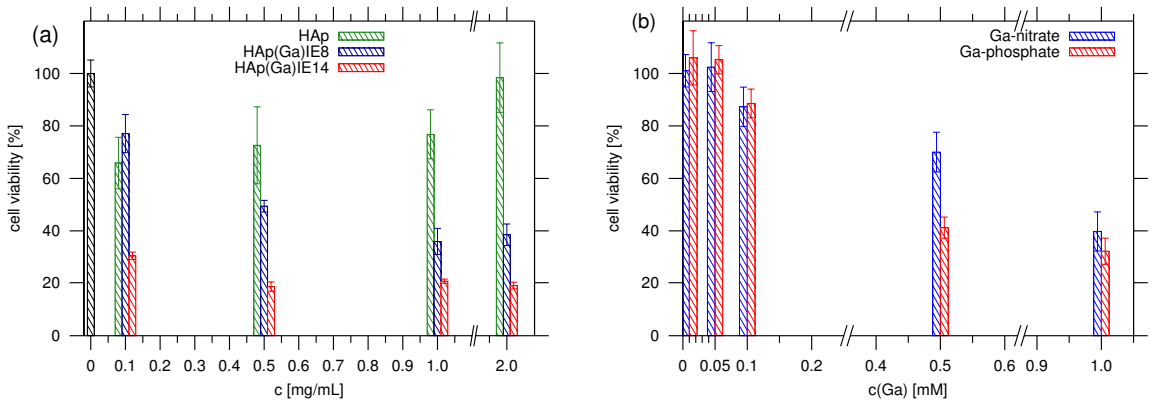


Figure 4.80: (a) Cytotoxicity of HAp(Ga)IE8 (MIC=0.1 g/L) and HAp(Ga)IE14 (MIC=0.1 g/L) with respect to U2OS human osteosarcoma cells. HAp is the negative control; (b) Cytotoxicity of $Ga(NO_3)_3$ (blue) and amorphous $GaPO_4$ hydrate (red) against L929 mouse fibroblasts.

alive in the presence of gallium phosphate in comparison with about 70 % of live cells in the presence of gallium nitrate (Figure 4.80 (b)). These results indicate that the rapidly increasing toxicity of the HAp(Ga)IE system with increasing Ga content is driven by the existence of the amorphous $GaPO_4$ phase that is concentrated at the surface. On the other hand, the investigation of cellular growth in the presence of the released ions from the HAp(Ga)IE15 material (Figure 4.81) points to the cytotoxicity of the released Ga(III). The survivability of both L929 and U2OS cells dropped to 50 % at 20 vol. %, which corresponds to around 60 μM Ga(III) concentration. Pure PBS did not affect the cell survivability at any volume fraction. As we recall, the MIC against *P. aeruginosa* for the PBS with released Ga(III) from HAp(Ga)IE15 was above (but close to) 181 μM (Section 4.7.1). Thus, the released Ga^{3+} ions from the HAp(Ga)IE15 exhibited higher toxicity for mammalian cells than bacterial cells. Moreover, their cytotoxicity is much higher than the cytotoxicity of $Ga(NO_3)_3$.

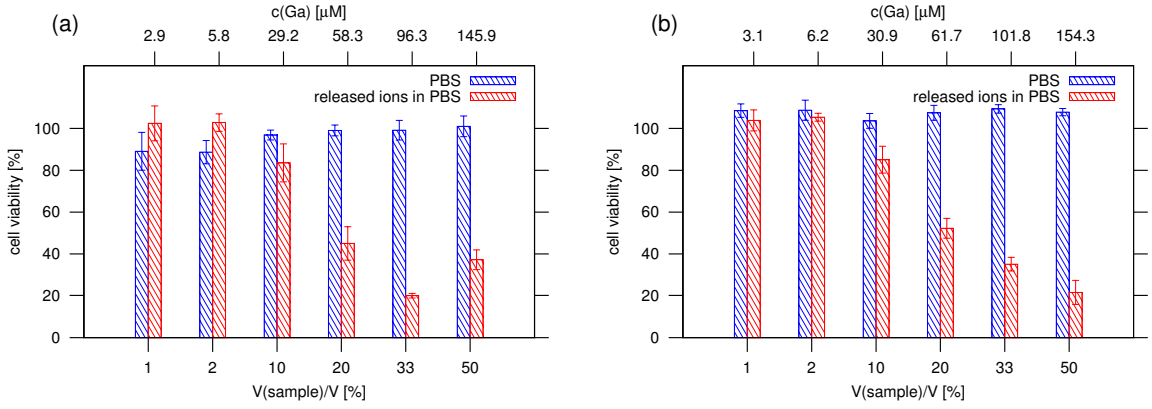


Figure 4.81: Cytotoxicity of the released Ga(III) from the HAp(Ga)IE: (a) Cytotoxicity of the liquid after 5-day ageing of HAp(Ga)IE15 in PBS for U2OS osteosarcoma cells; (b) Cytotoxicity of the liquid after 3-day ageing of HAp(Ga)IE15 in PBS for L929 mouse fibroblast cells.

4.8.2 Au/Arg@HAp(Ga) nanocomposite

The Au/Arg@HAp(Ga) nanocomposites, for which the antibacterial properties were presented in Section 4.7.2, were tested for their cytocompatibility with L929 murine fibroblast cells. The Au/Arg@HAp nanocomposite without Ga^{3+} ions was used as a reference. Its low cytotoxicity has been previously shown in IMR-90 human lung fibroblast and U2OS osteosarcoma cells and it has been confirmed in the L929 cell line by the results presented here (Figure 4.82). On the other hand, the cytotoxicity of the Ga(III)-containing nanocomposites correlated well with cytotoxicity of their HAp(Ga) precursors (Figure 4.82). Thus, the survivability of the L929 cells was below 40 % already at the 0.1 g/L concentration (MIC against *P. aeruginosa*) for the Au/Arg@HAp(Ga)IE16 and at 0.25 g/L (also close to MIC against *P. aeruginosa*) for the Au/Arg@HAp(Ga)IE4 nanocomposite. However, the Au/Arg@HAp(Ga)TR nanocomposite enabled the survival of more than 80 % of cells even at 0.5 g/L and led to 50 % survivability at 0.75 g/L concentration (Figure 4.82 c). Thus, this material has a useful therapeutic window from 0.2 to 0.75 g/L if *P. aeruginosa* bacteria are considered. The high cytotoxicity of the Au/Arg@HAp(Ga)IE16 was confirmed in the U2OS osteosarcoma cells (Figure 4.82 (d)).

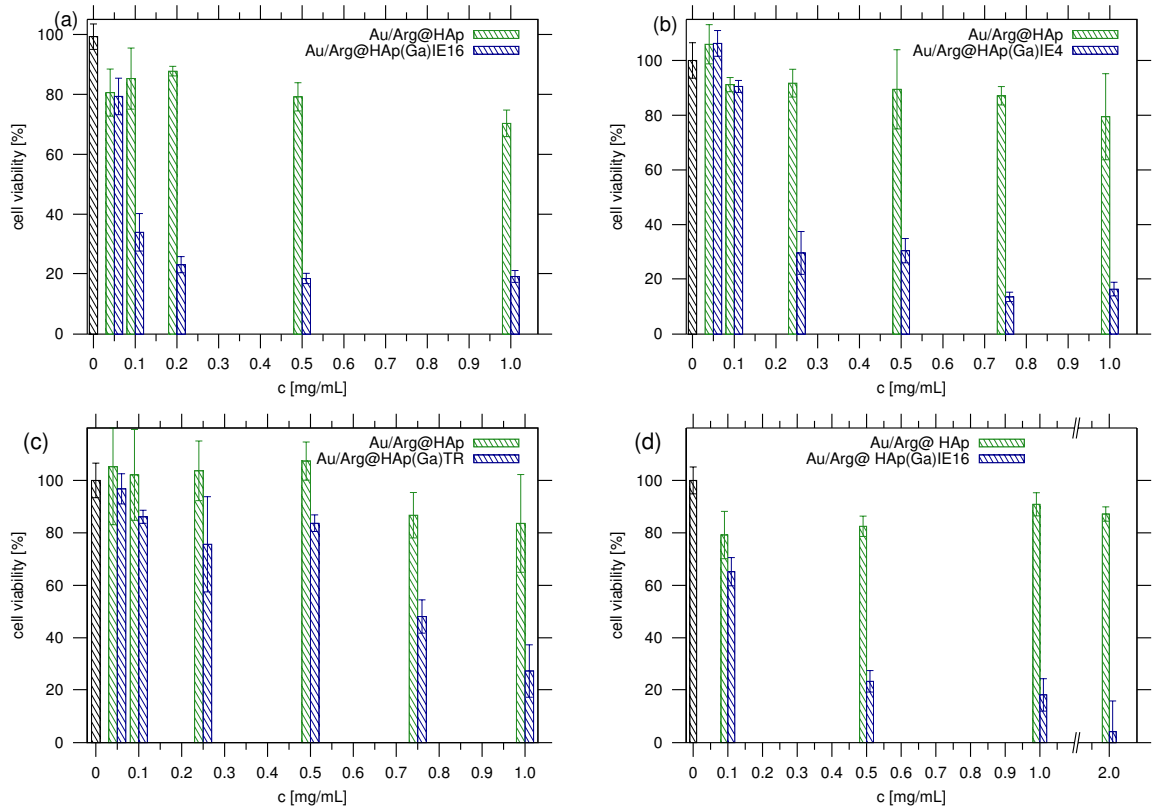


Figure 4.82: Cell viability of L929 in dependence of material concentration: (a) Au/Arg@HAp10 and Au/Arg@HAp(Ga)IE16; (b) Au/Arg@HAp14 and Au/Arg@HAp(Ga)IE4; (c) Au/Arg@HAp14 and Au/Arg@HAp(Ga)TR. (d) Cell viability of U2OS in dependence of material concentration: Au/Arg@HAp(Ga)IE16 in comparison with Au/Arg@HAp10.

4.8.3 Ga@HAp nanocomposite

The cytocompatibilty of the Ga@HAp16 nanocomposite with mammalian cells was investigated by *in vitro* cell viability tests on IMR-90 human lung fibroblasts and L929 mouse fibroblasts (Figure 4.83). Different concentrations from 0.1 to 1 g/L were tested and the results for the Ga@HAp16 nanocomposite were compared with the HAp and the Ag@HAp and their minimal inhibitory concentrations. IMR-90 cell viability is high even for 0.5 mg/mL Ga@HAp16, which is five times higher than MIC, and above 60 % at 0.75 g/L, while it drops to 50 % at 1 mg/mL (Figure 4.83 (a)). On the other hand, L929 survived

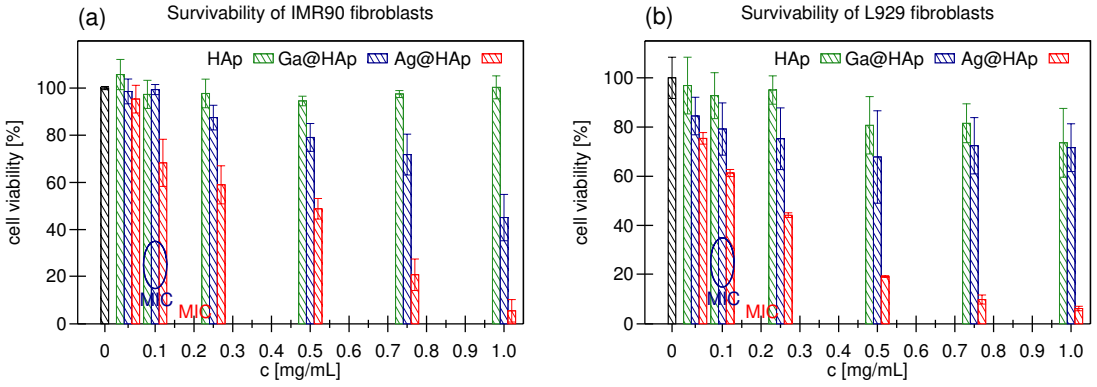


Figure 4.83: Cytotoxicity assays. (a) Survivability of IMR-90 human lung fibroblasts after 24-hour growth in the presence of the HAp (green), Ga@HAp16 (blue) and Ag@HAp (red) materials; (b) Survivability of L929 mouse fibroblasts after 24-hour growth in the presence of the HAp (green), Ga@HAp16 (blue) and Ag@HAp (red) materials. Minimal inhibitory concentration (MIC) for *P. aeruginosa* MW1 of the Ga@HAp nanocomposite is circled and indicated in blue while the MIC of the Ag@HAp is indicated in red. Figure published in ref. [352].

very well also in the presence of the 1 g/L Ga@HAp16 (Figure 4.83 (b)). By contrast, the Ag@HAp (containing the same chemical amount of antibacterial substance) revealed toxic properties already very near its MIC value and decreased the survivability of L929 below 50 % at 0.25 g/L (Figure 4.83 (b)). Evidently higher toxicity of Ag@HAp in comparison with Ga@HAp16 was observed also for the IMR-90 cell line with around 60 % survivability at 0.25 g/L and below 50 % at 0.5 g/L (Figure 4.83 (a)). By considering also minimal inhibitory concentrations for *P. aeruginosa* (see Section 4.7.3.1), Ga@HAp16 shows the desired properties of antibacterial action and low cytotoxicity in the concentration range from 0.1 to 1 mg/mL, which is a much wider therapeutic window than in case of Ag@HAp nanocomposite with antibacterial action and low cytotoxicity in the concentration range from 0.2 to 0.25 mg/mL.

Additionally, also the generation of reactive oxygen species (ROS) in the L929 mouse fibroblasts was examined (Figure 4.84). In the first experiment, a 0.5 g/L Ga@HAp16 concentration was tested, cell growth medium and hydroxyapatite were the negative controls and menadione was tested as a positive control. No significant difference in the ROS release was detected between hydroxyapatite and the Ga@HAp16, which confirmed the expected non-ROS and non-toxic antibacterial action of Ga nanoparticles. We need to point out that the ROS test was done at a 0.5 g/L concentration of the Ga@HAp16, which is five times higher than MIC and caused an already apparent reduction in the bacterial concentration and not only bacteriostatic effect. Moreover, although the incubation period was 16 hours (usually a significant ROS generation is observed already within 1 hour of

incubation as in the case of the positive control menadione), the level of the generated ROS was not significantly different than for the HAp sample.

In the second experiment of ROS generation in L929 cell line, a 0.1 g/L Ga@HAp16 concentration as well as 0.1 g/L Ag@HAp were tested with pure growth medium and HAp as the negative controls (Figure 4.85). The test again confirmed no increase of ROS for Ga@HAp in comparison with HAp. However, all three materials (Ga@HAp, Ag@HAp and pure HAp) exhibited significantly higher ROS increase in comparison with the pure growth medium and the largest amount of ROS was generated by pure HAp. Moreover, the histograms of cell population with respect to their fluorescence signal exhibited strange characteristics, especially for the Ag@HAp material, for which extreme quenching of fluorescence was observed leading to maximal cell population at very low fluorescence signal, much below the M1 region of the normal alive cells in pure culture medium. A possible explanation for this is that the flow cytometer detected agglomerates of materials as "cells", which resulted in false signals with lower intensity. Indeed, the granularity of the detected cells was not normal in case of samples other than the pure growth medium (Figure 4.86).

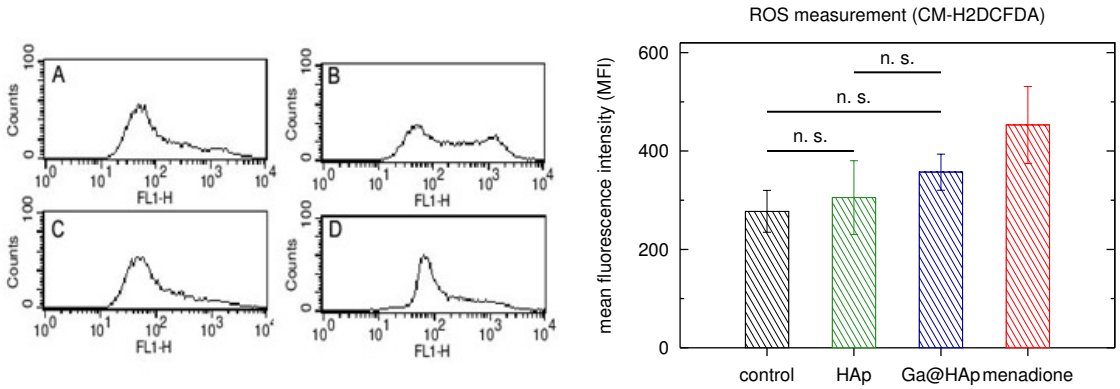


Figure 4.84: Generation of reactive oxygen species (ROS) in L929 fibroblasts. The left image displays the number of cells counted in the flow cytometer vs their fluorescence intensity in the channel FL-1 with excitation wavelength of 488 nm and emission wavelengths between 515 and 545 nm. The following samples were tested: A) negative control (pure medium), B) positive control (menadione), C) 0.5 mg/mL hydroxyapatite, D) 0.5 mg/mL Ga@HAp. The right graph shows the mean fluorescence intensity (MFI) for these 4 samples. A two-sided t test was used to determine the significance of the difference in comparison with the negative control; $p=0.04<0.05$ for menadione, while $p>0.05$ for HAp and Ga@HAp. The pairs of samples that are not significantly different are denoted "n. s.".

Among the other Ga@HAp nanocomposites, the three most efficient antimicrobials were tested for their cytotoxicity in L929 cell line. These tests revealed very good survivability of cells (above 80 % even at 1 g/L) for the Ga@HAp6-nano sample (Figure 4.87 (a)), like for the Ga@HAp16 nanocomposite. In accordance with higher Ga content, Ga@HAp32 caused lower survivability, but still enabled around 80 % survival at MIC and decreased it below 50 % at 0.25 g/L (Figure 4.87 (b)). Interestingly, Ga/OA@HAp containing only 3.2 wt % Ga but narrow size distribution, which was created by a different method involving surfactants (Section 3.2.5.2), exhibited similar cytotoxicity as Ga@HAp32 in spite of 10 times lower Ga content (Figure 4.87).

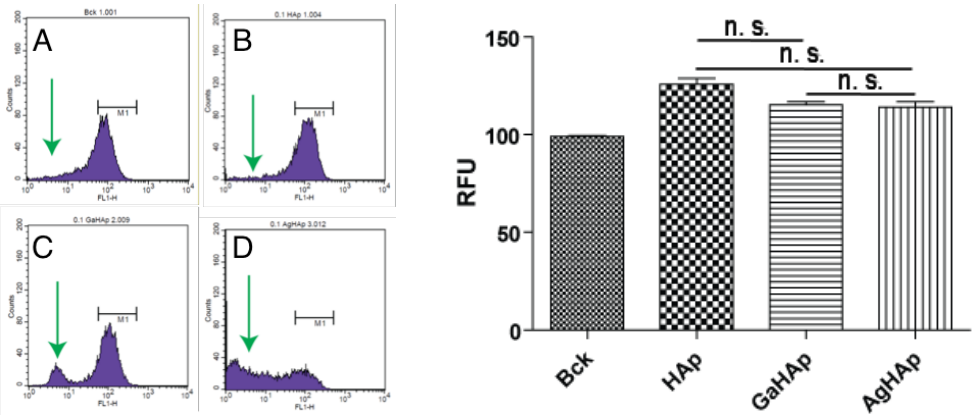


Figure 4.85: Generation of reactive oxygen species (ROS) in L929 fibroblasts. The left image displays the number of cells counted in the flow cytometer vs their fluorescence intensity in the channel FL-1 with excitation wavelength of 488 nm and emission wavelengths between 515 and 545 nm. The following samples were tested: A) negative control (pure medium), B) 0.1 mg/mL hydroxyapatite, C) 0.1 mg/mL Ga@HAp16, D) 0.1 mg/mL Ag@HAp. The right graph shows the mean fluorescence intensity (MFI) in relative fluorescence units (RFU) for these 4 samples. A two-sided t test was used to determine the significance of the difference in comparison with the negative control; $p<0.05$ for all three samples, while $p>0.05$ for comparisons of pairs of samples. The pairs of samples that are not significantly different are denoted "n. s.".

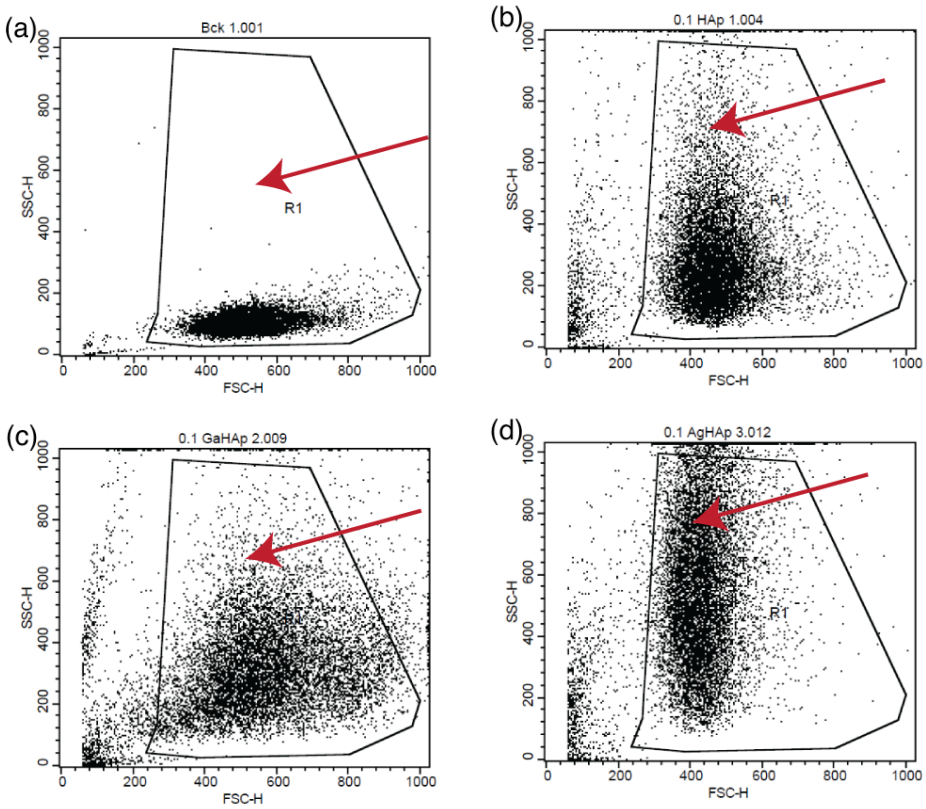


Figure 4.86: Dimensions of cells counted in the flow cytometer: (a) growth medium, (b) HAp, (c) Ga@HAp, (d) Ag@HAp.

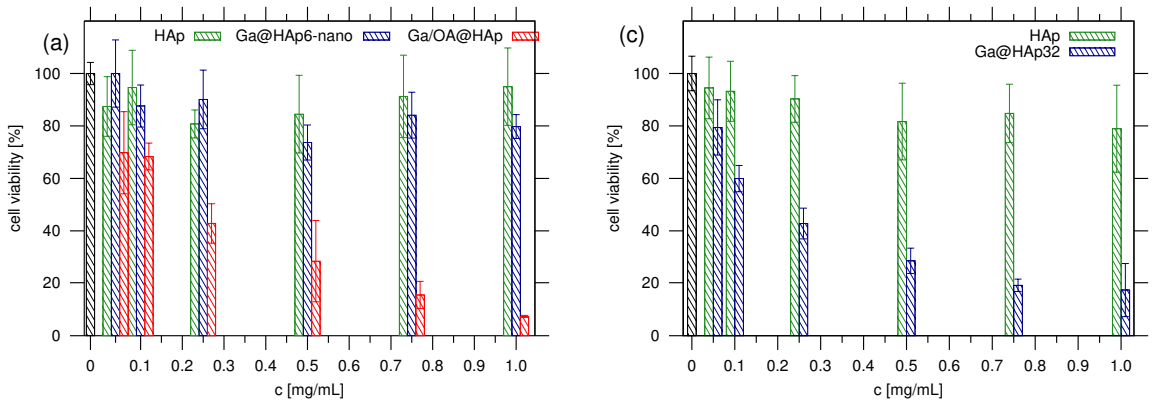


Figure 4.87: L929 cell viability in the presence of Ga@HAp nanocomposites: (a) a comparison of Ga@HAp6-nano (15-nm size, 70 % polydispersity, 6.3 wt % Ga, MIC=0.3 g/L) with Ga/OA@HAp (29-nm size, 20 % polydispersity, 3.2 wt % Ga, MIC=0.15 g/L); (b) Ga@HAp32 (33-nm size, 50 % polydispersity, 32.4 wt % Ga, MIC=0.05 g/L), with HAp as the negative control.

4.8.4 Cytotoxicity of Ga/Au core-shell nanoparticles on hydroxyapatite

The two materials that were tested for the Ga(III) ion release and antibacterial action against *P. aeruginosa* (Ga/Au@HAp and Ga/Au/Arg@HAp) were also tested for their cytotoxicity towards the L929 mouse fibroblasts (Figure 4.88). They both proved highly toxic already at (or even below) MIC. 0.1 g/L was the toxic concentration at which 50 % of the cells survived, which corresponds to around 0.2 mM concentration of released Ga^{3+} ions, which alone should not exhibit such high cytotoxicity. This indicates that some other causes are involved as well, which will be discussed in more detail in the next chapter.

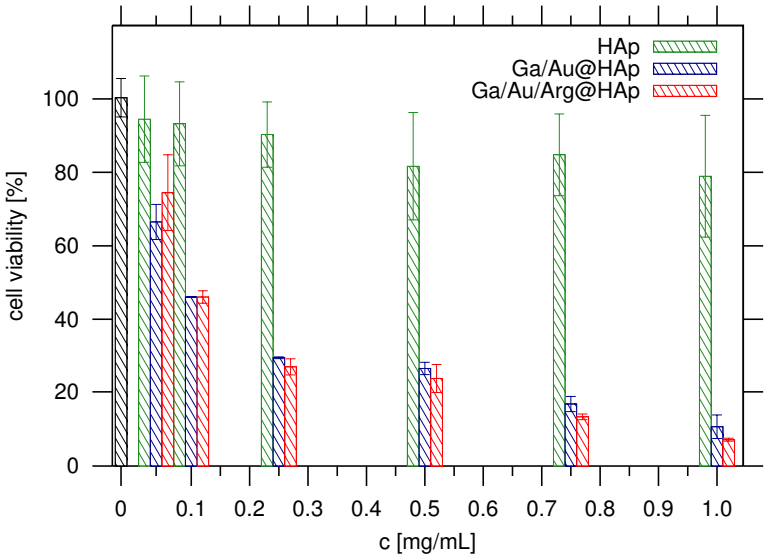


Figure 4.88: L929 cell viability in the presence of Ga/Au@HAp and Ga/Au/Arg@HAp nanocomposite, respectively. Hydroxyapatite is the negative control.

Chapter 5

Discussion

5.1 Core-Shell Structure of the Hydroxyapatite

Brought out by the NMR evidence, the apatitic core/amorphous surface layer model, described in Section 1.5.1, is widely accepted for the nano-hydroxyapatite today. As can be seen from the characterisation in sections 4.1 and 4.2, it applies also to the sub-micrometer laths used in this work. Apart from the NMR analysis, an evidence for such HAp structure is also the discrepancy between the Ca/P ratio of the sample and the Ca/P ratios of the best matching XRD reference patterns. Disagreements between the Ca/P ratios of the refined structures from the XRD pattern and the ones determined by the elemental or thermal transformation analysis have been noted in previous studies on HAp as well [380], [381]. According to the core-shell HAp theory, refinement gives larger Ca/P ratio than the other two methods because it takes only the crystalline apatitic core into account [287]. In this view, the Ca/P ratio of the crystalline core can be almost stoichiometric or above 1.67 due to carbonate incorporation, but the overall Ca/P ratio can be below 1.67 due to the Ca-deficiency of the disordered surface layer [287]. Rietveld refinement of the crystalline (core) part of the HAp prepared by the homogeneous precipitation with thermal degradation of urea under ultrasonication has been conducted previously using a stoichiometric HAp model and the determined cell parameters were a=b=9.4330 Å and c=6.8765 Å [273]. Such a change of the unit cell dimensions leading to an increased a/c ratio is usually a consequence of an A type carbonate substitution [277], [279], [280], [387], [395], [396], but since the IR spectra point to a predominantly B type incorporation, it was explained as a consequence of the water incorporation into the c-axis channel and vacancies [279], possibly forced by the ultrasonication [273].

The disordered surface layer is currently believed to be very similar to the amorphous calcium phosphate with a Ca/P ratio $\leq$1.5 [286], [287]. The Ca/P value of the disordered surface layer of HAp presented in this work was estimated with the use of NMR analysis to 1.33. The importance of this layer has been increasingly recognised recently and has been attributed to the fact that it is hydrated. It is responsible for the characteristic parallel orientation of the HAp nanocrystals, crucial for the proper assembly of bone/teeth, the flexibility of HAp (the ability to withstand large mechanical stress and to adsorb considerable amounts of foreign molecules and ions) giving bone a very important role in homeostasis of ions in body fluids, the high bioactivity of HAp, and its interactions with proteins, the organic matrix (e.g., collagen) and cells [275], [286], [396], [397], [398], [399].

The function of the ultrasound during the synthesis of hydroxyapatite can be to speed up the reaction (by the extremely high local temperature (up to 5000 °C) and pressure (>500 bar) after the collapse of a cavitation bubble) and to affect the morphology of the product (by particle collisions and crystal growth interruptions due to implosions of the

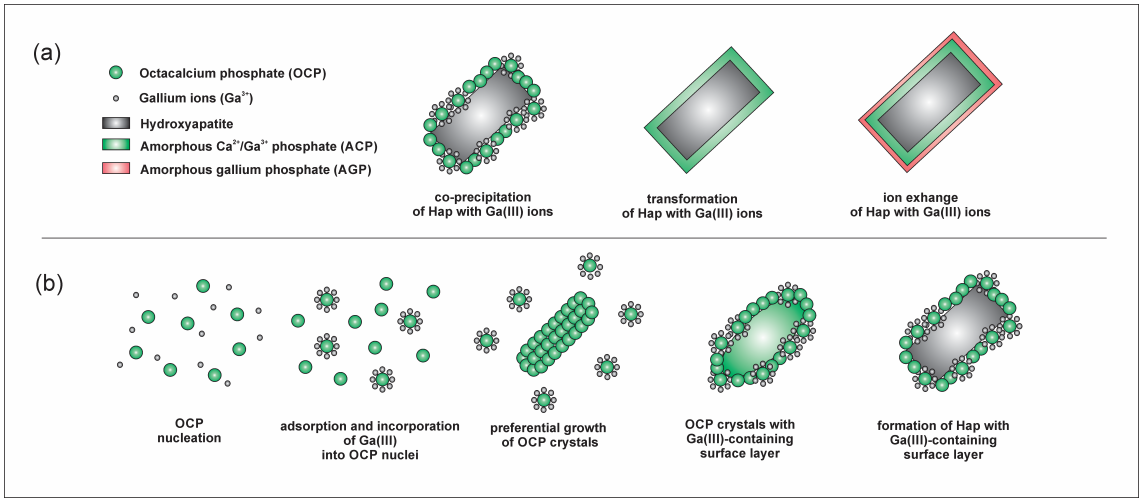


Figure 5.1: (a) Illustration of the structure of HAp(Ga) obtained by co-precipitation, transformation and ion exchange with Ga^{3+} ions and (b) the mechanism of formation of HAp(Ga)CP nanocrystals.

cavitation bubbles) [273], [356], [358], [400]. A comparison with a synthesis at boiling conditions without ultrasonication has revealed that the ultrasound mainly affects the morphology rather than the progress of the synthesis. Boiling is in fact more effective in enhancing the conversion of ACP/OCP to HAp. It is known that the ACP→OCP→HAp transformation is accelerated at higher temperatures and goes to completion within a few hours of boiling [260], [262]. Precipitation of HAp at elevated temperatures under reflux without ultrasonication was studied by Zhang *et al.* [401] and their synthesis times to achieve a monophase (HAp) product were much longer than the ones observed in my experiments, even at 95 °C. The reason for this might be that they used a 10 times higher concentration of reactants. We have seen that the higher concentration of reactants requires longer synthesis time and it has also been previously shown that the 10 times higher concentration resulted in additional phases after a 2-hour ultrasonication [356].

The change of HAp morphology from the fiber/whicker-like to lath/plate-like due to ultrasonication has already been reported by Jevtić *et al.* and it was explained as a result of particle collisions and the sintering effect of the microjets formed after the collapse of the cavitation bubble [273]. The results presented in this work indicate that even the long fibres, created at boiling conditions in the absence of ultrasonication, can be broken and "glued" into plate-like morphology by subjecting them to such high-power immediately after the synthesis. In this way, the long ultrasonication and the additional 15-hour ageing can be avoided. On the other hand, it was the two-step nature of the sonochemical synthesis (precipitation+OCP→HAp transformation) that enabled three different Ga-doped materials and consequently a better understanding of the Ga(III) incorporation and its influence on the biomedical properties of these materials.

5.2 Influence of Ga^{3+} Ions on the Formation and Properties of HAp(Ga)

The XRD, TEM and FTIR analyses revealed no change of the apatite crystal lattice due to the incorporation of Ga(III), but at the same time exhibited some disorder, either in the raised amorphous background (XRD), enlarged amorphous edge (TEM) or decreased

IR bands (especially the ones of the OH^- ions). These results are in agreement with the core-shell HAp model and confirm that the incorporated Ga^{3+} reside in the disordered surface layer retaining the pure nearly stoichiometric apatitic core. The decrease of the OH^- signal can be a consequence of two events:

(a) adsorption of Ga^{3+} onto the surface of the apatite structure that inhibits the surface OH^- vibrations;

(b) conversion of a part (most probably the outer one) of the crystalline core to the disordered Ca/Ga-phosphate structure due to the substitution of Ca^{2+} by Ga^{3+}, which lowers and broadens the OH^- band as part of the OH^- ions change from isolated ordered to disordered, while the crystallinity of the internal part without Ga^{3+} ions is well retained.

The first event contributes very little since OH^- ions are virtually absent in the disordered surface layer [390], [398], [402]. The second event can be explained by analogy to the Ca^{2+} substitution by ions of the lanthanoide group. As they are usually in 3+ oxidation state, the substitution of Ca(II) by Ln(III) is compensated by substitution of OH^- by O^{2-} to retain charge neutrality, which results in formula $Ca_{10-x}Ln_x(PO_4)_6(OH)_{2-x}O_x$, $0<x\leq 2$ [403]. However, Ga^{3+} ion is much smaller than a Ln^{3+} (e.g., Ce^{3+}) ion, which is of comparable size to Ca^{2+}, so that the apatite structure cannot be maintained anymore after the substitution by Ga^{3+}, but is rather converted to a disordered brushite structure. Clear evidence of the apatitic core-Ca/Ga-phosphate nonapatitic shell structure of the HAp(Ga) and the consumption of a part of the crystalline core for the formation of the amorphous Ga(III)-containing layer in the case of the HAp(Ga)TR and HAp(Ga)IE comes from the results of the NMR analyses. The apatitic phosphate signal (the narrow peak) decreased for the Ga(III)-containing materials in comparison with the pure HAp reference, while the additional broad signal increased. This is also evident from the ^1H NMR spectra. The ^1H NMR spectra of the HAp(Ga)TR and HAp(Ga)IE are very similar to the spectrum of the pure HAp, but with decreased OH^- peaks, which is in agreement with the OH^- band decrease in the IR spectra.

Moreover, the NMR analysis enabled also an estimation of the composition of the amorphous surface layer. The Ga(III) content in the amorphous surface layer is increasing in the order HAp(Ga)CP < HAp(Ga)TR < HAp(Ga)IE8 < HAp(Ga)IE16, which is the same as the order of increasing antibacterial action (MIC) and cytotoxicity. With increasing Ga(III) content the surface composition becomes more Ga phosphate than Ca phosphate. When the surface layer composition becomes predominantly Ga phosphate (for HAp(Ga)IE8 and HAp(Ga)IE16), an additional crystalline$GaPO_4$ phase is obtained upon calcination. Thus, it seems that the optimal HAp(Ga) leading to quantitative conversion into β-TCP(Ga) does not possess any prevailingly Ga-phosphate local environments in the disordered surface layer.

Furthermore, the Ca/P ratio, which is already lower in the ACP-like surface layer of pure HAp, is additionally decreased after Ga(III) incorporation and it decreases with increasing Ga(III) content (as confirmed by the EDS as well as NMR analysis). As a consequence, the Ca/P ratio of the amorphous surface layer becomes very low and decreases in the order HAp(Ga)CP > HAp(Ga)TR > HAp(Ga)IE8 > HAp(Ga)IE16. The estimations with the help of the NMR yielded values below 1 for Ca/P of HAp(Ga)IE8 and HAp(Ga)IE16. It is known that calcium phosphates with Ca/P ratio <1 are not useful for biomedical applications (implantation) due to their high solubility and acidity [260], [262], [263].

Investigation of the incorporation of Ga^{3+} ions into hydroxyapatite during different stages of the material's synthesis led us to interesting correlations between the structure

of the material and its physicochemical properties that significantly influence its interactions with bacterial and mammalian cells. Ga^{3+} ions have a strong effect on the growth of the apatite phase that results in important changes in the structural characteristics. Investigations led us to the mechanism for apatite formation, as illustrated in Figure 5.1.

5.2.1 HAp(Ga) by co-precipitation

When Ga^{3+} ions had been added before the precipitation began so that the apatite was co-precipitated with them, they inhibited the growth of the HAp laths, which resulted in very small nanocrystals of HAp(Ga) with a large surface area that could adsorb a lot of water. This material is very similar to the recently reported Ga(III)-containing HAp, which was also obtained by co-precipitation, but via a different synthesis method, and as a part of a calcium phosphate cement enabled successful bone healing after being presterilized and aseptically injected into the mouse bone [114]. The initial addition of the $Ga(NO_3)_3$ into the mixture of apatite precursors results in a drop of the pH to 2.9 and the subsequent decomposition of urea increases this value to 6.1. In this weakly acidic environment, the precipitation of ACP is inhibited and the OCP phase, with stability in the pH range from 5.5 to 7.0 [383], is formed. Due to the ability of Ga(III) to control the growth of the Ca-phosphate phase [326], [327], these ions will bind to and incorporate into the initially formed OCP nuclei, which will limit their further growth (Figure 5.1 b). With a further increase in the pH obtained by the degradation of urea, the concentration of the formed OCP nuclei will increase and a part of the nuclei will be free of adsorbed Ga^{3+} ions. These Ga(III)-free OCP nuclei aggregate and grow into a crystalline octacalcium phosphate phase, which is a typical step for the growth mechanism of hydroxyapatite [404]. However, Ga-containing OCP nuclei are not completely eliminated from the growth of the so-formed OCP crystals. Once they are formed from the Ga-free OCP nuclei, Ostwald ripening, which forces the ingrowth of smaller particles into the larger ones, will provide the attachment of Ga-containing OCP nuclei onto their surface. This is the critical step that will stop the further growth of the pre-formed OCP nanocrystals. During the transformation step the pH is increased to 7.1, which is in the pH stability range of the Ca-deficient HAp (pH = 6.5–9.5) [383]. The so-formed OCP nanocrystals are transformed into the hydroxyapatite structure while the surface Ga-OCP layer participates in the formation of the disordered surface layer that contains Ga^{3+} ions. The obtained material has some properties that are very interesting for biomedical applications owing to the nanoscale size, the high surface area and the capability to adsorb a large quantity of water. The higher specific surface area (>100 m^2/g) is important for the rapid exchange of ions with extracellular fluids and it also enhances sinterability and consequently mechanical properties [260], [275]. The HAp(Ga)CP also provides a high degree of control over the release of Ga^{3+} ions. From this point of view, it can be efficiently applied as a bioactive agent that releases low concentrations of Ga^{3+} ions, which are capable of stimulating the differentiation and growth of mammalian cells. However, with a very high MIC of 0.9 g/L, the HAp(Ga)CP material does not possess good self-protection against *P. aeruginosa*, so it is not an efficient antimicrobial agent.

5.2.2 HAp(Ga) by transformation

When Ga^{3+} ions were added to the mother liquid during the transformation step, they did not have such noticeable effect on the size of the HAp plate-like particles, which were similar to the pure HAp but with a more visible amorphous layer on the surface. Perhaps this layer increased the specific surface area of the HAp(Ga)TR laths to a two-times higher value with respect to the pure HAp reference. Due to the absence of the Ga^{3+} ions, the pH

of the initial precursor mixture was 4.5. After the initiation of the gradual decomposition of urea, the pH slowly increases and precipitation of the apatite phase follows the usual growth mechanism by OCP nucleation and ingrowth into the OCP particles [405], which are not influenced by the Ga^{3+} ions. Because of the absence of the limitation influence of the Ga^{3+} ions, these particles grow into sub-micrometre-sized crystals. At the end of the precipitation step the pH of the mother liquid is 6.3, which is within the stability range of OCP [383]. At this point the Ga^{3+} ions were added to the mother liquid. Their addition resulted in a decrease of the pH to 5.2, which is slightly below the stability range of OCP. We assume that this step resulted in the dissolution/transformation of the surface layer of the OCP crystals that induced the formation of the amorphous layer. Gallium ions can also substitute the Ca^{2+} ions in the OCP and precipitate with $HPO_4{}^{2-}$ and Ca^{2+} ions together, thus forming a mixed Ca/Ga amorphous phosphate (see Figure 4.9 (d)). These changes led to the increase of the pH in the mother liquid to 6.5, which is within the stability range of OCP and HAp. However, under these conditions HAp is more stable than OCP [383] and the transformation step resulted in the solid-state transformation of the OCP to the Ca-deficient apatite structure coated by an amorphous Ca/Ga-phosphate layer. The so-formed material has very interesting properties regarding the interactions with bacterial and mammalian cells. It has the ability to controllably release Ga^{3+} ions within the bioactive range under simulated physiological conditions in a similar way to the previously discussed HAp(Ga)CP. However, since the surface amorphous layer represents a smaller part of the material in comparison with the nanocrystalline HAp(Ga)CP sample, a similar overall Ga content (3 vs 4 wt %) means a larger amount of Ga(III) in the surface disordered layer in the case of the HAp(Ga)TR (Figure 5.1 a and Table 4.3). This improved the antibacterial efficiency of the HAp(Ga)TR (three times lower MIC) against *P. aeruginosa* in comparison with the HAp(Ga)CP. At the same time the material did not express cytotoxic interactions with fibroblast cells for the wide concentration range, starting from the concentration that inhibits bacterial growth and up to the end of the studied concentration range (from 0.3 mg/mL (MIC) to 1 mg/mL). From this point of view, the addition of Ga^{3+} ions during the transformation stage provided material with physicochemical properties that join together efficient antimicrobial activity and a high level of non-toxicity.

5.2.3 HAp(Ga) by ion exchange

In the third case the Ga^{3+} ions are introduced into the pre-formed apatite crystals and they do not have any influence, neither on the precipitation nor on the transformation of the apatite structures. In this case the apatite crystals are formed by the same synthesis as the pure HAp reference, which results in well-crystallized, sub-micrometre-sized plate-like particles (see sections 1.5.1 and 4.1), and Ga^{3+} ions are introduced by an ion-exchange procedure. The incorporation of Ga^{3+} ions into the hydroxyapatite during its synthesis is limited by their precipitation with $PO_4{}^{3-}$ and OH^- ions. Hence, the only way to incorporate larger amounts of Ga^{3+} ions is the ion exchange. However, this incorporation is limited by the low pH of the $Ga(NO_3)_3$ solution used as a medium for the exchange of the ions and may induce complete dissolution of hydroxyapatite. The addition of an aqueous solution of $Ga(NO_3)_3$ to HAp in the studied concentration range resulted in a reduced pH that triggered the dissolution of the HAp plate-like particles. The pH during the synthesis of the HAp(Ga)IE with 8 wt % of Ga raised from 4.75 to 5, while for the HAp(Ga)IE with 16 wt % it increased from 2.96 to 3.23. At this pH, HAp is not the only thermodynamically stable Ca-phosphate phase and it can co-exist with another, $CaHPO_4 \cdot 2\,H_2O$ (DCPD) phase (with stability at a pH between 2 and 6) [383]. Mellier *et al.* have demonstrated that the mixing of DCPA with an aqueous solution of $Ga(NO_3)_3$ in this concentration range

and Ga/Ca molar ratios higher than 0.075 results in the formation of amorphous $GaPO_4$ with some Ca^{2+} ions inside the distorted brushite structure, which gives a peak at -6 ppm in the 31P NMR spectrum [114], [333]. It seems that the same phase can be obtained by mixing our Ca-deficient HAp with $Ga(NO_3)_3$. The presence of the additional amorphous $GaPO_4$ phase at the surface of the HAp(Ga)IE significantly affected its properties under simulated physiological conditions and consequently influenced the interactions with bacterial and mammalian cells. The material was not able to provide the controlled release of Ga^{3+} ions and even showed a high initial burst release. Furthermore, in proportion to the larger content of incorporated Ga(III), the material's MIC against *P. aeruginosa* was significantly reduced in comparison with the MIC of HAp(Ga)TR to a three times lower value. However, it also increased the cytotoxicity. Although the percentage of the surviving cells was high at MIC, their rate dropped rapidly at higher concentrations. Even the HAp(Ga)IE material with a content close to the HAp(Ga)TR and the same MIC exhibited a narrower concentration range between MIC and TC_{50}. This implies that although the HAp(Ga)IE and HAp(Ga)TR are morphologically similar, the optimum therapeutic window for HAp(Ga)IE cannot be as wide as for the HAp(Ga)TR.

5.2.4 Disordered surface layer as a drug delivery system

HAp(Ga) by co-precipitation and transformation had a similar overall Ga content but a different morphology. Co-precipitation led to very small HAp(Ga) nanocrystals with a large fraction of the amorphous surface layer that contained a low amount of Ga(III). The addition of Ga^{3+} ions during transformation did not affect the size of the HAp crystals and resulted in sub-micrometre-sized HAp(Ga) laths with a similar overall Ga content, but a smaller fraction of the amorphous surface layer, which therefore contained a larger amount of Ga(III). HAp(Ga) by ion exchange had a morphology similar to HAp(Ga) by transformation but higher overall Ga content and hence an even larger amount of Ga(III) incorporated within the amorphous surface layer. The HAp(Ga) materials obtained by co-precipitation or transformation were capable of the controlled release of Ga^{3+} ions in the bioactive concentration range, whereas HAp(Ga) obtained by the ion exchange could not control the Ga^{3+} release, which contributed to an increase of both the antimicrobial and the cytotoxic effects. However, the HAp(Ga) by transformation exhibited a much better antibacterial action than the HAp(Ga) by co-precipitation, which indicates that the ion release is not the main property that determines the HAp(Ga) toxicity, but rather the composition of the amorphous surface layer (Figure 5.2).

How could the chemical composition of the surface layer influence the antibacterial action and toxicity? A sound explanation of the "contact-based" mechanism of doped hydroxyapatite materials has recently been provided for the silver-doped hydroxyapatite using the electric double layer model [295]. Upon contact with the material, cell membrane/wall is exposed to Ag^+ ions in the Stern layer, where their concentration is much higher than the average concentration of released Ag^+ ions in the medium [295]. In their calculations, the authors assumed that the Ag^+ ions were the only positively charged species that shielded the negative charge of the material and supported this assumption by the larger solubility of Ag salts than Ca salts [295]. A similar concept could be applied also to the HAp(Ga) materials, but due to the ACP-like or distorted brushite-like structure of the amorphous surface layer, which is more soluble than hydroxyapatite [262], and low solubility of Ga salts [113] the Stern layer would be populated with Ga^{3+} as well as Ca^{2+} ions. Thus, the Ga^{3+} concentration in the Stern layer, to which cell membrane would be exposed in contact with the HAp(Ga), would reflect the chemical composition of the amorphous surface layer, i.e., the fraction of Ga(III) in this layer. In fact, not only free (hydrated) cations could exist in the electric double layer, but also other positively as well as negatively charged

and neutral Ga(III) moieties, such as complexated/chelated ions or $GaPO_4$ molecules. The method used here for determining the released Ga^{3+} ions cannot distinguish among these various Ga(III) solutes. Hence, we should not exclude the possibility that the different HAp(Ga) materials release different Ga(III) species, among which some are more toxic than others. It is known that some forms of Ga(III) are stronger antimicrobials than others and some forms are more cytotoxic than others [118], [135]. Moreover, this can explain the much higher toxicity of the released Ga(III) from the HAp(Ga)IE15 in comparison with $Ga(NO_3)_3$. In this view, the nature of the surface disordered Ca/Ga phosphate layer governs the nature of the released Ga(III), which is concentrated in the electric double layer, and consequently the antibacterial and biocompatible properties. Furthermore, the observed dark circles/spots of around 2-nm diameter on the surface of the Ga(III)-doped HAp might indicate that Ga(III) is located in the amorphous surface layer in the form of Ca/Ga phosphate clusters/nanoparticles separated and connected by the non-doped Ca-phosphate phase. This assumption is supported by the NMR spectra exhibiting at least two different environments of P in the disordered surface layer of the HAp(Ga). Such nanoparticles could evolve from the Posner's clusters (with $\sim$ 1-nm diameter) that construct the ACP [260], [261]. The dark spots on the HAp(Ga)IE (the presumed $GaPO_4$ nanoparticles) look very much like the Ag_3PO_4 nanoparticles reported in the Ag_3PO_4@HAp nanocomposites, which were very efficient against *S. aureus* and *P. aeruginosa* but also highly toxic for human osteoblasts [344]. In this view, especially the HAp(Ga)IE16 material can be seen as a $GaPO_4$@HAp nanocomposite and its high antibacterial efficiency as well as high toxicity is in agreement with the Ag_3PO_4@HAp material. Our results have revealed higher cytotoxicity of amorphous $GaPO_4$ in comparison with $Ga(NO_3)_3$ and it is known that very small nanoparticles can easily penetrate into the cell and are usually found more toxic (see Section 1.3.2.3). Hence, this provides another explanation for the "contact-based" antibacterial action of HAp(Ga) and the targeted drug delivery by disordered surface layer of hydroxyapatite. A recent study has shown that the antibacterial-ion-doped amorphous surface layer of hydroxyapatite is a much more efficient drug delivery system than a mixture of ion-doped ACP+hydroxyapatite. The study compared the antibacterial efficacy against oral bacteria of three different Zn-doped calcium phosphate nanomaterials, in which Zn(II) was incorporated only into the ACP or ACP surface layer of hydroxyapatite [310]. Two HAp(Zn) materials contained a similar amount of Zn, but one consisted of HAp nanorods and ACP nanoparticles, while the other consisted of only HAp nanorods with Zn^{2+} ions in the disordered surface layer. The latter released much more Zn^{2+} and exhibited much stronger antibacterial action, which was attributed to the easier release of Zn(II) from the hydrated surface layer of HAp(Zn) than from the dehydrated ACP and HAp nanomaterials [310].

5.3 Ga@HAp

5.3.1 Top-down or bottom-up approach?

Among the available syntheses of Ga NPs, I have tried two different methods, one physical (top-down approach) and one chemical (bottom-up approach). Their characteristics are compared in Table 5.1. The main advantages of the ultrasonic emulsification method are the possibility to obtain Ga NPs in the presence of HAp and thus the Ga@HAp directly in a polar or even partially aqueous media, without a surfactant and without any byproducts. In water, the phase control is hindered by the sonochemical formation of GaOOH nanorods [192]. However, this reaction was successfully prevented either by using a water+acetonitrile mixture (in ratios 3:1 or less) or an ethylene glycol medium instead. These observations can be explained by the theory of ultrasonic cavitation and sonochemistry and

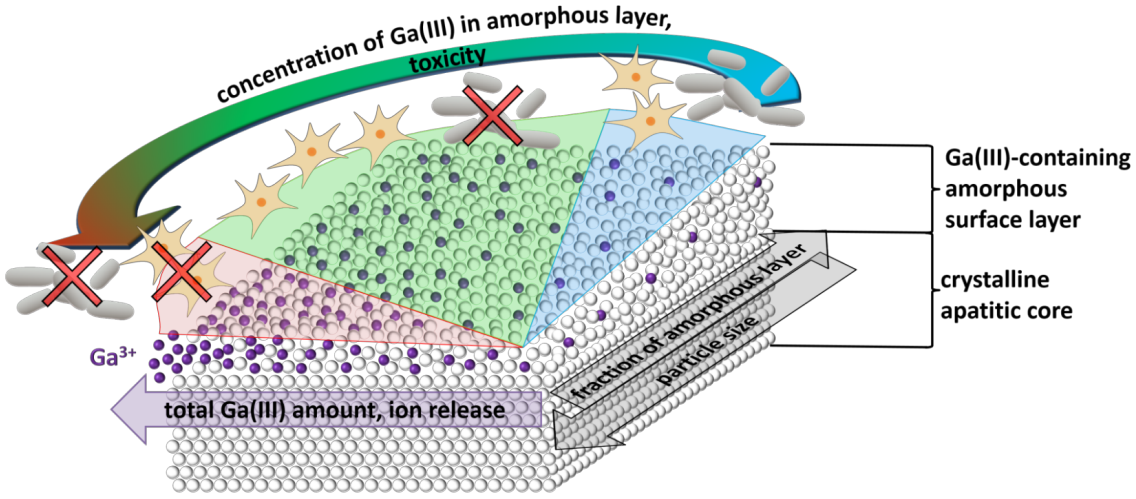


Figure 5.2: Graphical presentation of the Ga(III) incorporation into HAp and its influence on the biological properties of the HAp(Ga) biomaterial. The composition of the Ga(III) containing amorphous surface layer most importantly affects the biological response to HAp(Ga). It depends on the overall Ga(III) content and the fraction of the disordered surface layer, which depends on the size of the HAp particles that can also be affected by the presence of the Ga^{3+} ions.

represent an evidence that the formation of GaOOH nanorods by ultrasonication of Ga droplets in water is truly sonochemical. According to this theory, ultrasonication at 20 kHz and 750 W creates bubbles in the reaction medium, which grow during rarefaction cycles until the unstable size and then undergo a violent collapse which creates extreme conditions locally and instantly in their neighbourhood [406], [407]. The bubbles are filled with air (or the inert gas if in inert atmosphere) and the vapours of the liquid used as the dispersing medium [406], [407], [408], [409]. During the rarefaction cycle the water vapours fill the inside of the growing bubble, while the outside is in contact with liquid Ga. After the bubble collapses, the outside Ga comes into contact with the internal H_2O vapours instantly and under the extreme conditions of the bubble implosion, which results in the reaction of Ga with H_2O to give GaOOH as under hydrothermal conditions. When a part of the water medium is substituted by a more volatile liquid, such as acetonitrile, the bubbles are preferentially filled with the acetonitrile rather than the water vapours, so that the sonochemical reaction of Ga with H_2O does not occur. On the other hand, when water was completely substituted by a less volatile ethylene glycol, no sonochemical reaction occurred as well. The major weakness of the ultrasonic emulsification method is the size control. According to the Taylor's theory [410], the mode size depends on the properties of the dispersing medium, particularly its viscosity (η) and surface tension (γ):

$$diameter \approx \frac{\gamma_{ij}}{\eta \dot{\gamma}} \tag{5.1}$$

Here, γ_{ij} is the interfacial tension between the liquid being emulsified and the dispersing medium and $\dot{\gamma}$ is the shear rate. This equation is to be taken qualitatively and predicts that for creating smaller Ga particles a medium with a larger surface tension (due to very high surface tension of gallium) and/or larger viscosity is required. Interfacial tension can be effectively reduced also with the use of a surfactant. The ultrasound irradiation creates an extremely high shear rate ($\dot{\gamma} \geq 10^9\ s^{-1}$ [196], depending on the frequency and

Table 5.1: Comparison of two methods for creating the Ga@HAp nanocomposite.

	top-down (ultrasonication)	**bottom-up (thermal decomposition)**
reagents	Ga, HAp, acetonitrile/ethylene glycol, water, 2-propanol	tris(dimethylamido)gallium(III) dimer, octadecene, di-N-octylamine, oleic acid, chloroform, ethanol, HAp, THF, 2-propanol
byproducts	no	unreacted reagents (tris(dimethylamido)gallium(III) dimer, octadecene, di-N-octylamine), excess oleic acid
surfactant	no	yes
synthesis of Ga NPs in the presence of HAp	yes	no
mode size control	medium, centrifugation, temperature	precursor/surfactant ratio
size distribution control	centrifugation (EG), Ga concentration	reaction temperature, time
agglomeration of Ga NPs in Ga@HAp	low	high

the amplitude of the ultrasound waves), which breaks the liquid Ga into nanodroplets. Such high shear stress can break the thin oxide shell so that the inside Ga is again exposed to the medium [154]. Thus, Ga nanodroplets can be achieved even by the ultrasonication in the oxygen-containing atmosphere and without removing the gallium oxide layer. If we look at the properties of the three dispersing media that I have tried for the ultrasonic emulsification in my doctoral work (water, acetonitrile and ethylene glycol), we can see that ethylene glycol with its high viscosity (η =16 cP) and surface tension (γ = 48 mN/m) is a favourable medium over water (η =1 cP, γ = 73 mN/m) and acetonitrile (η =0.34 cP, γ = 29 mN/m) for breaking liquid Ga into nanodroplets and thus creating a nanoemulsion. This can qualitatively explain the observed smaller particles (22 nm) in the ethylene glycol in comparison with a water+acetonitrile medium (40 nm, see Section 4.4.3). Ethylene glycol also has some other favourable properties, such as a high boiling point (197 °C), low vapour pressure (7.5 Pa at 20 °C), low freezing point (-13 °C) and antifreezing properties in mixtures with water, which provide a wide temperature range during the synthesis.

As mentioned in Section 1.4.3.2, the influence of temperature and ultrasonication parameters on the mode size of Ga NPs has been explored recently by Yamaguchi *et al.* [193]. They found out that the ultrasonic power/amplitude did not affect much the mode size of the Ga NPs but only the time needed to achieve it, while the temperature during ultrasonication had a noticeable impact on the most frequent size of the Ga NPs [193]. They used 2-propanol as the dispersing medium, 400 W ultrasonic probe and up to 40 % amplitude, which yielded 35-nm Ga NPs at room T and 60-nm Ga NPs at 50 °C already after 20 min of ultrasonication. The larger size in comparison with Ga NPs in EG can be explained by lower viscosity and surface tension of 2-propanol (η =2 cP, γ = 23 mN/m) and higher ultrasonic power used in my experiments (750 W and 80 % amplitude). The

temperature during the major part of the Ga@HAp synthesis was around 50 °C, but it was decreased in the last 15 min of ultrasonication to and below room T (see Section 3.2.5.1). As demonstrated by Yamaguchi *et al.*, once an equilibrium size was reached at a lower temperature, it could not be increased by ultrasonication at higher temperature without the addition of HCl (to dissolve the protective surface oxide layer). On the other hand, the large size obtained at a higher temperature could be decreased by additional ultrasonication at a lower temperature [193]. Thus, the final mode size might have been established in the last 15 min of the Ga@HAp synthesis. However, the colloidal Ga NPs were of a very similar size even though they did not undergo the ultrasonication at lower temperatures. The size of the Ga NPs might not depend on the temperature so much in the EG medium and at the higher ultrasonic power.

An important parameter that has not been addressed by Yamaguchi *et al.* is the effect of Ga concentration on the size and the size distribution of the resulting Ga NPs. They used 50 g/L Ga in 2-propanol, which yielded Ga particles with a wide size distribution from 10 to 400 nm even after a 2-hour ultrasonication in the presence of a surface active agent. Although it was narrowed by extending the sonication time from 20 min to 1 hour, another hour of sonication did not further decrease the polydispersity of the Ga particles. This is in agreement with my observations on the synthesis of Ga@HAp using a 1–3 g/L Ga concentration in ethylene glycol and water-acetonitrile media, for which the size distribution could not be narrowed by longer sonication (over 1 h) or different pulse duration. I believe the reason for this is that not all parts of the sample experience the same amplitude as it decreases with increasing distance from the horn tip [408], [411], [412], so it could be improved in a continuous-flow reactor and shorter (milisecond) pulses. I solved this problem by removing the Ga particles with sizes above 100 nm by centrifugation after the ultrasonication. However, the polydispersity was evidently reduced also by using a lower Ga concentration (0.2 g/L), which indicates that the volume occupation by liquid Ga is also a very important factor for the width of the size distribution of the final Ga NPs.

The main advantage of the bottom-up (thermal decomposition) method is the possibility of a very good control over the mode size and the size distribution of the Ga/OA NPs, which could be prepared as monodisperse and with tunable size in the range between 12 and 46 nm [165] (see Section 1.4.3.2). However, for creating a Ga@HAp nanocomposite for biomedical applications, it has several drawbacks in comparison with the emulsification method:

(a) the Ga NPs are created in oxygen- and water-free conditions and in a medium consisting of three reagents; thus, hydroxyapatite cannot be present in the reaction mixture during the formation of the Ga NPs;

(b) hydroxyapatite cannot be added to the suspension of Ga NPs even directly after their synthesis as it is full of unreacted precursors (tris(dimethylamido)gallium(III) dimer, di-N-octylamine and octadecene), which are very difficult to be removed from the HAp and impede the attachment of the Ga NPs to the HAp. Thus, Ga NPs need to be cleaned before the HAp addition;

(c) the cleaning procedure brings in another surfactant (oleic acid) to give Ga/OA NPs;

(d) the final Ga/OA NPs are suspended very well to give stable colloidal solutions in organic media, such as chloroform or tetrahydrofuran, but are highly agglomerated in water;

(e) even in the Ga/OA@HAp nanocomposite created by ultrasonic dispersion of Ga/OA NPs onto hydroxyapatite in tetrahydrofuran, the Ga/OA NPs are much more agglom-

erated and less separated than in the Ga@HAp nanocomposite by ultrasonic emulsification.

5.3.2 Biomedical properties

Our hypothesis for the antibacterial properties of Ga nanoparticles was based on the known antibacterial action of gallium ions (Section 1.4.4), the connection between antibacterial nanometals and their antibacterial ions (Section 1.3 [35]), and the thermodynamically favourable oxidation of Ga to Ga^{3+} (Section 1.4.2). However, since the oxidation of Ga ends within a thin oxide layer, it is questionable as to whether the observed antibacterial action is really connected to the release of gallium ions, or whether the gallium nanoparticles have a different mechanism for the prevention of bacterial growth. Our ion-release study has shown that 1/3 of Ga in the nanocomposite is dissolved during 24-hour shaking incubation at 37 ^{o}C in PBS, while 1/2 of the contained Ga is released as Ga^{3+} ions during a similar incubation in the MH growth medium. This proves the expected release of ions. The next question that arises is whether Ga nanoparticles or only the released ions are antimicrobial. Since there are many different MIC values against *P. aeruginosa* reported for ionic gallium, depending on the strain, the growth medium and the gallium species (see Section 1.4.4 and Table 1.1), I rather compared the MIC for Ga@HAp with the MIC value of the released ions and the MIC value of $Ga(NO_3)_3$ obtained in my experiments on the *P. aeruginosa* MW1 strain. The MIC for the Ga@HAp nanocomposite is at 0.1 mg/mL, which corresponds to about 230 μM (0.2 mM) Ga. This agrees well with the MIC of $Ga(NO_3)_3$ at 211 μM and the MIC values of the Ga^{3+} ions released in different PBS media. However, the released ions in MH medium alone could not completely inhibit the growth of *P. aeruginosa* at such concentrations. Moreover, not all of the contained Ga in the Ga@HAp is released as ions in the MH medium after 24-hour incubation, so the antibacterial action of the Ga@HAp nanocomposite cannot be explained only by the antibacterial action of the released ions. There are three possible antibacterial sources: the Ga nanoparticles, the oxide shell or the Ga ions formed by the dissolution of the Ga nanoparticles (Figure 5.3).

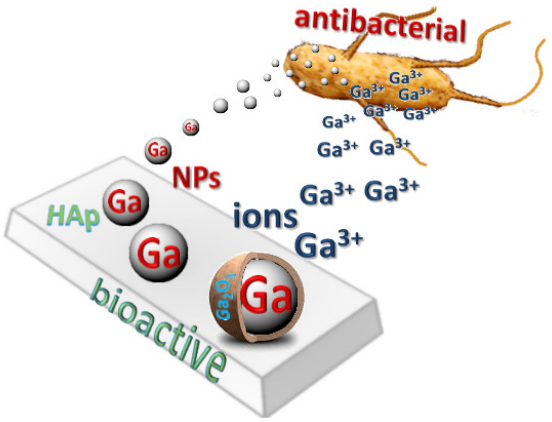


Figure 5.3: A graphical summary of the diverse properties of the Ga@HAp biomaterial and the proposed sources of its antibacterial action.

If the antibacterial properties come only from the release of ions, then the mechanism of antibacterial action is known (Section 1.4.4) and the Ga nanoparticles serve as reservoirs and deliverers of Ga ions, while their dissolution would also be a way for their elimination from the body. The observed large extent of dissolution of Ga NPs in the absence of any

cells and the fact that the antibacterial and cytotoxicity properties were well repeatable despite the wide Ga size distribution go in favour of this mechanism.

However, although the contribution of the nanoparticle to the antibacterial action apart from the ion release is still debatable in metallic nanoparticles, such as Ag nanoparticles (see Section 1.3.2.2), this possibility should not be excluded. Especially, because it obviously contributes at least to improved transport of Ga^{3+} ions into bacteria. The enhanced antibacterial activity in a minimal growth medium despite lower concentration of released Ga^{3+} ions is an evidence for this mechanism. However, ionic Ga(III) has also exhibited stronger antibacterial action in minimal growth media (see Section 1.4.4 and Table 1.1). The destruction of bacteria (the holes in cell membranes of the dead bacteria), observed under SEM, is another indication of the effect of nanoparticles, which is often (but not always) connected with the generation of reactive oxygen species (ROS) [413]. However, non-selective extracellular release of ROS is not expected for Ga nanoparticles under the studied conditions and the observed low cytotoxicity is also an indication against such mechanism. A recent investigation has proven that Ga_2O_3 nanoparticles do not produce any ROS in water without direct ultraviolet or visual light illumination [245]. Moreover, unlike Ag or Cu, Ga cannot undergo Fenton-like reactions that lead to ROS (sections 1.2.2.1 and 1.3.2.1). Instead, the endocytosis, fusion and dissolution of Ga nanoparticles without causing cytotoxicity could occur in a similar way as was observed for the GaIn eutectic nanoparticles in HeLa cells [248]. On the other hand, intracellular ROS could be caused indirectly by the released Ga^{3+} ions as a consequence of the Ga^{3+}-Fe^{3+} substitution inside the cells, as was shown for gallium nitrate and citrate, the FDA approved drugs, in *Pseudomonas* bacteria as well as human lymphoma cells [227], [233] (see Section 1.4.4). Since avoiding non-selective extracellular toxic ROS might be the greatest advantage of Ga nanoparticles over the existing antimicrobial nanomaterials in search of an efficient antibacterial protection that would not be harmful to mammalian cells, a more detailed insight into the mechanism of antibacterial action of Ga nanoparticles and generation of ROS seems a reasonable task in further investigation. We have investigated the intracellular generation of ROS in L929 by a standard flow-cytometry method for 0.1 and 0.5 Ga@HAp concentration and compared it to the ROS generation from a comparable Ag@HAp nanocomposite. Although our tests revealed no statistically significant increase in ROS for the Ga@HAp in comparison with pure HAp, they also exposed some errors when the flow-cytometry method is applied to such materials (especially in case of Ag@HAp), which render this method unreliable. Hence, other experiments and more detailed investigation is needed before proclaiming Ga@HAp a non-ROS antimicrobial.

Finally, if the gallium oxide layer is responsible for bacterial inhibition, the main question is whether Ga_2O_3-coated Ga NPs have any advantages over Ga_2O_3 NPs. The latter have not yet been shown to prevent the planktonic growth of *P. aeruginosa* and gallium oxides in general are very insoluble in water (Section 1.4.1). The thin oxide layer differs from the gallium oxides. It is amorphous [165], [414] and additionally contains gallium suboxide Ga_2O [159], [193], which is converted to hydroxide in aqueous media [238], [241], [415], [416]. Thus, it consists of amorphous $Ga(OH)_3$ and can be dissolved in the presence of complexants as explained in Section 1.4.1. This can explain its high dissolution in culture media, observed also for bulk gallium [417].

All three suggested mechanisms are probably connected in the Ga@HAp: the Ga NPs, the gallium oxide/hydroxide shell and the release of ions, with the major part coming from the ion release. Sahoo *et al.* explored the antibacterial properties of GaN nanoparticles on *Pseudomonas* strains and explained their mechanism by local damage of the cell wall, caused by nanoparticles, which led to the leakage of intracellular components, and a possible release of Ga ions inside the bacterial cells [246]. On the other hand, Lu *et*

al. have shown endocytosis, fusion and degradation of the eutectic GaIn nanoparticles with the release of Ga^{3+} ions inside HeLa cells [248]. In this view, the high efficiency and non-ROS activity of the Ga@HAp nanocomposite can also be explained by the local release of Ga^{3+} ions from the Ga nanoparticles in the vicinity of the nanocomposite and bacteria or even inside the bacteria. Further investigation will be needed to confirm or reject these hypotheses. The investigation of the mechanism will require a narrow size distribution of the Ga NPs, since the suggested mechanisms are most likely size-related. It is known that solubility increases with decreasing the size of particles [47], [418]. However, Ga nanoparticles, coated with amorphous oxide/hydroxide offer another parameter that affects their dissolution, i.e. the thickness of the oxide/hydroxide shell. Hence, the release of ions might be controlled by the size of the Ga nanoparticles and the thickness of the oxide/hydroxide layer. Based on the ion-release mechanism, the antibacterial action would also be controlled by these two parameters. Thus, smaller size and narrower size distribution should result in stronger antibacterial action. The experiments presented in Section 4.7.3.2 are in agreement with this statement. Ga@HAp6 with mode size of 15 nm and 83 % polydispersity and Ga@HAp6 with 22 nm and 50 % polydispersity had the same MIC (0.3 g/L), whereas Ga@HAp7 with mode size of 40 nm and 104 % polydispersity had a higher MIC value (0.4 g/L) in spite of a higher Ga content. Moreover, Ga/OA@HAp with a mode size of 29 nm and 20 % polydispersity had a lower MIC (close to 0.1 g/L) despite a lower Ga content (3.2 wt %). However, the enhanced antibacterial properties in this case might also be attributed to the presence of oleic acid on the surface apart from the narrower size distribution. Antibacterial properties of free fatty acids have been reported [419], [420], [421] and even though oleic acid did not possess effective antibacterial properties against *P. aeruginosa* [420], its attachment to the Ga NPs and combined antibacterial effect with Ga might have contributed to the observed improved antibacterial performance. Since free oleic acid is known for its strong antibacterial action on Gram-positive bacteria, such as group A beta-hemolytic streptococci and *S. aureus* [419], [420], the Ga/OA@HAp nanocomposite might also have a wider antibacterial activity in comparison with Ga@HAp. However, the Ga/OA@HAp nanocomposite also exhibited increased toxicity for mammalian cells (Section 4.8.3). Although free oleic acid is not considered a health hazard, several studies have shown its cytotoxicity [421], [422], [423]. Moreover, investigations comparing toxicity of uncoated nickel ferrite nanoparticles and nickel ferrite nanoparticles coated with oleic acid have revealed higher cytotoxicity of nanoparticles covered with oleic acid [424]. Similarly, investigations comparing toxicity of Fe_3O_4/OA NPs have revealed stronger anticancer properties than uncoated Fe_3O_4 NPs [425]. By contrast, oleic acid coating on ZnO NPs decreased their cytotoxicity due to a lowered generation of ROS [426]. Thus, increased toxicity of Ga/OA@HAp in comparison with Ga@HAp is another evidence that ROS is not the primary source of antibacterial action of Ga NPs. The important role of the molecules attached to the surface of the nanomaterials was already mentioned in Section 1.3.1. On the other hand, the surface of the nanocomposite biomaterial is also very important, and a more homogeneous Ga distribution on HAp might enable better growth of mammalian cells on the surface of the Ga@HAp material. In this view, the higher cytotoxicity of the Ga/OA@HAp can be explained by the observed higher agglomeration of Ga NPs in the Ga/OA@HAp nanocomposite. Furthermore, the requirement of non-aqueous media for its preparation might have decreased the bioactive properties of the disordered surface layer of hydroxyapatite. All in all, these results and a number of their possible explanations justified our choice of avoiding the use of a surface active agent in order to clearly investigate the antibacterial action of Ga nanoparticles. Hence, although the thermal decomposition method of Yarema *et al.* [165] enables great control over the size and size distribution of Ga NPs and the authors have also proposed a way to control

the thickness of their oxide shell, the formation of a stable aqueous suspension of these nanoparticles and substitution of the oleic acid with a biocompatible capping agent needs to be discovered before the mechanism and size dependence of Ga NPs can be precisely explored.

Nevertheless, the wider size distribution has also its advantages. Fast release is not always desired and larger particles or a combination of smaller and larger particles will be required for lower but prolonged release of Ga^{3+} ions. Moreover, smaller nanoparticles are often found more toxic for eukaryotic cells below a certain (optimal) size [102]. Furthermore, wide size distribution is actually a better representation of the industrially prepared and commercially available nanoparticles [427] and also a better representation of the realistic system that could evolve in the human body or environment [47], [428]. Hence, it is very encouraging that despite the inhomogeneous and wide size distribution of Ga nanoparticles on hydroxyapatite, for human lung fibroblasts and L929 mouse fibroblasts, the inhibitory and also the bactericidal concentrations for the Ga@HAp are below cytotoxic concentrations, which implies that the Ga@HAp biomaterial can prevent bacterial growth and enable normal growth of mammalian cells at the same time in a certain concentration range. Furthermore, for a human-friendly antibacterial protection of hydroxyapatite, in this study Ga NPs proved even better than silver nanoparticles that are most commonly used nowadays [29], [429]. The observed cytotoxicity of the Ag@HAp is in agreement with the previously reported toxicity for Ag nanoparticles and Ag@HAp nanocomposite against L929 [430] and IMR-90 fibroblasts [336], [431].

5.4 Attachment of Nanoparticles or Ion Incorporation?

Investigation of attachment of Ga NPs onto hydroxyapatite as well as incorporation of Ga^{3+} ions into hydroxyapatite gives us the opportunity to compare these two different types of surface modification. Both provided strong antibacterial action on *P. aeruginosa* that stemmed primarily from the released Ga^{3+} ions, but it exhibited also some contact-based characteristics and was stronger than the antibacterial action of the released ions alone. Ga@HAp16 released a larger amount of Ga^{3+} ions (more than 50 % of contained Ga) than HAp(Ga)IE16 (around 25 % of the contained Ga), but turned out to be much less toxic for mammalian cells (TC_{50} below 0.05 g/L for HAp(Ga)IE14 in comparison with TC_{50} above 1 g/L for Ga@HAp16 in L929 fibroblasts). The reason for this might be that the hydrated surface layer of the HAp is changed in case of Ga(III) ion incorporation, which decreases its bioactive properties. Moreover, the form of the released Ga(III) might be different for the Ga@HAp, as it might be different for different types of HAp(Ga) (see Section 5.2.4). The source of the released Ga(III) is different, as it comes from the dissolution of the thin amorphous oxide/hydroxide layer on Ga and then directly from the Ga core in case of Ga@HAp, whereas it comes from the dissolution of the thin amorphous Ca/Ga-phosphate layer on HAp in case of HAp(Ga). Even though the HAp(Ga) materials were also more efficient in bacterial growth inhibition, this difference was not so pronounced (for example MIC at 0.075 g/L for HAp(Ga)IE16 in comparison with 1 g/L for the Ga@HAp16 or a similar MIC for HAp(Ga)TR (containing 4 wt % Ga), HAp(Ga)IE5 and Ga@HAp6). Thus, the Ga@HAp material had a wide therapeutic window from at least 6 wt % content up to 32 wt % content, whereas the wide therapeutic window for the HAp(Ga) could be obtained only around 4 wt % Ga content. I must point out, however, that the biomedical properties of HAp(Ga) were very much dependent on the way of Ga(III) introduction into HAp and higher Ga contents were explored only for the HAp(Ga) materials prepared by ion exchange, which had a narrow therapeutic window also at Ga contents as low as 5 wt %. On the other hand, both HAp(Ga)TR and Ga@HAp6-nano had a similar range of concentrations

with inhibitory effect on *P. aeruginosa* and good biocompatibility with mammalian cells. Hence, both HAp(Ga) and Ga@HAp show useful properties for applicability in prevention of the implantation-related *P. aeruginosa* infections.

5.5 Nanocomposites Combining Hydroxyapatite, Gallium and Gold

Although all gallium-based materials performed very well against *P. aeruginosa*, they failed in preventing the proliferation of the *E. coli* bacteria. Moreover, a HAp(Ga) material was tested on *S. epidermidis* as well and it was also ineffective. This agrees very well with the much higher MIC values for Ga^{3+} ions against *E. coli* and *S. epidermidis* in comparison with *P. aeruginosa* (see Table 1.1 in Section 1.4.4). Since Au nanoparticles functionalised with arginine have exhibited effective antibacterial action towards *E. coli* and *S. aureus* with low toxicity for U2OS osteosarcoma and IMR-90 lung fibroblast cells [68], [350], our idea was that the addition of such functionalised nanogold to HAp(Ga) and Ga@HAp materials would improve their antibacterial performance without notably increasing their toxicity to mammalian cells.

5.5.1 Au/Arg nanoparticles on HAp(Ga)

The addition of the functionalised nanogold component to the HAp(Ga) materials is pretty straightforward. It follows the same procedure as the sonochemical formation of Au/Arg@HAp except that HAp(Ga) instead of HAp is used as the carrier of the Au/Arg NPs. Moreover, I have noticed that the progress of the Au/Arg nanoparticle formation is even enhanced on HAp(Ga) in comparison with HAp. Very easily a nanocomposite consisting of Au/Arg nanoparticles with narrow size distribution and attached and well separated on the HAp component. Au/Arg@HAp(Ga)TR has a useful therapeutic window from 0.2 to 0.75 g/L for preventing a *P. aeruginosa* infection and inhibits also the growth *E. coli* and *S. epidermidis*. These properties (illustrated in Figure 5.4) make the Au/Arg@HAp(Ga)TR nanocomposite a very promising biomaterial for prevention of implantation-related infections. *S. epidermidis* is one of the most frequent causes and *P. aeruginosa* is the most frequently found Gram negative bacterial species in the implantation-related infections [432].

The observed action against all three types of bacteria is a consequence of joining the antibacterial activity of functionalized Au nanoparticles and the antibacterial activity of Ga^{3+} ions. While the former is the most important for inhibition of *E. coli* and *S. epidermidis*, the latter markedly boosts the inhibitory effect against *P. aeruginosa*. Nevertheless, some synergism of the two antibacterial components has been observed as MIC against *P. aeruginosa* was lower for the Au/Arg@HAp(Ga)TR in comparison with HAp(Ga)TR, the inhibition zones against *E. coli* and *S. epidermidis* were larger for the Au/Arg@HAp(Ga)TR than for the Au/Arg@HAp and minimal toxic concentration for L929 fibroblasts was larger in case of Au/Arg@HAp(Ga)TR than upon exposure to the Au/Arg@HAp.

Since the experiments of my doctoral work were conducted on different bacteria and mammalian cells than in the previous investigations of the Au/Arg@HAp nanocomposites [68], [350], they brought some new knowledge about the Au/Arg@HAp nanocomposite as well. If we take all the results together, we can now say that the Au/Arg@HAp nanocomposite exhibits low toxicity for U2OS human osteosarcoma cells, IMR-90 human lung fibroblasts and L929 mouse fibroblasts and possesses antibacterial properties towards *E. coli*, *S. aureus* and *S. epidermidis*, but not towards *P. aeruginosa*. The latter observa-

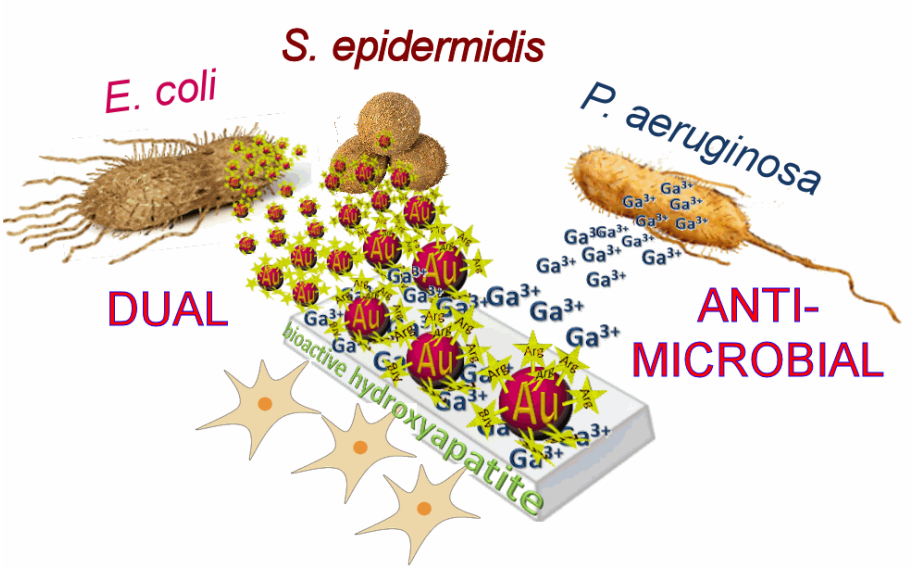


Figure 5.4: A graphical overview of the useful properties of the Au/Arg@HAp(Ga)TR nanocomposite: antibacterial action on *E. coli* and *S. epidermidis* primarily due to the functionalised Au nanocomponent as well as on *P. aeruginosa* primarily due to the ionic gallium component. At the same time they are well compatible with mammalian cells, primarily due to the bioactive hydroxyapatite component.

tion can be explained by the previously suggested antibacterial peptide mechanism of the Au/Arg NPs [350]. A very recent investigation of many antibacterial peptides differing in their amino acid sequence and composition on a wide variety of bacteria has revealed that by contrast to *E. coli* or *S. epidermidis*, the sensitivity of *P. aeruginosa* to antibacterial peptides depends a lot on the peptide composition, especially on the ratio of hydrophyllic and hydrophobic amino acids [433]. This ratio (hydrophyllic Arg and hydrophobic Au) in the tested Au/Arg@HAp nanocomposites may not be optimal for providing an efficient antibacterial effect on *P. aeruginosa*, which suggests that antibacterial action of the Au/Arg@HAp nanocomposite against *P. aeruginosa* could also be improved by tuning the Au/Arg ratio in the Au/Arg NPs.

5.5.2 Ga/Au/Arg core-shell nanoparticles on hydroxyapatite

Growth of one material (shell) on the surface of another (core) usually requires a certain relationship between the two materials. Epitaxial growth occurs if their crystal lattices are very similar (very small lattice mismatch) so that the shell is perfectly crystalline on the core [434]. On the other hand, if the lattice mismatch (calculated as 1-(core lattice constant/shell lattice constant)) is very large, the strain becomes too large and impedes the growth of the shell on top of the core material [434]. For the intermediate cases, the strain can be overcome by a mixed or disordered layer in between [435]. Gold crystalizes in a face-centered cubic (FCC) crystal structure with a unit cell dimension of a=4.0786 Å. Hence, its lattice mismatch with the orthorhombic α-Ga crystal structure (see Section 1.4.2) is not too large (-11 %), so it should enable fairly good (continuous and two-dimensional) growth of crystalline Au on the bulk crystalline α Ga. However, the α-Ga crystal structure stops existing in nanosize (Section 1.4.3.1). The lattice mismatch for the other Ga crystal structures that exist at smaller sizes (sections 1.4.2 and 1.4.3.1) is larger. Furthermore, growth on these structures would need to be conducted at very low temperatures due too extreme

undercooling of Ga NPs. And even if the crystalline Ga/Au core-shell nanostructures were created at such low temperatures, they would probably alloy already at a very low temperature due to a very low melting point of Ga NPs. Rapid spontaneous alloying/mixing (completed within as low as a second) at room temperature has been observed in core-shell bimetallic nanoparticles consisting of materials with much higher melting points than gallium [436], even though solid state diffusion is very slow at normal conditions. This was explained by the increased fraction of interfacial atoms, interfacial defects and surface diffusion [437], [438], [439], [440], [441], [442] and its occurrence depends on the temperature, nanoparticle size, surface tensions of the components and heat of mixing/solution, which is also size-dependent [437], [438], [443].

Nevertheless, the core-shell (non-mixed) structure can be stabilised thermodynamically as well as kinetically. A core-shell structure is thermodynamically stable if [444]

(a) core-core interatomic bonds are stronger than shell-shell interatomic bonds and core-shell interatomic bonds,

(b) surface energy of core > surface energy of shell,

(c) size of shell atoms > size of core atoms,

(d) electronegativities of core atoms and shell atoms are similar,

(e) the shell component binds more strongly to the ligands or surfactants (for passivated nanostructures),

(f) the arrangement of atoms in it leads to a stable electronic shell structure or electron spin interactions.

For example, if we prepare a not too small nanostructure with Ag core and Au shell, Au will tend to diffuse into the core and Ag out as Au prefers to be inside. This would lead to an Au_xAg_y alloy nanoshell with an empty core (hollow nanoshell), as was observed at 100 °C [445]. On the other hand, if mixed nanoalloy or a compound is favoured, the core and shell component will tend to mix spontaneously. Whether or not the mixing proceeds to completion is also very dependent on the core/shell ratio as consumption of the core leads to decrease of interfacial area and consequent decrease in the thermodynamic driving force for the interdiffusion [443], [446], which makes this process self-terminating.

Moreover, the core-shell structure can be stabilised also kinetically. Nanomaterials are often found almost spherical or cylindrical, so that the interface between the core and the shell material is curved. This curvature affects the gradients of the chemical potentials for the core and the shell atoms as well as for the vacancies (Gibbs-Thomson effect) [446], [447]. Consequently, an outward flux of vacancies exists, which counteracts (suppresses) the outward flux of the core component and prevents hollowing of the core-shell structure, based on faster diffusion of the core component [448]. Nevertheless, hollowing of a core-shell nanomaterial due to fast outward diffusion of the core component has been experimentally observed at elevated but moderate (<200 °C) temperatures [449], [450], [451]. However, it rarely proceeded to completion and, depending on the size, the diffusivity difference and the time of heating, it can consequently lead to shell shrinkage, dealloying (inverse Kirkendall effect) and re-filling of the void by the faster diffusing (core) component [447], [448], [450], [451], [452]. There is a competition between the Frenkel effect (Kirkendall voiding without annihilation and lattice shift), connected with gradients of chemical potentials and different diffusivities of the materials, and the Gibbs-Thomson effect, connected with the curved geometry and consequent vacancy gradient. The latter becomes stronger at smaller sizes and can entirely prevent the formation of the hollow nanoparticle [447], [448], [453]. On

the other hand, the Gibbs-Thomson effect can be the driving force for the spontaneous mixing due to the diffusion of the shell atoms inwards, especially when the faster diffusing material is in the shell. However, Laplace pressure increases towards the center of the core-shell particle and with every transportation of an atom gradients of stress increase due to the excess volume of the reaction product [446]. Hence, the interdiffusion slows down, becomes determined by the slower diffusing (core) component and often leads to incomplete mixing partially retaining the pure core as well as pure shell component [446], [454].

Let us now look at the Ga-Au system. The bulk phase diagram (Figure E.1) reveals several mixing possibilities and thermodynamically stable compounds. I used initial Ga/Au ratios corresponding to above 50 at. % and mostly above 70 %, gold was formed by consumption of Ga and no elemental Au was present in the system at the beginning. Therefore, the $GaAu_2$ compound is predicted as the major product of the Au shell growth on Ga by galvanic replacement according to the bulk phase diagram. Indeed, the face-centered cubic $AuGa_2$ phase was often observed also in my experiments presented in Section 4.5 and it was the only observed compound phase. However, pure gold phase was always present as well, which indicates that the compound does not form directly by reaction of Ga with $HAuCl_4$, but rather by subsequent reaction of Au with Ga. Further evidence for this was obtained by the electron microscopy with EDS analysis, which revealed that the Ga phase was retained and the Au phase was attached to its surface. Moreover, the formation of $GaAu_2$ phase was decreased at a lower temperature and prevented at a higher Ga/Au ratio. Hence, our hypothesis for the Au formation on Ga by galvanic reaction was confirmed.

What can make the Ga/Au core-shell structure stable? Among the aforementioned properties the high surface energy of the Ga core, covalent bonding in Ga and high affinity of gold for arginine in case of functionalised core-shell NPs, whereas the high electronegativity of Au and similar atom size have the opposite effect. Another important factor is that Au shell is formed from ionic gold in the galvanic replacement method, which gives the possibility of Au nanoparticles acting as catalysts of the gold reduction on their surface [455], [456], [457], [458] and thus contribute to the core-shell structure as the outcome of the synthesis. Galvanic replacement method usually gives core-shell nanoparticles if core particles are larger than 10 nm [435]. Rapid spontaneous alloying occurs for smaller core particles and hollowing with subsequent dealloying occurs at raised temperatures [435], [445], as described before. Syntheses of core-shell nanoparticles have been reported for a different type, size and shape of the core NPs, for different shell materials and in different reaction media [435], [445], [459], [460], [461].

Apart from the thermodynamic properties, several kinetic stabilisations are also possible for the Ga/Au core-shells, either by the $AuGa_2$ interface or the amorphous oxide/hydroxide layer on Ga NPs. The latter is known to prevent diffusion of oxygen inside the Ga nanoparticles (see Section 1.4.2), so it could present a barrier for the interdiffusion but at the same time also a barrier for the reduction of Au(III). The reaction obviously occurred, which indicates that the oxide/hydroxide layer was dissolved. It is known that acidic conditions and the presence of chloride ions, which are ensured during mixing of Ga with $HAuCl_4$, trigger the dissolution of the thin oxide layer (see Section 1.4.2). However, this quickly increases the surface tension of Ga and establishes another, gallium chloride protective layer. I believe that such surface becomes less accessible for the $AuCl_4^-$ ions, which leads to growth of Au only on the seeds established before the complete dissolution of the gallium oxide/hydroxide layer and results in the formation of isolated Au nanoparticles on the surface of the Ga NPs and the "nanoraspberry" morphology of the Ga/Au NPs observed in the Ga/Au@HAp nanocomposite. The growth of gold on the Au rather than

the Ga surface is further facilitated by the presence of arginine, which can be explained by the reducing properties of this amino acid (see further on). Reduction of gold by arginine is slow at low temperature but it can be enhanced by the Au seeds created on the Ga surface during dissolution of the oxide layer. Growth of Au nanoparticles during the Turkevich–Frens citrate reduction is also explained in this way [455], [456], [457], [458]:

$$AuCl_3OH^- + (^-OOCCH_2)_2C(OH)COO^- \longrightarrow AuClOH^- + (^-OOCCH_2)_2C{=}O + H^+ + CO_2 + 2\,Cl^- \tag{5.2a}$$

$$3\,AuClOH^- \xrightarrow{[Au]} Au_{(s)} + AuCl_3OH^- + 2\,OH^- \tag{5.2b}$$

This effect is even more pronounced by additional use of ultrasonication, which results in almost ring shaped Au nanophase and separate Au/Arg NPs. When pH was increased to 7, the Au shell was much more connected and better covered the surface of the Ga particles. This can be explained by conversion of $AuCl_4^-$ into $AuCl_3OH^-$ under such conditions [462], which decreases its ability to dissolve the oxide/hydroxide layer and increases its seeding ability. It creates much larger density of small (<5 nm) $Au(OH)_3$ precipitates [462] that are reduced to Au seeds on the Ga surface. This reduction also requires access to the elemental gallium, which implies passing the surface gallium oxide/hydroxide barrier. Perhaps the oxide shell was dissolved (arginine might have assisted in this process) and re-established after the $Au(OH)_3$ reduction due to the hydroxide form of Au(III). An evidence for this is the absence of $AuGa_2$ formation at higher pH. Anyway, the characteristics of the growth of Au on Ga NPs are very similar to the characteristics of the Au shell growth on amorphous silica nanoparticles [462], which may be due to the amorphous/liquid gallium form imposed by the extreme undercooling of Ga NPs and the goal of creating a Ga/Au/Arg@HAp nanocomposite. Nevertheless, effect of pH and amino acids on the shape of the core-shell nanoparticles has been observed also in the Ag/Au and Au/Ag systems [463], [464]. Apart from pH between 7 and 9, the coverage of the SiO_2 cores is usually notably improved by their surface functionalisation. Hence, I tried to prepare a functionalised Ga surface by ultrasonication in the presence of arginine and indeed the shell of the Ga/Arg/Au/Arg nanoparticles was the finest, which can be attributed to better interaction of Au seeds with the Ga surface. However, the creation of Ga/Au NPs also importantly differs from the synthesis of SiO_2/Au NPs in that the Ga core is used as a reducent as well. Thus, larger consumption of the gallium core was observed in case of Ga/Arg/Au/Arg@HAp nanocomposite, which can be ascribed to higher dissolution of Ga after functionalisation with arginine and/or at higher arginine concentration (large extent of dissolution of Ga NPs has also been observed in the ion-release experiments on Ga@HAp in media consisting of amino acids), but also to enhanced reaction with Au(III) due to better contact. On the other hand, it could also be explained by a dealloying process, which results in cracks and holes in the shell and exposure of the inner segregated core. If it occurs in the presence of the Au(III) ions, they further consume the exposed core and eventually the cracked Au shell is collapsed into a solid Au nanoparticle that retains the shape of the core particle. These events were carefully followed and explained in Ag/Au core-shell nanoparticles [435], [445]. Au nanoparticles with the shape of the preexisting Ga core were found also in the Ga/Arg/Au/Arg@HAp nanocomposite. The smaller Au size might have enhanced these interdiffusion-based events.

We have seen that many events can occur during the formation of Ga/Au/Arg functionalised core-shell nanoparticles and many factors affect their appearance and stability, which makes this kind of functionalised Au addition more difficult to control in comparison with the Au/Arg@HAp(Ga) materials, for which a very simple synthesis gives a fairly narrow distribution of functionalised Au nanoparticles. The progress of the core-shell formation depends very strongly on the homogeneity of the synthesis conditions and the initial core

appearance. However, multiple final products have been observed even for core nanoparticles with very narrow size distribution [435]. The main ideas behind the drug delivery with Ga/Au/Arg functionalised core-shell nanoparticles are:

(a) diffusion of the antibacterial Ga core outwards at physiological conditions and its dissolution upon exposure to the culture media;

(b) antibacterial action of the Au/Arg shell in a similar way as observed for Au/Arg NPs (mimicking antibacterial peptides);

(c) biocompatibility due to the Au/Arg surface, as observed for Au/Arg NPs.

In general, the hollowing of the core followed by dealloying, cracking of the shell and release of the antibacterial core would be a great way of drug delivery if it could be tuned to physiological conditions. Such tuning could be done by the precise control over the size of the core-shell nanoparticles. Unfortunately, for Ga/Au the interdiffusion appears to go on already at temperatures much below room temperature due to a low melting point of Ga, so such tuning seems very difficult if not even impossible. The experiments on Ga^{3+} ion release from the Ga/Au@HAp as well as Ga/Au/Arg@HAp revealed a very fast release of nearly all containing Ga within one day. It seems that the oxide layer in Ga@HAp nanocomposites enabled better control over ionic gallium release than the Au shell. This can be a consequence of a non-complete shell and/or lack of the passivating oxide shell, which render gallium very accessible to the medium and easily dissolvable. The two materials that released the high amount of Ga consequently exhibited strong antibacterial action against *P. aeruginosa* but also higher cytotoxicity to L929 than Ga@HAp. The uncontrolled release of almost two times higher Ga(III) concentration could be the main reason for increased cytotoxicity, but cannot account for the extent to which cytotoxicity was increased. Thus, perhaps the poor control over the size, shape and instability of the nanogold part after dissolution of the Ga core also contributes to it. Moreover, the two nanocomposites with the most continuous shell (Ga/Au/Arg@HAp formed at pH 7 and Ga/Arg/Au/Arg@HAp) were tested against *E. coli* and did not show any antibacterial action despite the functionalisation of the Au shell. There are several possible explanations for this observation:

1. The size of the Ga/Au/Arg NPs, Ga/Arg/Au NPs or the resulting Au/Arg NPs after Ga release is not even nearly the same as the size of the Au/Arg NPs in the Au/Arg@HAp(Ga) nanocomposites. The size and width of the size distribution of the starting Ga NPs were already larger than for the Au/Arg NPs and their size further increased during the formation of the core-shell structure, presumably due to dissolution of the protective oxide shell and consequent coalescence of the Ga NPs [193], although an increase in the core diameter during the formation of the shell has been reported also for Ag/Au nanoparticles [464]. The size of the nanoparticles is determinant for interactions with cells (see Section 1.3) and surely very important in the contact-based antibacterial action of the Au/Arg nanoparticles. Above a certain size or due to high agglomeration outside the cell, these interactions do not happen and no antibacterial action is found [465].

2. Uncompleted Au shell, which can also lead to different interactions in comparison with Au/Arg nanoparticles. Furthermore, the shell might have been converted to an $AuGa_2$ shell, which leads to the loss or change of functionalisation. Even if the alloyed shell does not form, the Ga core can affect the functionalisation of the Au shell.

3. Ga/Au/Arg and Au/Arg NPs differ in functionalisation. Functionalisation is capping of nanoparticles with molecules that give them a specific function and is commonly provided to gold nanoparticles via strong Au-S and Au-N bonds. The covalent nature of the Au-S bond is usually explained as a consequence of lanthanoide contraction and relativistic effect, which give Au a surprisingly high electronegativity value, roughly equal to the electronegativity of S [466], [467], [468], [469]. The 6s and 5d orbitals are close enough in energy for mixing to occur and yield more directed s-d hybrid orbitals that participate in covalent bonding [466], [467]. Although N has a higher electronegativity than S, the Au-N bonds have also been recognised as almost covalent [470], [471], [472]. However, the nature of these bonds depends on the pH [472], [473], [474], especially in case of arginine, which has amino groups in his side chain as well. It has been found that the interaction of arginine with Au NPs becomes electrostatic at pH 7 [472]. Since this was the pH at which Ga/Au/Arg NPs were formed but not the Au/Arg NPs, the Au-Arg bond might be different in these two types of NPs. Another difference is in the role amino acid plays during the formation of the Au/Arg or the Ga/Au/Arg NPs. In general, there are three ways of creating functionalised Au NPs: addition of the functionalising molecule after the formation of Au NPs (usually by citrate or $NaBH_4$ reduction), formation of Au in the presence of the functionalising molecule and formation of the Au NPs with the functionalising molecule. Formation of the Ga/Au/Arg NPs is of the second type, while formation of Au/Arg NPs is more of a third type, with amino acid acting as a reducent. It seems puzzling that all three methods give the same functionalized Au NPs. Some articles warn about the possibility of electrostatic rather than covalent attachment of amino acid to Au-citrate NPs or Au-borohydride NPs [474], [475], [476], [477]. It should also not be irrelevant whether or not the amine acts as a reducent. A few studies used NMR to prove oxidation and decarboxylation of amino acids during the Au reduction with amino acid [478], [479] in a similar way to the citrate oxidation during the Turkevich–Frens method (Eq. (5.2)). This might explain the higher toxicity of Au/Gly@HAp in comparison with Au/Arg@HAp, since Gly is converted to formic acid [480], [481]. On the other hand, some other studies also demonstrate the formation of radicals and polymerisation of amine that was used as the reducent to obtain functionalized Au [482]. In fact, sonochemical reactions are usually explained by radical-forming mechanisms and one such mechanism has been proposed also for the sonochemical creation of Au NPs with 2-propanol (Eq. (5.3)) [483]:

$$H_2O \longrightarrow {}^{\bullet}H + {}^{\bullet}OH \tag{5.3a}$$

$$CH_3CHOHCH_3 + {}^{\bullet}H({}^{\bullet}OH) \longrightarrow (CH_3)_2C^{\bullet}OH + H_2(H_2O) \tag{5.3b}$$

$$(CH_3)_2C^{\bullet}OH \longrightarrow \text{pyrolysisradicals} \tag{5.3c}$$

$$AuCl_4^- + 3\,H^{\bullet} \longrightarrow Au(0) + 4\,Cl^- + 3\,H^+ \tag{5.3d}$$

$$3\,(CH_3)_2C^{\bullet}OH + AuCl_4^- \longrightarrow 3\,(CH_3)_2C{=}O + Au(0) + 4\,Cl^- + 3\,H^+ \tag{5.3e}$$

Since the formation of Au/Arg nanoparticles in the Au/Arg@HAp(Ga) is sonochemical, it could lead to the formation of polyarginine, which is known to possess antibacterial properties [484], whereas this molecule cannot be obtained during the formation of Ga/Au/Arg NPs.

However, the majority of articles focus only on the reduction of Au. Au(III) complexes are square planar and free electrons of the ligands (Cl^-, R-NH or R-SH) form π bonds with the empty p_z orbital [485]. In Au(I) state the p orbitals are much less

involved in ligand bonding [486], [487], [488], [489] and d orbitals exhibit aurophilicity, a tendency to form multicore Au(I)-ligand complexes [467], [490], [491]. Such complexes are already similar to small clusters [491], [492]. Thus, reduction of Au is understood as merely a rearrangement of electrons, caused by activation energy, in the frames of the Marcus theory [482]. Charge transfer of electrons from Cl^- to d orbitals is already observed in Au(III) and Au(I) complexes, and for sulfides and amines it can be stabilised by protonation. Hence, the Au reduction with functionalizing molecule might be understood more in organic chemistry view by electron transfer and protonation/deprotonation and pH change. The thiol-protected Au clusters are composed of an Au core and Au(I)-thiol complexes on the surface that are attached to the core atoms through aurophillic interactions [493]. It is reasonable to understand the functionalisation in the Au/Arg NPs in this view as well, which was suggested by Vukomanović *et al.*, who confirmed both Au(0) and Au(I) oxidation states in the Au/Arg@HAp nanocomposite by XPS [350]. The question remains whether such functionalisation occured also in the Ga/Au/Arg@HAp nanocomposite, or the reduction on the Ga surface and different particle size triggered different Au states. Existence of Au(I) on the surface could also be very important for the antibacterial action of Au/Arg NPs. Au(I) complexes are known for their antibacterial activity [494], [495] and some scientists have reported also the antibacterial properties of Au(I)-amino acid binuclear complexes [496]. However, elemental Au phase can be observed in their XRD analysis, so they might have already obtained functionalised Au/amino acid nanoparticles.

As there are apparently many differences between the two explored ways of functional nanogold additions to the gallium-based modified hydroxyapatites, we cannot yet reject the hypothesis of the enhancement in the form of Ga/Au/Arg NPs, even though so far the Au/Arg@HAp(Ga) nanocomposite seems the most useful option, worthy of further investigation.

5.6 Metal ions, nanotechnology and other new or renewed trends to combat the antibiotic resistance

As already mentioned in Section 1.1, discovering a new antibiotic takes time while bacteria gain resistance to it very fast. In order to increase the available time for development of new antibiotics and their lifetime before the development of resistance we need to find some alternatives to antibiotics. The antibacterial mechanisms of the metal ions and nanomaterials have been presented in detail and compared to the mechanisms of antibiotics in Sections 1.1.1, 1.2.2 and 1.3.2. While each antibiotic acts on only one target, the action of one kind of inorganic ions or nanomaterials involves many different targets. The targets of the antibiotics are specific for bacteria, whereas the targets of the metal ions and nanomaterials are mostly non-selective for the different types of cells. Thus, the antibiotics are harmless to eukaryotic cells but also enable the resistance very easily. On the other hand, the development of the resistance to metal ions is more difficult, but they can also affect the eukaryotic cells. Moreover, even though usually not in connection with the antibiotic resistance, the bacteria have found many ways to resist metal ions as well, mainly by hindering their transport into the cell (Section 1.2.3). Hence, the additional ways of transport offered by nanomaterials and their additional interactions with biological macromolecules and cells further decrease the possibility for the resistance, but also add to the toxicity for eukaryotic cells. Since the antibacterial action of gallium is connected with its iron substitution (see Section 1.4.4.2), it is somewhat more specific and many bacteria

can find a way to avoid the use of Fe(III) to survive. This was seen also in my experiments, as gallium contributed notably to the antibacterial action against *P. aeruginosa* but not the other two types of bacteria. Limitations due to its cytotoxicity have also been revealed, particularly in the form of a thin amorphous $GaPO_4$ layer on hydroxyapatite. Since Ga NPs dissolved relatively fast already in growth media without any bacteria, the extent of increased transport was not very large. Nevertheless, the nanoparticles exhibited stronger antibacterial action than solely the released ions.

Inorganic ions and nanotechnology are not the only options for saving the antibiotics. Here I will compare them also to two other possible solutions for the antibiotic resistance problem that have received much interest recently: bacteriophages and antimicrobial peptides. Like metal ions, bacteriophages and antimicrobial peptides had been discovered and investigated already before the discovery of antibiotics and have regained attention after the antibiotic resistance alarms [497], [498], [499]. The number of available different bacteriophages and antimicrobial peptides is much larger than the number of different antibiotics and new bacteriophages and antimicrobial peptides can be designed much faster than new antibiotics. Both can be seen as advanced organic nanoparticles capable of recognising bacteria. Furthermore, bacteriophages additionally use bacteria to replicate them and can accommodate and evolve in response to the bacterial evolution [497], [498]. Thus, their concentration increases exponentially at site of infection until all targeted bacteria are destroyed and it is very unlikely that bacteria would develop a resistance to the viruses which they could not bypass soon [497], [500]. Bacteriophages are very specific for bacteria (they usually affect only a couple of strains of one bacterial species) and cannot directly affect the eukaryotic cells [501]. However, as already described in Section 1.1 (Figure 1.4), bacteriophages can participate in the spread of the resistance [502]. If they undergo a lysogenic instead of a lytic cycle, they can increase the virulence of bacteria [500]. Even if their high specificity is great for tissue cells as well as for preservation of the human normal microbiota, it has the disadvantage that it requires a very accurate infection diagnosis, which is often impossible, and a single type of phage is often not enough to prevent an infection, which can be caused by many different strains [501]. Thus, a mixture of different phages is usually required [498], [501]. Antimicrobial peptides, on the other hand, are not so specific, they act on a wide variety of bacteria, fungi and viruses, some of them are also cytotoxic [499], [503], [504]. In this view and in their mechanisms of action, which mainly involve cell wall/membrane damage but sometimes even intracellular interactions with important biomolecules and generation of ROS [499], [503], [505], they are very similar to the inorganic nanoparticles, but with generally higher selectivity for prokaryotic cells. Unlike bacteriophages the antibacterial peptides cannot evolve, so bacteria have already found many ways to defy their action, such as changing their cell wall, degrading the antimicrobial peptide or preventing its entrance into the cell [499], [505], [506]. This resistance, however, does not occur as fast and to such extent as in the case of antibiotics [504]. Apart from the cytotoxicity and resistance, the two other important drawbacks of the antimicrobial peptides are their potential proteolytic degradation and high cost of their synthesis and purification [499], [503].

Inorganic nanotechnology should learn from these highly advanced systems developed in nature and try to improve its major weakness, i.e., the non-selectivity for bacteria. Functionalised nanoparticles are already an important step towards this improvement. Their advantage over antimicrobial peptides and bacteriophages is better stability against enzymatic degradation and inability of mutation or influence on the virulence of bacteria. Nevertheless, the antibacterial inorganic nanomaterials are also prone to changes and modifications in the biological systems, such as agglomeration, passivation, capping and dissolution. The latter is often their main source of antibacterial action, as in the case of

Ga NPs. If nanoparticles were designed in such a way that their dissolution was triggered by the presence of the pathogen, then their action would approach the action of bacteriophages. Since the antibacterial Ga NPs are a very new discovery, the control over their dissolution is only in the first stage of development. The available tools for its improvement are the size of the Ga NPs, the thickness and the nature of the passivating layers, i.e., the oxide/hydroxide layer or any additional layers that could protect the inner Ga. I tried gold shell as one such layer, but the Ga/Au core/shell nanoparticles developed so far did not exhibit any better control over Ga(III) release.

An important advantage of bacteriophages and antimicrobial peptides in comparison with antibiotics is their large variety of the available types. A large variety of the available nanomaterials is achieved by changing the properties listed and described in Section 1.3.1: chemistry, bulk/ionic properties, size, shape and surface properties. Differences in antibacterial properties and cytotoxicity between Ga, Ag and Au have been revealed in this thesis. Particularly interesting is the different bacterial specificity of Ga and Au/Arg with the former being effective against *P. aeruginosa* and the latter against the other two species (*E. coli* and *S. epidermidis*). Moreover, the two antimicrobials were also successfully combined and resulted in synergism, in a similar way as combinations of antibiotics or bacteriophages, but with a slight increase in the cytotoxicity as well. Another particularly important property that can contribute a lot to the variety is functionalisation, in which the inorganic nanotechnology comes across the antibacterial peptides and bacteriophages. Except for the arginine functionalisation on Au NPs and testing the Ga NPs with oleic acid on the surface, this property was not varied much in this thesis, which leaves a lot of space for further development. The antibacterial action of inorganic antibacterial ions also varies very much with the chemistry of the central metal ion and the form of the ionic species, which was well explained and demonstrated in the Introduction. This fact was also used for one possible explanation of the different antibacterial action and cytotoxicity of the different HAp(Ga) materials, $Ga(NO_3)_3$, the released Ga^{3+} ions and $GaPO_4$.

Last but not least, the inorganic antibacterial ions and nanomaterials are easily combined with biomaterials, especially inorganic (such as hydroxyapatite), which makes them particularly useful for saving antibiotics in tissue engineering and implantation applications. Many different biomaterials based on Ga, Au and hydroxyapatite have been created during my doctoral work using relatively simple and fast synthesis methods without byproducts and without any complicated or expensive purifications. Moreover, the storage of the prepared nanocomposites is non-demanding, the nanopowders are stable under normal conditions and retain their antibacterial properties even after two years of storage. Even though the bulk Ga melts near room temperature, the extreme supercooling and passivation with self-terminating oxide layer make the liquid Ga NPs very stable in a wide temperature range, oxygen and humid atmosphere. Furthermore, due to mild conditions during the ultrasonic emulsification synthesis the Ga NPs are expected to combine well also with biopolymers. Examples of creating composites of Ga NPs with polymers by ultrasonic emulsification can already be found in the literature and were presented in Section 1.4.3.2.

Chapter 6

Conclusions

We came to the following conclusions:

1. Ga^{3+} ions can be incorporated into the non-apatitic disordered surface layer of HAp, from which they are released in simulated body fluids. This gives the HAp(Ga) biomaterial antibacterial properties against *P. aeruginosa*. By tuning the composition of the amorphous Ca/Ga phosphate surface layer and the overall Ga content of the HAp(Ga), we can attain the release of Ga^{3+} ions in the bioactive range, low toxicity and efficient antibacterial protection at the same time. Such tuning can be achieved by varying the added amount of Ga(III) or the size of the HAp(Ga) particles, which can also be controlled by adding Ga^{3+} ions at different stages of the synthesis of HAp.

2. Stable nanocomposite powder consisting of Ga NPs and HAp can be created using low-temperature ultrasonic emulsification. The sonochemical conversion of Ga to GaOOH is prevented in non-aqueous polar media (ethylene glycol) or by the addition of a more volatile polar organic liquid (acetonitrile) to water. The Ga@HAp nanocomposite possesses antibacterial properties against *P. aeruginosa*, which are based on the local release of the antibacterial Ga^{3+} ions from the Ga NPs. Moreover, the useful range of concentrations, in which the antibacterial activity of Ga@HAp against *P. aeruginosa* is high and its toxicity for fibroblasts is low, is much wider than for a comparable Ag@HAp nanocomposite.

3. Au/Arg@HAp(Ga) combines the antibacterial action of Au/Arg NPs and Ga^{3+} ions. The former are mainly responsible for its antibacterial activity against *E. coli* and *S. epidermidis*, while the latter mainly against *P. aeruginosa*. Thus, the antibacterial action against *P. aeruginosa* is weak for the Au/Arg@HAp and strong for the Au/Arg@HAp(Ga) nanocomposite, so combining the HAp(Ga) with Au/Arg nanoparticles broadens the strain diversity of the antibacterial activity and the new Au/Arg@HAp(Ga) nanocomposite presents an improvement with respect to the Au/Arg@HAp. The high selectivity between eukaryotic and prokaryotic cells is not retained as the Ga(III) addition increases the cytotoxicity as well. Nevertheless, the Au/Arg@HAp(Ga)TR has a useful therapeutic window.

4. Ga/Au core-shell nanoparticles can be formed by the galvanic method using Ga as the sacrificing core. Functionalised Ga/Au core-shell NPs are formed if $AuCl_4^-$ is reduced on the Ga NPs in the presence of amino acid. The morphology of the shell is directed by the nature of the Ga surface and the Au(III) form in dependence of the pH.

5. Combination of Ga and functionalised nanogold antimicrobial in the form of an Au/Arg@HAp(Ga) is favourable over the Ga/Au/Arg@HAp nanocomposite form.

The high antibacterial activity and biocompatibility make the HAp(Ga)TR, Ga@HAp and Au/Arg@HAp(Ga)TR very promising new biomaterials for future biomedical applications and a new direction towards an advanced biomaterial that can stimulate tissue growth while being self-protected against infection at the same time.

Appendix A

Mie Scattering Theory and Surface Plasmon Resonance

A.1 Metallic Nanoparticles

There are a few systematic and detailed books about the surface plasmon resonance and Mie theory [368], [507], [508]. Here I give a summary of these books for better understanding of this phenomenon and the calculated absorbance spectra.

Light is electromagnetic waving and its effect on the matter is a balance between its electric (and/or magnetic) force and the internal forces inside the matter:

$$\mathbf{F}_{\text{inertia}} + \mathbf{F}_{\text{damping}} + \mathbf{F}_{\text{repulsive}} = \mathbf{F}_{\text{electrical}} \tag{A.1}$$

As electrons are more influenced by the electric (and magnetic) force than the core/ions, atoms become polarized. The sum of the atomic dipole moments is called polarisation and is usually denoted as $\mathbf{P}$:

$$\mathbf{P} = \frac{1}{V}\sum_j N_j \mathbf{p}_j = \frac{1}{V}\sum_j N_j q_j \mathbf{r}_j \tag{A.2}$$

Polarisation of materials by electromagnetic waves is based on

- displacement of bound charges (both electrons and ions)
- electronic transitions between occupied and unoccupied electronic levels
- displacement of free electrons, if free electrons are present, which leads to absorption due to the created current

For small particles especially the electronic transitions between occupied and unoccupied electronic levels can lead to resonances. For metal particles additionally the free electrons can cause resonances in the metal particle. The extent to which such polarisation occurs in a material is expressed as susceptibility χ. For sufficiently small electric fields ($|\mathrm{E}| \leq 100$ V m^{-1}), which is fulfilled in most optical applications (moderate intensity), the relation between $\mathbf{P}$ and the incident electric field from light $\mathbf{E}$ is linear:

$$\mathbf{P} = \varepsilon_0 \chi \mathbf{E} \tag{A.3}$$

χ is a second-rank tensor for materials with anisotropic optical properties and a scalar for isotropic homogeneous materials. The electric displacement field (electrical flux density) $\mathbf{D}$ is then

$$\mathbf{D} = \varepsilon_0 \mathbf{E} + \mathbf{P} = \varepsilon_0 (1 + \chi)\mathbf{E} = \varepsilon_0 \varepsilon \mathbf{E}, \tag{A.4}$$

where $\varepsilon = 1+\chi$ is a dielectric constant (permittivity) of the matter. As already mentioned, in the presence of unbound charges in the bulk matter, for example, free electrons in metals or semiconductors, the electric field $\mathbf{E}$ additionally causes an electric current with current density $\mathbf{J}$ (Ohm's law):

$$\mathbf{J} = \sigma\mathbf{E} \tag{A.5}$$

where σ is the (optical) conductivity. The energy contained in $\mathbf{J} \cdot \mathbf{E}$ is transformed into oscillations of the crystal lattice (phonons) and is therefore missing in the energy transport between the incident, refracted, and scattered wave. It is absorbed in the particle.

Similarly to the electric field, also the magnetic field $\mathbf{H}$ causes two reactions of the material on the applied field, a magnetisation $\mathbf{M}$ and a current displacement $\partial D/\partial t$. The latter is the result of the Lorentz force on bound and free electrons. The magnetisation $\mathbf{M}$ contributes to the magnetic induction $\mathbf{B}$ in the particle:

$$\mathbf{B} = \mu_0\mathbf{H} + \mu_0\mathbf{M} = \mu_0(1 + \chi_m)\mathbf{H} = \mu\mathbf{H} \tag{A.6}$$

due to reorientation of permanent magnetic dipoles in the applied field. χ_m is magnetic susceptibility and $\mu = \mu_0(1 + \chi_m)$ is permeability. However, at frequencies ranging from the far-infrared to infinity $1+\chi_m \approx 1$ for all known materials, even for magnetic materials.

All the aforementioned quantities are connected through 4 Maxwell's equations:

$$\nabla \cdot \mathbf{D} = \nabla(\varepsilon\mathbf{E}) = \rho \tag{A.7a}$$

$$\nabla \times \mathbf{E} + \frac{\partial \mathbf{B}}{\partial t} = 0 \tag{A.7b}$$

$$\nabla \times \mathbf{H} = \frac{\partial \mathbf{D}}{\partial t} + \sigma \cdot \mathbf{E} \tag{A.7c}$$

$$\nabla \cdot \mathbf{B} = 0 \tag{A.7d}$$

The harmonic nature and the aforementioned time dependence of the EM waves has already been taken into account in these 4 expressions and no static charges were considered in Eq. (A.7a). Gustav Mie was the first to solve these four equations for $\mathbf{E}$ and $\mathbf{H}$ of the incident wave, the scattered wave and the internal wave to describe the size dependence of the colour of the gold colloids. In his honour, such theoretical description of the optical properties of nanoparticles is called the Mie theory. His assumptions were:

1. no static charges ($\rho = 0$),
2. harmonic plane waves with time dependence not being affected by the matter (elastic scattering),
3. homogeneous isotropic spherical particles,
4. nonabsorbing embedding medium (linear, isotropic, homogeneous).

According to the second assumption, the time dependence is expressed by the *ansatz* $\mathrm{e}^{-i(\omega t)}$:

$$\mathbf{E} = \mathbf{E}(\mathbf{r})\mathrm{e}^{-i(\omega t)} \tag{A.8a}$$

$$\mathbf{H} = \mathbf{H}(\mathbf{r})\mathrm{e}^{-i(\omega t)} \tag{A.8b}$$

After using the first two assumptions, the Maxwell's 4 equations change to

$$\nabla \cdot (\varepsilon_1\mathbf{E}) = \mathrm{div}(\varepsilon_1\mathbf{E}) = 0 \tag{A.9a}$$

$$\nabla \cdot \mathbf{B} = \mathrm{div}\mathbf{B} = 0 \tag{A.9b}$$

$$\nabla \times \mathbf{E} = \mathrm{curl}\mathbf{E} = i\omega\mu_0\mathbf{H} \tag{A.9c}$$

$$\nabla \times \mathbf{H} = \mathrm{curl}\mathbf{H} = (-i\varepsilon\varepsilon_0\omega + \sigma)\mathbf{E} \tag{A.9d}$$

The third assumption further simplifies Eq. (A.7a) to $\nabla \cdot \mathbf{E} = 0$. Taking into account $\mu = \mu_0$ and using the well-known mathematical relation $\nabla \times (\nabla \times \mathbf{A}) = \nabla \cdot (\nabla \cdot \mathbf{A}) - \nabla^2\mathbf{A}$, we come to only two similar differential equations:

$$\nabla^2\mathbf{E} + (\mu_0\varepsilon_0\omega^2\varepsilon + i\sigma\mu_0\omega)\mathbf{E} = 0 \tag{A.10a}$$

$$\nabla^2\mathbf{H} + (\mu_0\varepsilon_0\omega^2\varepsilon + i\sigma\mu_0\omega)\mathbf{H} = 0 \tag{A.10b}$$

Both are recognized as the Helmholtz type of partial differential equations $\nabla^2\mathbf{A} + k^2\mathbf{A} = 0$, where k is the angular wavenumber $k = \frac{\omega}{c}$. It is expressed in the above equations as

$$k^2 = \frac{\omega^2}{{c_0}^2}(\varepsilon + i \cdot \frac{\sigma}{\varepsilon_0\omega}) \tag{A.11}$$

Here the relation $\mu_o\varepsilon_0 = 1/{c_0}^2$ was already used. c_0 is the speed of light in vacuum, while c is the speed of light in the medium. Their ratio is refractive index $\tilde{n} = c_0/c$. We can see that this quantity is a complex function of ω like ε:

$$\tilde{n}(\omega) = \sqrt{\varepsilon + i \cdot \frac{\sigma}{\varepsilon_0\omega}} = \sqrt{\tilde{\varepsilon}(\omega)} = n + i\kappa \tag{A.12}$$

$\tilde{\varepsilon}$ is the frequency dependent complex dielectric function, which is usually expressed as

$$\tilde{\varepsilon}(\omega) = \varepsilon_1(\omega) + i\varepsilon_2(\omega) = \varepsilon + i \cdot \frac{\sigma}{\varepsilon_0\omega} \tag{A.13}$$

If the time dependence is separated from the space dependence by the *ansatz* $\mathrm{e}^{i(\omega t)}$, then the frequency dependence of the dielectric function is expressed as

$$\tilde{\varepsilon}(\omega) = \varepsilon_1(\omega) - i\varepsilon_2(\omega) \tag{A.14}$$

I will use the first option further on. The $\frac{\omega}{c} = \frac{2\pi}{\lambda}(n + i\kappa)$ is known as the dispersion relation, whereas $n + i\kappa = \sqrt{\varepsilon_1 + i\varepsilon_2}$ is known as the Maxwell's relation. n is the real refractive index and κ is the extinction coefficient. and they are both also frequency dependent. Usually their values at different frequencies/wavelengths are experimentally determined for every material (the most known database is the one by Edward D. Palik [509]). If only one of them is known, the other can be calculated from the Kramers-Krönig relation. But if none of the measured values is available, they can be modelled, usually by a harmonic oscillator+Drude free electron model. For gold, the values have been available for a large frequency range with very small steps for a long time. However, for gallium there was a confusion in the available data in the literature at the beginning of my doctoral study. Different articles were giving quantities and frequency ranges, often only showing a graph without the values. During my attempt of unifying the data by several conversions and recalculations, an article was published in 2014, in which Knight *et al.* did exactly this and additionally provided the $n(\lambda)$,$k(\lambda)$ table for liquid Ga nanoparticles. I used this table for my surface plasmon resonance calculations.

For spherical particles, the vector differential equations (A.10a) and (A.10b) are solved in spherical coordinates by first solving a scalar Helmholtz equation:

$$\nabla^2\psi + k^2\psi = 0 \tag{A.15}$$

The particular solutions are products of a spherical Bessel function z_L (the radial part) and a spherical harmonic (the angular dependence), which is a product of a trigonometric function and an associated Legendre polynomial P_L^m:

$$\psi_{emL} = \cos(m\phi) \cdot P_L^m(\cos\theta) \cdot z_L(k \cdot r) \tag{A.16a}$$

$$\psi_{omL} = \sin(m\phi) \cdot P_L^m(\cos\theta) \cdot z_L(k \cdot r) \tag{A.16b}$$

z_L represents any of the two Bessel functions, either of the 1st order:

$$j_L(x) = \sqrt{\frac{\pi}{2x}} J_{L+1/2}(x) = (-x)^L \left(\frac{1}{x}\frac{\mathrm{d}}{\mathrm{d}x}\right)^L \frac{\sin x}{x} \tag{A.17}$$

or of the 2nd order (also called Neumann function):

$$y_L(x) = \sqrt{\frac{\pi}{2x}} Y_{L+1/2}(x) = (-1)^{L+1} \sqrt{\frac{\pi}{2x}} J_{-L-1/2}(x) = -(-x)^L \left(\frac{1}{x}\frac{\mathrm{d}}{\mathrm{d}x}\right)^L \frac{\cos x}{x} \tag{A.18}$$

$$x = k \cdot r = \frac{2\pi\tilde{n}r}{\lambda} \tag{A.19}$$

Then two types of convenient vectors that satisfy the vector Helmholtz equation are introduced:

$$\mathbf{M} = \nabla \times (\psi \mathbf{r}) \tag{A.20a}$$

$$\mathbf{N} = \frac{\nabla \times \mathbf{M}}{k} \tag{A.20b}$$

Thus, for each particular solution of the scalar Helmholtz equation we obtain a particular vector harmonic as a solution of the vector Helmholtz equation. With the vector harmonics M and N the transverse magnetic (TM) mode or electric mode is given as

$$\mathbf{E}^{TM} = E_0 \mathbf{N} \tag{A.21a}$$

$$\mathbf{H}^{TM} = \frac{kE_0}{i\omega\mu_0} \mathbf{M} \tag{A.21b}$$

and the transverse electric (TE) mode or magnetic mode as

$$\mathbf{E}^{TE} = E_0 \mathbf{M} \tag{A.22a}$$

$$\mathbf{H}^{TE} = \frac{kE_0}{i\omega\mu_0} \mathbf{N} \tag{A.22b}$$

E_0 is the magnitude of the electric field. The general solution is then a linear combination of all particular solutions. Thus, electric and magnetic fields are written as infinite series expansions of TE and TM modes with different expansion coefficients satisfying different boundary conditions for the incident, internal and scattered wave. Thus, we obtain for the scattered waves:

$$\mathbf{E}_s = E_0 \sum_{L=1}^{\infty} i^L \frac{2L+1}{L(L+1)} \left(i a_L \mathbf{N}_{e1L}^{(3)} - b_L \mathbf{M}_{o1L}^{(3)} \right) \tag{A.23a}$$

$$\mathbf{H}_s = \frac{k}{\omega\mu} E_0 \sum_{L=1}^{\infty} i^L \frac{2L+1}{L(L+1)} \left(i b_L \mathbf{N}_{o1L}^{(3)} + a_L \mathbf{M}_{e1L}^{(3)} \right) \tag{A.23b}$$

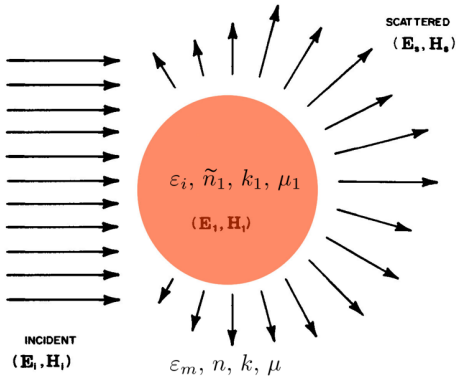


Figure A.1: A schematic of the system solved by Mie with notations used in the text [368].

The expansion coefficients are calculated by the following equations:

$$a_L = \frac{p^2 j_L(px)[x j_L(x)]' - j_L(x)[px j_L(px)]'}{p^2 j_L(px)[x h_L^{(1)}(x)]' - h_L^{(1)}(x)[px j_L(px)]'} \tag{A.24a}$$

$$b_L = \frac{j_L(px)[x j_L(x)]' - j_L(x)[px j_L(px)]'}{j_L(px)[x h_L^{(1)}(x)]' - h_L^{(1)}(x)[px j_L(px)]'} \tag{A.24b}$$

L denotes the mode (order) of the electromagnetic waves. $L = 1$ is the dipole mode, $L = 2$ the quadrupolar mode etc.

$$p = \frac{k_1}{k} = \frac{n_1 + i\kappa_1}{n} \tag{A.25}$$

$h_L^{(1)}$ is the Hankel function of the first order, a combination of both Bessel functions:

$$h_L^{(1)}(x) = j_L(x) + i \cdot y_L(x) \tag{A.26}$$

The index 1 denotes the properties of the particle, while no index is used for the surrounding medium (see Figure A.1). The surrounding medium is non-absorbing, so its wavenumber k and refractive index n are real values.

In fact, we do not need the electric and magnetic fields to obtain absorbance spectra, but only the expansion coefficients, since extinction cross section is expressed as

$$\sigma_{ext} = \frac{2\pi}{k^2} \sum_{L=1}^{\infty} (2L+1) \Re\{a_L + b_L\} \tag{A.27}$$

If suspension is sufficiently diluted (so that the particles do not take up more than 1 % of the cell volume), the extinction cross section σ_{ext} is correlated to the transmittance (Eq. (A.28)) and absorbance by the Beer-Lambert law (Eq. (A.29)):

$$T = \mathrm{e}^{-\sigma_{ext}(N/V)l} \tag{A.28}$$

$$A = -\log_{10} T = -\frac{\ln T}{\ln 10} = -\frac{\sigma_{ext} \cdot N \cdot l}{V \cdot \ln 10} \tag{A.29}$$

Here N is the number of spherical particles in the suspension with volume V and l is the length of the light path through the suspension of particles. Thus, absorbance spectra directly depend on the expansion coefficients, in which p and x give the wavelength dependence and x contains the particle size. An important property of a_L and b_L is that for

certain values of L, p and x, the denominator can approach zero value and consequently an expansion coefficient a very large value. Such condition is known as resonance and is given for the TM modes (a_L coefficients, see Eq. (A.24a)) by the following equation:

$$\frac{p^2 j_L(px)}{[pxj_L(px)]'} = \frac{h_L^{(1)}(x)}{[xh_L^{(1)}(x)]'}, \tag{A.30}$$

whereas for the TE modes (b_L coefficients, see (A.24b)) it is given by the following equation:

$$\frac{j_L(px)}{[pxj_L(px)]'} = \frac{h_L^{(1)}(x)}{[xh_L^{(1)}(x)]'} \tag{A.31}$$

Certain solutions (vector spherical harmonics or modes) of the wave equations in Mie theory have a property that the greater the order of the normal mode, the more the field is localized near the surface of the sphere. Therefore, they are designated "surface" modes. In metallic particles, such waves are transmitted over the surface by collective oscillations of the free ("plasma") electrons. The resonance of such modes is therefore termed *surface plasmon resonance* (SPR). It is the dominant resonance for metals, so usually all TM mode resonances are considered SPR for metallic nanoparticles. The conditions for such resonance are more clearly visible in a small particle (Rayleigh) approximation. For $\lambda >> 2r$(very small x):

$$j_L(x) = \frac{x^L}{1 \cdot 3 \cdot 5 \cdots (2L+1)} \left[1 - \frac{\frac{1}{2}x^2}{1!(2L+3)} + \frac{(\frac{1}{2}x^2)^2}{2!(2L+3)(2L+5)} - \ldots\right] \tag{A.32a}$$

$$y_L(x) = -\frac{1 \cdot 3 \cdot 5 \cdots (2L-1)}{x^{L+1}} \left[1 - \frac{\frac{1}{2}x^2}{1!(1-2L)} + \frac{(\frac{1}{2}x^2)^2}{2!(1-2L)(3-2L)} - \ldots\right] \tag{A.32b}$$

By inputing these approximations into the equation for the TM mode resonances, we can see that SPR is achieved when the real part of particle's dielectric function is negative:

$$\varepsilon_1 = -(2 + \frac{12}{5}x^2)\varepsilon_m \tag{A.33}$$

Usually, ε_1 is a decreasing function of wavelength, so a red shift of the SPR peak (towards longer wavelengths) occurs with increasing the particle size. Figure A.2 displays the calculated UV-VIS spectra for Ga and Au nanospheres with different diameters.

A.2 Core/Shell Nanoparticles

Aden and Kerker were the first to present the solutions for plane wave incident upon a sphere with a concentric spherical shell. The expansions for the fields are formally the same (see Equations (A.27), (A.28) and (A.29)), only coefficients a_L and b_L change [507]. There are 2 boundaries:

- the boundary between the core and the shell:

$$x_c = k_s a = k_s R_{core} \tag{A.34}$$

$$p_c = \frac{n_c}{n_s} \tag{A.35}$$

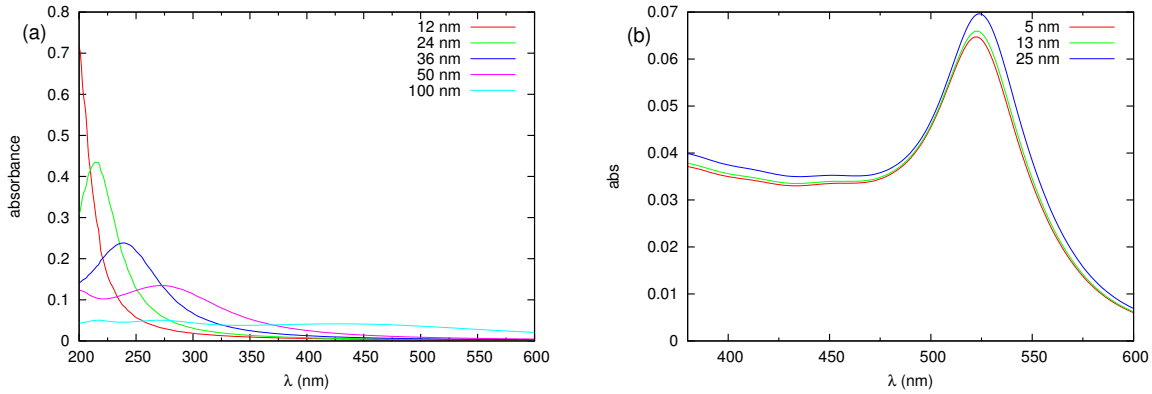


Figure A.2: Calculated UV-VIS spectra of different Au nanoparticles (left) and Ga nanoparticles (right).

- the boundary between the particle and the embedding medium:

$$x_s = kb = k(R_{core} + d) \tag{A.36}$$

$$p_s = \frac{n_s}{n} \tag{A.37}$$

The refractive indices of the core (n_c) and the shell (n_s) material can be complex numbers. The coefficients a_L and b_L are then calculated as

$$a_L = \frac{\xi_L(x_s)[\xi'_L(p_s x_s) + S_L\zeta'_L(p_s x_s)] - p_s\xi'_L(x_s)[\xi_L(p_s x_s) + S_L\zeta_L(p_s x_s)]}{\eta_L(x_s)[\xi'_L(p_s x_s) + S_L\zeta'_L(p_s x_s)] - p_s\eta'_L(x_s)[\xi_L(p_s x_s) + S_L\zeta_L(p_s x_s)]} \tag{A.38a}$$

$$b_L = \frac{p_s\xi_L(x_s)[\xi'_L(p_s x_s) + T_L\zeta'_L(p_s x_s)] - \xi'_L(x_s)[\xi_L(p_s x_s) + T_L\zeta_L(p_s x_s)]}{p_s\eta_L(x_s)[\xi'_L(p_s x_s) + T_L\zeta'_L(p_s x_s)] - \eta'_L(x_s)[\xi_L(p_s x_s) + T_L\zeta_L(p_s x_s)]}, \tag{A.38b}$$

where S_L and T_L are

$$S_L = -\frac{\xi_L(x_c)\xi'_L(p_c x_c) - p_c\xi'_L(x_c)\xi_L(p_c x_c)}{\zeta_L(x_c)\xi'_L(p_c x_c) - p_c\zeta'_L(x_c)\xi_L(p_c x_c)} \tag{A.39}$$

$$T_L = -\frac{p_c\xi_L(x_c)\xi'_L(p_c x_c) - \xi'_L(x_c)\xi_L(p_c x_c)}{p_c\zeta_L(x_c)\xi'_L(p_c x_c) - \zeta'_L(x_c)\xi_L(p_c x_c)} \tag{A.40}$$

The functions ξ_L, η_L and ζ_L are called Riccati-Bessel functions and expressed as

$$\xi_L(x) = x \cdot j_L(x) \tag{A.41a}$$

$$\eta_L(x) = x \cdot h_L^{(1)}(x) \tag{A.41b}$$

$$\zeta_L(x) = x \cdot y_L(x) \tag{A.41c}$$

After the coefficients a_L and b_L are calculated by Eq. (A.38), the extinction cross sections and absorbances are calculated from Equations (A.27), (A.28) and (A.29), respectively, for different wavelengths (using tables of optical constants in dependence on wavelength for the core and the shell material) to obtain the calculated UV-VIS spectra, such as

the ones presented in Section A.2.3. The extinction cross section can also be calculated approximately by Equation (A.42)

$$\sigma_{ext}(\lambda, R, d) \approx \frac{8\pi^2(R+d)^3\sqrt{\varepsilon_m}}{3\lambda}\Im\left\{\frac{(\varepsilon_s-\varepsilon_m)(\varepsilon_c+2\varepsilon_s)+\left(\frac{R}{R+d}\right)^3(\varepsilon_c-\varepsilon_s)(\varepsilon_m+2\varepsilon_s)}{(\varepsilon_c+2\varepsilon_s)(\varepsilon_s+2\varepsilon_m)+2\left(\frac{R}{R+d}\right)^3(\varepsilon_c-\varepsilon_s)(\varepsilon_s-\varepsilon_m)}\right\} \tag{A.42}$$

Although nowadays the full calculations of extinction cross sections and absorbance spectra are easily obtainable, it is insightful to look at some limiting cases of core-shell nanoparticles.

A.2.1 Dielectric-metal core/shell NPs

In this kind of core/shell NPs the dielectric function of the core ε_c is real and its imaginary part negligible. The resonances are achieved at negative values of shell dielectric function ε_s. Simple expressions are derived at the limiting conditions of a very small or a very large shell thickness.

A.2.1.1 Small shell thickness

At a very small shell thickness, the following approximation can be used:

$$\left(\frac{R}{R+d} \approx 1-\frac{d}{R}\right) \tag{A.43}$$

This yields two resonant dipole conditions:

(a)

$$\varepsilon_s \approx -\frac{R}{2d}(\varepsilon_c+2\varepsilon_m) = -2\varepsilon_m\frac{R}{2d}\left(1+\frac{\varepsilon_c}{2\varepsilon_m}\right) \tag{A.44}$$

ε_s must become more negative than for a compact metal sphere, mainly because of the factor R/ d. A more negative value is reached at longer wavelengths, meaning that the resonance is red shifted. The smaller the shell thickness d the larger the red shift.

(b)

$$\varepsilon_s \approx -\frac{1}{2}\varepsilon_c \tag{A.45}$$

The second condition is caused by the inner boundary between the core and shell.

With increasing core size, higher multipolar orders ($L \geq 2$) become clearly resolved:

$$\left(\varepsilon_s+\frac{L+1}{L}\varepsilon_m\right)\left(\varepsilon_c+\frac{L+1}{L}\varepsilon_s\right)+\frac{L+1}{L}\left(\frac{R}{R+d}\right)^3(\varepsilon_s-\varepsilon_m)(\varepsilon_c-\varepsilon_s)=0 \tag{A.46}$$

A.2.1.2 Large shell thickness

When the thickness of the shell is very large, the following relation holds true:

$$\left(\frac{R}{R+d} << 1\right) \tag{A.47}$$

This yields the following two resonant dipole conditions:

(a)

$$\varepsilon_s \approx -2\varepsilon_m \tag{A.48}$$

The first condition coincides with the condition for a homogeneous sphere. It is the limiting value for large shell thickness. Then, the metal-coated sphere with a dielectric core behaves like a compact metal sphere. However, as for the large thickness d the total size of the particle also increases and therefore the particle does not further fulfil the Rayleigh approximation, this limit will not be completely approached, but the extinction efficiency of the coated sphere will deviate from the extinction efficiency of the compact sphere.

(b)

$$\varepsilon_s \approx -\frac{1}{2}\varepsilon_c \tag{A.49}$$

With increasing core size, higher multipolar orders (L≥2) become clearly resolved:

$$\left(\varepsilon_s + \frac{L+1}{L}\varepsilon_m\right)\left(\varepsilon_c + \frac{L+1}{L}\varepsilon_s\right) + \frac{L+1}{L}\left(\frac{R}{R+d}\right)^3(\varepsilon_s - \varepsilon_m)(\varepsilon_c - \varepsilon_s) = 0 \tag{A.50}$$

A.2.2 Metal-dielectric core-shell NPs

For the inverse system – dielectric shell on a metal core particle – the denominator must be resolved for the dielectric function ε_c of the core. Resonance condition:

$$\varepsilon_c = -2\varepsilon_s \frac{(\varepsilon_s + 2\varepsilon_m) - \left(\frac{R}{R+d}\right)^3(\varepsilon_s - \varepsilon_m)}{(\varepsilon_s + 2\varepsilon_m) + 2\left(\frac{R}{R+d}\right)^3(\varepsilon_s - \varepsilon_m)} \tag{A.51}$$

For small d the expression for uncoated sphere is obtained:

$$\varepsilon_c = -2\varepsilon_m \tag{A.52}$$

For large d we get a compact sphere in the surrounding medium with a dielectric function ε_s:

$$\varepsilon_c = -2\varepsilon_s \tag{A.53}$$

This limiting case cannot actually be approached, since for large d the total size of the sphere exceeds the limits of the Rayleigh approximation and a full Mie theory must be applied.

A.2.3 Metal-metal core-shell NPs

UV-VIS spectra of metal-metal core-shell nanoparticles differ from the UV-VIS spectra of a mixture of the two metallic nanoparticles or the spectra of alloyed nanoparticles. Figure A.3 compares calculated absorbance spectra for Ag_xAu_y alloyed NPs and Ag/Au core-shell nanoparticles. While the SPR peak is redshifted in dependence of the Au content for the Ag_xAu_y NPs, two SPR peaks are seen for the Ag/Au core-shell nanoparticles, but their intensities are decreased and the one at the longer wavelength shifts with increasing shell thickness. I have used the same system to test my modified program for calculation of absorbance spectra of core-shell nanospheres. The result of my calculation is presented in Figure A.4 and a comparison with Figure A.3 reveals a very good match.

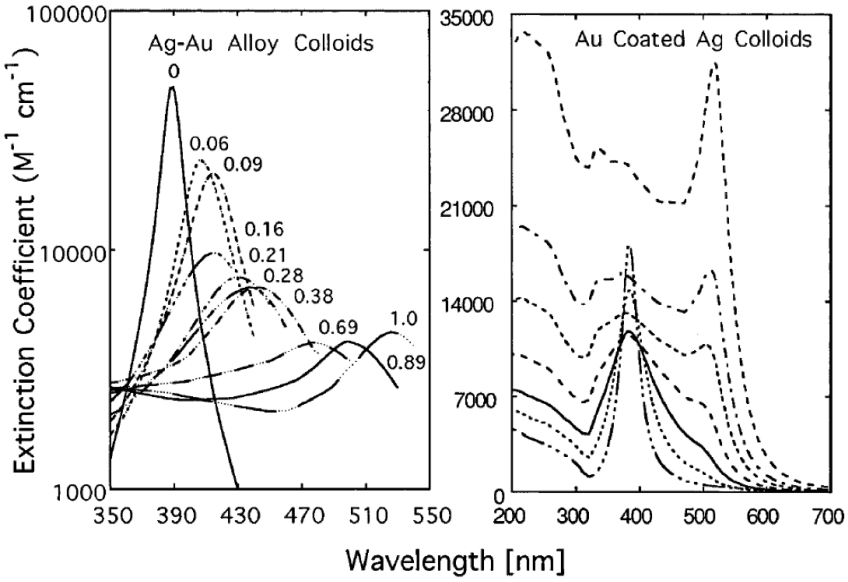


Figure A.3: Calculated spectra of AuAg nanoalloys and Ag/Au core/shell NPs from the literature. *Left:* Calculated spectra of 6 nm-sized particles of AuAg alloys of various composition in water using full Mie equations [510]. No mean free path effects were used, since the damping frequency in the alloys is unknown. The numbers refer to the mole fraction of gold. *Right:* Calculated spectra of Au-coated Ag colloids in water. Core radius $\sim$ 3.0 nm. Note the silver plasmon band is strongly damped but does not shift. Thick coatings show a surface plasmon resonance in the gold layer close to 500 nm. Surface scattering in the core is included. Gold layer thicknesses used were 0, 0.32, 0.6, 1.0, 1.5, 2.0, and 3.0 nm [510].

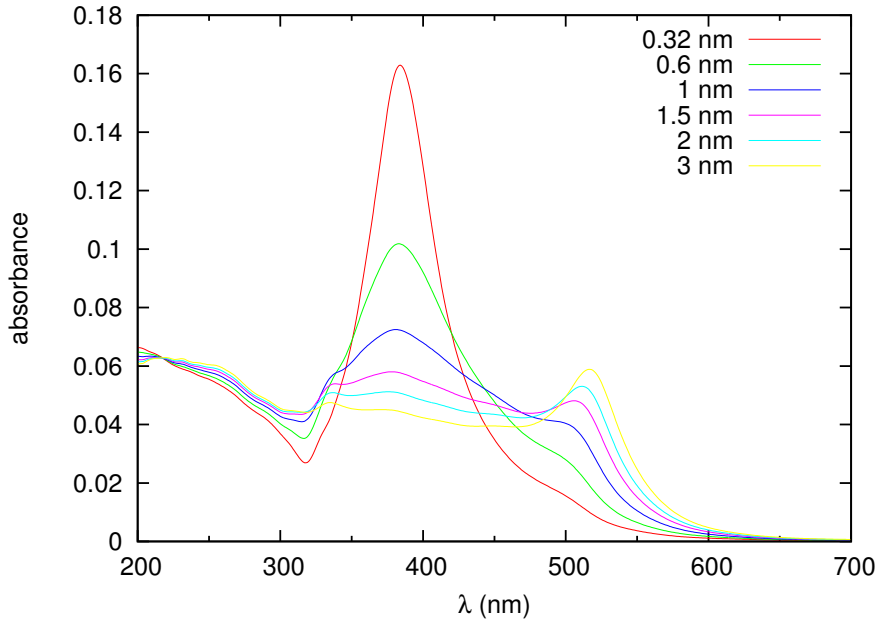


Figure A.4: My calculations of UV-VIS spectra of Ag/Au core-shell nanoparticles.

Appendix B

Reference X-Ray Diffraction Patterns of Hydroxyapatite and Ga Nanoparticles

Since hydroxyapatite was used as the bioactive component in all the investigated materials in this thesis, it was present in almost all the presented X-ray diffractograms. Due to a large number of diffraction maxima of this phase I have decided to avoid peak indexing on the experimental diffractograms and rather include the indexed HAp reference pattern in the Appendix. Thus, it is presented in Figure B.1. I have also included here the XRD

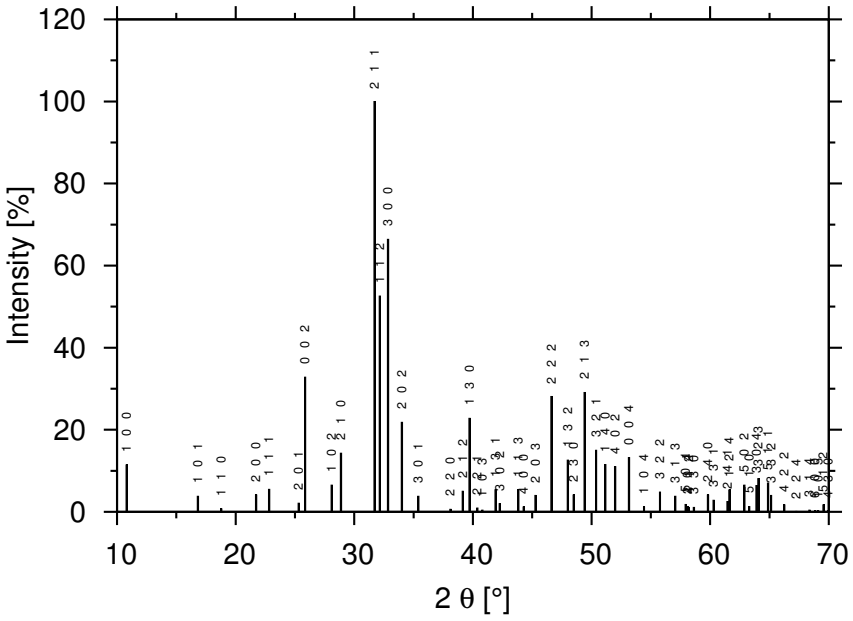


Figure B.1: Indexed XRD pattern of hydroxyapatite (PDF number 01-089-6438).

patterns of the monodisperse Ga NPs by Yarema *et al.* [165] that helped me identify the Ga phase in the Ga@HAp nanocomposites also from the XRD patterns. They were originally recorded by a Mo anode, so I converted them to the Cu anode values for proper comparison. The converted XRD patterns are shown in Figure B.2.

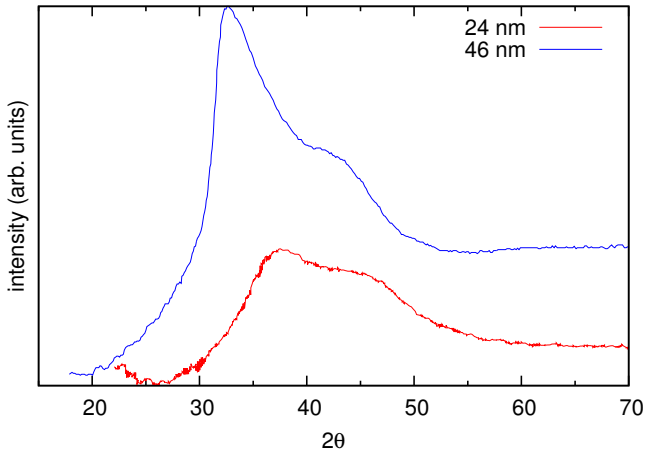


Figure B.2: X-ray diffractogram of 24-nm and 46-nm Ga NPs from the work of Yarema *et al.* [165], converted from the Mo anode to the Cu anode for comparison with the experiments presented in this thesis.

Appendix C

Fourier Transform Infrared (FT-IR) Spectroscopy of Hydroxyapatite

Many conclusions in this thesis have been drawn from the FT-IR spectrum of materials containing hydroxyapatite. Hence, I present a FT-IR spectrum with designated bands for hydroxyapatite, created by the same method as in my doctoral work (Figure C.1 left). The IR spectrum of nanocrystalline hydroxyapatite is also given here to provide a better reference for the HAp(Ga)CP material with a smaller size (Figure C.1 right). The main

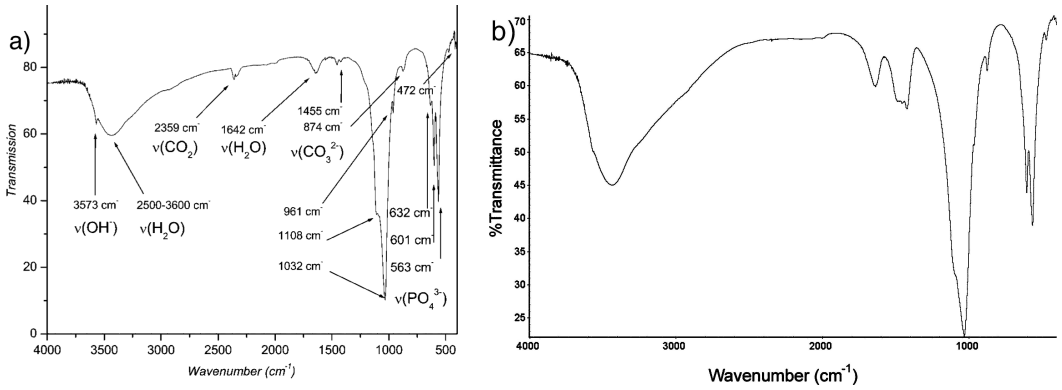


Figure C.1: IR spectra of HAp from the literature. *Left:* IR spectrum of hydroxyapatite obtained by the same method as the one presented in this work [273]. *Right:* IR spectrum of nanocrystalline hydroxyapatite [385].

bands of hydroxyapatite and their assignments are given in Table C.1.

Table C.1: FT-IR band positions and explanations for hydroxyapatite [273], [280], [387], [388], [395], [511], [512], [513], [514], [515].

position (cm^{-1})	assignment	description
3756	H_2O	asymmetric stretching mode (ν_3)
3657	H_2O	symmetric stretching mode (ν_1)
3660	H_2O	water molecules replacing OH^- ions, stretching mode
3572	OH^-	stretching mode (ν_S), weak and sharp
3400	HPO_4^{2-}	vibration of the hydrogen atoms belonging to the hydrogen phosphate group
3800–3000	H_2O	adsorbed water molecules (broad peak at 3400 cm^{-1})
2400	HPO_4^{2-}	characteristic peak of hydrogen phosphate group, non-distinguishable
1630	H_2O	bending mode, ν_2
1595	H_2O	bending mode, ν_2
1540-1550, 1450-1465	A-type CO_3^{2-}	ν_3 (asymmetric stretching vibration) doublet
1452-1462, 1410-1430	B-type CO_3^{2-}	ν_3 doublet
1540-1550 (A), 1449-1470 (A+B), 1409-1418 (B)	AB-type CO_3^{2-}	ν_3 triplet
1215	HPO_4^{2-}	non-degenerate in-plane bending mode of the hydrogen belonging to the HPO_4^{2-} group
1087-1108, 1046, 1032	PO_4^{3-}	triply degenerated asymmetric stretching mode of the P–O bond (ν_3), strong and sharp
961-962	PO_4^{3-}	non-degenerate symmetric stretching mode (ν_1) of the P–O bonds, weak
877-883	A-type CO_3^{2-}	out-of-plane bending vibration (ν_2), singlet
871-876	B-type CO_3^{2-}	ν_2 singlet
879-880, 870-875	AB-type CO_3^{2-}	ν_2 doublet
875	HPO_4^{2-}	characteristic peak of hydrogen phosphate group, non-distinguishable peak
868	HPO_4^{2-}	symmetric stretching mode (ν_5) of the P–O(H) bond of the HPO_4^{2-} group
631	OH^-	librational mode (ν_L), medium
601-602, 574-583, 561	PO_4^{3-}	triply degenerated bending mode (ν_4) of the O–P–O bonds, medium and sharp
600–300	H_2O	translational mode
472, 462	PO_4^{3-}	double degenerate bending vibration (ν_2) of the O–P–O bonds, weak and sharp
355	OH^-	translational mode (ν_T), shoulder
342	OH^-	translational mode (ν_T), weak, shoulder

Appendix D

Solid-State NMR of Hydroxyapatite

Solid-state nuclear magnetic resonance has brought important discoveries about the structure of hydroxyapatite, especially in its nanosized and disordered form, and the role of water in its structure. It is also very useful for the determination of proton positions, which is very difficult with a Rietveld refinement from the XRD.

D.1 ^{1}H NMR

D.1.1 Bulk hydroxyapatite

Bulk stoichiometric hydroxyapatite with very small specific surface area exhibits only one peak in the ^{1}H NMR spectrum, i.e., the OH peak at 0-0.3 ppm (dashed line in Figure D.1 a). The extremely high upfield shift value for the structural OH group reflects very weak hydrogen bonding [516], which is a consequence of the organisation of the hydroxyl groups in the ...O–H O–H O–H O–H... columns inside the apatitic c-axis channels. The consecutive hydroxyls are too distant from each other to form hydrogen bonds (the O–O distance of 3.44 Å) [516], [517]. On the other hand, for anhydrous calcium-deficient hydroxyapatite with formula $Ca_9HPO_4(PO_4)_5OH$ the OH^- peak is shifted to 0.8 ppm and an additional HPO_4^{2-} peak at 6 ppm is observed [517]. The downfield chemical shift of the OH^- peak in this case and the upfield chemical shift for acidic proton of the HPO_4^{2-} ion (it would be expected at around 10 ppm) are explained with hydrogen bonds between the HPO_4 and OH groups through ion-exchange tunnels along the hexagonal axis of the apatitic structure [517].

D.1.2 Nanocrystalline hydroxyapatite

Due to increased surface/volume ratio, nanocrystalline hydroxyapatite exhibits several peaks in NMR spectrum (solid line in Figure D.1 a):

(a) Hydroxyl (OH) peak at 0-0.3 ppm: 0.4-0.5 ppm in wet material due to hydrogen bonds with water; shifts upfield upon drying [398]

(b) HCO_3^- peak at 1.3 ppm [513]

(c) a peak at 1.4 ppm due to OH^- ion in a hydrogen-bonding environment (H-bonded to neighbouring PO_4^{3-}, CO_3^{2-} near defects, such as Ca defects due to carbonate substitution) [398]

(d) OCP peak at 1.5 ppm (very weak peak): OCP in central planar defects, one unit cell thick, or OCP unit cells on the surface [516]

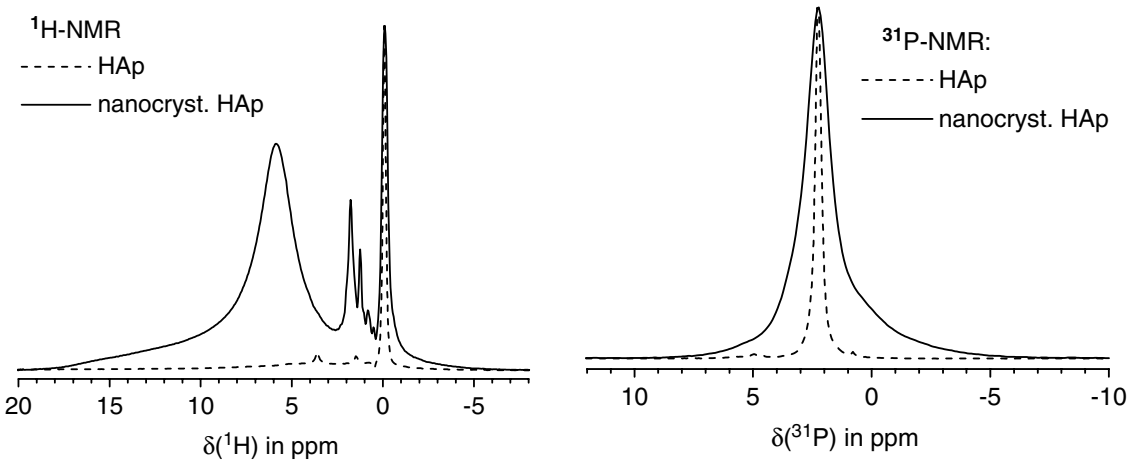


Figure D.1: (a) Comparison of ^{1}H NMR lineshapes of nanocrystalline and a highly crystalline HAp sample; (b) Comparison of the ^{31}P MAS NMR lineshapes of nanocrystalline and a highly crystalline HAp sample.

(e) weak and narrow peaks between 1 and 2 ppm connected to water inside crystal (in apatite channels)

(f) H_2O peak at 2.2 ppm: isolated water molecules in the hydroxide ion channel (occupying isolated OH- vacancies) [398]

(g) H_2O peak at 4.3 ppm (at elevated T>200 °C)

(h) water in the disordered surface layer: 5–6 ppm, either adsorbed or structural (occupying crystal lattice positions)

(i) nonapatitic acidic phosphate (HPO_4^{2-}) peak: 8–13 ppm (extending from 3 to 17 ppm)

(j) If hydroxyapatite is not dried before the NMR measurement, instead of (h) and (i) peaks, only one narrow peak at 4.85 ppm exists which belongs to the adsorbed water, while the HPO_4^{2-} ions peak is absent [286]

D.2 ^{31}P NMR

A difference between the bulk and nanocrystalline can be observed also in the ^{31}P NMR spectrum (Figure D.1 b):

1. Bulk hydroxyapatite yields only one PO_4^{3-} peak at 2.3-3.3 ppm (2.9 for stoichiometric HAp, 3.0 for calcium-deficient HAp and 3.3 for poorly crystalline HAp);

2. Nanocrystalline hydroxyapatite exhibits a broader PO_4^{3-} peak at 2.3-3 ppm and a broad foot of this peak attributed to the phosphate ions and HPO_4^{2-} ions in the disordered surface layer [286], [287], [398].

Nassif *et al.* noticed downfield (left) centered foot of the peak in ^{31}P with a shoulder at 5.6-5.7 ppm [518], whereas Mellier *et al.* obtained a symmetrical foot (on both sides of the peak) [114].

D.3 NMR Investigation of HAp(Ga)

^{1}H NMR of HAp(Ga) is the same as for the nanocrystalline HAp. No information about Ga can be obtained from this spectrum [114]. In ^{31}P NMR there is the narrow peak of the apatitic phosphates at the same position (2.9 ppm) as in HAp, but the broad foot is shifted upfield, so that its center is at 0.6 ppm (Figure D.2 a,b). This shift is attributed to the incorporation of Ga^{3+} into the disordered outer layer of HAp. As the position of the narrow peak does not change in comparison with HAp, the Ga^{3+} are obviously not incorporated into the crystalline apatitic core. Moreover, the 2D ^{1}H–^{31}P HETCOR spectra (Figure D.2 c) have revealed that the ^{31}P peak at 2.9 ppm is correlated to the ^{1}H peak at 0 ppm, whereas the broad foot at 0.6 ppm is correlated with ^{1}H peaks for H_2O (6 ppm) and HPO_4^{2-} (12 ppm) [114]. Hence, HAp(Ga) nanoparticles consist of an ordered hydroxyapatite core with very few structural defects and a disordered outer shell mainly containing HPO_4^{2-} and PO_4^{3-} non-apatitic environments, structural water molecules and incorporating the Ga^{3+} ions [114]. ^{71}Ga NMR measurements have also been conducted and have revealed that the HAp(Ga) nanocrystals exhibit three gallium resonances with asymmetric lineshapes characteristic of a distribution of the quadrupolar interaction: a major one (ca. 67 %) corresponding to GaO_6 environment and two other signals of weaker intensities assigned to GaO_5 and GaO_4 units, indicating that most of the Ga ions are incorporated in the disordered surface layer as GaO_6 octahedral units [114].

D.4 Amorphous $GaPO_4$ Hydrate

This phase can be obtained if $Ga(NO_3)_3$ is mixed with a phosphate buffer or with DCPA [114] or with HAp precursors at Ga/Ca molar ratio >0.075 [333]. It was recognised as a limiting and undesired phase by Mellier *et al.* [333]. It exhibits the following NMR peaks:

(a) ^{1}H NMR: broad peak at 5.4-5.5 ppm that does not shift with increasing $Ga(NO_3)_3$ amount [114], probably corresponding to H_2O;

(b) ^{31}P NMR: a broad resonance at -3.6 to -3.7 ppm, which is shifted toward lower frequencies (-6.0 ppm) when a larger amount of gallium nitrate is added [114]; after calcination at 1000 °C this peak is at -9 ppm [333];

(c) ^{71}Ga NMR: an intense resonance at -14 to -17 ppm associated with GaO_6 and a peak of weaker intensity at 127-134 ppm associated with GaO_4 units [114]; after calcination at 1000 °C there is only one peak at 117 ppm [333] (conversion of $GaPO_4 \cdot 2\,H_2O$ into $GaPO_4$).

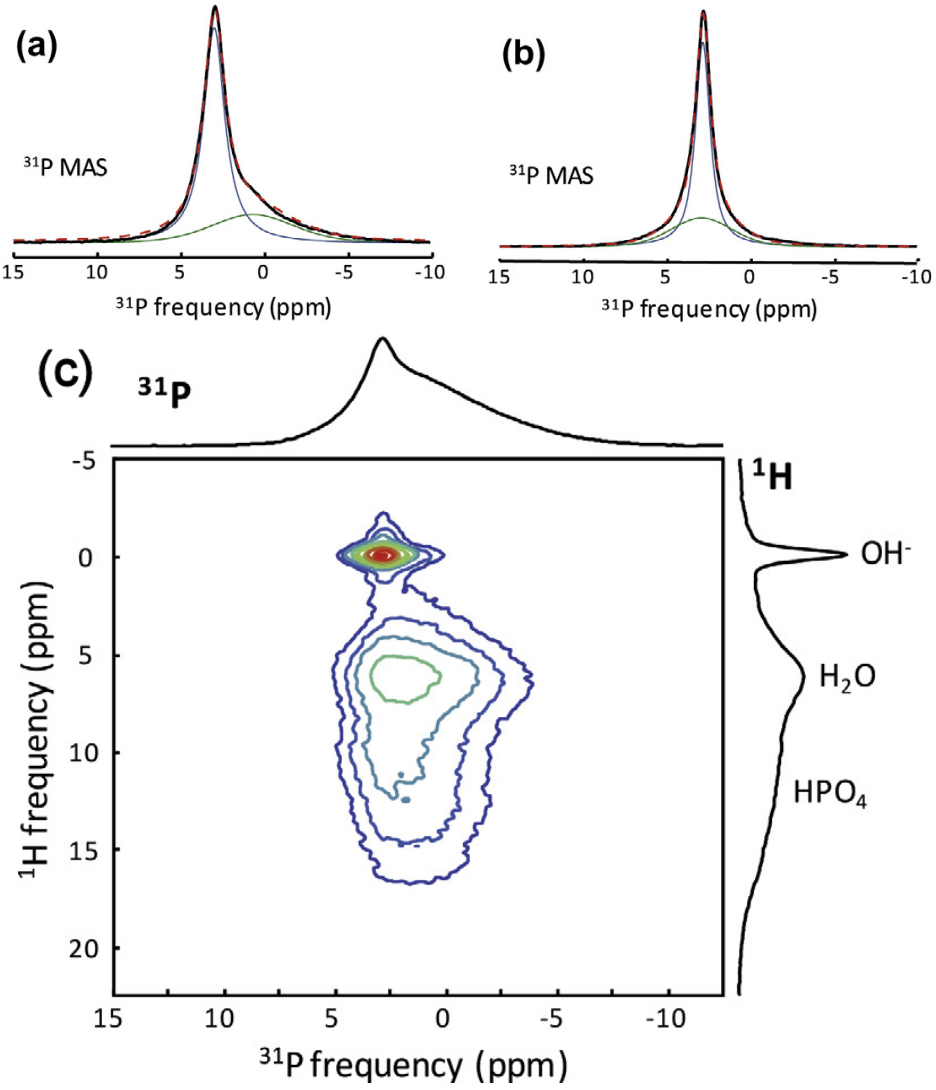


Figure D.2: NMR spectra of HAp(Ga) from the literature. (a) ^{31}P quantitative MAS NMR spectrum of a 3 wt. % gallium-doped calcium-deficient hydroxyapatite, (b) ^{31}P MAS spectra of an undoped calcium-deficient hydroxyapatite sample recorded under the same experimental conditions. The best fits of the experimental spectra considering two contributions associated to the ordered core (blue line) and the disordered surface layer (green line) of the nanoparticles are shown as dashed red lines [114]; (c) 2D 1H–31P HETCOR MAS spectra of a 3 wt. % gallium-doped CDHA, recorded using a magnetisation transfer time of 0.25 ms. Characteristic ^{1}H frequencies of OH^{-}, H_2O and HPO_4^{2-} groups at 0, 6.0 and 12.0 ppm, respectively, are indicated on the ^{1}H axis [114].

Appendix E

Phase Diagram of the Ga and Au Mixture

As I was developing nanoparticles consisting of elemental gallium and gold, it was important to know the phase diagram of this system. Such bulk phase diagram is drawn in Figure E.1.

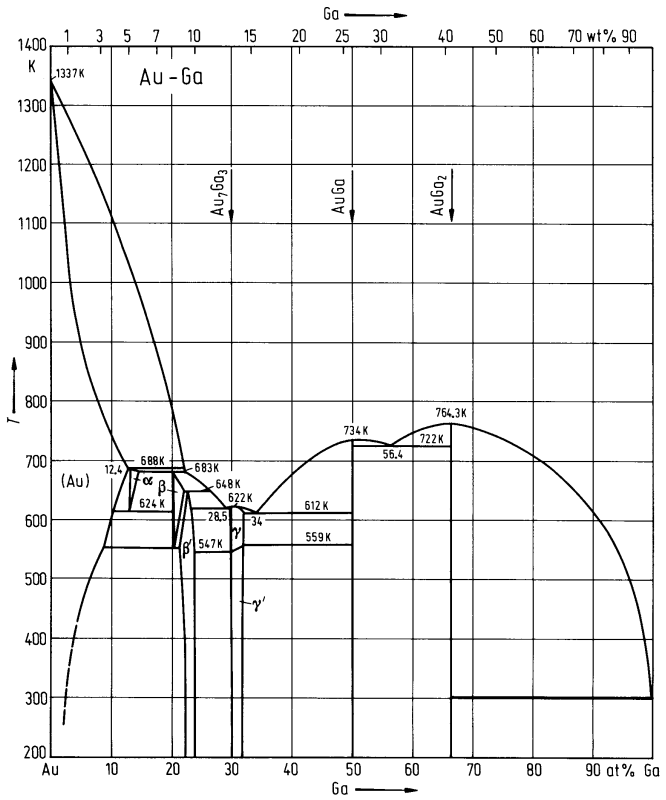


Figure E.1: Gallium-gold bulk phase diagram [519].

References

[1] L. B. Rice, "Federal Funding for the Study of Antimicrobial Resistance in Nosocomial Pathogens: No ESKAPE," *The Journal of Infectious Diseases*, vol. 197, no. 8, pp. 1079–1081, 2008.

[2] H. W. Boucher, G. H. Talbot, J. S. Bradley, J. E. Edwards, D. Gilbert, L. B. Rice, M. Scheld, B. Spellberg, and J. Bartlett, "Bad Bugs, No Drugs: No ESKAPE! An Update from the Infectious Diseases Society of America," *Clinical Infectious Diseases*, vol. 48, no. 1, pp. 1–12, 2009.

[3] C. G. Giske, D. L. Monnet, O. Cars, and Y. Carmeli, "Clinical and Economic Impact of Common Multidrug-Resistant Gram-Negative Bacilli," *Antimicrobial Agents and Chemotherapy*, vol. 52, no. 3, pp. 813–821, 2008.

[4] A. I. Hidron, J. R. Edwards, J. Patel, T. C. Horan, D. M. Sievert, D. A. Pollock, and S. K. Fridkin, "Antimicrobial-Resistant Pathogens Associated With Healthcare-Associated Infections: Annual Summary of Data Reported to the National Healthcare Safety Network at the Centers for Disease Control and Prevention, 2006-2007," *Infection Control and Hospital Epidemiology*, vol. 29, no. 11, pp. 996–1011, 2008.

[5] S. B. Levy, "Factors impacting on the problem of antibiotic resistance," *The Journal of Antimicrobial Chemotherapy*, vol. 49, no. 1, pp. 25–30, 2002.

[6] B. Spellberg, R. Guidos, D. Gilbert, J. Bradley, H. W. Boucher, W. M. Scheld, J. G. Bartlett, and J. Edwards, "The Epidemic of Antibiotic-Resistant Infections: A Call to Action for the Medical Community from the Infectious Diseases Society of America," *Clinical Infectious Diseases*, vol. 46, no. 2, pp. 155–164, 2008.

[7] B. Marshall, D. Ochieng, and S. Levy, "Commensals: Underappreciated Reservoir of Antibiotic Resistance," *Microbe*, vol. 4, no. 5, pp. 231–238, 2009.

[8] R. E. Lenski, "Bacterial evolution and the cost of antibiotic resistance," *International Microbiology*, vol. 1, no. 4, pp. 265–270, 1998.

[9] D. I. Andersson and D. Hughes, "Antibiotic resistance and its cost: is it possible to reverse resistance?" *Nature Reviews Microbiology*, vol. 8, no. 4, pp. 260–271, 2010.

[10] C. Walsh, "Molecular mechanisms that confer antibacterial drug resistance," *Nature*, vol. 406, no. 6797, pp. 775–781, 2000.

[11] M. N. Alekshun and S. B. Levy, "Molecular Mechanisms of Antibacterial Multidrug Resistance," *Cell*, vol. 128, no. 6, pp. 1037–1050, 2007.

[12] G. D. Wright, "Molecular mechanisms of antibiotic resistance," *Chemical Communications*, vol. 47, no. 14, pp. 4055–4061, 2011.

[13] Infectious Diseases Society of America (IDSA), "Bad Bugs, No Drugs: As Antibiotic Discovery Stagnates, A Public Health Crisis Brews," Tech. Rep. July, 2004, pp. 1–38.

[14] G. Taubes, "The Bacteria Fight Back," *Science*, vol. 321, no. 5887, pp. 356–361, 2008.

[15] Centers for Disease Control and Prevention (CDC). (2012). Antibiotic Development is Dwindling, [Online]. Available: `http://www.cdc.gov/getsmart/campaign-materials/week/promotional-media.html` (visited on 01/25/2013).

[16] Infectious Diseases Society of America (IDSA), "Combating Antimicrobial Resistance: Policy Recommendations to Save Lives," *Clinical Infectious Diseases*, vol. 52, no. suppl 5, S397–S428, 2011.

[17] A. J. Huh and Y. J. Kwon, "'Nanoantibiotics': A new paradigm for treating infectious diseases using nanomaterials in the antibiotics resistant era," *Journal of Controlled Release*, vol. 156, no. 2, pp. 128–145, 2011.

[18] V. M. D'Costa, K. M. McGrann, D. W. Hughes, and G. D. Wright, "Sampling the Antibiotic Resistome," *Science*, vol. 311, no. 5759, pp. 374–377, 2006.

[19] M. O. A. Sommer, G. Dantas, and G. M. Church, "Functional Characterization of the Antibiotic Resistance Reservoir in the Human Microflora," *Science*, vol. 325, no. 5944, pp. 1128–1131, 2009.

[20] M. Madigan, J. Martinko, and J. Parker, *Brock Biology of Microorganisms*, 10th ed. Pearson Education, 2003.

[21] J. A. Lemire, J. J. Harrison, and R. J. Turner, "Antimicrobial activity of metals: mechanisms, molecular targets and applications," *Nature Reviews Microbiology*, vol. 11, no. 6, pp. 371–384, 2013.

[22] J. L. Hobman and L. C. Crossman, "Bacterial antimicrobial metal ion resistance," *Journal of Medical Microbiology*, vol. 64, no. 5, pp. 471–497, 2014.

[23] J. J. Harrison, H. Ceri, and R. J. Turner, "Multimetal resistance and tolerance in microbial biofilms," *Nature Reviews Microbiology*, vol. 5, no. 12, pp. 928–38, 2007.

[24] M. L. Workentine, J. J. Harrison, P. U. Stenroos, H. Ceri, and R. J. Turner, "Pseudomonas fluorescens' view of the periodic table," *Environmental Microbiology*, vol. 10, no. 1, pp. 238–250, 2008.

[25] C. A. Moyer, L. Brentano, D. L. Gravens, H. W. Margraf, and W. W. Monafo, "Treatment of Large Human Burns With 0.5% Silver Nitrate Solution," *Archives of Surgery*, vol. 90, pp. 812–867, 1965.

[26] W. W. Monafo and C. A. Moyer, "The treatment of extensive thermal burns with 0.5% silver nitrate solution," *Annals of the New York Academy of Sciences*, vol. 150, no. 3, pp. 937–945, 1968.

[27] H. J. Klasen, "A historical review of the use of silver in the treatment of burns. II. Renewed interest for silver," *Burns*, vol. 26, no. 2, pp. 131–138, 2000.

[28] B. S. Atiyeh, M. Costagliola, S. N. Hayek, and S. A. Dibo, "Effect of silver on burn wound infection control and healing: Review of the literature," *Burns*, vol. 33, no. 2, pp. 139–148, 2007.

[29] S. Chernousova and M. Epple, "Silver as antibacterial agent: Ion, nanoparticle, and metal," *Angewandte Chemie – International Edition*, vol. 52, no. 6, pp. 1636–1653, 2013.

[30] O. M. Goudouri, E. Kontonasaki, U. Lohbauer, and A. R. Boccaccini, "Antibacterial properties of metal and metalloid ions in chronic periodontitis and peri-implantitis therapy," *Acta Biomaterialia*, vol. 10, no. 8, pp. 3795–3810, 2014.

[31] T. N. Phan, T. Buckner, J. Sheng, J. D. Baldeck, and R. E. Marquis, "Physiologic actions of zinc related to inhibition of acid and alkali production by oral streptococci in suspensions and biofilms," *Oral Microbiology and Immunology*, vol. 19, no. 1, pp. 31–38, 2004.

[32] B. Aydin Sevinç and L. Hanley, "Antibacterial activity of dental composites containing zinc oxide nanoparticles," *Journal of Biomedical Materials Research Part B: Applied Biomaterials*, vol. 94B, no. 1, pp. 22–31, 2010.

[33] J. T. Seil and T. J. Webster, "Antimicrobial applications of nanotechnology: methods and literature," *International Journal of Nanomedicine*, vol. 7, pp. 2767–2781, 2012.

[34] J. Sheng, P. T. M. Nguyen, and R. E. Marquis, "Multi-target antimicrobial actions of zinc against oral anaerobes," *Archives of Oral Biology*, vol. 50, no. 8, pp. 747–757, 2005.

[35] G. Borkow and J. Gabbay, "Copper, An Ancient Remedy Returning to Fight Microbial, Fungal and Viral Infections," *Current Chemical Biology*, vol. 3, no. 3, pp. 272–278, 2009.

[36] J. O'Gorman and H. Humphreys, "Application of copper to prevent and control infection. Where are we now?" *Journal of Hospital Infection*, vol. 81, no. 4, pp. 217–223, 2012.

[37] I. Iakovidis, I. Delimaris, and S. M. Piperakis, "Copper and its complexes in medicine: a biochemical approach," *Molecular Biology International*, vol. 2011, p. 594 529, 2011.

[38] M. Rizzoto, "Metal Complexes as Antimicrobial Agents," in *A Search for Antibacterial Agents*, V. Bobbarala, Ed., InTech, 2012, pp. 73–88.

[39] S. Silver, L. T. Phung, and G. Silver, "Silver as biocides in burn and wound dressings and bacterial resistance to silver compounds," *Journal of Industrial Microbiology and Biotechnology*, vol. 33, no. 7, pp. 627–634, 2006.

[40] J. Kolmas, E. Groszyk, and D. Kwiatkowska-Różycka, "Substituted hydroxyapatites with antibacterial properties," *BioMed Research International*, vol. 2014, p. 178 123, 2014.

[41] H.-J. Park, J. J. Y. Kim, J. J. Y. Kim, J.-h. Lee, J.-S. Hahn, M. B. Gu, J. Yoon, J. Yeon, J. J. Y. Kim, J.-H. Lee, J.-S. Hahn, M. Bock, and J. Yoon, "Silver-ion-mediated reactive oxygen species generation affecting bactericidal activity," *Water Research*, vol. 43, no. 4, pp. 1027–1032, 2009.

[42] K. Mijnendonckx, N. Leys, J. Mahillon, S. Silver, and R. Van Houdt, "Antimicrobial silver: Uses, toxicity and potential for resistance," *Biometals*, vol. 26, no. 4, pp. 609–621, 2013.

[43] M. Valko, H. Morris, and M. T. D. Cronin, "Metals, Toxicity and Oxidative Stress," *Current Medicinal Chemistry*, vol. 12, no. 10, pp. 1161–1208, 2005.

[44] G. Grass, C. Rensing, and M. Solioz, "Metallic copper as an antimicrobial surface," *Applied and Environmental Microbiology*, vol. 77, no. 5, pp. 1541–1547, 2011.

[45] L. M. Gaetke and C. K. Chow, "Copper toxicity, oxidative stress, and antioxidant nutrients," *Toxicology*, vol. 189, no. 1-2, pp. 147–163, 2003.

[46] P. P. Fu, Q. Xia, H.-M. Hwang, P. C. Ray, and H. Yu, "Mechanisms of nanotoxicity: generation of reactive oxygen species," *Journal of Food and Drug Analysis*, vol. 22, no. 1, pp. 64–75, 2014.

[47] B. Reidy, A. Haase, A. Luch, K. A. Dawson, and I. Lynch, "Mechanisms of silver nanoparticle release, transformation and toxicity: A critical review of current knowledge and recommendations for future studies and applications," *Materials*, vol. 6, no. 6, pp. 2295–2350, 2013.

[48] W. K. Jung, H. C. Koo, K. W. Kim, S. Shin, S. H. Kim, and Y. H. Park, "Antibacterial activity and mechanism of action of the silver ion in Staphylococcus aureus and Escherichia coli," *Applied and Environmental Microbiology*, vol. 74, no. 7, pp. 2171–2178, 2008.

[49] D. Cummins, "Zinc citrate/Triclosan: a new anti-plaque system for the control of plaque and the prevention of gingivitis: short-term clinical and mode of action studies," *Journal of Clinical Periodontology*, vol. 18, no. 6, pp. 455–461, 1991.

[50] M. Rai, A. Yadav, and A. Gade, "Silver nanoparticles as a new generation of antimicrobials," *Biotechnology Advances*, vol. 27, no. 1, pp. 76–83, 2009.

[51] R. Rawashdeh and Y. Haik, "Antibacterial Mechanisms of Metallic Nanoparticles: A Review," *Dynamic Biochemistry, Process Biotechnology and Molecular Biology*, vol. 3, no. 2, pp. 12–20, 2009.

[52] M. Yamanaka, K. Hara, and J. Kudo, "Bactericidal Actions of a Silver Ion Solution on Escherichia coli , Studied by Energy-Filtering Transmission Electron Microscopy and Proteomic Analysis," *Applied and Environmental Microbiology*, vol. 71, no. 11, pp. 7589–7593, 2005.

[53] R. B. Thurman and C. P. Gerba, "The molecular mechanisms of copper and silver ion disinfection of bacteria and viruses," *Critical Reviews in Environmental Control*, vol. 18, no. 4, pp. 295–315, 1989.

[54] A. B. G. Landsdown, "Zinc in the healing wound," *Lancet*, vol. 347, no. 9003, pp. 706–707, 1996.

[55] M. Jakubowski, "Zinc and cadmium compounds," in *Patty's Toxicology*, E. Bingham and B. Cohrssen, Eds. John Wiley & Sons, Inc., 2012.

[56] G. Borkow and J. Gabbay, "Copper as a Biocidal Tool," *Current Medicinal Chemistry*, vol. 12, no. 18, pp. 2163–2175, 2005.

[57] R. Choudhury and S. Srivastava, "Zinc resistance mechanisms in bacteria," *Current Science*, vol. 81, no. 7, pp. 768–775, 2001.

[58] L. M. Cavaco, H. Hasman, and F. M. Aarestrup, "Zinc resistance of Staphylococcus aureus of animal origin is strongly associated with methicillin resistance," *Veterinary Microbiology*, vol. 150, no. 3-4, pp. 344–348, 2011.

[59] J. C. Wataha, C. T. Hanks, and R. G. Craig, "The in vitro effects of metal cations on eukaryotic cell metabolism," *Journal of Biomedical Materials Research*, vol. 25, no. 9, pp. 1133–1149, 1991.

[60] G. Schmalz, D. Arenholt-Bindslev, S. Pfüller, and H. Schweikl, "Cytotoxicity of Metal Cations used in Dental Cast Alloys," *Alternatives to Laboratory Animals*, vol. 25, no. 3, pp. 323–330, 1997.

[61] A. Schedle, P. Samorapoompichit, X. H. Rausch-Fan, A. Franz, W. Füreder, W. R. Sperr, W. Sperr, A. Ellinger, R. Slavicek, G. Boltz-Nitulescu, and P. Valent, "Response of L-929 fibroblasts, human gingival fibroblasts, and human tissue mast cells to various metal cations," *Journal of Dental Research*, vol. 74, no. 8, pp. 1513–1520, 1995.

[62] A. Yamamoto, R. Honma, and M. Sumita, "Cytotoxicity evaluation of 43 metal salts using murine fibroblasts and osteoblastic cells," *Journal of Biomedical Materials Research*, vol. 39, no. 2, pp. 331–340, 1998.

[63] S. Y. Liau, D. C. Read, W. J. Pugh, J. R. Furr, and A. D. Russell, "Interaction of silver nitrate with readily identifiable groups: relationship to the antibacterial action of silver ions," *Letters in Applied Microbiology*, vol. 25, no. 1994, pp. 279–283, 1997.

[64] G. Mulley, A. T. A. Jenkins, and N. R. Waterfield, "Inactivation of the antibacterial and cytotoxic properties of silver ions by biologically relevant compounds," *PLoS ONE*, vol. 9, no. 4, pp. 2–10, 2014.

[65] A. B. G. Lansdown, "Silver and gold," in *Patty's Toxicology*, E. Bingham and B. Cohrssen, Eds., vol. 1, New York: John Wiley & Sons, Inc., 2012, ch. 4, pp. 75–112.

[66] N. German, D. Doyscher, and C. Rensing, "Bacterial killing in macrophages and amoeba: do they all use a brass dagger?" *Future Microbiology*, vol. 8, no. 10, pp. 1257–1264, 2013.

[67] R. Dastjerdi and M. Montazer, "A review on the application of inorganic nano-structured materials in the modification of textiles: Focus on anti-microbial properties," *Colloids and Surfaces B: Biointerfaces*, vol. 79, no. 1, pp. 5–18, 2010.

[68] M. Vukomanović, "Sonochemical synthesis and characterization of hydroxyapatite/metal–based composite materials for biomedical applications," PhD thesis, Jožef Stefan International Postgraduate School, 2012.

[69] V. R. Rai and J. A. Bai, "Nanoparticles and their potential application as antimicrobials," in *Science against microbial pathogens: Communicating current research and technological advances*, A. Méndez-Vilas, Ed., Badajos (Spain): Formatex, 2011, pp. 197–209.

[70] E.-J. Yang, J. Jang, S. Kim, and I.-H. Choi, "Silver Nanoparticles as a Smart Antimicrobial Agent," *Journal of Bacteriology and Virology*, vol. 42, no. 2, p. 177, 2012.

[71] S. Pal, Y. K. Tak, and J. M. Song, "Does the Antibacterial Activity of Silver Nanoparticles Depend on the Shape of the Nanoparticle? A Study of the Gram-Negative Bacterium *Escherichia coli*," *Applied and Environmental Microbiology*, vol. 73, no. 6, pp. 1712–1720, 2007.

[72] A. Sirelkhatim, S. Mahmud, A. Seeni, N. H. M. Kaus, L. C. Ann, S. K. M. Bakhori, H. Hasan, and D. Mohamad, "Review on zinc oxide nanoparticles: Antibacterial activity and toxicity mechanism," *Nano-Micro Letters*, vol. 7, no. 3, pp. 219–242, 2015.

[73] H. Zhang and G. Chen, "Potent antibacterial activities of Ag/TiO_2 nanocomposite powders synthesized by a one-pot sol-gel method," *Environmental Science and Technology*, vol. 43, no. 8, pp. 2905–2910, 2009.

[74] N. Khlebtsov and L. Dykman, "Biodistribution and toxicity of engineered gold nanoparticles: a review of in vitro and in vivo studies," *Chemical Society Reviews*, vol. 40, no. 3, pp. 1647–1671, 2011.

[75] W. Jiang, "Bacterial toxicity of oxide nanoparticles and their effects on bacterial surface biomolecules," PhD thesis, University of Massachusetts - Amherst, 2011.

[76] M. Moritz and M. Geszke-Moritz, "The newest achievements in synthesis, immobilization and practical applications of antibacterial nanoparticles," *Chemical Engineering Journal*, vol. 228, pp. 596–613, 2013.

[77] W. He, Y. T. Zhou, W. G. Wamer, M. D. Boudreau, and J. J. Yin, "Mechanisms of the pH dependent generation of hydroxyl radicals and oxygen induced by Ag nanoparticles," *Biomaterials*, vol. 33, no. 30, pp. 7547–7555, 2012.

[78] S. H. Kim, H. S. Lee, D. S. Ryu, S. J. Choi, and D. S. Lee, "Antibacterial Activity of Silver-nanoparticles Against Staphylococcus aureus and Escherichia coli," *Korean Journal of Microbiology and Biotechnology*, vol. 39, no. 1, pp. 77–85, 2011.

[79] D. Zvekić, V. V. Srdić, M. A. Karaman, and M. N. Matavulj, "Antimicrobial properties of ZnO nanoparticles incorporated in polyurethane varnish," *Processing and Application of Ceramics*, vol. 5, no. 1, pp. 41–45, 2011.

[80] G. Applerot, J. Lellouche, A. Lipovsky, Y. Nitzan, R. Lubart, A. Gedanken, and E. Banin, "Understanding the antibacterial mechanism of CuO nanoparticles: Revealing the route of induced oxidative stress," *Small*, vol. 8, no. 21, pp. 3326–3337, 2012.

[81] A. B. G. Lansdown, "A review of the use of silver in wound care: facts and fallacies," *British Journal of Nursing*, vol. 13, no. Sup1, S6–S19, 2004.

[82] L. G. Ovington, "The truth about silver," *Ostomy/Wound Management*, vol. 50, no. 9A Suppl, 1S–10S, 2004.

[83] R. P. Singh and P. Ramarao, "Cellular uptake, intracellular trafficking and cytotoxicity of silver nanoparticles," *Toxicology Letters*, vol. 213, no. 2, pp. 249–259, 2012.

[84] Z.-M. Xiu, Q.-B. Zhang, H. L. Puppala, V. L. Colvin, and P. J. J. Alvarez, "Negligible particle-specific antibacterial activity of silver nanoparticles," *Nano Letters*, vol. 12, no. 8, pp. 4271–4275, 2012.

[85] R. Foldbjerg, X. Jiang, T. Miclăuş, C. Chen, H. Autrup, and C. Beer, "Silver nanoparticles – wolves in sheep's clothing?" *Toxicology Research*, vol. 4, no. 3, pp. 563–575, 2015.

[86] N. Durán, M. Durán, M. B. de Jesus, A. B. Seabra, W. J. Fávaro, and G. Nakazato, "Silver nanoparticles: A new view on mechanistic aspects on antimicrobial activity," *Nanomedicine: Nanotechnology, Biology, and Medicine*, vol. 12, no. 3, pp. 789–799, 2016.

[87] S. J. Yu, J. B. Chao, J. Sun, Y. G. Yin, J. F. Liu, and G. B. Jiang, "Quantification of the uptake of silver nanoparticles and ions to HepG2 cells," *Environmental Science and Technology*, vol. 47, no. 7, pp. 3268–3274, 2013.

[88] X. Jiang, T. Miclăuş, L. Wang, R. Foldbjerg, D. S. Sutherland, H. Autrup, C. Chen, and C. Beer, "Fast intracellular dissolution and persistent cellular uptake of silver nanoparticles in CHO-K1 cells: implication for cytotoxicity," *Nanotoxicology*, vol. 9, no. 2, pp. 181–189, 2015.

[89] Q. Li, S. Mahendra, D. Y. Lyon, L. Brunet, M. V. Liga, D. Li, and P. J. Alvarez, "Antimicrobial nanomaterials for water disinfection and microbial control: Potential applications and implications," *Water Research*, vol. 42, no. 18, pp. 4591–4602, 2008.

[90] K. K. Y. Wong and X. Liu, "Silver nanoparticles-the real "silver bullet"in clinical medicine?" *Medicinal Chemical Communications*, vol. 1, no. 2, pp. 125–131, 2010.

[91] S. Agnihotri, S. Mukherji, and S. Mukherji, "Immobilized silver nanoparticles enhance contact killing and show highest efficacy: elucidation of the mechanism of bactericidal action of silver," *Nanoscale*, vol. 5, no. 16, pp. 7328–7340, 2013.

[92] I. Sondi and B. Salopek-Sondi, "Silver nanoparticles as antimicrobial agent: a case study on E. coli as a model for Gram-negative bacteria," *Journal of Colloid and Interface Science*, vol. 275, no. 1, pp. 177–182, 2004.

[93] J. R. Morones, J. L. Elechiguerra, A. Camacho, K. Holt, J. B. Kouri, J. T. Ramírez, and M. J. Yacaman, "The bactericidal effect of silver nanoparticles," *Nanotechnology*, vol. 16, no. 10, pp. 2346–2353, 2005.

[94] F. Mirzajani, A. Ghassempour, A. Aliahmadi, and M. A. Esmaeili, "Antibacterial effect of silver nanoparticles on staphylococcus aureus," *Research in Microbiology*, vol. 162, no. 5, pp. 542–549, 2011.

[95] D. G. Romero-Urbina, H. H. Lara, J. J. Velázquez-Salazar, M. J. Arellano-Jiménez, E. Larios, A. Srinivasan, J. L. Lopez-Ribot, and M. J. Yacamán, "Ultrastructural changes in methicillin-resistant staphylococcus aureus induced by positively charged silver nanoparticles," *Beilstein Journal of Nanotechnology*, vol. 6, pp. 2396–2405, 2015.

[96] E. E. Fröhlich and E. Fröhlich, "Cytotoxicity of Nanoparticles Contained in Food on Intestinal Cells and the Gut Microbiota," *International Journal of Molecular Sciences*, vol. 17, no. 4, p. 509, 2016.

[97] O. Choi and Z. Hu, "Size dependent and reactive oxygen species related nanosilver toxicity to nitrifying bacteria," *Environmental Science and Technology*, vol. 42, no. 12, pp. 4583–4588, 2008.

[98] F. Zhao, Y. Zhao, Y. Liu, X. Chang, C. Chen, and Y. Zhao, "Cellular uptake, intracellular trafficking, and cytotoxicity of nanomaterials," *Small*, vol. 7, no. 10, pp. 1322–1337, 2011.

[99] A. M. Alkilany and C. J. Murphy, "Toxicity and cellular uptake of gold nanoparticles: what we have learned so far?" *Journal of Nanoparticle Research*, vol. 12, no. 7, pp. 2313–2333, 2010.

[100] C. Lasagna-Reeves, D. Gonzalez-Romero, M. A. Barria, I. Olmedo, A. Clos, V. M. Sadagopa Ramanujam, A. Urayama, L. Vergara, M. J. Kogan, and C. Soto, "Bioaccumulation and toxicity of gold nanoparticles after repeated administration in mice," *Biochemical and Biophysical Research Communications*, vol. 393, no. 4, pp. 649–655, 2010.

[101] R. Shukla, V. Bansal, M. Chaudhary, A. Basu, R. R. Bhonde, and M. Sastry, "Biocompatibility of Gold Nanoparticles and Their Endocytotic Fate Inside the Cellular Compartment: A Microscopic Overview," *Langmuir*, vol. 21, no. 23, pp. 10 644–10 654, 2005.

[102] L. Shang, K. Nienhaus, and G. U. Nienhaus, "Engineered nanoparticles interacting with cells: size matters," *Journal of nanobiotechnology*, vol. 12, no. 1, p. 5, 2014.

[103] B. D. Chithrani, A. A. Ghazani, and W. C. W. Chan, "Determining the size and shape dependence of gold nanoparticle uptake into mammalian cells," *Nano Letters*, vol. 6, no. 4, pp. 662–668, 2006.

[104] D. Yohan, C. Cruje, X. Lu, and D. B. Chithrani, "Size-dependent gold nanoparticle interaction at nano–micro interface using both monolayer and multilayer (tissue-like) cell models," *Nano-Micro Letters*, vol. 8, no. 1, pp. 44–53, 2016.

[105] Y.-H. Gao, N.-C. Zhang, Y.-W. Zhong, H.-H. Cai, and Y.-l. Liu, "Preparation and characterization of antibacterial Au/C core-shell composite," *Applied Surface Science*, vol. 256, no. 22, pp. 6580–6585, 2010.

[106] Y. Zhao, Y. Tian, Y. Cui, W. Liu, W. Ma, and X. Jiang, "Small Molecule-Capped Gold Nanoparticles as Potent Antibacterial Agents That Target Gram-Negative Bacteria," *Journal of the American Chemical Society*, vol. 132, no. 35, pp. 12 349–12 356, 2010.

[107] M. Vukomanović, S. D. Škapin, and D. Suvorov, "Kompozitni materiali na osnovi keramične faze in kovine s funkcionalizirano površino, kot okolju prijazni materiali z antibakterijskim delovanjem, metoda priprave in njihova uporaba," 201 200 204, 2012.

[108] Y. Cui, Y. Zhao, Y. Tian, W. Zhang, X. Lü, and X. Jiang, "The molecular mechanism of action of bactericidal gold nanoparticles on Escherichia coli," *Biomaterials*, vol. 33, no. 7, pp. 2327–2333, Mar. 2012.

[109] J. L. Graves, M. Tajkarimi, Q. Cunningham, A. Campbell, H. Nonga, S. H. Harrison, and J. E. Barrick, "Rapid evolution of silver nanoparticle resistance in escherichia coli," *Frontiers in Genetics*, vol. 6, p. 42, 2015.

[110] H. L. Karlsson, P. Cronholm, J. Gustafsson, and L. Möller, "Copper oxide nanoparticles are highly toxic: A comparison between metal oxide nanoparticles and carbon nanotubes," *Chemical Research in Toxicology*, vol. 21, no. 9, pp. 1726–1732, 2008.

[111] E. Sadauskas, H. Wallin, M. Stoltenberg, U. Vogel, P. Doering, A. Larsen, and G. Danscher, "Kupffer cells are central in the removal of nanoparticles from the organism," *Particle and fibre toxicology*, vol. 4, no. 3, p. 10, 2007.

[112] E. Sadauskas, G. Danscher, M. Stoltenberg, U. Vogel, A. Larsen, and H. Wallin, "Protracted elimination of gold nanoparticles from mouse liver," *Nanomedicine: Nanotechnology, Biology, and Medicine*, vol. 5, no. 2, pp. 162–169, 2009.

[113] L. R. Bernstein, "Mechanisms of Therapeutic Activity for Gallium," *Pharmacological reviews*, vol. 50, no. 4, pp. 665–682, 1998.

[114] C. Mellier, F. Fayon, F. Boukhechba, E. Verron, M. LeFerrec, G. Montavon, J. Lesoeur, V. Schnitzler, D. Massiot, P. Janvier, O. Gauthier, J.-M. Bouler, and B. Bujoli, "Design and properties of novel gallium-doped injectable apatitic cements," *Acta Biomaterialia*, vol. 24, pp. 322–332, 2015.

[115] J. Zhang, Z. Liu, C. Lin, and J. Lin, "A simple method to synthesize β-Ga2O3 nanorods and their photoluminescence properties," *Journal of Crystal Growth*, vol. 280, no. 1-2, pp. 99–106, Jun. 2005.

[116] Y. Zhao, R. L. Frost, and W. N. Martens, "Synthesis and characterization of gallium oxide nanostructures via a soft-chemistry route," *The Journal of Physical Chemistry C*, vol. 111, no. 44, pp. 16 290–16 299, 2007.

[117] B. Hacht, "Gallium (III) ion hydrolysis under physiological conditions," *Bulletin of the korean chemical society*, vol. 29, no. 2, pp. 372–376, 2008.

[118] O. Rzhepishevska, B. Ekstrand-Hammarström, M. Popp, E. Björn, A. Bucht, A. Sjöstedt, H. Antti, and M. Ramstedt, "The Antibacterial Activity of Ga^{3+} Is Influenced by Ligand Complexation as Well as the Bacterial Carbon Source," *Antimicrobial Agents and Chemotherapy*, vol. 55, no. 12, pp. 5568–5580, 2011.

[119] T. Sato and T. Nakamura, "Studies of the Crystallisation of Gallium Hydroxide Precipitated from Hydrochloric Acid Solutions by Various Alkalis," *Journal of Chemical Technology and Biotechnology*, vol. 32, pp. 469–475, 1982.

[120] M. Sun, D. Li, W. Zhang, X. Fu, Y. Shao, W. Li, G. Xiao, and Y. He, "Rapid microwave hydrothermal synthesis of GaOOH nanorods with photocatalytic activity toward aromatic compounds," *Nanotechnology*, vol. 21, no. 35, p. 355 601, 2010.

[121] M. Ristić, S. Popović, and S. Musić, "Application of sol–gel method in the synthesis of gallium(III)-oxide," *Materials Letters*, vol. 59, no. 10, pp. 1227–1233, 2005.

[122] H.-S. Qian, P. Gunawan, Y.-X. Zhang, G.-F. Lin, J.-W. Zheng, and R. Xu, "Template-Free Synthesis of Highly Uniform α-GaOOH Spindles and Conversion to α-Ga_2O_3 and β-Ga_2O_3," *Crystal Growth and Design*, vol. 8, no. 4, pp. 1282–1287, 2008.

[123] S. Avivi, Y. Mastai, G. Hodes, and A. Gedanken, "Sonochemical hydrolysis of Ga^{3+} ions: synthesis of scroll-like cylindrical nanoparticles of gallium oxide hydroxide," *Journal of the American Chemical Society*, vol. 121, no. 17, pp. 4196–4199, 1999.

[124] A. C. Tas, P. J. Majewski, and F. Aldinger, "Synthesis of gallium oxide hydroxide crystals in aqueous solutions with or without urea and their calcination behavior," *Journal of the American Ceramic Society*, vol. 85, no. 6, pp. 1421–1429, 2002.

[125] H. Y. Playford, A. C. Hannon, E. R. Barney, and R. I. Walton, "Structures of uncharacterised polymorphs of gallium oxide from total neutron diffraction," *Chemistry–A European Journal*, vol. 19, no. 8, pp. 2803–2813, 2013.

[126] V. B. Kumar, A. Gedanken, and Z. Porat, "Facile synthesis of gallium oxide hydroxide by ultrasonic irradiation of molten gallium in water," *Ultrasonics Sonochemistry*, vol. 26, pp. 340–344, 2015.

[127] R. Roy, V. G. Hill, and E. F. Osborn, "Polymorphism of Ga_2O_3 and the System Ga_2O_3–H_2O," *Journal of the American Chemical Society*, vol. 74, no. 3, pp. 719–722, 1952.

[128] K. K. Banger and A. F. Hepp, "Gallium: Inorganic chemistry," in *Encyclopedia of Inorganic Chemistry*. John Wiley & Sons, Ltd, 2006.

[129] G. H. Wagner and W. H. Gitzen, "Gallium," *Journal of Chemical Education*, 1952.

[130] F. Gray, D. A. Kramer, and J. D. Bliss, "Gallium and gallium compounds," in *Kirk-Othmer Encyclopedia of Chemical Technology*, M. Howe-Grant and R. E. Kirk, Eds., 4th ed., New York: John Wiley & Sons, 1998, pp. 158–166.

[131] N. N. Greenwood and A. Earnshaw, "7 - Aluminium, Gallium, Indium and Thallium," in *Chemistry of the Elements*, N. N. Greenwood and A. Earnshaw, Eds., 2nd ed., Oxford: Butterworth-Heinemann, 1997, pp. 216–267.

[132] V. Y. Prokhorenko, V. V. Roshchupkin, M. A. Pokrasin, S. V. Prokhorenko, and V. V. Kotov, "Liquid gallium: Potential uses as a heat-transfer agent," *High Temperature*, vol. 38, no. 6, pp. 954–968, 2000.

[133] L. A. Giannuzzi and F. A. Stevie, "A review of focused ion beam milling techniques for TEM specimen preparation," *Micron*, vol. 30, pp. 197–204, 1999.

[134] M. Bernasconi, G. L. Chiarotti, and E. Tosatti, "Ab initio calculations of structural and electronic properties of gallium solid-state phases," *Physical Review B*, vol. 52, pp. 9988–9998, 14 Oct. 1995.

[135] F. Minandri, C. Bonchi, E. Frangipani, F. Imperi, and P. Visca, "Promises and failures of gallium as an antibacterial agent," *Future microbiol.*, vol. 9, pp. 379–397, 2014.

[136] E. Frangipani, C. Bonchi, F. Minandri, F. Imperi, and P. Visca, "Pyochelin potentiates the inhibitory activity of gallium on Pseudomonas aeruginosa," *Antimicrob. agents chemother.*, vol. 58, no. 9, pp. 5572–5575, 2014.

[137] A. Jayaraman, W. Klement, R. Newton, and G. Kennedy, "Fusion curves and polymorphic transitions of the group III elements–Aluminum, gallium, indium and thallium–At high pressures," *Journal of Physics and Chemistry of Solids*, vol. 24, no. 1, pp. 7–18, 1963.

[138] L. Bosio, "Crystal structures of Ga(II) and Ga(III)," *The Journal of Chemical Physics*, vol. 68, no. 3, p. 1221, 1978.

[139] R. D. Heyding, W. Keeney, and S. L. Segel, "Metastable phases in gallium dispersions," *Journal of Physics and Chemistry of Solids*, vol. 34, no. 1, pp. 133–136, 1973.

[140] L. Comez, A. Di Cicco, J. Itié, and A. Polian, "High-pressure and high-temperature x-ray absorption study of liquid and solid gallium," *Physical Review B*, vol. 65, no. 1, pp. 1–10, 2001.

[141] S. I. Simak, U. Häussermann, R. Ahuja, S. Lidin, and B. Johansson, "Gallium and indium under high pressure," *Physical Review Letters*, vol. 85, pp. 142–145, 1 2000.

[142] T. Kenichi, K. Kazuaki, and A. Masao, "High-pressure bct-fcc phase transition in ga," *Physical Review B*, vol. 58, pp. 2482–2486, 5 1998.

[143] L. Bosio, A. Defrain, and I. Epelboin, "Changements de phase du gallium à la pression atmosphérique," *Journal de Physique*, vol. 27, no. 1-2, pp. 61–71, 1966.

[144] L. Bosio, A. Defrain, H. Curien, and A. Rimsky, "Structure cristalline du gallium β," *Acta Crystallographica Section B*, vol. 25, no. 5, p. 995, May 1969.

[145] P. Ghigna, G. Spinolo, G. B. Parravicini, A. Stella, A. Migliori, and R. Kofman, "Metallic versus Covalent Bonding: Ga Nanoparticles as a Case Study," *Journal of the American Chemical Society*, vol. 129, no. 25, pp. 8026–8033, 2007.

[146] O. Hunderi, "Amorphous gallium – a free electron metal," *Journal of Physics F: Metal Physics*, vol. 4, no. 11, p. 2096, 1974.

[147] S. F. Tsay, "Relation between the β and rapidly quenched liquid phases of gallium," *Physical Review B*, vol. 50, no. 1, pp. 103–107, 1994.

[148] P. Ascarelli, "Atomic radial distributions and ion-ion potential in liquid gallium," *Physical review*, vol. 143, no. 1, pp. 36–47, 1966.

[149] Bizid, A., Defrain, A., Bellissent, R., and Tourand, G., "Neutron diffraction investigation and structural model for liquid gallium from room temperature up to 1 303 k," *Journal de Physique*, vol. 39, no. 5, pp. 554–560, 1978.

[150] R. Trittibach, C. Grütter, and J. H. Bilgram, "Surface melting of gallium single crystals," *Physical Review B*, vol. 50, no. 4, pp. 2529–2536, 1994.

[151] A. I. Denisyuk, K. F. MacDonald, F. J. G. de Abajo, and N. I. Zheludev, "Towards Femtojoule Nanoparticle Phase-Change Memory," *Japanese Journal of Applied Physics*, vol. 48, no. 3S1, 03A065, 2009.

[152] K.-l. Tsai and J. L. Dye, "Synthesis, Properties, and Characterization of Nanometer-Size Metal Particles by Homogeneous Reduction with Alkalides and Electrides in Aprotic Solvents," *Chemistry of Materials*, vol. 5, no. 13, pp. 540–546, 1993.

[153] D. Brito, H.-C. Nataf, P. Cardin, J. Aubert, and J.-P. Masson, "Ultrasonic Doppler velocimetry in liquid gallium," *Experiments in Fluids*, vol. 31, no. 6, pp. 653–663, 2001.

[154] Q. Xu, N. Qudalov, Q. Guo, H. Jaeger, and E. Brown, "Effect of oxidation on the mechanical properties of liquid gallium and eutectic gallium-indium," *Physics of fluids*, vol. 24, no. 6, p. 063 101, 2012.

[155] J. M. Sanz, D. Ortiz, R. Alcaraz De La Osa, J. M. Saiz, F. González, A. S. Brown, M. Losurdo, H. O. Everitt, and F. Moreno, "UV plasmonic behavior of various metal nanoparticles in the near- and far-field regimes: Geometry and substrate effects," *The Journal of Physical Chemistry C*, vol. 117, no. 38, pp. 19 606–19 615, 2013.

[156] M. D. Dickey, "Emerging applications of liquid metals featuring surface oxides," *ACS Applied Materials and Interfaces*, vol. 6, no. 21, pp. 18 369–18 379, 2014.

[157] W. H. Hoather, "The density and coefficient of expansion of liquid gallium over a wide range of temperature," *Proceedings of the physical society*, vol. 48, pp. 814–814, 1936.

[158] R. Kofman, P. Cheyssac, and J. Richard, "Optical properties of Ga monocrystal in the 0.3-5-eV range," *Physical Review B*, vol. 16, no. 12, pp. 5216–5225, 1977.

[159] D. Kim, P. Thissen, G. Viner, D. W. Lee, W. Choi, Y. J. Chabal, and J. B. Lee, "Recovery of nonwetting characteristics by surface modification of gallium-based liquid metal droplets using hydrochloric acid vapor," *ACS Applied Materials and Interfaces*, vol. 5, no. 1, pp. 179–185, 2013.

[160] M. R. Khan, C. B. Eaker, E. F. Bowden, and M. D. Dickey, "Giant and switchable surface activity of liquid metal via surface oxidation," *Proceedings of the National Academy of Sciences of the United States of America*, vol. 111, no. 39, pp. 14 047–14 051, 2014.

[161] J. Zhang, L. Sheng, and J. Liu, "Synthetically chemical-electrical mechanism for controlling large scale reversible deformation of liquid metal objects," *Scientific Reports*, vol. 4, p. 7116, 2014.

[162] V. Venugopal, K. Upadhyaya, K. Kumar, and S. Shivaprasad, "Ion induced compositional changes and nanodroplet formation on GaN surface," *Applied Surface Science*, Feb. 2014.

[163] M. D. Dickey, R. C. Chiechi, R. J. Larsen, E. A. Weiss, D. A. Weitz, and G. M. Whitesides, "Eutectic Gallium Indium (EGaIn): A Liquid Metal Alloy for the Formation of Stable Structures in Microchannels at Room Temperature," *Advanced Functional Materials*, vol. 18, no. 7, p. 10 971 104, 2008.

[164] L. Bosio, H. Curien, M. Dupont, and A. Rimsky, "Structure cristalline de Ga γ," *Acta Crystallographica Section B*, vol. 28, no. 6, pp. 1974–1975, 1972.

[165] M. Yarema, M. Wörle, M. D. Rossell, R. Erni, R. Caputo, L. Protesescu, K. V. Kravchyk, D. N. Dirin, K. Lienau, F. von Rohr, A. Schilling, M. Nachtegaal, and M. V. Kovalenko, "Monodisperse Colloidal Gallium Nanoparticles: Synthesis, Low Temperature Crystallization, Surface Plasmon Resonance and Li-Ion Storage," *Journal of the American Chemical Society*, vol. 136, pp. 12 422–12 430, 2014.

[166] L. Bosio, H. Curien, M. Dupont, and A. Rimsky, "Structure cristalline de Gaδ," *Acta Crystallographica Section B*, vol. 29, no. 2, pp. 367–368, 1973.

[167] X. M. Chen, G. T. Fei, and K. Zheng, "The solid state phase transition of gallium particles and its size dependence," *Journal of Physics: Condensed Matter*, vol. 21, no. 24, p. 245 403, 2009.

[168] A. Di Cicco, "Phase Transitions in Confined Gallium Droplets," *Physical Review Letters*, vol. 81, no. 14, pp. 2942–2945, 1998.

[169] A. D. Cicco, S. Fusari, and S. Stizza, "Phase transitions and undercooling in confined gallium," *Philosophical Magazine Part B*, vol. 79, no. 11-12, pp. 2113–2120, 1999.

[170] H. He, G. T. Fei, P. Cui, K. Zheng, L. M. Liang, Y. Li, and L. De Zhang, "Relation between size and phase structure of gallium: Differential scanning calorimeter experiments," *Physical Review B*, vol. 72, p. 073 310, 7 2005.

[171] G. B. Parravicini, A. Stella, P. Ghigna, G. Spinolo, A. Migliori, F. D'Acapito, and R. Kofman, "Extreme undercooling (down to 90 K) of liquid metal nanoparticles," *Applied Physics Letters*, vol. 89, no. 2006, p. 033 123, 2006.

[172] X. F. Li, G. T. Fei, X. M. Chen, Y. Zhang, K. Zheng, X. L. Liu, and L. D. Zhang, "Size-temperature phase diagram of gallium," *Europhysics Letters*, vol. 94, no. 1, p. 16 001, 2011.

[173] C. Tien, E. Charnaya, W. Wang, Y. Kumzerov, and D. Michel, "Possible liquid-liquid transition of gallium confined in opal," *Physical Review B*, vol. 74, no. 2, p. 024 116, 2006.

[174] B. F. Soares, K. F. MacDonald, V. A. Fedotov, and N. I. Zheludev, "Light-Induced Switching between Structural Forms with Different Optical Properties in a Single Gallium Nanoparticulate," *Nano Letters*, vol. 5, no. 10, pp. 2104–2107, 2005.

[175] M. Losurdo, A. Suvorova, S. Rubanov, K. Hingerl, and A. S. Brown, "Thermally stable coexistence of liquid and solid phases in gallium nanoparticles," *Nature Materials*, vol. 15, no. 9, pp. 995–1002, 2016.

[176] K. F. MacDonald, V. A. Fedotov, S. Pochon, G. Stevens, F. V. Kusmartsev, V. I. Emel'yanov, and N. I. Zheludev, "Controlling the coexistence of structural phases and the optical properties of gallium nanoparticles with optical excitation," *Europhysics Letters*, vol. 67, no. 4, p. 614, 2004.

[177] S. Pochon, K. MacDonald, R. Knize, and N. Zheludev, "Phase Coexistence in Gallium Nanoparticles Controlled by Electron Excitation," *Physical Review Letters*, vol. 92, no. 14, p. 145 702, 2004.

[178] S. Bissa and A. K. Nagar, "Ultrashort Laser Induced Optical Switching Effects of Ga Nanoparticle Films," *Journal of Ovonic Research*, vol. 6, no. 1, pp. 51–56, 2010.

[179] D. Teske and J. E. Drumheller, "Phases of gallium nucleated by small particles," *Journal of Physics: Condensed Matter*, vol. 11, no. 25, p. 4935, 1999.

[180] L. Bosio and C. G. Windsor, "Observation of a Metastability Limit in Liquid Gallium," *Physical Review Letters*, vol. 35, no. 24, pp. 1652–1655, 1975.

[181] S. Nunez, J. M. Lopez, and A. Aguado, "Neutral and charged gallium clusters: Structures, physical properties and implications for the melting features," *Nanoscale*, vol. 4, no. 20, pp. 6481–6492, 2012.

[182] J. M. McMahon, S. K. Gray, and G. C. Schatz, "Ultraviolet Plasmonics: The Poor Metals Al, Ga, In, Sn, Tl, Pb, and Bi," pp. 1–33, 2009.

[183] P. Albella, B. Garcia-Cueto, F. González, F. Moreno, P. C. Wu, T. H. Kim, A. Brown, Y. Yang, H. O. Everitt, and G. Videen, "Shape matters: Plasmonic nanoparticle shape enhances interaction with dielectric substrate," *Nano Letters*, vol. 11, no. 9, pp. 3531–3537, 2011.

[184] Y. Yang, N. Akozbek, T.-H. Kim, J. M. Sanz, F. Moreno, M. Losurdo, A. S. Brown, and H. O. Everitt, "Ultraviolet–Visible Plasmonic Properties of Gallium Nanoparticles Investigated by Variable-Angle Spectroscopic and Mueller Matrix Ellipsometry," *ACS Photonics*, vol. 1, no. 7, pp. 582–589, 2014.

[185] M. W. Knight, T. Coenen, Y. Yang, B. J. M. Brenny, M. Losurdo, A. S. Brown, H. O. Everitt, and A. Polman, "Gallium Plasmonics: Deep Subwavelength Spectroscopic Imaging of Single and Interacting Gallium Nanoparticles," *ACS Nano*, vol. 9, no. 2, pp. 2049–2060, 2015.

[186] D. Tonova, M. Patrini, P. Tognini, A. Stella, P. Cheyssac, and R. Kofman, "Ellipsometric study of optical properties of liquid Ga nanoparticles," *Journal of Physics: Condensed Matter*, vol. 11, pp. 2211–2222, 1999.

[187] P. C. Wu, T. H. Kim, A. S. Brown, M. Losurdo, G. Bruno, and H. O. Everitt, "Real-time plasmon resonance tuning of liquid Ga nanoparticles by in situ spectroscopic ellipsometry," *Applied Physics Letters*, vol. 90, no. 10, p. 103 119, 2007.

[188] P. C. Wu, M. Losurdo, T.-H. Kim, S. Choi, G. Bruno, and A. S. Brown, "In situ spectroscopic ellipsometry to monitor surface plasmon resonant group-III metals deposited by molecular beam epitaxy," *Journal of Vacuum Science and Technology B*, vol. 25, no. 3, pp. 1019–1023, 2007.

[189] M. Kang, T. W. Saucer, M. V. Warren, J. H. Wu, H. Sun, V. Sih, and R. S. Goldman, "Surface plasmon resonances of Ga nanoparticle arrays," *Applied Physics Letters*, vol. 101, no. 8, pp. 1–5, 2012.

[190] G. B. Parravicini, a. Stella, P. Tognini, P. G. Merli, a. Migliori, P. Cheyssac, and R. Kofman, "Insight into the premelting and melting processes of metal nanoparticles through capacitance measurements," *Applied Physics Letters*, vol. 82, no. 2003, pp. 1461–1463, 2003.

[191] M. F. Meléndrez, G. Cárdenas, and J. Arbiol, "Synthesis and characterization of gallium colloidal nanoparticles," *Journal of Colloid and Interface Science*, vol. 346, no. 2, pp. 279–287, 2010.

[192] V. B. Kumar, A. Gedanken, G. Kimmel, and Z. Porat, "Ultrasonic cavitation of molten gallium: formation of micro- and nano-spheres," *Ultrasonics Sonochemistry*, vol. 21, no. 3, pp. 1166–1173, May 2014.

[193] A. Yamaguchi, Y. Mashima, and T. Iyoda, "Reversible size control of liquid-metal nanoparticles under ultrasonication," *Angewandte Chemie – International Edition*, vol. 54, no. 43, pp. 12 809–12 813, 2015.

[194] F. G. N. Cloke and P. L. Arnold, "Metal Vapour Synthesis; Principles and Practice," in *Comprehensive Organometallic Chemistry III*, D. M. P. Mingos and R. H. Crabtree, Eds., Elsevier, 2006, pp. 219–238.

[195] M. Nisoli, S. Stagira, S. De Silvestri, A. Stella, P. Tognini, P. Cheyssac, and R. Kofman, "Ultrafast Electronic Dynamics in Solid and Liquid Gallium Nanoparticles," *Physical Review Letters*, vol. 78, no. 18, pp. 3575–3578, 1997.

[196] Z. H. Han, B. Yang, Y. Qi, and J. Cumings, "Synthesis of low-melting-point metallic nanoparticles with an ultrasonic nanoemulsion method," *Ultrasonics*, vol. 51, no. 4, pp. 485–488, 2011.

[197] H. Friedman, S. Reich, R. Popovitz-Biro, P. von Huth, I. Halevy, Y. Koltypin, A. Gedanken, and Z. Porat, "Micro- and nano-spheres of low melting point metals and alloys, formed by ultrasonic cavitation," *Ultrasonics Sonochemistry*, vol. 20, no. 1, pp. 432–444, 2013.

[198] Y. B. Li, Y. Bando, D. Golberg, and Z. W. Liu, "Ga-filled single-crystalline MgO nanotube: Wide-temperature range nanothermometer," *Applied Physics Letters*, vol. 83, no. 5, pp. 999–1001, 2003.

[199] C. Bonchi, F. Imperi, F. Minandri, P. Visca, and E. Frangipani, "Repurposing of gallium-based drugs for antibacterial therapy," *Biofactors*, vol. 40, pp. 303–312, 2014.

[200] L. R. Bernstein, "Gallium, therapeutic effects," in *Encyclopedia of Metalloproteins*, R. H. Kretsinger, V. N. Uversky, and E. A. Permyakov, Eds. New York, NY: Springer New York, 2013, pp. 823–835.

[201] A. Rangel-Vega, L. R. Bernstein, E. A. Mandujano-Tinoco, S. J. García-Contreras, and R. García-Contreras, "Drug repurposing as an alternative for the treatment of recalcitrant bacterial infections," *Frontiers in Microbiology*, vol. 6, p. 282, 2015.

[202] O. Olakanmi, B. E. Britigan, and L. S. Schlesinger, "Gallium Disrupts Iron Metabolism of Mycobacteria Residing within Human Macrophages," *Infection and Immunity*, vol. 68, no. 10, pp. 5619–5627, 2000.

[203] Y. Kaneko, M. Thoendel, O. Olakanmi, B. E. Britigan, and P. K. Singh, "The transition metal gallium disrupts Pseudomonas aeruginosa iron metabolism and has antimicrobial and antibiofilm activity," *Journal of Clinical Investigation*, vol. 117, no. 4, pp. 877–888, 2007.

[204] K. DeLeon, F. Balldin, C. Watters, A. Hamood, J. Griswold, S. Sreedharan, and K. P. Rumbaugh, "Gallium Maltolate Treatment Eradicates *Pseudomonas aeruginosa* Infection in Thermally Injured Mice," *Antimicrobial Agents and Chemotherapy*, vol. 53, no. 4, pp. 1331–1337, 2009.

[205] O. Olakanmi, B. Kesavalu, R. Pasula, M. Y. Abdalla, L. S. Schlesinger, and B. E. Britigan, "Gallium nitrate is efficacious in murine models of tuberculosis and inhibits key bacterial Fe-dependent enzymes," *Antimicrobial Agents and Chemotherapy*, vol. 57, no. 12, pp. 6074–6080, 2013.

[206] C. H. Goss, D. B. Hornick, M. L. Aitken, G. Anderson, and E. Caldwell, "Phase 1 Pharmacokinetic and Safety Study of Intravenous Ganite (Gallium Nitrate) in Cystic Fibrosis Patients," *Pediatric pulmonology*, vol. 47, no. S35, p. 303, 2012.

[207] E. Banin, A. Lozinski, K. M. Brady, E. Berenshtein, P. W. Butterfield, M. Moshe, M. Chevion, E. P. Greenberg, and E. Banin, "The potential of desferrioxamine-gallium as an anti-Pseudomonas therapeutic agent," *Proceedings of the National Academy of Sciences of the United States of America*, vol. 105, no. 43, pp. 16 761–16 766, 2008.

[208] I. Stojiljkovic, V. Kumar, and N. Srinivasan, "Non-iron metalloporphyrins: Potent antibacterial compounds that exploit haem/Hb uptake systems of pathogenic bacteria," *Molecular Microbiology*, vol. 31, no. 2, pp. 429–442, 1999.

[209] A. B. Kelson, M. Carnevali, and V. Truong-Le, "Gallium-based anti-infectives: Targeting microbial iron-uptake mechanisms," *Current Opinion in Pharmacology*, vol. 13, no. 5, pp. 707–716, 2013.

[210] S. P. Valappil, D. Ready, E. A. Abou Neel, D. M. Pickup, L. A. O'Dell, W. Chrzanowski, J. Pratten, R. J. Newport, M. E. Smith, M. Wilson, and J. C. Knowles, "Controlled delivery of antimicrobial gallium ions from phosphate-based glasses," *Acta Biomaterialia*, vol. 5, no. 4, pp. 1198–1210, 2009.

[211] Pourshahrestani, Sara and Zeimaran, Ehsan and Adib Kadri, Nahrizul and Gargiulo, Nicola and Samuel, Shani and Naveen, Sangeetha Vasudevaraj and Kamarul, Tunku and Towler, Mark R., "Gallium-containing mesoporous bioactive glass with potent hemostatic activity and antibacterial efficacy," *Journal of Materials Chemistry B*, vol. 4, no. 1, pp. 71–86, 2016.

[212] R. Sahdev, T. I. Ansari, S. M. Higham, and S. P. Valappil, "Potential use of gallium-doped phosphate-based glass material for periodontitis treatment," *Journal of Biomaterials Applications*, vol. 30, no. 1, pp. 85–92, 2015.

[213] S. P. Valappil, H. H. P. Yiu, L. Bouffier, C. K. Hope, G. Evans, J. B. Claridge, S. M. Higham, and M. J. Rosseinsky, "Effect of novel antibacterial gallium-carboxymethyl cellulose on Pseudomonas aeruginosa," *Dalton Transactions*, vol. 42, no. 5, pp. 1778–1786, 2013.

[214] S. Shruti, A. J. Salinas, G. Lusvardi, G. Malavasi, L. Menabue, and M. Vallet-Regi, "Mesoporous bioactive scaffolds prepared with cerium-, gallium- and zinc-containing glasses," *Acta Biomaterialia*, vol. 9, no. 1, pp. 4836–4844, 2013.

[215] M. Franchini, G. Lusvardi, G. Malavasi, and L. Menabue, "Gallium-containing phospho-silicate glasses: Synthesis and in vitro bioactivity," *Materials Science and Engineering C: Materials for Biological Applications*, vol. 32, no. 6, pp. 1401–1406, 2012.

[216] G. Lusvardi, G. Malavasi, L. Menabue, and S. Shruti, "Gallium-containing phosphosilicate glasses: Functionalization and in-vitro bioactivity," *Materials Science and Engineering C: Materials for Biological Applications*, vol. 33, no. 6, pp. 3190–3196, 2013.

[217] A. Cochis, B. Azzimonti, C. Della Valle, R. Chiesa, C. R. Arciola, and L. Rimondini, "Biofilm formation on titanium implants counteracted by grafting gallium and silver ions," *Journal of Biomedical Materials Research Part A*, vol. 103, no. 3, pp. 1176–1187, 2015.

[218] E. Peeters, H. J. Nelis, and T. Coenye, "Resistance of planktonic and biofilm-grown Burkholderia cepacia complex isolates to the transition metal gallium," *The Journal of Antimicrobial Chemotherapy*, vol. 61, no. 5, pp. 1062–1065, 2008.

[219] O. Rzhepishevska, S. Hakobyan, B. Ekstrand-Hammarström, Y. Nygren, T. Karlsson, A. Bucht, M. Elofsson, J.-F. Boily, and M. Ramstedt, "The gallium(III)-salicylidene acylhydrazide complex shows synergistic anti-biofilm effect and inhibits toxin production by Pseudomonas aeruginosa," *Journal of Inorganic Biochemistry*, vol. 138, pp. 1–8, 2014.

[220] H. Ma, E. T. Darmawan, M. Zhang, L. Zhange, and J. D. Bryers, "Development of a poly (ether urethane) system for the controlled release of two novel anti-biofilm agents based on gallium or zinc and its efficacy to prevent bacterial biofilm formation," *Journal of Controlled Release*, vol. 172, no. 3, pp. 1–25, 2013.

[221] D. Baldoni, A. Steinhuber, W. Zimmerli, and A. Trampuz, "In vitro activity of gallium maltolate against staphylococci in logarithmic, stationary, and biofilm growth phases: Comparison of conventional and calorimetric susceptibility testing methods," *Antimicrobial Agents and Chemotherapy*, vol. 54, no. 1, pp. 157–163, 2010.

[222] C. R. Chitambar, "Medical Applications and Toxicities of Gallium Compounds," *International Journal of Environmental Research and Public Health*, vol. 7, no. 5, pp. 2337–2361, 2010.

[223] R. García-Contreras, E. Lira-Silva, R. Jasso-Chávez, I. L. Hernández-González, T. Maeda, T. Hashimoto, F. C. Boogerd, L. Sheng, T. K. Wood, and R. Moreno-Sánchez, "Isolation and characterization of gallium resistant Pseudomonas aeruginosa mutants," *International Journal of Medical Microbiology*, vol. 303, no. 8, pp. 574–582, 2013.

[224] A. Ross-Gillespie, M. Weigert, S. P. Brown, and R. Kümmerli, "Gallium-mediated siderophore quenching as an evolutionarily robust antibacterial treatment," *Evolution, Medicine and Public Health*, vol. 2014, no. 1, pp. 18–29, 2014.

[225] C. R. Chitambar, "Gallium nitrate, apoptotic effects," in *Encyclopedia of Metalloproteins*, R. H. Kretsinger, V. N. Uversky, and E. A. Permyakov, Eds. New York, NY: Springer New York, 2013, pp. 807–812.

[226] O. Olakanmi, J. S. Gunn, S. Su, S. Soni, D. J. Hassett, and B. E. Britigan, "Gallium disrupts iron uptake by intracellular and extracellular Francisella strains and exhibits therapeutic efficacy in a murine pulmonary infection model," *Antimicrobial Agents and Chemotherapy*, vol. 54, no. 1, pp. 244–253, 2010.

[227] R. Bériault, R. Hamel, D. Chenier, R. J. Mailloux, H. Joly, and V. D. Appanna, "The overexpression of NADPH-producing enzymes counters the oxidative stress evoked by gallium, an iron mimetic," *Biometals*, vol. 20, no. 2, pp. 165–176, 2007.

[228] D. Chenier, R. Beriault, R. Mailloux, M. Baquie, G. Abramia, J. Lemire, and V. Appanna, "Involvement of Fumarase C and NADH Oxidase in Metabolic Adaptation of *Pseudomonas fluorescens* Cells Evoked by Aluminum and Gallium Toxicity," *Applied and Environmental Microbiology*, vol. 74, no. 13, pp. 3977–3984, 2008.

[229] S. Cescau, H. Cwerman, S. Létoffé, P. Delepelaire, C. Wandersman, and F. Biville, "Heme acquisition by hemophores," *Biometals*, vol. 20, no. 3, pp. 603–613, 2007.

[230] M. L. Cartron, S. Maddocks, P. Gillingham, C. J. Craven, and S. C. Andrews, "Feo – transport of ferrous iron into bacteria," *Biometals*, vol. 19, no. 2, pp. 143–157, 2006.

[231] R. García-Contreras, B. Pérez-Eretza, E. Lira-Silva, R. Jasso-Chávez, R. Coria-Jiménez, A. Rangel-Vega, T. Maeda, and T. K. Wood, "Gallium induces the production of virulence factors in Pseudomonas aeruginosa," *Pathogens and disease*, vol. 70, no. 1, pp. 95–98, 2014.

[232] C. Auger, J. Lemire, V. Appanna, and V. D. Appanna, "Gallium in bacteria, metabolic and medical implications," in *Encyclopedia of Metalloproteins*, R. H. Kretsinger, V. N. Uversky, and E. A. Permyakov, Eds. New York, NY: Springer New York, 2013, pp. 800–807.

[233] M. Yang and C. R. Chitambar, "Role of oxidative stress in the induction of metallothionein-2A and heme oxygenase-1 gene expression by the antineoplastic agent gallium nitrate in human lymphoma cells," *Free Radical Biology and Medicine*, vol. 45, no. 6, pp. 763–772, 2008.

[234] J. E. Chandler, H. H. Messer, and G. Ellender, "Cytotoxicity of gallium and indium ions compared with mercuric ion," *Journal of Dental Research*, vol. 73, no. 9, pp. 1554–1559, 1994.

[235] A. Milheiro, K. Nozaki, C. J. Kleverlaan, J. Muris, H. Miura, and A. J. Feilzer, "In vitro cytotoxicity of metallic ions released from dental alloys," *Odontology*, vol. 104, no. 2, pp. 136–142, 2016.

[236] A. W. Wren, M. C. Jones, S. T. Misture, A. Coughlan, N. L. Keenan, M. R. Towler, and M. M. Hall, "A preliminary investigation into the structure, solubility and biocompatibility of solgel SiO_2-CaO-Ga_2O_3 glass-ceramics," *Materials Chemistry and Physics*, vol. 148, no. 1-2, pp. 416–425, 2014.

[237] J. C. Wataha, C. T. Hanks, and R. G. Craig, "In Vitro Synergistic, Antagonistic, and Duration of Exposure Effects of Metal Cations on Eukaryotic Cells," *Journal of Biomedical Materials Research*, vol. 26, no. 10, pp. 1297–309, 1992.

[238] J. Kubásek, D. Vojtěch, J. Lipov, and T. Ruml, "Structure, mechanical properties, corrosion behavior and cytotoxicity of biodegradable Mg-X (X=Sn, Ga, In) alloys," *Materials Science and Engineering C: Materials for Biological Applications*, vol. 33, no. 4, pp. 2421–2432, 2013.

[239] H. C. Blair, S. L. Teitelbaum, H. L. Tan, and P. H. Schlesinger, "Reversible inhibition of osteoclastic activity by bone-bound gallium (III)," *Journal of Cellular Biochemistry*, vol. 48, no. 4, pp. 401–410, 1992.

[240] E. Verron, M. Masson, S. Khoshniat, L. Duplomb, Y. Wittrant, M. Baud'huin, Z. Badran, B. Bujoli, P. Janvier, J. C. Scimeca, J. M. Bouler, and J. Guicheux, "Gallium modulates osteoclastic bone resorption in vitro without affecting osteoblasts," *British Journal of Pharmacology*, vol. 159, no. 8, pp. 1681–1692, 2010.

[241] G. Repetto and A. del Peso, "Gallium, indium, and thallium," in *Patty's Toxicology*, E. Bingham and B. Cohrssen, Eds., 6th ed., vol. 1, New York: John Wiley & Sons, Inc., 2012, ch. 10, pp. 257–354.

[242] L. R. Bernstein, T. Tanner, C. Godfrey, and B. Noll, "Chemistry and Pharmacokinetics of Gallium Maltolate, a Compound with High Oral Gallium Bioavailability," *Metal Based Drugs*, vol. 7, no. 1, pp. 33–47, 2000.

[243] P. S. Murthy, V. P. Venugopalan, P. Sahoo, S. Dhara, A. Das, and A. K. Tyagi, "Gallium Oxide Nanoparticle Induced Inhibition of Bacterial Adhesion and Biofilm Formation," in *2011 International Conference on Nanoscience, Engineering and Technology (ICONSET)*, 2011, pp. 490–493.

[244] K. Girija, S. Thirumalairajan, and D. Mangalaraj, "Morphology controllable synthesis of parallely arranged single-crystalline β-Ga_2O_3 nanorods for photocatalytic and antimicrobial activities," *Chemical Engineering Journal*, vol. 236, pp. 181–190, 2014.

[245] Z. Tzitrinovich, A. Lipovsky, A. Gedanken, and R. Lubart, "Visible light-induced OH radicals in Ga_2O_3: an EPR study," *Physical Chemistry Chemical Physics*, vol. 15, no. 31, pp. 12 977–12 981, 2013.

[246] P. Sahoo, P. S. Murthy, S. Dhara, V. P. Venugopalan, A. Das, and A. K. Tyagi, "Probing the cellular damage in bacteria induced by GaN nanoparticles using confocal laser Raman spectroscopy," *Journal of Nanoparticle Research*, vol. 15, p. 1841, 2013.

[247] M. S. Kandanapitiye, B. Valley, L. D. Yang, A. M. Fry, P. M. Woodward, and S. D. Huang, "Gallium analogue of soluble Prussian blue $KGa[Fe(CN)_6]\cdot nH_2O$: synthesis, characterization, and potential biomedical applications," *Inorganic Chemistry*, vol. 52, no. 6, pp. 2790–2792, 2013.

[248] Y. Lu, Q. Hu, Y. Lin, D. B. Pacardo, C. Wang, W. Sun, F. S. Ligler, M. D. Dickey, and Z. Gu, "Transformable liquid-metal nanomedicine," *Nature Communications*, vol. 6, p. 10 066, 2015.

[249] K. Adolfsson, M. Schneider, G. Hammarin, U. Häcker, and C. N. Prinz, "Ingestion of gallium phosphide nanowires has no adverse effect on drosophila tissue function," *Nanotechnology*, vol. 24, no. 28, p. 285 101, 2013.

[250] P. Narayanasamy, B. L. Switzer, and B. E. Britigan, "Prolonged-acting, Multitargeting Gallium Nanoparticles Potently Inhibit Growth of Both HIV and Mycobacteria in Co-Infected Human Macrophages," *Scientific Reports*, vol. 5, p. 8824, 2015.

[251] M. Managa, E. Antunes, and T. Nyokong, "Conjugates of platinum nanoparticles with gallium tetra – (4-Carboxyphenyl) porphyrin and their use in photodynamic antimicrobial chemotherapy when in solution or embedded in electrospun fiber," *Polyhedron*, vol. 76, pp. 94–101, Jul. 2014.

[252] G. Cierny and D. Dipasquale, "Treatment of Chronic Infection," *Infection*, vol. 14, no. 10, pp. 105–110, 2006.

[253] J. L. Del Pozo and R. Patel, "Infection associated with prosthetic joints," *New England Journal of Medicine*, vol. 361, no. 8, pp. 787–794, 2009.

[254] D. P. Lew and F. A. Waldvogel, "Osteomyelitis," *Lancet*, vol. 364, no. 9431, pp. 369–379, 2004.

[255] W. A. Jiranek, A. D. Hanssen, and A. S. Greenwald, "Antibiotic-loaded bone cement for infection prophylaxis in total joint replacement," *The Journal of Bone and Joint surgery – American Volume*, vol. 88, no. Table I, pp. 2487–2500, 2006.

[256] M. Biondi, F. Ungaro, F. Quaglia, and P. A. Netti, "Controlled drug delivery in tissue engineering," *Advanced Drug Delivery Reviews*, vol. 60, pp. 229–242, 2008.

[257] M. Zilberman and J. J. Elsner, "Antibiotic-eluting medical devices for various applications," *Journal of Controlled Release*, vol. 130, no. 3, pp. 202–215, 2008.

[258] P. A. Ostermann, S. L. Henry, and D. Seligson, "The role of local antibiotic therapy in the management of compound fractures," *Clinical Orthopaedics and Related Research*, no. 295, pp. 102–111, 1993.

[259] W. Leach and N. Wilson, "Trends in infection prophylaxis in orthopaedics," *Journal of the Royal College of Surgeons of Edinburgh*, vol. 37, no. 4, pp. 265–266, 1992.

[260] S. V. Dorozhkin, "Calcium Orthophosphates in Nature, Biology and Medicine," *Materials*, vol. 2, no. 2, pp. 399–498, 2009.

[261] S. V. Dorozhkin, "Amorphous calcium (ortho)phosphates," *Acta Biomaterialia*, vol. 6, no. 12, pp. 4457–4475, Dec. 2010.

[262] S. V. Dorozhkin, "Calcium orthophosphates," *Journal of Materials Science*, vol. 42, no. 4, pp. 1061–1095, 2007.

[263] S. V. Dorozhkin, "Calcium orthophosphate bioceramics," *Ceramics International*, vol. 12, no. 3-4, pp. 247–258, 2015.

[264] L. C. Chow, "Development of self-setting calcium phosphate cements," *Journal of the Ceramic Society of Japan*, vol. 99, no. 1154, pp. 954–964, 1991.

[265] R. G. Carrodeguas and S. D. Aza, "α-Tricalcium phosphate: Synthesis, properties and biomedical applications," *Acta Biomaterialia*, vol. 7, no. 10, pp. 3536–3546, 2011.

[266] C. J. Liao, F. H. Lin, K. S. Chen, and J. S. Sun, "Thermal decomposition and reconstitution of hydroxyapatite in air atmosphere," *Biomaterials*, vol. 20, no. 19, pp. 1807–1813, 1999.

[267] S. V. Dorozhkin, "Calcium Orthophosphate Cements and Concretes," *Materials*, vol. 2, no. 1, pp. 221–291, 2009.

[268] F. Barrère, C. A. van Blitterswijk, and K. de Groot, "Bone regeneration: molecular and cellular interactions with calcium phosphate ceramics," *International Journal of Nanomedicine*, vol. 1, no. 3, pp. 317–332, 2006.

[269] P. Wang, L. Zhao, J. Liu, M. D. Weir, X. Zhou, and H. H. K. Xu, "Bone tissue engineering via nanostructured calcium phosphate biomaterials and stem cells," *Bone Research*, vol. 2, p. 14 017, 2014.

[270] M. Epple, K. Ganesan, R. Heumann, J. Klesing, A. Kovtun, S. Neumann, and V. Sokolova, "Application of calcium phosphate nanoparticles in biomedicine," *Journal of Materials Chemistry*, vol. 20, no. 1, pp. 18–23, 2010.

[271] M.-P. P. Ginebra, C. Canal, M. Espanol, D. Pastorino, and E. B. Montufar, "Calcium phosphate cements as drug delivery materials," *Advanced Drug Delivery Reviews*, vol. 64, no. 12, pp. 1090–1110, 2012.

[272] B. Wopenka and J. D. Pasteris, "A mineralogical perspective on the apatite in bone," *Materials Science and Engineering C: Materials for Biological Applications*, vol. 25, no. 2, pp. 131–143, 2005.

[273] M. Jevtić, M. Mitrić, S. D. Škapin, B. Jančar, N. Ignjatović, and D. Uskoković, "Crystal structure of hydroxyapatite nanorods synthesized by sonochemical homogeneous precipitation," *Crystal Growth and Design*, vol. 8, no. 7, pp. 2217–2222, 2008.

[274] E. Boanini, M. Gazzano, and a. Bigi, "Ionic substitutions in calcium phosphates synthesized at low temperature," *Acta Biomaterialia*, vol. 6, no. 6, pp. 1882–1894, 2010.

[275] S. V. Dorozhkin, "Nanodimensional and Nanocrystalline Apatites and Other Calcium Orthophosphates in Biomedical Engineering, Biology and Medicine," *Materials*, vol. 2, no. 4, pp. 1975–2045, 2009.

[276] J. D. Pasteris, C. H. Yoder, and B. Wopenka, "Minerals in the human body: Molecular water in nominally unhydrated carbonated hydroxylapatite: The key to a better understanding of bone mineral," *American Mineralogist*, vol. 99, no. 1, pp. 16–27, 2014.

[277] J. C. Elliott, R. M. Wilson, and S. E. P. Dowker, "Apatite Structures," *Advances in X-ray Analysis*, vol. 45, pp. 172–181, 2002.

[278] S. Peroos, Z. Du, and N. H. De Leeuw, "A computer modelling study of the uptake, structure and distribution of carbonate defects in hydroxy-apatite," *Biomaterials*, vol. 27, no. 9, pp. 2150–2161, 2006.

[279] T. I. Ivanova, O. Frank-Kamenetskaya, A. B. Kol'tsov, and V. Ugolkov, "Crystal Structure of Calcium-Deficient Carbonated Hydroxyapatite. Thermal Decomposition," *Journal of solid state chemistry*, vol. 160, no. 2, pp. 340–349, 2001.

[280] I. R. Gibson and W. Bonfield, "Novel synthesis and characterization of an AB-type carbonate-substituted hydroxyapatite," *Journal of Biomedical Materials Research*, vol. 59, no. 4, pp. 697–708, 2002.

[281] S. Raynaud, E. Champion, D. Bernache-Assollant, and P. Thomas, "Calcium phosphate apatites with variable Ca/P atomic ratio I. Synthesis, characterisation and thermal stability of powders," *Biomaterials*, vol. 23, no. 4, pp. 1065–1072, 2002.

[282] I. R. Gibson, I. Rehman, S. M. Best, and W. Bonfield, "Characterization of the transformation from calcium-deficient apatite to β-tricalcium phosphate," *Journal of Materials Science: Materials in Medicine*, vol. 12, pp. 799–804, 2000.

[283] S. Raynaud, E. Champion, D. Bernache-Assollant, and J.-P. Laval, "Determination of Calcium / Phosphorus Atomic Ratio of Apatites Using X-ray Diffractometry," *Journal of the American Ceramic Society*, vol. 84, pp. 359–366, 2001.

[284] S. C. Liou and S. Y. Chen, "Transformation mechanism of different chemically precipitated apatitic precursors into β-tricalcium phosphate upon calcination," *Biomaterials*, vol. 23, no. 23, pp. 4541–4547, 2002.

[285] A. Destainville, E. Champion, D. Bernache-Assollant, and E. Laborde, "Synthesis, characterization and thermal behavior of apatitic tricalcium phosphate," *Materials Chemistry and Physics*, vol. 80, pp. 269–277, 2003.

[286] Y. Wang, S. Von Euw, F. M. Fernandes, S. Cassaignon, M. Selmane, G. Laurent, G. Pehau-Arnaudet, C. Coelho, L. Bonhomme-Coury, M.-M. Giraud-Guille, F. Babonneau, T. Azaïs, and N. Nassif, "Water-mediated structuring of bone apatite," *Nature Materials*, vol. 12, no. 12, pp. 1144–1153, 2013.

[287] C. Jäger, T. Welzel, W. Meyer-Zaika, and M. Epple, "A solid-state NMR investigation of the structure of nanocrystalline hydroxyapatite," *Magnetic Resonance in Chemistry*, vol. 44, no. 6, pp. 573–580, 2006.

[288] G. A. Fielding, M. Roy, A. Bandyopadhyay, and S. Bose, "Antibacterial and biological characteristics of silver containing and strontium doped plasma sprayed hydroxyapatite coatings," *Acta Biomaterialia*, vol. 8, no. 8, pp. 3144–3152, 2012.

[289] M. Roy, G. Fielding, H. Beyenal, A. Bandyopadhyay, and S. Bose, "Mechanical, In Vitro Antimicrobial and Biological Properties of Plasma Sprayed Silver-Doped Hydroxyapatite Coating," vol. 4, no. 3, pp. 1341–1349, 2013.

[290] Ž. Radovanović, B. Jokić, D. Veljović, S. Dimitrijević, V. Kojić, R. Petrović, and D. Janaćković, "Antimicrobial activity and biocompatibility of Ag^{+}- and Cu^{2+}-doped biphasic hydroxyapatite/α-tricalcium phosphate obtained from hydrothermally synthesized Ag^{+}- and Cu^{2+}-doped hydroxyapatite," *Applied Surface Science*, vol. 307, pp. 513–519, 2014.

[291] R. J. Chung, M. F. Hsieh, C. W. Huang, L. H. Perng, H. W. Wen, and T. S. Chin, "Antimicrobial effects and human gingival biocompatibility of hydroxyapatite sol-gel coatings," *Journal of Biomedical Materials Research Part B: Applied Biomaterials*, vol. 76, no. 1, pp. 169–178, 2006.

[292] K. S. Oh, K. J. Kim, Y. K. Jeong, and Y. H. Choa, "Effect of Fabrication Processes on the Antimicrobial Properties of Silver Doped Nano-Sized HAp," *Key Engineering Materials*, vol. 240–242, pp. 583–586, 2003.

[293] J. W. Choi, H. M. Cho, E. K. Kwak, T. G. Kwon, H. M. Ryoo, Y. K. Jeong, K. S. Oh, and H. I. Shin, "Effect of Ag-Doped Hydroxyapatite as a Bone Filler for Inflamed Bone Defects," *Key Engineering Materials*, vol. 254-256, no. 3, pp. 47–50, 2004.

[294] B. Singh, A. K. Dubey, S. Kumar, N. Saha, B. Basu, and R. Gupta, "In vitro biocompatibility and antimicrobial activity of wet chemically prepared $Ca_{10-x}Ag_x(PO_4)_6(OH)_2$ ($0.0 \leq x \leq 0.5$) hydroxyapatites," *Materials Science and Engineering C: Materials for Biological Applications*, vol. 31, no. 7, pp. 1320–1329, 2011.

[295] C. Shi, J. Gao, M. Wang, Y. Shao, L. Wang, D. Wang, and Y. Zhu, "Functional hydroxyapatite bioceramics with excellent osteoconductivity and stern-interface induced antibacterial ability," *Biomaterials Science*, pp. 699–710, 2016.

[296] N. Rameshbabu, T. S. Sampath Kumar, T. G. Prabhakar, V. S. Sastry, K. V. G. K. Murty, and K. Prasad Rao, "Antibacterial nanosized silver substituted hydroxyapatite: synthesis and characterization," *Journal of Biomedical Materials Research Part A*, vol. 80A, no. 3, pp. 581–591, 2007.

[297] A. Peetsch, C. Greulich, D. Braun, C. Stroetges, H. Rehage, B. Siebers, M. Köller, and M. Epple, "Silver-doped calcium phosphate nanoparticles: Synthesis, characterization, and toxic effects toward mammalian and prokaryotic cells," *Colloids and Surfaces B: Biointerfaces*, vol. 102, pp. 724–729, 2013.

[298] C. Shi, J. Gao, M. Wang, J. Fu, D. Wang, and Y. Zhu, "Ultra-trace silver-doped hydroxyapatite with non-cytotoxicity and effective antibacterial activity," *Materials Science and Engineering C: Materials for Biological Applications*, vol. 55, pp. 497–505, 2015.

[299] V. Stanić, D. Janaćković, S. Dimitrijević, S. B. Tanasković, M. Mitrić, M. S. Pavlović, A. Krstić, D. Jovanović, and S. Raičević, "Synthesis of antimicrobial monophase silver-doped hydroxyapatite nanopowders for bone tissue engineering," *Applied Surface Science*, vol. 257, no. 9, pp. 4510–4518, 2011.

[300] A. Costescu, C. S. Ciobanu, S. L. Iconaru, R. V. Ghita, C. M. Chifiriuc, L. G. Marutescu, and D. Predoi, "Fabrication, Characterization, and Antimicrobial Activity, Evaluation of Low Silver Concentrations in Silver-Doped Hydroxyapatite Nanoparticles," *Journal of Nanomaterials*, vol. 2013, p. 1, 2013.

[301] C. S. Ciobanu, S. L. Iconaru, M. C. Chifiriuc, A. Costescu, P. Le Coustumer, and D. Predoi, "Synthesis and Antimicrobial Activity of Silver-Doped Hydroxyapatite Nanoparticles," *BioMed Research International*, vol. 2013, no. 916218, pp. 1–10, 2013.

[302] C. S. Ciobanu, S. L. Iconaru, I. Pasuk, B. S. Vasile, A. R. Lupu, A. Hermenean, A. Dinischiotu, and D. Predoi, "Structural properties of silver doped hydroxyapatite and their biocompatibility," *Materials Science and Engineering C: Materials for Biological Applications*, vol. 33, no. 3, pp. 1395–1402, 2013.

[303] R. J. Wiglusz, A. Kedziora, A. Lukowiak, W. Doroszkiewicz, and W. Strek, "Hydroxyapatites and Europium(III) doped hydroxyapatites as a carrier of silver nanoparticles and their antimicrobial activity," *Journal of Biomedical Nanotechnology*, vol. 8, no. 4, pp. 605–612, 2012.

[304] I. Noda, F. Miyaji, Y. Ando, H. Miyamoto, T. Shimazaki, Y. Yonekura, M. Miyazaki, M. Mawatari, and T. Hotokebuchi, "Next Generation Antibacterial Hydroxyapatite Coating: Antibacterial Activity of Ag Ions in Serum," *Bioceramics Development and Applications*, vol. 1, pp. 1–3, 2010.

[305] N. A. Trujillo, R. A. Oldinski, H. Ma, J. D. Bryers, J. D. Williams, and K. C. Popat, "Antibacterial effects of silver-doped hydroxyapatite thin films sputter deposited on titanium," *Materials Science and Engineering C: Materials for Biological Applications*, vol. 32, no. 8, pp. 2135–2144, 2012.

[306] M. Honda, Y. Kawanobe, K. Ishii, T. Konishi, M. Mizumoto, N. Kanzawa, M. Matsumoto, and M. Aizawa, "In vitro and in vivo antimicrobial properties of silver-containing hydroxyapatite prepared via ultrasonic spray pyrolysis route," *Materials Science and Engineering C: Materials for Biological Applications*, vol. 33, no. 8, pp. 5008–5018, 2013.

[307] Y. Li, J. Ho, and C. P. Ooi, "Antibacterial efficacy and cytotoxicity studies of copper (II) and titanium (IV) substituted hydroxyapatite nanoparticles," *Materials Science and Engineering C: Materials for Biological Applications*, vol. 30, no. 8, pp. 1137–1144, 2010.

[308] V. Stanić, S. Dimitrijević, J. Antić-Stanković, M. Mitrić, B. Jokić, I. B. Plećaš, and S. Raičević, "Synthesis, characterization and antimicrobial activity of copper and zinc-doped hydroxyapatite nanopowders," *Applied Surface Science*, vol. 256, no. 20, pp. 6083–6089, 2010.

[309] Y. Huang, X. Zhang, R. Zhao, H. Mao, Y. Yan, and X. Pang, "Antibacterial efficacy, corrosion resistance, and cytotoxicity studies of copper-substituted carbonated hydroxyapatite coating on titanium substrate," *Journal of Materials Science*, vol. 50, no. 4, pp. 1688–1700, 2015.

[310] X. Chen, Q. L. Tang, Y. J. Zhu, C. L. Zhu, and X. P. Feng, "Synthesis and antibacterial property of zinc loaded hydroxyapatite nanorods," *Materials Letters*, vol. 89, pp. 233–235, 2012.

[311] E. S. Thian, T. Konishi, Y. Kawanobe, P. N. Lim, C. Choong, B. Ho, and M. Aizawa, "Zinc-substituted hydroxyapatite: A biomaterial with enhanced bioactivity and antibacterial properties," *Journal of Materials Science: Materials in Medicine*, vol. 24, no. 2, pp. 437–445, 2013.

[312] A. Gristina, "Biomaterial-centered infection: Microbial adhesion versus tissue integration," *Science*, vol. 237, no. 4822, pp. 1588–1595, 1987.

[313] A. Ewald, D. Hösel, S. Patel, L. M. Grover, J. E. Barralet, and U. Gbureck, "Silver-doped calcium phosphate cements with antimicrobial activity," *Acta Biomaterialia*, vol. 7, no. 11, pp. 4064–4070, 2011.

[314] T. N. Kim, Q. L. Feng, J. O. Kim, J. Wu, H. Wang, G. C. Chen, and F. Z. Cui, "Antimicrobial effects of metal ions (Ag^{+}, Cu^{2+}, Zn^{2+}) in hydroxyapatite," *Journal of Materials Science: Materials in Medicine*, vol. 9, pp. 129–134, 1998.

[315] C. Hu, J. Guo, J. Qu, and X. Hu, "Efficient destruction of bacteria with Ti(IV) and antibacterial ions in co-substituted hydroxyapatite films," *Applied Catalysis B: Environmental*, vol. 73, no. 3, pp. 345–353, 2007.

[316] O. Lysenko, O. Dubok, A. Borysenko, and O. Shinkaruk, "The biological properties of the silver- and copper-doped ceramic biomaterial," *Journal of Nanoparticle Research*, vol. 17, no. 4, p. 178, 2015.

[317] C. Rodríguez-Valencia, M. López-Álvarez, B. Cochón-Cores, I. Pereiro, J. Serra, and P. González, "Novel selenium-doped hydroxyapatite coatings for biomedical applications," *Journal of Biomedical Materials Research Part A*, vol. 101A, no. 3, pp. 853–861, 2013.

[318] J. Kolmas, E. Oledzka, M. Sobczak, and G. Nałęcz-Jawecki, "Nanocrystalline hydroxyapatite doped with selenium oxyanions: A new material for potential biomedical applications," *Materials Science and Engineering C: Materials for Biological Applications*, vol. 39, pp. 134–142, 2014.

[319] J. Kolmas, E. Groszyk, and U. Piotrowska, "Nanocrystalline hydroxyapatite enriched in selenite and manganese ions: Physicochemical and antibacterial properties," *Nanoscale Research Letters*, vol. 10, no. 1, pp. 1–9, 2015.

[320] Y. Lin, Z. Yang, and J. Cheng, "Preparation, characterization and antibacterial property of cerium substituted hydroxyapatite nanoparticles," *Journal of Rare Earths*, vol. 25, no. 4, pp. 452–456, 2007.

[321] S.-L. Iconaru, M. Motelica-Heino, and D. Predoi, "Study on europium-doped hydroxyapatite nanoparticles by fourier transform infrared spectroscopy and their antimicrobial properties," *Journal of Spectroscopy*, vol. 2013, no. 284285, p. 10, 2013.

[322] D. Gopi, S. Sathishkumar, A. Karthika, and L. Kavitha, "Development of ce3+/eu3+ dual-substituted hydroxyapatite coating on surgical grade stainless steel for improved antimicrobial and bioactive properties," *Industrial and Engineering Chemistry Research*, vol. 53, no. 52, pp. 20 145–20 153, 2014.

[323] G. Ciobanu, A. M. Bargan, and C. Luca, "New cerium(IV)-substituted hydroxyapatite nanoparticles: Preparation and characterization," *Ceramics International*, vol. 41, no. 9, Part B, pp. 12 192–12 201, 2015.

[324] M. Kurtjak, M. Vukomanović, A. Krajnc, L. Kramer, B. Turk, and D. Suvorov, "Designing Ga(III)-containing hydroxyapatite with antibacterial activity," *RSC Advances*, vol. 6, pp. 112 839–112 852, 114 2016.

[325] R. S. Bockman, A. L. Boskey, N. C. Blumenthal, N. W. Alcock, and R. P. Warrell, "Gallium increases bone calcium and crystallite perfection of hydroxyapatite," *Calcified Tissue International*, vol. 39, no. 6, pp. 376–81, Dec. 1986.

[326] R. Donnelly and A. Boskey, "The Effect of Gallium on Seeded Hydroxyapatite Growth," *Calcified Tissue International*, vol. 44, pp. 138–142, 1989.

[327] C. Blumenthal, V. Cosma, and S. Levine, "Effect of Gallium on the in Vitro Formation, Growth, and Solubility of Hydroxyapatite," *Calcified Tissue International*, vol. 45, pp. 81–87, 1989.

[328] E. Verron, A. Loubat, G. F. Carle, C. Vignes-Colombeix, I. Strazic, J. Guicheux, N. Rochet, J. M. Bouler, and J. C. Scimeca, "Molecular effects of gallium on osteoclastic differentiation of mouse and human monocytes," *Biochemical Pharmacology*, vol. 83, no. 5, pp. 671–679, 2012.

[329] R. D. Shannon, "Revised effective ionic radii and systematic studies of interatomic distances in halides and chalcogenides," *Acta Crystallographica Section A*, vol. 32, no. 5, pp. 751–767, Sep. 1976.

[330] M. Korbas, E. Rokita, W. Meyer-Klaucke, and J. Ryczek, "Bone tissue incorporates in vitro gallium with a local structure similar to gallium-doped brushite," *Journal of Biological Inorganic Chemistry*, vol. 9, no. 1, pp. 67–76, 2004.

[331] P. Melnikov, A. Teixeira, A. Malzac, and M. de B. Coelho, "Gallium-containing hydroxyapatite for potential use in orthopedics," *Materials Chemistry and Physics*, vol. 117, no. 1, pp. 86–90, 2009.

[332] B. Bujoli, J.-M. Bouler, P. Janvier, I. Khairoun, and V. Schnitzler, "Gallium-doped phosphocalcic compounds," WO/2010/100209, 2010.

[333] C. Mellier, F. Fayon, V. Schnitzler, P. Deniard, M. Allix, S. Quillard, D. Massiot, J. M. Bouler, B. Bujoli, and P. Janvier, "Characterization and Properties of Novel Gallium-Doped Calcium Phosphate Ceramics," *Inorganic chemistry*, vol. 50, no. 17, pp. 8252–8260, 2011.

[334] R. Nirmala, F. A. Sheikh, M. A. Kanjwal, J. H. Lee, S.-J. Park, R. Navamathavan, and H. Y. Kim, "Synthesis and characterization of bovine femur bone hydroxyapatite containing silver nanoparticles for the biomedical applications," *Journal of Nanoparticle Research*, vol. 13, no. 5, pp. 1917–1927, 2011.

[335] A. Rajendran, R. C. Barik, D. Natarajan, M. S. Kiran, and D. K. Pattanayak, "Synthesis, phase stability of hydroxyapatite-silver composite with antimicrobial activity and cytocompatability," *Ceramics International*, vol. 40, no. 7, Part B, pp. 10 831–10 838, 2014.

[336] M. Vukomanović, U. Repnik, T. Zavašnik-Bergant, R. Kostanjšek, S. D. Škapin, and D. Suvorov, "Is Nano-Silver Safe within Bioactive Hydroxyapatite Composites?" *ACS Biomaterials Science and Engineering*, vol. 1, no. 10, pp. 935–946, 2015.

[337] R. Torrecillas, M. Díaz, F. Barba, M. Miranda, F. Guitián, and J. S. Moya, "Synthesis and antimicrobial activity of a silver-hydroxyapatite nanocomposite," *Journal of Nanomaterials*, vol. 2009, pp. 1–7, 2009.

[338] X. Liu, Y. Mou, S. Wu, and H. C. Man, "Synthesis of silver-incorporated hydroxyapatite nanocomposites for antimicrobial implant coatings," *Applied Surface Science*, vol. 273, pp. 748–757, 2013.

[339] M. Miranda, A. Fernández, M. Díaz, L. Esteban-Tejeda, S. López-Esteban, F. Malpartida, R. Torrecillas, and J. S. Moya, "Silver-hydroxyapatite nanocomposites as bactericidal and fungicidal materials," *International Journal of Materials Research*, vol. 101, no. 1, pp. 122–127, 2010.

[340] M. Miranda, A. Fernández, S. Lopez-Esteban, F. Malpartida, J. S. Moya, and R. Torrecillas, "Ceramic/metal biocidal nanocomposites for bone-related applications," *Journal of Materials Science: Materials in Medicine*, vol. 23, no. 7, pp. 1655–1662, 2012.

[341] G. Sahni, P. Gopinath, and P. Jeevanandam, "A novel thermal decomposition approach to synthesize hydroxyapatite-silver nanocomposites and their antibacterial action against GFP-expressing antibiotic resistant E. coli," *Colloids and Surfaces B: Biointerfaces*, vol. 103, pp. 441–447, 2013.

[342] C. M. Xie, X. Lu, K. F. Wang, F. Z. Meng, O. Jiang, H. P. Zhang, W. Zhi, and L. M. Fang, "Silver nanoparticles and growth factors incorporated hydroxyapatite coatings on metallic implant surfaces for enhancement of osteoinductivity and antibacterial properties," *ACS Applied Materials and Interfaces*, vol. 6, no. 11, pp. 8580–8589, 2014.

[343] A. Akhavan, N. Sheikh, F. Khoylou, F. Naimian, and E. Ataeivarjovi, "Synthesis of antimicrobial silver/hydroxyapatite nanocomposite by gamma irradiation," *Radiation Physics and Chemistry*, vol. 98, pp. 46–50, 2014.

[344] J. Suwanprateeb, F. Thammarakcharoen, K. Wasoontararat, W. Chokevivat, and P. Phanphiriya, "Preparation and characterization of nanosized silver phosphate loaded hydroxyapatite by single step co-conversion process," *Materials Science and Engineering C: Materials for Biological Applications*, vol. 32, no. 7, pp. 2122–2128, 2012.

[345] M. R. Elahifard, S. Rahimnejad, S. Haghighi, and M. R. Gholami, "Apatite-coated Ag/AgBr/TiO_2 visible-light photocatalyst for destruction of bacteria," *Journal of the American Chemical Society*, vol. 129, no. 31, pp. 9552–9553, 2007.

[346] M. R. Elahifard, S. Rahimnejad, R. Pourbaba, S. Haghighi, and M. R. Gholami, "Photocatalytic mechanism of action of apatite-coated Ag/AgBr/TiO_2 on phenol and Escherichia coli and Bacillus subtilis bacteria under various conditions," *Progress in Reaction Kinetics and Mechanism*, vol. 36, no. 1, pp. 38–52, 2011.

[347] M. Azimzadehirani, M. Elahifard, S. Haghighi, and M. Gholami, "Highly efficient hydroxyapatite/TiO_2 composites covered by silver halides as E. coli disinfectant under visible light and dark media," *Photochemical & photobiological sciences : Official journal of the european photochemistry association and the european society for photobiology*, vol. 12, no. 10, pp. 1787–1794, 2013.

[348] L. Grenho, F. Jorge Monteiro, and M. Pia Ferraz, "In vitro analysis of the antibacterial effect of nanohydroxyapatite-ZnO composites," *Journal of Biomedical Materials Research Part A*, vol. 102, no. 10, pp. 3726–3733, 2014.

[349] A. Gupta, D. Singh, P. Raj, H. Gupta, S. Verma, and S. Bhattacharya, "Investigation of ZnO-Hydroxyapatite Nanocomposite Incorporated in Restorative Glass Ionomer Cement to Enhance Its Mechanical and Antimicrobial Properties," *Journal of Bionanoscience*, vol. 9, no. 3, pp. 190–196, 2015.

[350] M. Vukomanović, M. Logar, S. D. Škapin, and D. Suvorov, "Hydroxyapatite/gold/arginine: designing the structure to create antibacterial activity," *Journal of Materials Chemistry B*, vol. 2, no. 11, pp. 1557–1564, 2014.

[351] A. A. Mostafa, H. Oudadesse, and M. M. H. El-Sayed, "A quantitative approach for studying the bioactivity of nanohydroxyapatite/gold composites," *Journal of Biomedical Materials Research Part A*, vol. 103, no. 11, pp. 3483–3492, 2015.

[352] M. Kurtjak, M. Vukomanović, L. Kramer, and D. Suvorov, "Biocompatible nanogallium/ hydroxyapatite nanocomposite with antimicrobial activity," *Journal of Materials Science: Materials in Medicine*, vol. 27, no. 11, p. 170, 2016.

[353] M. Kurtjak, M. Vukomanović, and D. Suvorov, "Antibacterial nanocomposite of functionalized nanogold and gallium-doped hydroxyapatite," *Materials Letters*, vol. 193, pp. 126–129, 2017.

[354] P. Melnikov, V. A. Nascimento, and L. Z. Z. Consolo, "Thermal decomposition of gallium nitrate hydrate and modeling of thermolysis products," *Journal of Thermal Analysis and Calorimetry*, vol. 107, no. 3, pp. 1117–1121, 2012.

[355] Š. Miklavič, P. Kogovšek, V. Hodnik, J. Korošec, A. Kladnik, G. Anderluh, I. Gutierrez-Aguirre, P. Maček, and M. Butala, "The Pseudomonas aeruginosa RhlR-controlled aegerolysin RahU is a low-affinity rhamnolipid-binding protein," *FEMS Microbiology Letters*, vol. 362, no. 10, fnv069, 2015.

[356] L.-Y. Cao, C.-B. Zhang, and J.-F. Huang, "Influence of temperature, [Ca^{2+}], Ca/P ratio and ultrasonic power on the crystallinity and morphology of hydroxyapatite nanoparticles prepared with a novel ultrasonic precipitation method," *Materials Letters*, vol. 59, no. 14-15, pp. 1902–1906, 2005.

[357] L.-Y. Cao, C.-B. Zhang, and J.-F. Huang, "Synthesis of hydroxyapatite nanoparticles in ultrasonic precipitation," *Ceramics International*, vol. 31, no. 8, pp. 1041–1044, 2005.

[358] M. Jevtić and D. Uskoković, "Influence of Urea as Homogeneous Precipitation Agent on Sonochemical Hydroxyapatite Synthesis," *Materials Science Forum*, vol. 555, pp. 285–290, 2007.

[359] J. Wang, P. Layrolle, M. Stigter, and K. de Groot, "Biomimetic and electrolytic calcium phosphate coatings on titanium alloy: physicochemical characteristics and cell attachment," *Biomaterials*, vol. 25, no. 4, pp. 583–592, 2004.

[360] E. Landi, A. Tampieri, G. Celotti, and S. Sprio, "Densification behaviour and mechanisms of synthetic hydroxyapatites," *Journal of the European Ceramic Society*, vol. 20, no. 14-15, pp. 2377–2387, 2000.

[361] A. Person, H. Bocherens, J.-F. Saliege, F. Paris, V. Zeitoun, and M. Gérard, "Early Diagenetic Evolution of Bone Phosphate : An X-ray Diffractometry Analysis," *Journal of Archaeological Science*, vol. 22, no. 2, pp. 211–221, 1995.

[362] B. E. Warren, *X-ray diffraction*, ser. Dover Books on Physics. Dover Publications, 1990.

[363] J. I. Langford and A. J. C. Wilson, "Scherrer after sixty years: A survey and some new results in the determination of crystallite size," *Journal of Applied Crystallography*, vol. 11, no. 2, pp. 102–113, 1978.

[364] J. I. Langford, "The use of the voigt function in determining microstructural properties from diffraction data by means of pattern decomposition," in *Accuracy in powder diffraction II : proceedings of the international conference, May 26-29, 1992*, E. Prince, J. K. Stalick, International Union of Crystallography, JCPDS–International Centre for Diffraction Data, and National Institute of Standards and Technology (U.S.), Eds., National Institute of Standards and Technology, 1992, pp. 110–126.

[365] S. Weiner and O. Bar-Yosef, "States of preservation of bones from prehistoric sites in the near east: A survey," *Journal of Archaeological Science*, vol. 17, no. 2, pp. 187–196, 1990.

[366] M. M. Beasley, E. J. Bartelink, L. Taylor, and R. M. Miller, "Comparison of transmission FTIR, ATR, and DRIFT spectra: Implications for assessment of bone bioapatite diagenesis," *Journal of Archaeological Science*, vol. 46, no. 1, pp. 16–22, 2014.

[367] C. Mätzler, "Matlab functions for Mie scattering and absorption," Institut für Angewandte Physik, Jun. 2002.

[368] C. Bohren and D. R. Huffman, *Absorption and scattering of light by small particles*. New York: Wiley Interscience, 1998.

[369] A. L. Aden and M. Kerker, "Scattering of Electromagnetic Waves from Two Concentric Spheres," *Journal of applied physics*, vol. 22, no. 10, p. 1242, 1951.

[370] T. L. McMeekin, M. L. Groves, and N. J. Hipp, "Refractive Indices of Amino Acids, Proteins, and Related Substances," in *Amino Acids and Serum Proteins*, J. A. Stekol, Ed., ch. 4, pp. 54–66.

[371] T. Allen, "Particle size, shape and distribution," in *Particle Size Measurement*. Dordrecht: Springer Netherlands, 1990, pp. 124–191.

[372] S. King, C. Washington, and R. Heenan, "Polyoxyalkylene block copolymers adsorbed in hydrocarbon and fluorocarbon oil-in-water emulsions," *Physical Chemistry Chemical Physics*, vol. 7, no. 1, pp. 143–149, 2005.

[373] M. Dykstra, *Biological electron microscopy: Theory, techniques, and troubleshooting*. Springer US, 2012.

[374] C. T. K.-H. Stadtländer, "Scanning Electron Microscopy and Transmission Electron Microscopy of Mollicutes: Challenges and Opportunities," in *Modern Research and Educational Topics in Microscopy*, A. Méndez-Vilas and J. Díaz, Eds., Formatex, 2007, pp. 122–131.

[375] Z. Marczenko and M. Balcerzak, *Separation, Preconcentration and Spectrophotometry in Inorganic Analysis*, 1st ed. Amsterdam: Elsevier, 2001, p. 199.

[376] Y. Hasegawa, T. Inagake, Y. Karasawa, and A. Fujita, "Spectrophotometric determination of gallium (III) after solvent extraction of its chloro-complex with rhodamine B," *Talanta*, vol. 30, no. 9, pp. 721–723, 1983.

[377] M. Ericsson, D. Hanstorp, P. Hagberg, J. Enger, and T. Nyström, "Sorting Out Bacterial Viability with Optical Tweezers," *Journal of bacteriology*, vol. 182, no. 19, pp. 5551–5555, 2000.

[378] M. Floreani and F. Carpenedo, "One- and two-electron reduction of menadione in guinea-pig and rat cardiac tissue," *General pharmacology: The vascular system*, vol. 23, no. 4, pp. 757–762, 1992.

[379] R. M. Wilson, J. C. Elliott, S. E. P. Dowker, and R. I. Smith, "Rietveld structure refinement of precipitated carbonate apatite using neutron diffraction data," *Biomaterials*, vol. 25, no. 11, pp. 2205–2213, 2004.

[380] R. M. Wilson, J. C. Elliott, S. E. P. Dowker, and L. M. Rodriguez-Lorenzo, "Rietveld refinements and spectroscopic studies of the structure of Ca-deficient apatite," *Biomaterials*, vol. 26, no. 11, pp. 1317–1327, Apr. 2005.

[381] C. Mochales, R. M. Wilson, S. E. Dowker, and M.-P. Ginebra, "Dry mechanosynthesis of nanocrystalline calcium deficient hydroxyapatite: Structural characterisation," *Journal of Alloys and Compounds*, vol. 509, no. 27, pp. 7389–7394, 2011.

[382] Sonics & materials, "Cavitation Erosion of Ultrasonic probes," Mar. 2017, [Online]. Available: `http://www.sonics.com/liquid-processing/resources/product-literature-manuals/`.

[383] S. V. Dorozhkin and M. Epple, "Biological and medical significance of calcium phosphates," *Angewandte Chemie – International Edition*, vol. 41, no. 17, pp. 3130–46, Sep. 2002.

[384] S. Somrani, C. Rey, and M. Jemal, "Thermal evolution of amorphous tricalcium phosphate," *Journal of Materials Chemistry*, vol. 13, no. 4, pp. 888–892, 2003.

[385] G. Celotti, A. Tampieri, S. Sprio, E. Landi, L. Bertinetti, G. Martra, and C. Ducati, "Crystallinity in apatites: how can a truly disordered fraction be distinguished from nanosize crystalline domains?" *Journal of Materials Science: Materials in Medicine*, vol. 17, no. 11, pp. 1079–1087, 2006.

[386] C. Yoder, J. Pasteris, K. Worcester, D. Schermerhorn, M. Sternlieb, J. Goldenberg, and Z. Wilt, "Dehydration and Rehydration of Carbonated Fluor- and Hydroxylapatite," *Minerals*, vol. 2, no. 2, pp. 100–117, 2012.

[387] A. Krajewski, M. Mazzocchi, P. L. Buldini, A. Ravaglioli, A. Tinti, P. Taddei, and C. Fagnano, "Synthesis of carbonated hydroxyapatites: Efficiency of the substitution and critical evaluation of analytical methods," *Journal of Molecular Structure*, vol. 744-747, pp. 221–228, 2005.

[388] S. Koutsopoulos, "Synthesis and characterization of hydroxyapatite crystals: a review study on the analytical methods," *Journal of Biomedical Materials Research*, vol. 62, no. 4, pp. 600–612, 2002.

[389] N. Blumenthal, A. Posner, and J. Holmes, "Effect of preparation conditions on the properties and transformation of amorphous calcium phosphate," *Materials Research Bulletin*, vol. 7, no. 11, pp. 1181–1189, 1972.

[390] J. D. Pasteris, B. Wopenka, J. J. Freeman, K. Rogers, E. Valsami-Jones, J. A. M. Van Der Houwen, and M. J. Silva, "Lack of OH in nanocrystalline apatite as a function of degree of atomic order: Implications for bone and biomaterials," *Biomaterials*, vol. 25, no. 2, pp. 229–238, 2004.

[391] M. Vukomanović, I. Bračko, I. Poljanšek, D. Uskoković, S. D. Škapin, and D. Suvorov, "The Growth of Silver Nanoparticles and Their Combination with Hydroxyapatite To Form Composites via a Sonochemical Approach," *Crystal Growth and Design*, vol. 11, pp. 3802–3812, 2011.

[392] A. Perro, S. Reculusa, S. Ravaine, E. Bourgeat-Lami, and E. Duguet, "Design and synthesis of janus micro- and nanoparticles," *Journal of Materials Chemistry*, vol. 15, no. 35-36, pp. 3745–3760, 2005.

[393] W. Xie, C. Herrmann, K. Kömpe, M. Haase, and S. Schlücker, "Synthesis of Bifunctional Au/Pt/Au Core/Shell Nanoraspberries for in Situ SERS Monitoring of Platinum-Catalyzed Reactions," *Journal of the American Chemical Society*, vol. 133, no. 48, pp. 19 302–19 305, 2011.

[394] A. Walther and A. H. E. Müller, "Janus Particles: Synthesis, Self-Assembly, Physical Properties, and Applications," *Chemical Reviews*, vol. 113, no. 7, pp. 5194–5261, 2013.

[395] G. S. Kumar, A. Thamizhavel, Y. Yokogawa, S. N. Kalkura, and E. K. Girija, "Synthesis, characterization and in vitro studies of zinc and carbonate co-substituted nano-hydroxyapatite for biomedical applications," *Materials Chemistry and Physics*, vol. 134, no. 2-3, pp. 1127–1135, 2012.

[396] M. Šupova, "Substituted hydroxyapatites for biomedical applications: A review," *Ceramics International*, vol. 41, pp. 9203–9231, 2015.

[397] C. Eichert, C. Combes, C. Drouet, and C. Rey, "Formation and Evolution of Hydrated Surface Layers of Apatites," *Key Engineering Materials*, vol. 284-286, pp. 3–6, 2005.

[398] E. E. Wilson, A. Awonusi, M. D. Morris, D. H. Kohn, M. M. J. Tecklenburg, and L. W. Beck, "Three structural roles for water in bone observed by solid-state NMR," *Biophysical Journal*, vol. 90, no. 10, pp. 3722–3731, 2006.

[399] Y. H. Tseng, Y. L. Tsai, T. W. T. Tsai, J. C. H. Chao, C. P. Lin, S. H. Huang, C. Y. Mou, and J. C. C. Chan, "Characterization of the phosphate units in rat dentin by solid-state NMR spectroscopy," *Chemistry of Materials*, vol. 19, no. 25, pp. 6088–6094, 2007.

[400] M. Sadat-Shojai, M.-T. Khorasani, E. Dinpanah-Khoshdargi, and A. Jamshidi, "Synthesis methods for nanosized hydroxyapatite with diverse structures," *Acta Biomaterialia*, vol. 9, no. 8, pp. 7591–7621, 2013.

[401] H. Zhang, Y. Wang, Y. Yan, and S. Li, "Precipitation of biocompatible hydroxyapatite whiskers from moderately acid solution," *Ceramics International*, vol. 29, no. 4, pp. 413–418, 2003.

[402] L. Pajchel and W. Kolodziejski, "Solid-state MAS NMR, TEM, and TGA studies of structural hydroxyl groups and water in nanocrystalline apatites prepared by dry milling," *Journal of Nanoparticle Research*, vol. 15, no. 8, pp. 1–15, 2013.

[403] A. Serret, M. V. Cabañas, and M. Vallet-Regí, "Stabilization of Calcium Oxyapatites with Lanthanum(III)-Created Anionic Vacancies," *Chemistry of Materials*, vol. 12, no. 12, pp. 3836–3841, 2000.

[404] S. V. Dorozhkin, "Calcium orthophosphates: occurrence, properties, biomineralization, pathological calcification and biomimetic applications," *Biomatter*, vol. 1, no. 2, pp. 121–164, 2011.

[405] M. S. Johnsson and G. H. Nancollas, "The Role of Brushite and Octacalcium Phosphate in Apatite Formation," *Critical Reviews in Oral Biology and Medicine*, vol. 3, no. 1-2, pp. 61–82, 1992.

[406] T. J. Mason, "Sonochemistry - beyond synthesis," *Education in Chemistry*, vol. 46, no. 5, pp. 140–144, 2009.

[407] J. H. Bang and K. S. Suslick, "Applications of Ultrasound to the Synthesis of Nanostructured Materials," *Advanced Materials*, vol. 22, no. 10, pp. 1039–1059, 2010.

[408] K. Yasui, T. Tuziuti, and Y. Iida, "Dependence of the characteristics of bubbles on types of sonochemical reactors," *Ultrasonics Sonochemistry*, vol. 12, no. 1–2, pp. 43–51, 2005, Ninth Conference of the European Society of Sonochemistry.

[409] K. Yasui, "Fundamentals of acoustic cavitation and sonochemistry," in *Theoretical and Experimental Sonochemistry Involving Inorganic Systems*, M. Ashokkumar, Ed. Dordrecht: Springer Netherlands, 2011, pp. 1–29.

[410] G. I. Taylor, "The formation of emulsions in definable fields of flow," *Proceedings of the Royal Society of London A: Mathematical, Physical and Engineering Sciences*, vol. 146, no. 858, pp. 501–523, 1934.

[411] T. Leighton, *The acoustic bubble*. Academic Press, 1994.

[412] D. Ensminger and L. J. Bond, *Ultrasonics: Fundamentals, technologies, and applications*, 3rd ed., ser. Dekker Mechanical Engineering. CRC Press, 2011.

[413] A. J. Kora and J. Arunachalam, "Assessment of antibacterial activity of silver nanoparticles on Pseudomonas aeruginosa and its mechanism of action," *World Journal of Microbiology and Biotechnology*, vol. 27, no. 5, pp. 1209–1216, 2011.

[414] M. J. Regan, H. Tostmann, P. S. Pershan, O. M. Magnussen, E. DiMasi, B. M. Ocko, and M. Deutsch, "X-ray study of the oxidation of liquid-gallium surfaces," *Physical Review B*, vol. 55, pp. 10 786–10 790, 16 1997.

[415] J. M. Epp and J. G. Dillard, "Effect of ion bombardment on the chemical reactivity of gallium arsenide(100)," *Chemistry of Materials*, vol. 1, no. 3, pp. 325–330, 1989.

[416] N. Horasawa, H. Nakajima, S. Takahashi, and T. Okabe, "Behavior of pure gallium in water and various saline solutions," *Dental Materials Journal*, vol. 16, no. 2, pp. 200–208, 226, 1997.

[417] J. C. Wataha, H. Nakajima, C. T. Hanks, and T. Okabe, "Correlation of cytotoxicity with element release from mercury- and gallium-based dental alloys in vitro," *Dental Materials*, vol. 10, no. 5, pp. 298–303, 1994.

[418] G. Kaptay, "On the size and shape dependence of the solubility of nano-particles in solutions," *International Journal of Pharmaceutics*, vol. 430, no. 1–2, pp. 253–257, 2012.

[419] J. J. Kabara, D. M. Swieczkowski, A. J. Conley, and J. P. Truant, "Fatty acids and derivatives as antimicrobial agents," *Antimicrobial Agents and Chemotherapy*, vol. 2, no. 1, pp. 23–28, 1972.

[420] C. J. Zheng, J.-S. Yoo, T.-G. Lee, H.-Y. Cho, Y.-H. Kim, and W.-G. Kim, "Fatty acid synthesis is a target for antibacterial activity of unsaturated fatty acids," *FEBS Letters*, vol. 579, no. 23, pp. 5157–5162, 2005.

[421] A. P. Desbois and V. J. Smith, "Antibacterial free fatty acids: Activities, mechanisms of action and biotechnological potential," *Applied Microbiology and Biotechnology*, vol. 85, no. 6, pp. 1629–1642, 2010.

[422] M. Okamoto and P. S. Ibanez, "3: Final report on the safety assessment of oleic acid, lauric acid, palmitic acid, myristic acid, and stearic acid," *Journal of the American College of Toxicology*, vol. 6, no. 3, pp. 321–401, 1987.

[423] "Oleic acid," in *Occupational toxicants: Critical data evaluation for mak values and classification of carcinogens*, H. Greim, Ed., 1st ed., ser. The MAK-Collection for Occupational Health and Safety. Part I: MAK Value Documentations (DFG). Wiley-VCH Verlag GmbH & Co. KGaA, 2002, vol. 17.

[424] H. Yin, H. Too, and G. Chow, "The effects of particle size and surface coating on the cytotoxicity of nickel ferrite," *Biomaterials*, vol. 26, no. 29, pp. 5818–5826, 2005.

[425] R. Ghosh, L. Pradhan, Y. P. Devi, S. S. Meena, R. Tewari, A. Kumar, S. Sharma, N. S. Gajbhiye, R. K. Vatsa, B. N. Pandey, and R. S. Ningthoujam, "Induction heating studies of Fe_3O_4 magnetic nanoparticles capped with oleic acid and polyethylene glycol for hyperthermia," *Journal of Materials Chemistry*, vol. 21, pp. 13 388–13 398, 35 2011.

[426] H. Yin, P. S. Casey, M. J. McCall, and M. Fenech, "Effects of surface chemistry on cytotoxicity, genotoxicity, and the generation of reactive oxygen species induced by zno nanoparticles," *Langmuir*, vol. 26, no. 19, pp. 15 399–15 408, 2010.

[427] D. Berhanu and E. Valsami-jones, "Chapter 4 nanotoxicity: Are we confident for modelling? - an experimentalist's point of view," in *Towards efficient designing of safe nanomaterials: Innovative merge of computational approaches and experimental techniques*, The Royal Society of Chemistry, 2012, pp. 54–68.

[428] R. D. Glover, J. M. Miller, and J. E. Hutchison, "Generation of metal nanoparticles from silver and copper objects: Nanoparticle dynamics on surfaces and potential sources of nanoparticles in the environment," *ACS Nano*, vol. 5, no. 11, pp. 8950–8957, 2011.

[429] X. Chen and H. J. Schluesener, "Nanosilver: A nanoproduct in medical application," *Toxicology Letters*, vol. 176, no. 1, pp. 1–12, 2008.

[430] A. S. Takamiya, D. R. Monteiro, D. G. Bernabé, L. F. Gorup, E. R. Camargo, J. E. Gomes-Filho, S. H. P. Oliveira, and D. B. Barbosa, "In Vitro and in Vivo Toxicity Evaluation of Colloidal Silver Nanoparticles Used in Endodontic Treatments," *Journal of endodontics*, vol. 42, no. 6, pp. 953–960, 2016.

[431] P. V. AshaRani, G. Low Kah Mun, M. P. Hande, and S. Valiyaveettil, "Cytotoxicity and genotoxicity of silver nanoparticles in human cells," *ACS Nano*, vol. 3, no. 2, pp. 279–290, 2009.

[432] D. Campoccia, L. Montanaro, and C. R. Arciola, "The significance of infection related to orthopedic devices and issues of antibiotic resistance," *Biomaterials*, vol. 27, no. 11, pp. 2331–2339, 2006.

[433] R. Mikut, S. Ruden, M. Reischl, F. Breitling, R. Volkmer, and K. Hilpert, "Improving short antimicrobial peptides despite elusive rules for activity," *Biochimica et Biophysica Acta – Biomembranes*, vol. 1858, no. 5, pp. 1024–1033, 2016.

[434] J. Ayers, T. Kujofsa, P. Rago, and J. Raphael, *Heteroepitaxy of Semiconductors: Theory, Growth, and Characterization*, 2nd ed. CRC Press, 2016.

[435] Y. Zhang, J. Xu, P. Xu, Y. Zhu, X. Chen, and W. Yu, "Decoration of ZnO nanowires with Pt nanoparticles and their improved gas sensing and photocatalytic performance," *Nanotechnology*, vol. 21, no. 28, p. 285 501, 2010.

[436] H. Yasuda, H. Mori, M. Komatsu, K. Takeda, and H. Fujita, "In Situ Observation of Spontaneous Alloying in Atom Clusters," *Journal of Electron Microscopy*, vol. 41, no. 4, pp. 267–269, 1992.

[437] T. Shibata, B. Bunker, and Z. Zhang, "Size-dependent spontaneous alloying of Au-Ag nanoparticles," *Journal of the American Chemical Society*, vol. 124, no. 40, pp. 11 989–11 996, 2002.

[438] G. Ouyang, X. Tan, C. Wang, and G. Yang, "Physical and chemical origin of size-dependent spontaneous interfacial alloying of core–shell nanostructures," *Chemical Physics Letters*, vol. 420, no. 1-3, pp. 65–70, Mar. 2006.

[439] H. Mehrer, *Diffusion in Solids: Fundamentals, Methods, Materials, Diffusion-controlled Processes*, ser. Springer series in solid state science. Springer London, Limited, 2007.

[440] D. L. Beke, Z. Erdélyi, I. A. Szabó, G. A. Langer, G. Katona, and C. Cserhati, "Diffusion in Nanoscale," *Archives of Metallurgy and Materials*, vol. 49, no. 2, pp. 219–235, 2004.

[441] Z. Erdélyi and D. L. Beke, "Nanoscale volume diffusion," *Journal of Materials Science*, vol. 46, no. 20, pp. 6465–6483, Jul. 2011.

[442] T. Niiyama, S.-i. Sawada, K. S. Ikeda, and Y. Shimizu, "A numerical study upon the atomistic mechanisms of rapid diffusion in nanoclusters," *Chemical Physics Letters*, vol. 503, no. 4-6, pp. 252–255, Feb. 2011.

[443] G. Ouyang, C. X. Wang, and G. W. Yang, "Surface Energy of Nanostructural Materials with Negative Curvature and Related Size Effects," *Chemical Reviews*, vol. 109, no. 9, pp. 4221–4247, 2009.

[444] R. Ferrando, J. Jellinek, and R. L. Johnston, "Nanoalloys: from theory to applications of alloy clusters and nanoparticles," *Chemical Reviews*, vol. 108, no. 3, pp. 845–910, 2008.

[445] Y. Sun and Y. Xia, "Mechanistic study on the replacement reaction between silver nanostructures and chloroauric acid in aqueous medium," *Journal of the American Chemical Society*, vol. 126, no. 12, pp. 3892–3901, 2004.

[446] G. Schmitz, C.-B. Ene, and C. Nowak, "Reactive diffusion in nanostructures of spherical symmetry," *Acta Materialia*, vol. 57, no. 9, pp. 2673–2683, 2009.

[447] A. Gusak and K. Tu, "Interaction between the Kirkendall effect and the inverse Kirkendall effect in nanoscale particles," *Acta Materialia*, vol. 57, no. 11, pp. 3367–3373, Jun. 2009.

[448] A. M. Gusak and T. V. Zaporozhets, "Hollow nanoshell formation and collapse in binary solid solutions with large range of solubility," *Journal of Physics: Condensed Matter*, vol. 21, no. 41, p. 415 303, 2009.

[449] Y. Yin, R. M. Rioux, C. K. Erdonmez, S. Hughes, G. a. Somorjai, and a. P. Alivisatos, "Formation of hollow nanocrystals through the nanoscale Kirkendall effect," *Science*, vol. 304, no. 5671, pp. 711–714, 2004.

[450] Y. Yin, C. K. Erdonmez, A. Cabot, S. Hughes, and A. P. Alivisatos, "Colloidal Synthesis of Hollow Cobalt Sulfide Nanocrystals," *Advanced Functional Materials*, vol. 16, no. 11, pp. 1389–1399, 2006.

[451] H. J. Fan, U. Gösele, and M. Zacharias, "Formation of nanotubes and hollow nanoparticles based on Kirkendall and diffusion processes: A review," *Small*, vol. 3, no. 10, pp. 1660–71, 2007.

[452] K. N. Tu and U. Gösele, "Hollow nanostructures based on the Kirkendall effect: Design and stability considerations," *Applied Physics Letters*, vol. 86, no. 9, p. 093 111, 2005.

[453] A. M. Gusak and N. V. Storozhuk, "Competition of K and F sinks during void formation," *The Physics of Metals and Metallography*, vol. 114, no. 3, pp. 197–206, 2013.

[454] Z. Erdélyi, B. Parditka, and D. Beke, "Stress effects on the kinetics of nanoscale diffusion processes," *Scripta Materialia*, vol. 64, no. 10, pp. 938–941, 2011.

[455] C. H. Gammons, Y. Yu, and A. Williams-Jones, "The disproportionation of gold(I) chloride complexes at 25 to 200 °C," *Geochimica et Cosmochimica Acta*, vol. 61, no. 10, pp. 1971–1983, 1997.

[456] S. Kumar, K. S. Gandhi, and R. Kumar, "Modeling of Formation of Gold Nanoparticles by Citrate Method," *Industrial and Engineering Chemistry Research*, vol. 46, no. 10, pp. 3128–3136, 2007.

[457] I. Ojea-Jiménez and J. Campanera, "Molecular modeling of the reduction mechanism in the citrate-mediated synthesis of gold nanoparticles," *The Journal of Physical Chemistry C*, vol. 116, pp. 23 682–23 691, 2012.

[458] M. Wuithschick, A. Birnbaum, S. Witte, M. Sztucki, U. Vainio, N. Pinna, K. Rademann, F. Emmerling, R. Kraehnert, and J. Polte, "Turkevich in New Robes: Key Questions Answered for the Most Common Gold Nanoparticle Synthesis," *ACS Nano*, vol. 9, no. 7, pp. 7052–7071, 2015.

[459] J. Yang, J. Y. Lee, and H.-P. Too, "Core–Shell Ag–Au Nanoparticles from Replacement Reaction in Organic Medium," *The Journal of Physical Chemistry B*, vol. 109, no. 41, pp. 19 208–19 212, 2005.

[460] Q. Zhang, J. Xie, J. Y. Lee, J. Zhang, and C. Boothroyd, "Synthesis of Ag@AgAu Metal Core/Alloy Shell Bimetallic Nanoparticles with Tunable Shell Compositions by a Galvanic Replacement Reaction," *Small*, vol. 4, no. 8, pp. 1067–1071, 2008.

[461] R. Ghosh Chaudhuri and S. Paria, "Core/shell nanoparticles: Classes, properties, synthesis mechanisms, characterization, and applications," *Chemical Reviews*, vol. 112, no. 4, pp. 2373–2433, 2012.

[462] J. C. Y. Kah, N. Phonthammachai, R. C. Y. Wan, J. Song, T. White, S. Mhaisalkar, I. Ahmadb, C. Shepparda, and M. Olivoc, "Synthesis of gold nanoshells based on the depositionprecipitation process," *Gold Bulletin*, vol. 41, no. 1, pp. 23–36, 2008.

[463] Y.-F. Huang, Y.-W. Lin, and H.-T. Chang, "Growth of various Au–Ag nanocomposites from gold seeds in amino acid solutions," *Nanotechnology*, vol. 17, no. 19, pp. 4885–4894, 2006.

[464] S. Soulé, J. Allouche, J.-C. Dupin, and H. Martinez, "Design of Ag–Au nanoshell core/mesoporous oriented silica shell nanoparticles through a sol–gel surfactant templating method," *Microporous and Mesoporous Materials*, vol. 171, pp. 72–77, 2013.

[465] W. Cui, J. Li, Y. Zhang, H. Rong, W. Lu, and L. Jiang, "Effects of aggregation and the surface properties of gold nanoparticles on cytotoxicity and cell growth," *Nanomedicine: Nanotechnology, Biology and Medicine*, vol. 8, no. 1, pp. 46–53, 2012.

[466] L.-S. Wang, "Covalent gold," *Physical Chemistry Chemical Physics*, vol. 12, no. 31, pp. 8694–8705, 2010.

[467] H. Häkkinen, "The gold–sulfur interface at the nanoscale," *Nature Chemistry*, vol. 4, no. 6, pp. 443–455, 2012.

[468] A. Laguna, "Front matter," in *Modern Supramolecular Gold Chemistry*. Wiley-VCH Verlag GmbH & Co. KGaA, 2009, pp. I–XX.

[469] M. C. Gimeno, "The chemistry of gold," in *Modern Supramolecular Gold Chemistry*, A. Laguna, Ed. Wiley-VCH Verlag GmbH & Co. KGaA, 2009, pp. 1–63.

[470] D. V. Leff, L. Brandt, and J. R. Heath, "Synthesis and Characterization of Hydrophobic, Organically- Soluble Gold Nanocrystals Functionalized with Primary Amines," *Langmuir*, vol. 12, no. 20, pp. 4723–4730, 1996.

[471] A. H. Pakiari and Z. Jamshidi, "Interaction of amino acids with gold and silver clusters," *The Journal of Physical Chemistry A*, vol. 111, pp. 4391–4396, 2007.

[472] D. Zare, A. Akbarzadeh, M. Barkhi, K. Khoshnevisan, N. Bararpour, M. Noruzi, and M. Tabatabaei, "L-Arginine and L-Glutamic Acid Capped Gold Nanoparticles at Physiological pH: Synthesis and Characterization Using Agarose Gel Electrophoresis," *Synthesis and Reactivity in Inorganic, Metal-Organic, and Nano-Metal Chemistry*, vol. 42, no. 2, pp. 266–272, 2012.

[473] Z. Zhong, S. Patskovskyy, P. Bouvrette, J. H. T. Luong, and A. Gedanken, "The Surface Chemistry of Au Colloids and Their Interactions with Functional Amino Acids," *The Journal of Physical Chemistry B*, vol. 108, no. 13, pp. 4046–4052, 2004.

[474] G. Tomoaia, P. T. Frangopol, O. Horovitz, L.-D. Bobos, A. Mocanu, and M. Tomoaia-Cotisel, "The Effect of Arginine on Gold Nanoparticles in Colloidal Solutions and in Thin Films," *Journal of Nanoscience and Nanotechnology*, vol. 11, no. 9, pp. 7762–7770, 2011.

[475] F. Porta, Ž. Krpetić, L. Prati, A. Gaiassi, and G. Scarì, "Gold-ligand interaction studies of water-soluble aminoalcohol capped gold nanoparticles by NMR," *Langmuir*, vol. 24, no. 14, pp. 7061–7064, 2008.

[476] A. Majzik, L. Fülöp, E. Csapó, F. Bogár, T. Martinek, B. Penke, G. Bíró, and I. Dékány, "Functionalization of gold nanoparticles with amino acid, β-amyloid peptides and fragment," *Colloids and Surfaces B: Biointerfaces*, vol. 81, no. 1, pp. 235–241, 2010.

[477] M. Rani, L. Moudgil, B. Singh, A. Kaushal, A. Mittal, G. S. S. Saini, S. K. Tripathi, G. Singh, and A. Kaura, "Understanding the mechanism of replacement of citrate from the surface of gold nanoparticles by amino acids: a theoretical and experimental investigation and their biological application," *RSC Advances*, vol. 6, no. 21, pp. 17 373–17 383, 2016.

[478] B. D. Glišić, U. Rychlewska, and M. I. Djuran, "Reactions and structural characterization of gold(III) complexes with amino acids, peptides and proteins," *Dalton Transactions*, vol. 41, no. 23, pp. 6887–901, 2012.

[479] A. Alexandrova and W. Jorgensen, "On the Mechanism and Rate of Spontaneous Decomposition of Amino Acids," *The Journal of Physical Chemistry B*, vol. 115, no. 46, pp. 13 624–13 632, 2011.

[480] J. Zou, Z. Guo, J. A. Parkinson, Y. Chen, and P. J. Sadler, "Gold(III)-induced oxidation of glycine," *Chemical Communications*, vol. 8, no. June, pp. 1359–1360, 1999.

[481] J. Zou, J. A. Par, and P. J. Sadler, "Gold(III)-Induced Oxidation of Amino Acids and Malonic Acid: Reaction Pathways Studied by NMR Spectroscopy with Isotope Labelling," *Journal of the Chinese Chemical Society*, vol. 49, pp. 499–504, 2002.

[482] J. D. S. Newman and G. J. Blanchard, "Formation of gold nanoparticles using amine reducing agents," *Langmuir*, vol. 22, no. 13, pp. 5882–5887, 2006.

[483] T. Mortier, "An experimental study on the preparation of gold nanoparticles and their properties," PhD thesis, Faculteit Wetenschappen KU Leuven, 2006.

[484] A. Pinazo, M. A. Manresa, A. M. Marques, M. Bustelo, M. J. Espuny, and L. Perez, "Amino acid-based surfactants: New antimicrobial agents," *Advances in Colloid and Interface Science*, vol. 228, pp. 17–39, 2015.

[485] H. B. Gray and C. J. Ballhausen, "A Molecular Orbital Theory for Square Planar Metal Complexes," *Journal of the American Chemical Society*, vol. 85, no. 3, pp. 260–265, 1963.

[486] P. Schwerdtfeger, P. D. W. Boyd, A. K. Burrell, W. T. Robinson, and M. J. Taylor, "Relativistic effects in gold chemistry. 3. Gold(I) complexes," *Inorganic Chemistry*, vol. 29, no. 18, pp. 3593–3607, 1990.

[487] P. Schwerdtfeger, P. D. W. Boyd, S. Brienne, and A. K. Burrell, "Relativistic effects in gold chemistry. 4. Gold(III) and gold(V) compounds," *Inorganic Chemistry*, vol. 31, no. 16, pp. 3411–3422, 1992.

[488] W.-L. Li, Y. Li, C.-Q. Xu, X.-B. Wang, E. Vorpagel, and J. Li, "Periodicity, Electronic Structures, and Bonding of Gold Tetrahalides $[AuX_4^-]$ (X = F, Cl, Br, I, At, Uus)," *Inorganic Chemistry*, vol. 54, no. 23, pp. 11 157–11 167, 2015.

[489] C. Q. Xu, X. G. Xiong, W. L. Li, and J. Li, "Periodicity and Covalency of $[MX_2]^-$ (M = Cu, Ag, Au, Rg; X = H, Cl, CN) Complexes," *European Journal of Inorganic Chemistry*, vol. 2016, no. 9, pp. 1395–1404, 2016.

[490] P. Pyykkö, "Theoretical chemistry of gold," *Angewandte Chemie – International Edition*, vol. 43, no. 34, pp. 4412–4456, 2004.

[491] O. Crespo, "Gold–gold interactions," in *Modern Supramolecular Gold Chemistry*, A. Laguna, Ed. Wiley-VCH Verlag GmbH & Co. KGaA, 2009, pp. 65–129.

[492] E. J. Fernández and M. Monge, "Gold nanomaterials," in *Modern Supramolecular Gold Chemistry*, A. Laguna, Ed. Wiley-VCH Verlag GmbH & Co. KGaA, 2009, pp. 131–179.

[493] D. M. P. Mingos, "Structural and bonding patterns in gold clusters," *Dalton Transactions*, vol. 44, no. 15, pp. 6680–95, 2015.

[494] B. D. Glisic and M. I. Djuran, "Gold complexes as antimicrobial agents: An overview of different biological activities in relation to the oxidation state of the gold ion and the ligand structure," *Dalton Transactions*, vol. 43, pp. 5950–5969, 16 2014.

[495] T. P. Shareena Dasari, Y. Zhang, and H. Yu, "Antibacterial Activity and Cytotoxicity of Gold (I) and (III) Ions and Gold Nanoparticles," *Biochemistry and Pharmacology*, vol. 4, no. 6, p. 199, 2015.

[496] A. H. Atta, A. I. El-Shenawy, M. S. Refat, and K. M. Elsabawy, "Preparation and characterization of some gold nanometric compounds with simple organic materials as precursor: Spectroscopic, biological and anti-cancer assessments," *Journal of Molecular Structure*, vol. 1039, pp. 51–60, 2013.

[497] R. M. Carlton, "Phage Therapy: Past History and Future Prospects," *Archivum Immunologiae et Therapiae Experimentalis (Warszava)*, vol. 47, no. 5, pp. 267–274, 1999.

[498] C. Potera, "Phage renaissance: new hope against antibiotic resistance," *Environmental Health Perspectives*, vol. 121, no. 2, A48–A53, 2013.

[499] D. I. Andersson, D. Hughes, and J. Z. Kubicek-Sutherland, "Mechanisms and consequences of bacterial resistance to antimicrobial peptides," *Drug Resistance Updates*, vol. 26, pp. 43–57, 2016.

[500] R. Bragg, W. van der Westhuizen, J.-Y. Lee, E. Coetsee, and C. Boucher, "Bacteriophages as Potential Treatment Option for Antibiotic Resistant Bacteria," in *Infectious Diseases and Nanomedicine I: First International Conference (ICIDN – 2012), Dec. 15-18, 2012, Kathmandu, Nepal*, R. Adhikari and S. Thapa, Eds. New Delhi: Springer India, 2014, pp. 97–110.

[501] A. S. Nilsson, "Phage therapy–constraints and possibilities," *Upsala Journal of Medical Sciences*, vol. 119, no. 2, pp. 192–198, 2014.

[502] J. L. Balcazar, "Bacteriophages as Vehicles for Antibiotic Resistance Genes in the Environment," *PLoS Pathogens*, vol. 10, no. 7, e1004219, 2014.

[503] J. P. Bradshaw, "Cationic Antimicrobial Peptides," *BioDrugs*, vol. 17, no. 4, pp. 233–240, 2003.

[504] A. K. Marr, W. J. Gooderham, and R. E. W. Hancock, "Antibacterial peptides for therapeutic use: obstacles and realistic outlook," *Current Opinion in Pharmacology*, vol. 6, no. 5, pp. 468–472, 2006.

[505] F. Guilhelmelli, N. Vilela, P. Albuquerque, L. Derengowski, I. Silva-Pereira, and C. M. Kyaw, "Antibiotic development challenges: the various mechanisms of action of antimicrobial peptides and of bacterial resistance," *Frontiers in Microbiology*, vol. 4, p. 353, 2013.

[506] S. Maria-Neto, K. C. de Almeida, M. L. R. Macedo, and O. L. Franco, "Understanding bacterial resistance to antimicrobial peptides: From the surface to deep inside," *Biochimica et Biophysica Acta - Biomembranes*, vol. 1848, no. 11, Part B, pp. 3078–3088, 2015.

[507] M. Quinten, *Optical properties of nanoparticle systems*, 1st ed. Wiley-VCH Verlag GmbH & Co. KGaA, 2011.

[508] U. Kreibig and M. Vollmer, *Optical Properties of Metal Clusters*, 1st ed., ser. Springer Series in Materials Science. Berlin: Springer, 1995, vol. 25.

[509] E. D. Palik, *Handbook of Optical Constants of Solids*, 1st ed. Burlington: Academic Press, 2002.

[510] P. Mulvaney, "Surface Plasmon Spectroscopy of Nanosized Metal Particles," *Langmuir*, vol. 12, no. 3, pp. 788–800, Jan. 1996.

[511] R. N. Panda, M. F. Hsieh, R. J. Chung, and T. S. Chin, "FTIR, XRD, SEM and solid state NMR investigations of carbonate-containing hydroxyapatite nanoparticles synthesized by hydroxide-gel technique," *Journal of Physics and Chemistry of Solids*, vol. 64, no. 2, pp. 193–199, 2003.

[512] M. E. Fleet and X. Liu, "Local structure of channel ions in carbonate apatite," *Biomaterials*, vol. 26, no. 36, pp. 7548–7554, 2005.

[513] H. E. Mason, A. Kozlowski, and B. L. Phillips, "Solid-state NMR study of the role of H and Na in AB-type carbonate hydroxylapatite," *Chemistry of Materials*, vol. 20, no. 1, pp. 294–302, 2008.

[514] M. E. Fleet, "Infrared spectra of carbonate apatites: ν_2-Region bands," *Biomaterials*, vol. 30, no. 8, pp. 1473–1481, 2009.

[515] M. E. Fleet, X. Liu, and X. Liu, "Orientation of channel carbonate ions in apatite: Effect of pressure and composition," *American Mineralogist*, vol. 96, no. 7, pp. 1148–1157, 2011.

[516] J. P. Yesinowski and H. Eckert, "Hydrogen environments in calcium phosphates: proton MAS NMR at high spinning speeds," *Journal of the American Chemical Society*, vol. 109, no. 21, pp. 6274–6282, 1987.

[517] J. Miquel, L. Facchini, A. P. Legrand, C. Rey, and J. Lemaitre, "Solid state NMR to study calcium phosphate ceramics," *Colloids and Surfaces*, vol. 45, pp. 427–433, 1990.

[518] N. Nassif, F. Martineau, O. Syzgantseva, F. Gobeaux, M. Willinger, T. Coradin, S. Cassaignon, T. Azaïs, and M. M. Giraud-Guille, "In Vivo Inspired Conditions to Synthesize Biomimetic Hydroxyapatite," *Chemistry of Materials*, vol. 22, no. 12, pp. 3653–3663, 2010.

[519] B. Predel, "Au-Ga (Gold-Gallium)," in *Landolt-Börnstein - Group IV Physical Chemistry*, O. Madelung, Ed., ser. Phase Equilibria, Crystallographic and Thermodynamic Data of Binary Alloys. Berlin, Heidelberg: Springer Berlin Heidelberg, 1991, vol. 5, ch. Ac-Au – Au-Zr, pp. 1–5.

Bibliography

Publications Related to the Thesis

Journal Articles

M. Kurtjak, M. Vukomanović, A. Krajnc, L. Kramer, B. Turk, and D. Suvorov, "Designing Ga(III)-containing hydroxyapatite with antibacterial activity," *RSC Advances*, vol. 6, pp. 112 839–112 852, 114 2016.

M. Kurtjak, M. Vukomanović, L. Kramer, and D. Suvorov, "Biocompatible nano-gallium/hydroxyapatite nanocomposite with antimicrobial activity," *Journal of Materials Science: Materials in Medicine*, vol. 27, no. 11, p. 170, 2016.

M. Kurtjak, M. Vukomanović, and D. Suvorov, "Antibacterial nanocomposite of functionalized nanogold and gallium-doped hydroxyapatite," *Materials Letters*, vol. 193, pp. 126–129, 2017.

Book chapter

M. Kurtjak, N. Aničić, and M. Vukomanović, "Inorganic Nanoparticles: Innovative tools for Antimicrobial agents," in *Antibacterial Agents*. InTech, 2017, accepted for publication.

Conference Papers

M. Kurtjak, M. Vukomanović, and D. Suvorov, "Ga(III)-containing nanocomposite based on functionalized Au and hydroxyapatite," in *Program and abstract book, 8th Young Researchers' Day*, (Ljubljana), V. Žunič, N. Aničić, T. Sever, M. Kurtjak, S. Jovanović, and D. Klement, Eds., Ljubljana (Slovenia): Jožef Stefan Institute, Feb. 2014, p. 46.

M. Kurtjak, M. Vukomanović, and D. Suvorov, "New materials with antibacterial action of functionalized Au nanoparticles and Ga^{3+} ions," in *Final programme, 26th Annual Conference of European Society for Biomaterials*, Liverpool, Aug. 2014, P–90.

M. Kurtjak, M. Vukomanović, and D. Suvorov, "Gallium nanoparticles on hydroxyapatite," in *Program and book of abstracts, 22nd International Conference on Materials and Technology*, (Portorož (Slovenia)), M. Godec, Č. Donik, I. Paulin, A. Kocijan, Institute of Metals and Technology, National Institute of Chemistry, and Jožef Stefan Institute, Eds., Ljubljana: Institute of Metals and Technology, Oct. 2014, p. 136.

M. Kurtjak, M. Vukomanović, and D. Suvorov, "Antibacterial protection of hydroxyapatite with Ga^{3+} ions and functionalized Au nanoparticles," in *9th Young researchers' day, program and abstract book*, (Ljubljana), N. Kavčič, M. Orehek, K. Pegan, and A. Taler-Verčič, Eds., Ljubljana: Jožef Stefan Institute, Apr. 2015, p. 43.

M. Kurtjak, M. Vukomanović, and D. Suvorov, "Gallium-based antibacterial protection of hydroxyapatite," in *Program and book of abstracts, 23rd International Conference on Materials and Technology*, (Portorož (Slovenia)), M. Godec, Č. Donik, I. Paulin, A. Kocijan, Institute of Metals and Technology, National Institute of Chemistry, and Jožef Stefan Institute, Eds., Ljubljana: Institute of Metals and Technology, Sep. 2015, p. 151.

M. Kurtjak, M. Vukomanović, and D. Suvorov, "Doping of hydroxyapatite with Ga(III) ions for antibacterial protection," in *10th Young researchers' day, program and abstract book*, (Ljubljana (Slovenia)), S. Prpar Mihevc, M. Prunk, and J. Pungerčar, Eds., Ljubljana: Jožef Stefan Institute, Mar. 2016, p. 12.

M. Vukomanović, V. Žunič, M. Kurtjak, N. Aničić, and D. Suvorov, "Novel platforms for designing antimicrobial biomaterials," in *Programme and the book of abstracts, Eighteenth Annual Conference YUCOMAT 2016*, (Herceg Novi (Montenegro)), D. Uskoković and V. Radmilović, Eds., Belgrade (Serbia): Materials Research Society of Serbia, Aug. 2016, p. 29.

Other Publications

Journal Articles

M. Kurtjak and T. Urbič, "Water in the presence of inert Lennard-Jones obstacles," *Molecular Physics*, vol. 112, no. 8, pp. 1132–1148, 2014.

M. Kurtjak and T. Urbič, "A simple water model in the presence of inert Lennard-Jones obstacles II: The hydrophobic effect," *Molecular Physics*, vol. 113, no. 7, pp. 727–738, 2015.

V. Žunič, M. Kurtjak, and D. Suvorov, "Bifunctional bridging linker-assisted synthesis and characterization of TiO_2/Au nanocomposites," *Journal of Nanoparticle Research*, vol. 18, no. 11, p. 336, 2016.

Biography

The author of this thesis has obtained his secondary education at the Gimnazija Jože Plečnik Ljubljana, which he finished in 2007 as the best pupil with only the highest grades and maximum points at the Matura exam. He then studied both chemistry and guitar at the same time. In 2006 he started with the musical studies at the Academy of Music of the University of Ljubljana, where he graduated in september 2010 with an average grade of 9.92, grade 10 for the diploma recital and additional award "summa cum laude". He started studying chemistry in 2007 at the Faculty of Chemistry and Chemical Engineering of the University of Ljubljana. As a student, he was a member of the faculty's scientific team on the »Tehnologijada 2012« in Umag. He graduated in 2012 with an average grade of 9.8 and grade 10 for his diploma work in the field of theoretical Physical Chemistry, entitled "Lastnosti vode v poroznih materialih po modelu Mercedes-Benz". In 2012 he began his doctoral study in the field of Nanosciences and Nanotechnologies at the Jožef Stefan International Postgraduate School and working as a young researcher at the Advanced Materials department of the Jožef Stefan Institute. During the doctoral study he attended the Young Researchers' day three times (in 2014, 2015 and 2016) having an oral presentation in 2016, two times (in 2014 and 2015) the International conference on materials and technologies in Portorož with oral presentations and the 26th Annual Conference of the European Society for Biomaterials in Liverpool in 2014 with a poster.